LBL-16999
c.2

Lawrence Berkeley Laboratory
UNIVERSITY OF CALIFORNIA

RECEIVED
LAWRENCE
BERKELEY LABORATORY
NOV 20 1984
LIBRARY AND
DOCUMENTS SECTION

Materials & Molecular Research Division

A MICROSTRUCTURAL STUDY ON THE PROCESSING AND PROPERTIES OF HIGH-FIELD A15 SUPERCONDUCTING MATERIALS

I.-W.D. Wu
(Ph.D. Thesis)

August 1984

TWO-WEEK LOAN COPY
This is a Library Circulating Copy
which may be borrowed for two weeks.

LBL-16999
c.2

Prepared for the U.S. Department of Energy under Contract DE-AC03-76SF00098

DISCLAIMER

This document was prepared as an account of work sponsored by the United States Government. While this document is believed to contain correct information, neither the United States Government nor any agency thereof, nor the Regents of the University of California, nor any of their employees, makes any warranty, express or implied, or assumes any legal responsibility for the accuracy, completeness, or usefulness of any information, apparatus, product, or process disclosed, or represents that its use would not infringe privately owned rights. Reference herein to any specific commercial product, process, or service by its trade name, trademark, manufacturer, or otherwise, does not necessarily constitute or imply its endorsement, recommendation, or favoring by the United States Government or any agency thereof, or the Regents of the University of California. The views and opinions of authors expressed herein do not necessarily state or reflect those of the United States Government or any agency thereof or the Regents of the University of California.

LBL-16999

A MICROSTRUCTURAL STUDY ON THE PROCESSING AND PROPERTIES OF HIGH-FIELD A15 SUPERCONDUCTING MATERIALS

I-Wei Daniel Wu
Ph.D. Thesis

Lawrence Berkeley Laboratory
University of California
Berkeley, California 94720

August 1984

This work was supported by the Director, Office of Energy Research, Office of Basic Energy Sciences, Materials Science Division, and by the Director, Division of High Energy Physics, U.S. Department of Energy, under Contract No. DE-AC03-76SF00098.

A MICROSTRUCTURAL STUDY ON THE PROCESSING AND PROPERTIES OF HIGH-FIELD A15 SUPERCONDUCTING MATERIALS

ABSTRACT

Superconducting properties of high-field A15 materials were studied in terms of the physical and chemical states of the A15 phases. Higher critical current is achieved through microstructural control, which is based on knowledge of the relationships between processing variables, microstructure, and the resultant properties. The A15 materials investigated include the V_3Ga and Nb_3Al phases formed by a direct-precipitation process, the multifilamentary Nb_3Sn formed by the bronze-process, and the bronze-processed Nb_3Sn with a Mg addition.

The direct-precipitation process has been found to have an intrinsically inferior critical current and lower stability, due to the large effective grain size, off-stoichiometric composition, and the high stability of BCC films between A15 grains. For the bronze-processed Nb_3Sn multifilamentary wire, microscopic examination reveals that the reacted layer consists of a three-shell composite structure. A mechanism to account for the formation of this structure is proposed. The critical current density is apparently determined by the areal fraction, grain size and composition of the central, fine-grained layer. Isothermal aging at intermediate temperatures (700-730°C) yields the best combination of microstructural features and the highest critical current. Double-aging treatments that start at 700°C and finish at 730°C

improve the microstructural state of the A15 layer, and enhance the critical current density by approximately 50% at fields between 10 and 15T. Magnesium addition to the bronze matrix increases the attainable critical current density (100-300%) in bronze-processed multifilamentary Nb_3Sn wires as compared to the Mg-free wire at the nearly fully reacted heat treatment conditions. The Mg segregates almost completely to the Nb_3Sn layer, and resides predominately within the A15 matrix. The most obvious effect of the Mg addition is to retard grain coarsening during growth of the A15 layer, yielding a uniformly fine-grained A15 layer.

The theories of superconductivity, flux pinning, and the metallurgical principles of A15 conductors are critically examined. A mathematical model for calculating the free energy increase of a superconducting body by the passage of an external current is proposed, based on the increase in kinetic energy of the electrons. A new interpretation of inductive T_c measurement and H_{c2} estimation is also discussed.

Ph.D.

Department of Materials
Science and Mineral Eng.

J. W. Morris, Jr.
Chairman of Committee

ACKNOWLEDEGEMENT

The author is deeply indebted to Professor J. W. Morris, Jr. for the guidence, understanding, and generous support, which he willingly provided thoughout the course of this research. Without his efforts toward establishing a superconducting materials research center for fusion at Berkeley, this study would have been impossible. Special thanks are extended to Professors D. R. deFontaine and T. Van Duzer, who in their respective fields of metallurgy and electrical engineering, spent some precious time reviewing this lengthy manuspcript. Thanks are also extended to my colleagues, especially to Drs. B. Fultz, H. J. Kim, H. J. Lee, and W. V. Hassenzahl for their many useful comments and suggestions.

I would also like to acknowledge the members of the superconducting subgroup, past and present, who had provided a pleasurable environment to work with and supported each other closely. The special thanks are due to Mr. D. R. Dietderich, J. T. Holthuis, and Ms. P. Johnson-Walls and J. Glazer.

Acknowledgement is also due for the assistance provided by the supporting staff of the Materials and Molecular Research Division, Lawrence Berkeley Laboratory. In particular I would like to thank Ms. G. Pelatowski (line drawing), E. Fong (SEM), and Mr. K. Gaugler (Auger), J. Jacobson (optical and wire drawing), D. Newhart (ingot), W. Wong (machining), and J. Servence (electrical).

I am also grateful to Ms. J. Shull and M. Pelton, and Mr. P. J. Shen for their assistance in prepareing this manuscript.

Thanks are extented to Dr. S. Wen and M. Hong for their help in the theoretical strain energy study. Mr. D. E. Wedge taught me patiently computer programing to solve the strain energy problem is deeply acknowledged. Professor L. J. Chen of National Tsing Hua University, who strongly recommended and encouraged me to come to Berkeley four years ago, is also gratefully acknowledged.

Very, very special thanks is owed to my mother, Meimin Wu-Lin, and my sisters and their housbands. Their love, understanding and encouragement though the years have been my emotional support.

Acknowledgement and thanks for the support of this research are also due to the Director, Office of Energy Research, Office of Basic Energy Sciences, Materials Science Division, and to the Director, Division of High Energy Physics, US Dept. of Energy under contract No. DE-AC03-76SF00098, and to the International Business Machine Corp. though the 1982 T. J. Watson Scholarship.

TABLE OF CONTETS

I. Introduction ---------- 1

References ---------- 6

II. Fundamental Phenomena of Superconductivity ---------- 7

A. Theory of Superconductivity ---------- 7

1. Microscopic Theory ---------- 7

2. Thermodynamics of Superconductivity ---------- 8

3. The phenomenological Theories of Type-I Superconductors 10

4. Type-II Superconductors ---------- 11

B. Thermodynamics Variables and Principles of Property Measurements ---------- 13

1. The Gibbs Free Energy of an Electro-Magnetic Body ----- 13

2. The increase of Internal Energy ---------- 14

3. Phase Transition and the Derivatives of Free Energy --- 18

4. Measurements of Superconducting Properties ---------- 21

References ---------- 24

III. Theory of Flux Pinning ---------- 25

A. Irreversible Properties of Type-II Superconductors ------- 25

B. Theories of Flux Pinning ---------- 28

1. Specific Pinning Forces ---------- 28

2. Summation of Specific Pinning Forces ---------- 32

C. Pinning Mechanism of Flux Lines by Grain Boundaries ------ 35

References ---------- 39

IV. Metallurgy of A15 Conductors ---------- 43

A. Introduction ---------- 43

B. Stability of A15 Compounds ---------- 44

C. Advantages and Disadvantages of Various Fabrication Techniques for Contious Filament Conductors ---------- 49

1. Conventional Bronze Process ---------- 50

2. The External Bronze Process ---------- 52

3. The Internal Tin Bronze Process ---------- 54

4. The Internal Tubing Process ---------- 56

5. The ECN Powder Method ---------- 57

6. The Modified Jelly-Roll Method ---------- 58

D. A15 Superconducting Wires Produced by Discontious Filament 59

1. The in-situ Method ---------- 59

2. Powder Metallurgy ---------- 60

3. Infiltration Process ---------- 61

4. Controlled Precipitation Process ---------- 62

Table IV ---------- 64

References ---------- 65

V. Experimental Procedure ---------- 70

A. Materials Preparation and Heat Treatment ---------- 70

1. Direct Precipitated V_3Ga and Nb_3Al ---------- 70

2. Conventional Bronze Processed Nb_3Sn Multifilamentart Wire ---------- 71

3. Bronze Processed Multifilamentary Nb_3Sn Wires with Magnesium Addition to the Bronze ---------- 71

B. Materials Characterization ---------- 73

1. Optical and Scanning Electron Microscopy ---------- 73

2. Transmission Electron Microscopy ---------- 74

3. Convergent Beam Electron Diffraction ---------- 76

4. The STEM/EDXS Analysis ---------- 76

5. The Electron Microprobe Analysis ---------- 77

6. The Scanning Auger Microprobe Analysis ---------- 77

C. Superconducting Property Measurements ---------- 78

1. Inductive Transition Temperature Measurement ---------- 78

2. Critical Current Characteristics Measurement ---------- 79

3. The Upper Critical Field ---------- 80

Table V ---------- 81

References ---------- 82

VI. The Microstructures of Direct-Precipitated V_3Ga and Nb_3Al --- 83

A. Introduction ---------- 83

B. Superconducting Properties ---------- 88

1. The Transition Temperature Measurement ---------- 88

2. The Upper Critical $Field_{c2}$ ---------- 89

3. Critical Current Characteristics ---------- 89

C. Results ---------- 90

1. The Recovery of Deformation ---------- 90

2. The Microstructures of Precipitated V-15.6 at%Ga ------ 91

3. The Microstructures of Precipitated V-18 at%Ga -------- 94

4. The Microstructures of precipitated Nb-17.8 at%Al ----- 96

5. Grain Sizes of Precipitated A15 Phases ---------- 97

6. The Crystallographic Orientation Relationship --------- 98

7. The Microstructures of Fully Annealed V-18 at%Ga ------ 100

D. Discussion ---------- 102

1. Formation Mechanism and Microstructures of A15 -------- 102

2. Correlations of Superconducting Properties and the Physical-chemical State of Precipitates ---------- 111

E. Summary ---------- 115

References ---------- 118

VII. The Influence of Heat Treatment on the Structure and Properties of Bronze-Processed Multifilamentary Nb_3Sn Superconducting Wire ---------- 121

A. Introduction ---------- 121

B. Experimental Procedure ---------- 123

1. Sample Geometry and Heat Treatment ---------- 123

2. Materials Characterization ---------- 123

3. Superconducting Property Measurements ---------- 125

C. Results and Discussion ---------- 126

1. Conventional Heat Treatments ---------- 127

2. Double-Aging Treatments ---------- 141

D. Conclusion ---------- 146

Tables VII ---------- 149

References ---------- 153

VIII. The Influence of Magnesium Addition to the Bronze on the Critical Current of Bronze-Processed Multifilamentary Nb_3Sn Superconducting Wires ---------- 156

A. Introduction ---------- 156

B. Experimental ---------- 157

1. Wire Manufacture ---------- 157

2. Heat Treatment ---------- 158

3. Measurement of the Critical Current Density ---------- 159

4. Materials Characteriztion ---------- 159

C. Results and Discussion ---------- 160

1. The Influence of Mg on Wire Drawing and Reaction Rate - 160

2. The Influence of Mg on the Critical Current Density --- 161

3. The Distribution of Mg in the Reacted Wire ---------- 163

4. The Influence of Mg on the Grain Size ---------- 164

5. The Influence of Mg on the Composition of the Reacted Layer ---------- 165

D. Summary ---------- 166

Tables VIII ---------- 168

References ---------- 170

IX. Conclusions ---------- 172

A. Theoretical Consideration of Free Energy ---------- 173

B. The Direct Precipitated V_3Ga and Nb_3Al ---------- 173

C. Conventional Bronze Processed Nb_3Sn Multifilamentary wire ---------- 174

D. Bronze Processed Multifilamentary Nb_3Sn Wires with Mg Addition to the Matrix ---------- 176

E. Inductive T_c and Extrapolated H_{c2} Measurements ---------- 176

Figures and Figure Captions ---------- 178

A. Chapter I Figures ---------- 179

B. Chapter II Figures ---------- 181

C. Chapter III Figures ---------- 184

D. Chapter IV Figures ---------- 186

E. Chapter V Figures ---------- 195

F. Chapter VI Figures ---------- 198

G. Chapter VII Figures ---------- 249

H. Chapter VIII Figures ---------- 283

I. Chapter IX Figures ---------- 300

I. INTRODUCTION

Superconductivity, discovered by Kamerlingh Onnes in 1911 [1], is the complete loss of resistivity and the nearly perfect diamagnetism at some low, but finite, temperature. It is a property of the metallic state, in that all known superconductors are metallic under the conditions that cause them to exhibit superconductivity*. This phenomena is not particularly rare as a quarter of the elements and over 1000 alloys and compounds are superconductors [2]. Metals that are not superconductors are usually either good electrical conductors at normal temperatures, such as the alkali and noble metals, or transition metals with strong magnetic moments. Superconductivity appears below a critical temperature, T_c, which is a characteristic of each material. Above T_c, superconductors behave exactly as normal metals, their resistivity decreases with decreasing temperature. At T_c, the resistivity drops sharply to zero and remains zero at all temperatures below T_c. Critical temperatures are of the order of a few degrees Kelvin--the element with the highest T_c is niobium (9.2K) and the highest known T_c is 23.4K for Nb_3Ge.

Almost immediately after the discovery of superconductivity, Onnes found that superconductivity was destroyed by the passage of a transport current density greater than a critical value J_c, or by the application of an external field greater than a critical value, H_c [4]. The J_c, H_c

* A few nonmetallic materials can be made to superconduct, i.e., under high pressure. The pressure, however, converts them to metals before they become superconducting.

and T_c of a particular material not only depend on each other but are also influenced by the metallurgical state of the material.

The factors determining the metallurgical state of a superconductor are: composition, long-range-order parameter, state of strain, and microstructures. A closed volume within the critical surface in the J, H and T three-dimensional space is the superconducting phase region. An example of A critical surface of a Nb-Ti alloy in the J, H and T three-dimensional space is shown in Fig. I-1.

Modern high-field superconductors are capable of carrying high current without energy dissipation. Figure I-2 shows the critical current densities J_c versus applied magnetic field H at 4.2K for superconducting Nb_3Sn and NbTi as compared with the normal conductor in a conventional iron-core electromagnet.

The high J_c allows the construction of highly compact machines, and the absence of energy loss reduces the necessity for internal cooling. Many large scale industrial applications of superconductivity have been proposed in the areas of high energy physics, thermonuclear fusion reactor, magnetohydrodynamics, and energy storage, transformation, and transmission.

Many factors will affect whether or not the above applications ultimately prove feasible. However, the most important factor underlying any technological application is the understanding of the superconducting material and the optimization of its properties.

In this work, high resolution microstructural analysis techniques were used successfully to study the correlations between processing and properties of A15-type superconducting materials (V_3Ga, Nb_3Al and Nb_3Sn)

fabricated by the 'direct precipitation process' and the 'bronze process'. The direct precipitation process is a monolithic method where the superconducting A15 phase (brittle in nature) is precipitated out in the relatively ductile BCC matrix. Microstructural analyses revealed the formation mechanism of the A15 phase: the nucleation is assisted by lattice defects that can be controlled by prior deformation; the growth of A15 grains follows a usual grain growth mechanism, and the morphology of the microstructure varies with different binary systems, composition, and prior deformation. The resulting superconducting properties are presented and correlated with microstructural observation.

The most common method for producing high-field Nb_3Sn superconducting wires is the "internal bronze" process. In this method, niobium rods are inserted into a Cu-Sn bronze billet and drawn into a fine, multifilamentary wire. The wire is then heat treated to form the A15 superconducting phase of Nb_3Sn through a diffusion reaction at the niobium-bronze interface. This work was undertaken to characterize the microstructure of a typical wire with a fixed internal geometry, to establish a general connection between the microstructure and the heat treatment, and to identify and correlate the microstructure parameters determining the superconductive properties. This work led to an effort to design heat treatments that would improve the microstructural state of the A15 layer so as to enhance the critical current characteristics. The success of the modification in heat treatment has obvious engineering implications, but it also gives credence to the qualitative relations between processing, microstructure and properties that emerge from the characterization studies.

A further improvement of the current carrying capacity of a bronze-route wire is of great importance. From the understanding of the correlations between processing, microstructure and properties, it is hoped that the microstructural state of the A15 layer and, hence, the critical current could be improved by the addition of a small amount of a ternary element into the bronze matrix, . Magnesium was selected for this purpose for reasons that will be given. This led to an effort to fabricate multifilamentary wire on a laboratory scale for the fundamental studies. The wires with various concentrations of Sn and Mg in the bronze matrix containing 133, 8-13μm diameter, niobium filaments were successfully fabricated by swaging and drawing processes. Microstructural and microchemical analyses revealed that the magnesium segregates into the reacted A15 layer and retards grain coarsening during growth of the A15 layer, yielding a uniformly fine-grained product. The reaction rate of the A15 phase formation is significantly altered from wire to wire by the addition of Mg and the small variation in the processing. Therefore, the comparison of the effect of Mg addition on the critical current density is made by comparing the J_c of samples at their nearly fully reacted conditions. The critical current densities of the magnesium-containing wires were enhanced compared with the magnesium-free wires. These results are presented and discussed in Chapter VIII.

In the next chapter, the fundamental theory of superconductivity is reviewed, and the principles of various property measurement methods are discussed. Particular attention will be given to the free energy describing the superconducting to normal transition, and a model of calculating the increase of free energy by the passage of electrical current is proposed. Chapter III concentrates on the theory of flux

pinning and the metallurgical parameters influencing superconducting properties. The metallurgy of A15 superconductors and various fabrication techniques to produce A15 superconductors and their advantages or drawbacks are discussed in Chapter IV. The details of experimental procedures are presented in Chapter V. The results and discussions on the microstructures and properties of V_3Ga and Nb_3Al precipitates in BCC matrixes are given in Chapter VI. In Chapter VII, the study of the influence of heat treatment on the structure and properties of a bronze-processed Nb_3Sn multifilamentary wire is presented. The following chapter discusses the influence of magnesium addition to the bronze on the critical current of bronze-processed Nb_3Sn multifilamentary wire. The conclusions of this work are given in the final chapter.

REFERENCES

1. H.K. Onnes, Phys. Lab. Univ. Leiden Nos, 119b, 120b, 122b (1911).
2. B.W. Roberts, J. Phys. Chem. Ref. Data, 5, 581 (1976). Natl. Bur. Stand. Tech. Note, 983 (1978).
3. H.K. Onnes, Commun. Phys. Lab. Univ. Leiden Suppl., 34, 133d (1913).
4. H. K. Onnes, Ibid, No. 139f (1914).

II. FUNDAMENTAL PHENOMENA OF SUPERCONDUCTIVITY

In this chapter the fundamental phenomena of superconductivity are presented. The microscopic theory (BCS theory) and thermodynamics are first reviewed, followed by the phenomenological descriptions of superconductivity. The reader who is familiar with superconductivity may proceed directly to section II.A.2 where the thermodynamic variables and principles of properties measurement are discussed.

A. THEOTY OF SUPERCONDUCTIVITY

1. Microscopic theory. The occurrence of superconductivity in bulk metals is marked by: (1) the disappearance of resistivity ($\rho_n > 0$), and (2) a near perfect diamagnetism ($x_n = -1$). (3) The normal to superconducting transition is a second order phase transformation, and (4) the transition temperature T_c depends upon the mass of the positive ion:

$$T_c m^a = constant \tag{1}$$

where α is a constant on the order of 1/2 and depends on the material. These four fundamental properties characterized the superconducting phase. Bardeen, Cooper and Schrieffer [1] suggested a microscopic theory of superconductivity that can describe all the above mentioned properties known as the BCS theory. It was shown that a net attractive potential can occur between two electrons with their momenta slightly greater than the Fermi surface due to an electron-phonon interaction. The total energy of electrons can be decreased if the decrease in the potential energy is greater than the increase in the kinetic energy.

This is possible for paired Bloch states where one electron is in the kth state and the second in the -kth state. These two electrons are bound together through the lattice disturbance (phonon) produced by each other. Two paired electrons in this state are known as the Cooper pair [3]. The distance over which this coupling occurs is of the order of the coherence length. Any scattering process will only cause an interchange of momentum between the paired electrons and the total momentum is conserved. The result of this interaction is the loss of electrical resistivity.

Using the uncertainty principle, Pippard [2] argued that the size of a bound pair is not less than about $\hbar v_f/E_b$, where the v_f is the Fermi velocity. This binding energy, E_b, turns out to be on the order of $k_b T_c$. The BCS theory supplies the proportionality constant and defines the spatial extend of a Cooper pair by the coherence length, ξ_o, where

$$\xi_o \approx 0.18 \frac{\hbar V_f}{k_b T_c} \qquad (2)$$

This distance is much larger than the interelectron spacing and the Cooper pairs are strongly overlap.

The success of the BCS theory is that it explains how the properties of superelectrons arise from first principles and a microscopic view.

2. <u>Thermodynamics of Superconductivity</u>. Although the free energy density g_n of a metal in the normal state is independent of the strength H_a of the applied magnetic field, in the superconducting state the application of a magnetic field raises the free energy density G_s of the metal by an amount $1/2\ \mu_o H_a^2$. The critical field H_c is that field

strength which would be required to raise the free energy of the superconducting state above that of the normal state. The difference in free energy density between the normal and superconducting states is,

$$g_n - g_s(H_a) = \frac{1}{2}\mu_o(H_c^{c2} - H_a^2) \tag{3}$$

By using the first law of thermodynamics [4], the difference in entropy per unit volume is:

$$S_n - S_s = -\mu_o H_c \frac{dH_c}{dT} \tag{4}$$

since H_a does not depend on T. The critical field always decreases with increasing temperature, and the right hand side of this equation must be positive. Therefore, the superconducting state has a higher degree of order than the normal state. This is in agreement with the BCS microscopic description of superconductivity [1] according to which the electrons in a superconductor condense into a highly correlated system of electron pairs.

As a consequence of thermodynamic laws, if a superconducting material is placed in an external magnetic field, the magnetic field will be excluded from the body of the superconductor. However, the superconducting and normal phases may coexist under appropriate conditions. For Type-I superconductors the interfacial energy between normal and superconducting phases is positive and the co-existence can only occur for special sample geometry in which there is a non-zero demagnetization coefficient. On the other hand, Type-II superconductors have a negative interfacial energy between normal and superconducting region.

Therefore, a spontaneous decomposition into normal and superconducting regions will result with an external field greater than a certain strength, H_{c1}. This decomposition will yield the lowest free energy when the normal region is a regular array of long rods each containing a flux quantum. The rods are called vortices or fluxoids as a result of the supercurrents surrounding them, and the regular array of the fluxoids are known as the flux-line-lattice (FLL). A FLL is depicted in Fig. II.1. Notice the directions of surface and vortex supercurrent. The net macroscopic effect is that the sample exhibits a non-perfect diamagnetism ($-1 < x_m < 0$). When the external field increases, the lattice spacing between the vortices decreases. Eventually at a critical field strength, H_{c2} the vertices overlap and superconductivity is destroyed.

3. <u>The Phenomenological Theories of Type I Superconductors</u>. Type I superconductors typically have critical field below 0.1 tesla. The Londons [5] proposed a set of equations to describe the infinite conductivity and near perfect diamagnetism of this state:

$$\mu_0 \lambda^2 d\frac{\mathbf{J}}{dt} = \mathbf{E} \tag{5}$$

and

$$\lambda^2 \nabla \times \mathbf{J} = -\mathbf{H} \tag{6}$$

where $\lambda^2 = m/\mu_0 n_s e^2$, the penetration depth, typically in the range of 500 angstrom. The penetration depth describes the depth of magnetic

field decay into the superconductor. As a result of this penetration, even Type I superconductors are not perfectly diamagnetic.

The Ginzburg-Landau theory [6] is an alternative to the London theory. To an extent, it is also a phenomenological theory in the sense that it makes certain assumptions whose justification is that they correctly describe the phase transition in zero field and T near T_c. But unlike the London theory it uses quantum mechanics to predict the effect of a magnetic field. The first assumption of the theory is that the behavior of the superconducting electrons may be described by an 'effective wave function' Ψ, which has the significance that $|\Psi|^2$ is equal to the density of superconducting electrons. It is then assumed that the difference in free energy density can be described by a power series in $|\Psi|^2$. After minimizing the free energy with respect to $|\Psi|^2$ and the vector potential, **A**, the London equations were derived with a new penetration depth,

$$\lambda^2 = \frac{m}{\mu_0 e^2 |\Psi|^2} \tag{7}$$

the penetration depth is allowed to vary spatially through $|\Psi(x)|^2$.

The consequences of the Ginzburg-Landau theory is that the penetration depth not only is field-dependent but also thickness-dependent. It also correctly predicts the change from first to second order transitions with decreasing sample thickness.

4. <u>Type-II Superconductors</u>. The Ginzburg-Landau theory leads explicitly to the concept of a surface energy between the normal and superconducting region. This interfacial energy is required by the fact that the wave functions can only vary over a finite distance. In the theory, a dimensionless parameter is introduced:

$$\kappa = \frac{\lambda(T)}{\xi(T)} \tag{8}$$

The crossover from positive to negative surface energy was found to occur for kappa equal to $1/(2^{0.5})$. Abrikosov [7] showed that for kappa greater than $1/(2^{0.5})$ the negative surface energy forces the flux surrounding normal regions to subdivide until each region contains a single quantum of flux. He went on to demonstrate that these fluxoids form a regular lattice with the wave function going to zero at lattice points. These materials are defined as Type II superconductors.

For all superconducting materials, Type I or Type II, the area under the reversible magnetization curve corresponds to the condensation energy,

$$\int M dH = \mu_0 H_c^2 \tag{9}$$

Equation 9 defines the themodynamic critical field, H_c, for a Type II superconductor. The upper and lower critical fields can be related to the thermodynamic field using the Ginzburg-Landau parameter, κ [7]:

$$H_{c1} = \frac{H_c}{\sqrt{2}\,\kappa(\ln\kappa + 0.08)} \tag{10}$$

and

$$H_{c2} = \sqrt{2}\kappa H_c \tag{11}$$

κ is related to ρ_n, the normal state resistivity, and γ, the temperature coefficient of the electronic specific heat by the relationship:

$$\kappa = \kappa_0 + 7.5\times10^{-3}\,\gamma^{\frac{1}{2}}\rho_n \tag{12}$$

where κ_0 is an intrinsic materials constant.

B. THERMODYNAMIC VARIABLES AND PRINCIPLES OF PROPERTY MEASUREMENTS.

1. The Gibbs Free Energy of an Electro-Magnetic Body. The work done by an applied magnetic field, H, to produce a change of magnetic moment, dM, of a magnetic material can be described by:

$$dW_M = \mu_o H dM \tag{13}$$

where μ_o is the magnetic permeability of free space.

By the same analogy, the work done by an applied electric field, E, to produce a change of polarization P_e of a dielectric material is:

$$dW_E = \epsilon_o E dP_e \tag{14}$$

where ε_o is the electric permeability of free space.

The Gibbs free energy of a body in the presence of electric and magnetic field is [8]

$$G = U - TS + PV - \mu_o HM - \epsilon_o EP_e \tag{15}$$

Small changes in the conditions will produce a change in G given by

$$\begin{aligned} dG = {} & dU - TdS - SdT + PdV + VdP - \mu_o HdM - \mu_o MdH \\ & - \epsilon_o EdP_e - \epsilon_o P_e dE \end{aligned} \tag{16}$$

If the temperature and pressure are kept constant (dT = dP = 0), we have

$$\begin{aligned} dG = {} & dU - TdS + PdV - \mu_o HdM - \mu_o MdH \\ & - \epsilon_o EdP_e - \epsilon_o P_e dE \end{aligned} \tag{17}$$

From the first law of thermodynamics,

$$dU = dQ - dW = TdS - PdV + \mu_o HdM + \epsilon_o EdP_e \tag{18}$$

as a result of equations 13 and 14. Therefore,

$$dG = -\mu_o MdH - \epsilon_o P_e dE \tag{19}$$

and the difference in free energy of a body when it is magnetized and polarized by an electrical and magnetic field is:

$$G(H,E) - G_o = -\mu_o \int_o^H MdH - \epsilon_o \int_o^E P_e dE \tag{20}$$

If we remove the conditions of constant temperature and pressure, i.e., dT and dP not zero, then:

$$dG = -SdT + VdP - \mu_o MdH - \epsilon_o P_e dE \tag{21}$$

This change of free energy of a dielectric and magnetic body is described in equation 21. For a superconducting body, however, the last term $-\varepsilon_o P_e dE$ is zero. This is because the ability to polarize by an external electric field is zero. Therefore, a different thermodynamic work function has to be found to describe the increase in internal energy by the passage of electric current.

2. <u>The Increase of Internal Energy</u>. The work done by a passage of external current, i.e., the increase in the internal energy, of a

superconducting body is a very complicated one. In a dielectric material, where the applied electric field, E, causes a polarization, P_e, the work done or the increase in internal energy can be described by $\varepsilon_0 P_e E$. However, by the passage of an electric current, the internal energy of a superconducting body increases, even if there is no electric field inside the body and the $\varepsilon_0 P_e E$ term is zero. In the following, I will first describe the work done by an external current using a simple two fluid model [9]. Then, in order to discuss a deeper insight of the physical meaning, a quantum mechanics treatment will be pointed out. The superconducting to normal transition critical current can then be discussed.

In the two-fluid model, a superconductor can be regarded as consisting of two interpenetrating electronic fluids, the normal electrons and superelectrons with densities n_n and n_s, respectively. At the ground state, the distribution of electrons in momentum space is isotropic, i.e., there are as many electrons travelling one way as the other. If an external current, I, is applied to the superconducting body, then each Cooper pair will have a resultant momentum, **P**, which is the same for all pairs. And an additional kinetic energy as compared with the ground state internal energy: $n_s P^2/8m$ will be observed. Therefore, the work done by the external current is

$$W_E = n_s \frac{P^2}{8m} \tag{22}$$

where m is the effective mass of the electron. The current density of the body is related to the net momentum:

$$J = en_s \frac{P}{2m} \tag{23}$$

therefore,

$$W_E \approx \frac{m}{2en_s} J^2 \tag{24}$$

Also, from the simple two fluid model, the first approximation of stored energy (or work) can be obtained, it should be noted that equation 24 is not a thermodynamic work function. The real thermodynamic work function should be able to separate explicitly by the product of an intensive and an extensive variable. However, equation 24 yields a first approximation of the value of a thermodynamic work fuction, W_e. The change of Gibbs free energy of a superconducting body, equation 24, can be rewritten as:

$$dG = -sdT + VdP - \mu_o MdH - dW_E \tag{25}$$

A more rigorous treatment can be derived from the microscopic theory. Here, only some physical meaning and the line of procedure will be argued. The mathematic derivation is still in progress, in the hope that the intensive and extensive variables can be found and correlated with the properties.

In a simplest consideration, the ground state of a superconducting body can be visualized in momentum space as depicted in Fig. II.2. there is an empty (unoccupied) shell of states below the Fermi surface, and an occupied shell of states above the Fermi surface P_f. The width

of the band is $(4m\Delta)^{0.5}$, where Δ is the half of BCS energy gap. Below the Fermi surface are the normal electrons and, above the Fermi surface, are the superelectrons. The passage of an electric current I is equivalent to a shift of momentum space by an amount **P**/2. This situation is also depicted in Figure II-3. In this case, the states which make up the pair wavefunction have momenta of the form

$$\left[\left(\mathbf{P}_i+\frac{\mathbf{P}}{2}\right)\uparrow,\left(-\mathbf{P}_i+\frac{\mathbf{P}}{2}\right)\downarrow\right]$$

instead of $(\mathbf{P}_i\uparrow, -\mathbf{P}_i\downarrow)$. The electron pairs are still able to take part in a large number of scattering processes which conserve the total momentum:

$$\left[\left(\mathbf{P}_i+\frac{\mathbf{P}}{2}\right)\uparrow,\left(-\mathbf{P}_i+\frac{\mathbf{P}}{2}\right)\downarrow\right] \Leftrightarrow \left[\left(\mathbf{P}_j+\frac{\mathbf{P}}{2}\right)\uparrow,\left(-\mathbf{P}_j+\frac{\mathbf{P}}{2}\right)\downarrow\right] \tag{26}$$

Therefore, no resistance occurs. The theoretical limit of P before the Cooper pairs start to depair into quasi-particles can be obtained from the energy consideration of Fig. II.3. The decrease in kinetic energy by depairing into quasi-particles has a higher tendency for the Cooper pairs with their total momentum in the opposite direction of **P**. It will be energetically favorable for the pair to split up if

$$P_{max} > \frac{2m\Delta}{P_l} \tag{27}$$

This is the theoretical transition momentum.

To obtain the increase of kinetic energy at certain $|P| < P_{max}$, it is possible to calculate and compare (at least for the simplest case) the total energy of the excited and ground states. Figure II.3 shows how such a task can be fulfilled. In region I, the electrons have the same states and there is no energy change. Region II was the superconducting states and becomes the normal state at the excited state, and the reverse is true for the correspondent region II. Therefore, the number of Cooper pairs bondings remain unchanged and there is no change in kinetic energy either. The internal energy of the states in region III has no change. All the increase in total energy comes from region IV. The total energy change is the sum of kinetic energy increase of electrons and the potential energy decrease due to the decrease of Cooper pair density. The density of Cooper pair is a function of condensation energy, Δ, which decreases with increaing current density. To solve the problem of total energy change by a passage of external current is a complicated one, involving the knowledge of density of states, electron distribution function, energy gap, and their dependence with temperature and net momentum, etc. Perhaps it is not even analytically solvable. This question is still in pursuit.

3. <u>Phase Transition and the Derivatives of Free Energy</u>. The normal to superconducting transition is characterized by both the first- and second-order phase transition. In the absence of applied magnetic field, the transition is a second-order one: the partial derivatives of G with respect to the extensive variables are continuous but not the second derivative. In an applied magnetic field, the transition is first-order: both the first and second partial derivatives of G are discontinuous. The intensive variables are defined in equation 21

including S, V, M: and the extensive variables are T, P, and H. There should be two more variables describing dW_e, we can designate them to be X_e and Y_e. Where X_e is the extensive variable and Y_e is the intensive variable.

$$dW_e = -Y_E dX_E \tag{28}$$

Then,

$$\begin{aligned} dG &= -SdT + VdP - \mu_o MdH - Y_E dX_E \\ &= \sum_i Y_i dX_i \end{aligned} \tag{29}$$

And by the 1st and 2nd laws of thermodynamics,

$$Y_i = \left(\frac{\partial G}{\partial X_i}\right)_{Y_{j \neq i}} \tag{30}$$

Since the first-order transition is characterized by the continuity of the first derivatives of the free energy, in the absence of a magnetic field, all the intensive variables are continuous, i.e.,

$$Y_{i(s)} = Y_{i(n)} \tag{31}$$

The second derivatives of free energy with respect to extensive variables (X_i) are discontinuous:

$$\left(\frac{\partial^2 G}{\partial X_i^2}\right)_{(S)} = \left(\frac{\partial Y_i}{\partial X_i}\right)_{(S)} \neq \left(\frac{\partial Y_i}{\partial X_i}\right)_{(N)} = \left(\frac{\partial^2 G}{\partial X_i^2}\right)_{(N)} \tag{32}$$

These quantities can be correlated to physically measurable quantities:

$$\left(\frac{\partial^2 G}{\partial T^2}\right) = -\frac{C}{VT} \tag{33a}$$

$$\left(\frac{\partial^2 G}{\partial P^2}\right) = -\kappa V \tag{33b}$$

and

$$\left(\frac{\partial^2 G}{\partial H^2}\right) = -\frac{\chi_H}{\mu_o} \tag{33c}$$

where C is the specific heat: V is the volume of the body: kappa is the compressibility, x_h is the magnetic susceptibility and μ_o is the magnetic permeability of free space (all the partial differentiations here are under the condition such that all other extensive variables are constant). The electric work function is not described here because of the lack of a simple analytical solution. However, the same thermodynamic equations are still valid. It can be visualized that the resistivity has to be one of several measurable quantities in which the mutual product represents a higher order derivative of free energy. The sharp decrease to zero of resistivity when the body is undergoing normal to superconducting transition provides the discontinuity of the derivative of the free energy. However, if the resistivity is a function in the second derivative of free energy, then the first derivative has to be constant. From the derivation of the increase of the internal energy by a net momentum, **P** in E.2., this can not be the case. Therefore, the

resistivity must be expressed by (or be one of the functions) a higher order derivative of free energy.

4. Measurements of Superconducting Property. In the last section, I have correlated the physically measurable quantities to the free energy of a superconductting body. This is driven by the belief that any external macroscopic measurement of the physical property at phase transtion is a thermodynamic one, and the physical quantity measured can be expressed by the free energy or its derivative. The most straight forward and accurate measurements are those involving a discontinuity in the thermodynamical quantity at transition. In this section, various superconducitng properties measurements are described in light of the thermodynamical variables.

a. Inductive transition temperature measurement. The principle of the measurement is based on equation 33c, the second derivative of free energy with respect to applied magnetic fijeld is discontinuous at the transition. This discontinuity is represented by x_n/μ_o. The magnetic susceptibility of the normal state is close to zero (paramagnetism) and is close to -1 for the superconducting state (diamagnetism). The general experimental setup is that a small ripple field with strength of a few kG is applied to the sample with a slowly varying temperature. The induction signal was then picked up by an inductive coil surrounding the sample. The small strength of the magnetic field prevents the disturbance of the transition temperature and monitors the change in the slop of the M-H curve close to the transition temperature in the absence of the magnetic field.

When a sample consists of superconducting phases with different transition temperatures, the inductive signal will have a gradual rise

with decreasing temperature. Instead of a sharp rise for samples that have only one phase with homogeneous T_c. Theoretically, this gradual rise of the inductive signal corresponds directly to the volume of the superconducting phase with varying T_c. However, in the real situation, this correspondence also depends upon the geometry and shielding effect, as well as the volume fractions. It is not a simple function to deconvolute and there is a lot of misinterpretation in the literature on the inductive measurement. This point will be discussed along with the experimental observations for different superconducting phase geometries in Chapters VI and VII.

b. Specific Heat Measurement. Much of the understanding of superconductors has been derived from measurements of their specific heat [10-12]. The principle of the specific heat measurement is based on equation 33a. In this measurement, joule heat is measured directly by using a differential thermo analyzer with respect to the change in temperature. At transition, there is a sudden jump on the specific heat:

$$(C_s - C_n)_{T_c} = VT_c\mu_0\left(\frac{dH_c}{dT}\right)^2_{T_c} \tag{34}$$

This is known as Rutgers' formula. By measuring the change in specific heat and the transition temperature, the slope of the critical field at T_c can be obtained and vice versa.

For a body which consists of several different T_c superconductors, the specific heat measurement can yield the information about the volume

fraction of each phase. The limitation of the method is much less than the inductive measurement, since there are no complex magnetic flux movement and geometry restrictions. The specific heat for each different phase is simply additive regardless of the geometry. However, the quantitative information is still difficult to obtain due to the high requirement of sensitivity and deconvolution of data.

c. Resistivity Measurement. The principle of the resistivity measurement is simple: the resistivity is finite at normal state and zero at superconducting state. This property, however, is not straight forward in free energy consideration because it is a high order derivative of free energy as discussed in the previous section. The measurement is done by either passing a current and observing the voltage drop in a condition that all other extensive variables are kept constant or observing the voltage drop of a very small current while changing temperature. The major difficulty of this measurement is that, in a Type II superconductor, the current transfer and flux flow-induced voltage is quite different for different field strengths, superconducting phase geometry, and experimental setup [13-14]. These points will be discussed in the following chapters.

REFERENCES

1. J. Bardeen, L. N. Cooper and J. R. Schrieffer, Phys. Rev., 106, 162 (1957).
2. A. B. Pippard, Proc. Roy. Soc. (London), A216, 547 (1953).
3. L. N. Cooper, Phys. Rev., 104, 1189 (1956).
4. A. C. Rose-Innes and E. H. Rhoderick, Introduction to Superconductivity, 2nd ed., Pergamon Press, Oxford, p. 55 (1978).
5. H. London and F. London, Proc. Roy. Soc. (London), A149, 71 (1935)μ Physica, 2, 341 (1935).
6. V. L. Ginzburg and L. D. Landau, J.E.T.P., 20, 1064 (1950).
7. A. A. Abrikosov, Sov. Phys. J.E.T.P., 5, 1174 (1957).
8. A. B. Pippard, Classical Thermodynamics, Cambridge University Press, p. 26 (1957).
9. A. B. Pippard, Physica, 19, 765 (1953).
10. P. Manuel and J. J. Veyssie, Phys. Lett., 41A, 235 (1972).
11. P. Sullivan and G. Seidel, Phys. Rev., 173, 679 (1968).
12. P. Manuel, H. Niedoba and J. J. Veyssie, Rev. Phys. Appl., 7, 107 (1972).

III. THEORY OF FLUX PINNING

Many properties of superconductors are sensitive to changes in the microstructure of these materials but none are quite as sensitive as the critical current density J_c. Increases in J_c of two or three order of magnitude are possible as a result of thermomechanical treatments in ductile superconductors and refinement of grain size in brittle materials.

The connection between the microstructure and J_c is through the immobilization of the flux line lattice (FLL) by lattice defects, a phenomenon known as flux pinning. This phenomenon was first recognized by Livingston and Schadler in 1964 [1]. They found that flux pinning is responsible for the existence of J_c and irreversible magnetization. It can be regarded as the heart and soul of most applications of superconductivity. In tunnel junction applications, however, pinning is detrimental. In this chapter, the theory of flux pinning is reviewed, with special attention given to applications of knowledge to high-field, high current superconductors.

A. IRREVERSIBLE PROPERTIES OF TYPE II SUPERCONDUCTORS.

For a Type I superconductor, the critical current is found empirically to be the current which just produces the critical field at the surface of the superconductor. which is known as the Silsbee hypothesis [2]. The critical currents of Type II superconductors below H_{c1} satisfy the Silsbee hypothesis, but above H_{c1} they are much lower than would be expected by inserting H_{c2} to the Silsbee rule, and the variation with an applied field can be quite complicated.

Flux lines in the mixed state of Type II superconductor experience a Lorentz force, F_L when a current flows in the superconductor, and can be described by:

$$\mathbf{F}_L = \mathbf{J} \times \mathbf{B} \tag{3.1}$$

where **J** is the current density and **B** is the flux density or magnetic field induction. Unless otherwise prevented, the flux lines will move in the direction of this force and, in so doing, induce an electric field, **E** = **V** x **B**, where **V** is the velocity of flux lines.

The J_c is usually defined as the current density which just produces a detectable voltage across the specimen (e.g. 1μ v/cm), and is therefore that current which first causes the flux line to flow. If there is no hindrance to the motion of flux lines, then the J_c above H_c is zero and the superconductor is reversible. It is possible to pin flux lines and prevent them from moving by interaction with microstructural features of the material, and a pinning force, $\mathbf{F}_p$ is exerted on the flux lines that opposes $\mathbf{F}_L$. The J_c is then determined by the magnitude of the pinning force:

$$\mathbf{J}_c \times \mathbf{B} = \mathbf{F}_p \tag{3.2}$$

When flux is pinned, it is reluctant to enter the specimen in an increasing field, and when the flux does penetrate, it does so slowly and penetration is not complete until the applied field is equal to H_c. On reducing the field, the flux is reluctant to leave the specimen and there is remanent flux when the external field is zero. Reversal of the

field causes the specimen to describe a complete magnetization hysteresis loop. The area of the loop is greater the stronger the flux pinning, and may be related to the critical current density of the material directly. Figure III-1(a) shows the schematic M-H curves for the same material with different levels of flux pinning. The corresponding $J_c(H)$ characteristics are shown in Fig. III-1(b).

Pinning is due to crystal lattice defects, such as dislocations, impurities, precipitates, voids, dislocation cell walls and grain boundaries. Strong pinning materials are metallurgically dirty and, by analogy with mechanically strong or magnetically hard materials, irreversible superconductors are called hard superconductors. The critical current is not a property of a particular composition but of a particular sample of superconductor and is strongly influenced by the sample's metallurgical history. Just as for mechanical strength, its value cannot be predicted with any accuracy.

The complexity can be illustrated by appealing to the analogous problem of mechanical strengthening by a hard particle dispersion in a ductile metal. The corresponding problem there is to compute the number of particles contacted by a dislocation line. For weak particles the answer depends both on the strength of the particle and on the rigidity of the dislocation line. As in the dispersion-strengthening example, we need to know the number of pins that fully contribute their f_p to F_b and the flux pinning answer will also depend on both the strength of the elementary interaction, f_p, and on the rigidity of the FLL. Unlike the dislocation case, however, the 'rigidity' is strongly dependent upon temperature and magnetic field as is the elementary force f_p.

Many empirical expressions have been proposed to describe the relation between F_p and B. A milestone in the phenomenology of flux pinning was the paper by Fietz and Webb [3]. For a number of Nb-based alloys that had been heavily cold worked, they found the pinning force density appeared to obey a scaling law of the form

$$F_p = [H_{c2}(T)]^{2.5} f(h) \tag{3.3}$$

where f(h) is a function only of the reduced magnetic field $h = H/H_{c2}$. From equation 3, it can be seen that at least for these materials, one could measure F_p and thus f(h) at one temperature, and then immediately be able to predict F_p at other temperatures simply by scaling the results $[H_{c2}(T)]^{2.5}$.

B. THEORIES OF FLUX PINNING.

1. <u>Specific pinning forces</u>. Any theory of flux pinning consists of two parts, the local interaction between one flux line and one pinning center, and the summation of this local force over the entire lattice. These two factors are not necessarily independent and further complications are introduced by their dependence upon the type of pinning center and the possibility of their changing with the field, temperature, scale of the microstructure, and the presence of more than one type of pinning center in any given sample. Experiments carried out on model systems, such as pure niobium [4], niobium alloys [3] and precipitations in vanadium [5], may give results that are not directly applicable to the high κ materials of practical interest [6].

Flux lines interact with pinning centers because the superconducting properties of the latter differ from those of the bulk of the superconductor. The strength of the interaction is related to the magnitude of this difference.

Three types of pinning interaction can be recognized: elastic, core, and magnetic [7], since the core of a fluxoid is characterized by a different atomic volume* from that of the superconducting matrix ($\sim -10^{-6}$), a fluxoid behaves like an elastic inclusion and gives rise to a permanent elastic stress field. This stress field, in turn, interacts with the dilation associated with lattice defects (first-order interaction) [8-11]. Furthermore, since the fluxoid core and matrix are characterized by dissimilar elastic moduli, the fluxoid behaves like an elastic inhomogeneity and displays an induced stress field that also interacts with the defects (second-order interaction) [10-14]. According to linear elasticity theory, these two interactions can be analyzed independently [15-17]. The first-order interaction is believed to predominate over the second-order interaction.

The core interaction results from a local change in the superconducting condensation energy at the pinning center. The normal core of the flux line represents a volume, $\pi\xi^2$ per unit length, of energy per unit volume $\sim 1/2\mu_o H_c^2$. If the pinning center is a normal particle or void of diameters $a > \xi$, then the pinning force is [20]:

$$f_p = \frac{1}{2}\mu_o H_c^2 \pi \xi a \tag{3.4}$$

* Superconducting transition is a first-order one in the presence of H.

Campbell and Evetts [6] considered that at high fields, the available condensation energy goes down as (1-b), where b is the induced field divided by the H_{c2}. Also, the length of the interacting flux line continuously decreases from a to 0 as the flux line moves away from a diameter of a defect, and the pinning force becomes:

$$f_p = \frac{1}{2}\mu_o H_c^2 \pi \xi^2 (1-b) \tag{3.5}$$

If the diameter a < ξ, then

$$f_p = \frac{1}{2}\mu_o H_c^2 \left(\frac{V}{\xi}\right)(1-b) \tag{3.6}$$

where V is the volume of the center. However, because of the small size, the center must be considered as being capable of producing only a small fluctuation in the superconducting properties. Expressing this fluctuation in the Ginzburg-Landau free energy [6] it is found:

$$f_p = \frac{1}{2}\mu_o H_c^2 \frac{\delta H_{c2}}{H_{c2}} \frac{V}{\xi}(1-b) \tag{3.7}$$

An identical result is found if the center itself represents a small change in superconducting properties, for example, as would be produced by a change in κ, due to a local variation in normal-state resistivity. Substituting for H_c in terms κ and H_{c2}, gives for the pinning force

$$f_p = \mu_o \frac{1}{4} H_{c2}^2 \frac{\Delta\kappa}{\kappa^3} \frac{V}{\xi}(1-b) \tag{3.8a}$$

for small (a < ξ) centers, and

$$f_p = \mu_o \frac{1}{4} H_{c2}^2 \left(\frac{\Delta\kappa}{\kappa^3}\right) \pi\xi a(1-b) \tag{3.8b}$$

for spherical centers (a > ~ ξ), and

$$f_p = \mu_o \frac{1}{4} H_{c2}^2 \left(\frac{\Delta\kappa}{\kappa^3}\right) \pi\xi a(1-b) \tag{3.8c}$$

for large centers.

If the center is larger than the inter-flux-line spacing d (= 1.07 (ϕ_o/B)$^{1/2}$), where ϕ_o is a magnetic quantum, then the center will contain a volume of the flux-line lattice, and it is necessary to consider magnetic andinter-flux-line interactions in addition to the core interaction. By considering the Gibbs function in mixed state and the variation of the order parameter, the pinning force per unit length of flux line for a normal center or void is [21,22]:

$$f_p = \mu_o \pi \phi_o \frac{(H_{c2} - H)^2}{2.32(2\kappa_2^2 - 1)} Bd \tag{3.9}$$

The magnetic interaction occurs when the pinning center is even larger, large enough that its dimensions exceed the superconducting penetration depth, λ. This distance is the range over which the

induction can vary appreciably, and only in a region of dimensions $>\lambda$ can an equilibrium induction be established. If the pinning center is a normal precipitate, the pinning force is derived by Campbell et al. [23]:

$$f_p = \frac{\phi_o (H_{c2} - H)}{1.16(2\kappa^2 - 1)\lambda} \tag{3.10}$$

If the pinning center is a region that can be characterized as having a value of κ slightly different from that of the main body of the superconductor, the pinning force is obtained by differentiating equation 10 with respect to κ [24]:

$$f_p = \phi_o \frac{(H_{c2} - 2H)\Delta\kappa}{2.32\kappa^3\lambda} \tag{3.11}$$

This function goes to zero and changes sign at $H = 1/2\ H_{c2}$, leading to a minimum in the pinning force versus the H curve. This means that flux prefers to be in high- κ regions at low fields and in the low- κ regions at high fields.

2. <u>Summation of specific pinning forces</u>. The second step toward the understanding of materials behavior and the verification of the theory is to decide how these individual forces are to be summed over the whole FLL. It is most strightforward to simply add all of the individual interactions. This method assumes that the flux lines act

individually and ignores any inter-flux-line forces. The alternative approach, due to Labusch [25], is to assume that the primary forces produce local elastic distortions of the FLL. The flux lines undergo limited displacement and cannot take up positions of minimum energy. The total pinning force is related to the dissipation of the stored energy in the lattice, and is proportional to $n_v f_p^2/C$, where n_v is the density of pinning sites per unit volume and C is some appropriate lattice elastic constant. In practice, all traces of simplicity are lost in this summation step. Kramer [26] studied the summation curves for voids and dislocation loops in irradiated superconductors, and found that these curves fall between the two extremes of the direct-summation and the statistical theory of Labusch [25]. The current status of the theory, its limitations, and the uncertainty about the values of the elastic constants are discussed by Kramer [26-28].

Much of the experimental evidence on samples with strong flux pinning supports the direct summation approach [29]. The total pinning force per unit volume for point pins, described by equations 4-8, is given by

$$F_p = f_p n_v \tag{3.12}$$

If the average distance between pinning sites, L, is greater than the inter-flux-line spacing d, then all pins are occupied by flux lines and $n_v \sim 1/L^3$. If $L < d$, then not all pins intercept the flux lines at any one time, and $n_v \sim B/(L \times \Phi_o)$. For large pins, described by equations 9-11, the interaction occurs at the interface between pins and matrix,

$$F_p = f_p\left(\frac{S_v}{1.07}\right)\left(\frac{B}{\phi_o}\right) \tag{3.13}$$

where S_v is the surface area per unit volume perpendicular to the direction of motion of the flux lines.

Another significant advancement of the theory of flux pinning was suggested by Kramer [30]. He has shown that the ultimate pinning force that can be exerted must correspond to the shear strength of the FLL. As the Lorentz force becomes equal to the lattice shear strength, regions of the FLL that are less strongly pinned will shear past more strongly pinned regions. The lattice shear strength, at high fields, is proportional to $h^{1/2}(1 - h)^2$, going to zero at H_{c2} (h=1), as depicted schematically in Fig. III-2. At lower fields, flux motion occurs primarily by unpinning of line pins. As the pinning strength increases, the peak in $F_p = J_c B$ should occur at lower fields. Such a trend, found for many materials is not universal. If the pinning sites are isotropic, it is not easy to understand why, on the average, any one region of the FLL should be less strongly pinned than any other, though statistical fluctuations could become appreciable over sufficiently small volumes.

There would appear to be no single universal theory of flux pinning. The theory appropriate to a particular material will depend upon the microstructure, i.e., the nature of the flux-pinning center, its size, and its distribution. However, the present theory does provide guidelines to interpret the behavior of materials and to develop methods to enhance their current-carrying capacity.

C. PINNING MECHANISM OF FLUX LINES BY GRAIN BOUNDARIES.

The critical current in brittle A15, Type II superconductors, which is the main interest of this study, has frequently been found proportional to the inverse of the mean grain size [31-39]. Until recently, pinning by grain boundaries and dislocation cell walls was poorly understood principally because the mechanism for f_p was uncertain. For example, there are at least three possible interaction mechanisms between a grain boundary and the FLL. These are:

(1). The interaction between grain boundary strain fields and the stress field of the FLL [40].

(2). The interaction between the grain boundary and the FLL due to the anisotropy of the upper critical field H_{c2} (crystalline anisotropic interaction).

(3). The interaction between the grain boundary and the FLL due to the electron scattering from the boundary (electron scattering interaction).

The stress field interaction has recently been shown to vanish for high-angle grain boundaries [1]. The magnitude of the crystal anisotropy contribution can be estimated from Equation 7. Since the magnitude of the H_{c2} anisotropy is decreased as the impurity content of the materials is increased [41], one expects the anisotropy interaction to decrease with the impurity parameter $\alpha = 0.88\xi_o/l$, where l is the electron mean free path.

The experimental tests of these ideas have been aided significantly by the development of techniques to measure flux pinning from single grain boundaries in bi-crystals, thus eliminating the summation problem.

The elegant work of Das Gupta et al. [4] on niobium bi-crystals used the fact that f_p for any planar defect is strongly decreased when the FLL makes a small angle to the plane of defect. By measuring the anisotropy of F_p with respect to the magnetic induction, they were able to isolate the specific pinning force from single, symmetric, high-angle tilt boundaries. Such boundaries should have negligible stress and anisotropy interactions. The results gave the specific pinning force on the order of $100N/m^2$, rather strong pinning, which must be attributed to the electron-scattering mechanism.

The electron-scattering mechanism by the grain boundary was first mentioned by Van Gurp [32] who suggested that at the boundary and the region of adjacent material, will have a shorter electron mean free path, and its value of κ will be higher than that of the grain interior. It might be thought that the width of the grain boundary, ~3 atomic spacings or 10 angstroms, would be too small in comparison with the coherence length ξ (1 ~ 40 angstroms in A15 materials) to have any effect. However, the effect of scattering from a grain boundary will persist over a distance in the order of normal electron mean free path from the boundary. The most important theoretical advance has been a paper by Zerweck [42] in which he developed the model for the electron scattering from the grain boundary. A similar, but modified model, was developed later by Yatter[43] and Kramer [28]. The assumptions of their treatment are as follows:

(1). Electrons are scattered with a probability, P, by the boundry, for random high angle grain boundaries, P is close to 1 [44].

(2). Using this fact, the electron mean free path is computed at various points from the grain boundary using a simple geometrical averaging model.

(3). Assuming a local relation between the Ginzburg-Landau parameter, κ, and l, the increase in κ is computed at various positions from the boundary. For high purity materials, the increase in κ is small but extends far from the boundry, whereas for lower purity materials, the κ change is large and more localized.

At high magnetic induction, b, the resulting f_p is estimated [43] to be:

$$f_p = \left(\frac{\sqrt{2\pi}}{3}\right)(1-b)\mu_o H_c^2 g_1 \frac{\Delta\kappa(g_1)}{\kappa(g_1)} \tag{3.14}$$

where g_1 is the shortest reciprocal lattice vector of the FLL and $\Delta\kappa(g_1)/\kappa(g_1)$ is the one-dimensional Fourier transform of the relative change in κ as a function of distance from the grain boundary. It was found that f_p is a strong function of α, the impurity parameter, increasing rapidly at low α. The Zerweck model predicts a maximum at $\alpha \sim 1$, and a subsequently slow decrease for higher α's, while the revised version of Yatter and Kramer model puts the maximum at a much higher than $\Delta = 10$.

The physical insight into why the electron scattering mechanism is not an important pinning effect for point or line pins can be understood as follows:

The decrease in l occurs primarily from the truncation by the plane of a spherical region with a radius equal to l. Since point or line pins do not cast appreciable 'shadows', they do not perturb either l or

KAPPA locally, and thus do not give rise to an appreciable electron-scattering interaction.

The structure of a dislocation cell wall produced by severe plastic deformation and followed by intermediate annealing of metals and alloys usually consists of a very high density of dislocations. Its electron-scattering properties, therefore, should not be much different from a high-angle grain boundary. The idea from the Zerweck model that an isolated dislocation should produce a negligible local change in κ may well account for the earlier observations that only small increases in flux pinning were produced by plastic deformation until plastic strains at which the cell wall structure begins to form is exceeded, or followed by annealing processes where the cell walls are polygonized [45,46].

Another important prediction of this model is that equilibrium monolayer segregation of solute atoms to the boundary should produce little if any change in f_p. This is because, if the scattering probability, P, is already close to 1, adding solute atoms to the plane of the boundary can do little to enhance it. Yetter[43], in experiments where he allowed Pd or Tl to diffuse down the boundaries in the columnar grain structure of a Pd-Bi film, has confirmed this prediction in that appreciable changes in the f_p occur only when solute atoms have time to diffuse a distance approximately ξ from the boundary.

As shown by Abrikosov [47], the factor $\langle \Psi / |\Psi|^2 \rangle$ decreases linearly to zero when the mean flux density approaches B_{c2}. Thus, it is expected that the elementary pinning force is independent of the applied field for low and medium fields, and decreases linearly to zero near the upper critical field. Combining the results of Das Gupta et al. [4]

with the magnetization data of Finnemore et al. [48], it has been shown [42] that F_p indeed is approximately constant for inductions $\mu_o H < 0.2T$ and decreases for higher fields. Thus, the decrease of f_p with increasing applied field in Fig. III-2 can be alternatively described.

The importance of the boundary structure within a high-angle boundaries not yet been quantitatively assessed, but it would seem likely that special boundaries such as high-coincidence site boundaries (e.g. twin boundaries) would scatter electrons less strongly and have a smaller f_p since the good fit at such boundaries would reduce the density of defects in the boundary. In support of such a role, a comparison of a niobium bicrystal boundary, which is nearly a symmetric twin orientation, with a symmetric random high-angle boundary (with negligible crystal anisotropy contribution) reveals that the inferred f_p from the twin is about half that of the random boundary.

Given these discussions, it seems likely that the electron-scattering mechanism in alloy superconductors is the most important grain boundary and cell-wall-pinning mechanism. Since A15 compounds are often in the clean limit, the H_{c2} anisotropy may play a more important role there [49]. From the evidence in niobium, it would appear descirble to attempt to produce 'dirty' A15 compounds (without reducing T_c and H_c. Not only would this increase f_p for the grain boundary, but it would also increase F_p at high fields by increasing H_{c2}.

REFERENCES

1. D. Livingston and H. W. Schadler, Prog. Mater. Sci., 12, 185 (1964).
2. A. C. Rose-Innes and E. H. Rhoderick, Intro. to Superconductivity, 2nd ed., Pergamon, Oxford, p. 83 (1978).
3. W. A. Fietz and W. W. Webb, Phys. Rev., 178, 657 (1969).
4. A. Das Gupta, C. C. Koch, D. M. Kroeger and Y. T. Chou, Phil. Mag., 38, 367 (1978).
5. A. J. Marker, R. W. Reed, F. G. Brickwedde, R. L. Schuyler and W. B. Bitler, J. Low Temp. Phys., 31, 175 (1978).
6. A. M. Campbell and J. E. Evetts, Adv. Phys., 21, 199 (1972).
7. D. Dew-Hughes, Treatise on Mater. Sci. β Tech., 14, 1 (1979).
8. E. J. Kramer and C. L. Baner, Philos. Mag., 15, 1189 (1967).
9. V. P. Galaiko, Sov. Phys.-JETP Lett., 7, 230 (1968).
10. U. Kammerer, Z. Phys., 227, 125 (1969).
11. H. Kronmuller and A. Seeger, Phys. Status Solidi, 34, 781 (1969).
12. W. W. Webb, Phys. Rev. Lett., 11, 191 (1963).
13. R. L. Fleischer, Phys. Lett., 3, 111 (1963).
14. K. Miyahara, F. Irie and K. Yamafuji, J. Phys. Soc. Jpn., 27, 290 (1969).
15. J. D. Eshelby, Solid St. Phys., 3, 79 (1957).
16. A. G. Khachaturyan, Soviet Phys.-Solid St., 8, 2163 (1967).
17. A. G. Khachaturyan and G. A. Shatalov, Soviet Phys.-Solid St., 11, 118 (1969).
18. F. R. N. Nabarro and A. I. Quintanilha, Mater. Res. Bull, 5, 669 (1970).

19. E. J. Kramer, J. Nucl. Mater., 72, 5 (1978).

20. P. W. Anderson, Phys. Rev. Lett., 9, 309 (1962).

21. B. B. Goodman, Rep. Prog. Phys., 29, 445 (1966).

22. R. G. Hampshire and M. T. Taylor, J. Phys. F, 2, 89 (1972).

23. A. M. Campbell, J. E. Evetts and D. Dew-Hughes, Philos. Mag., 18, 313 (1968).

24. D. Dew-Hughes and M. J. Witcomb, Philos. Mag., 26, 73 (1972).

25. R. Labusch, Cryst. Lattice Defects, 1, 1 (1969).

26. E. J. Kramer, J. Appl. Phys., 49, 742 (1978).

27. E. J. Kramer, J. Nucl. Mater., 72, 5 (1978).

28. E. J. Kramer, Adv. Cryo. Engr., 28, 307 (1982).

29. D. Dew-Hughes, Philos. Mag., 30, 293 (1974).

30. E. J. Kramer, J. Appl. Phys., 44, 1360 (1973).

31. J. J. Hanak and R. E. Enstrom, Proc. of the 10th Conf. on Low Temperature Physics, LT-10, IIA, 10 (1967).

32. G. J. Van Gurp, Phil. Res. Rep., 22, 10 (1967).

33. H. Conrad, L. Rice, E. L. Fletcher and F. Vernon, Mat. Sci. Eng., 1, 360 (1967).

34. K. J. Gifkins, C. Makeed and W. A. Rachinger, Scripta Met., 2, 141 (1968).

35. G. R. Love and C. C. Koch, Appl. Phys. Lett., 14, 250 (1969).

36. E. Nembach and K. Tachikawa, J. Less-Comm. Met., 19, 359 (1969).

37. R. M. Scanlan, W. A. Fietz and E. F. Koch, J. Appl. Phys., 46, 2244 (1975).

38. B. J. Shaw, J. Appl. Phys., 47, 2143 (1976).

39. A. W. West and R. D. Rawlings, J. Mat. Sci., 12, 1862 (1977).

40. C. S. Pande and M. Suenaga, Appl. Phys. Lett., 29, 443 (1976).

41. E. Seidl and H. W. Weber, Anisotropy Effects in Superconductors, H. H. Weber, ed., Plenum Press, New York, p. 57 (1977).

42. G. Zerweck, J. Low Temp. Phys., 42, 1 (1981).

43. W. Yatter, Ph.D. Thesis, Cornell University, Ithaca, NY (1980).

44. R. A. Brown, J. Phys. F, 7, 1477 (1977).

45. A. V. Narlikhar and D. Dew-Hughes, Phys. Status Solidi, 6, 383 (1964).

46. M. J. Witcomb and D. Dew-Hughes, J. Mater. Sci., 8, 1383 (1973).

47. A. A. Abrikosov, Zh. Eksp. Theor. Fiz., 32, 1442 (1957).

48. D. K. Finnemore, T. F. Stromberg and C. A. Swenson, Phys. Rev., 149, 231 (1966).

49. K. Togano and K. Tachikawa, J. Appl. Phys., 50, 3495 (1979).

IV. METALLURGY OF A15 CONDUCTORS

A. INTRODUCTION.

A large number of A15 intermetallic compounds are superconducting [1], but only a few (listed in Table IV.1) having critical temperature above ~15K and critical field above 20 tesla are of practical interest. Also, in the present context a superconductor is practical only if it can be fabricated in long continuous, flexible lengths with a multifilamentary geometry. Because all A15 compounds are brittle, the preparation of useful conductors requires special techniques. The crystal structure of the A15 phase is shown in Fig. IV-1.

Due to the inherent brittle nature of these compounds, the "wind-and-react" method is the most practical way of producing magnets. In this method, the conductor is first wound into a coil and then converted to A15 phase by heat treatment of the entire coil. A favorable configuration of the conductor will be in a multifilamentary geometry (whether it has continuous or discontinuous filaments). This will control the diffusion reaction to yield the maximum attainable A15 volume and minimize the grain size. Another advantage of multifilamentary geometry is that the superconducting A15 phase can be more easily stablized by copper against flux jumps and quenches.

Historically, Kunzler et al. [2] made the first successful attempt in 1961 to construct a magnet using an A15 material. They packed a mixture of Nb and Sn powders in a Nb tube and then mechanically elongated the tube, coiled it into a magnet and heat treated it to produce Nb_3Sn. An extension of this technique was to use fine Nb filaments

coated with Sn [3,4]. The severe limitations of Kunzler's approach are the low overall critical current density and lack of stability.

A large number of processing methods for A15 conductors has been reported. However, the most significant advance in the technology is the successful development of a method for fabricating Nb_3Sn [5,6] and V_3Ga [7] conductors which relies on the fact that these A15 compounds can be formed at the interface of Nb(V) and Cu-Sn(Ga) bronze at elevated temperatures. This processing method is generally known as the "bronze process". In this chapter the thermodynamic stability of A15 compounds is discussed and various processing methods are reviewed, with special attention to the metallurgical principles of the bronze process and direct precipitation process. Current status of processes and their advantages and disadvantages as compared with the conventional bronze process are discussed.

B. STABILITY OF A15 COMPOUNDS.

Of the many known superconducting A15 compounds, only two, V_3Ga and Nb_3Sn have as yet been developed as commercial conductors. Three binary compounds, Nb_3Al, Nb_3Ga, and Nb_3Ge, and one ternary compound, Nb_3 (Al, Ge), have higher values of T_c and H_{c2} than do Nb_3Sn and V_3Ga (See Table IV-1) but none of these has yet been successfully developed into a commercial conductor. The reason for this failure is that the latter compounds have not be produced either by reacting solid Nb with the appropriate liquid or by a solid state diffusion between Nb and an appropriate bronze.

In the Nb-Sn and V-Ga binary system the A15 compounds are the only stable ones above 930 and 1300°C [8], respectively. The Nb-Sn binary phase diagram is shown in Fig. IV-2. This high temperature thermodynamic stability permits direct compound formation by heat treatment of elemental diffusion couples. For example, reaction of Sn-dipped Nb tape above 930°C results in Nb_3Sn formation at the Nb-Sn interface. Sn-coated Nb heat treated at temperatures less than 930°C produces a spectrum of interfacial compounds, including Nb_3Sn, Nb_6Sn_5, and $NbSn_2$ [9], as demanded by thermodynamic law. Heat treatment of V-Ga couples below 1300°C produces V_3Ga_2 and VGa_2 [10]. The presence of these undesirable compounds restricts A15 compound formation (the A15 layer will be very irregular) by consuming the available Sn or Ga, thereby degrading the superconducting properties. Furthermore, the requirement of a high temperature heat treatment inhibits control of the microstructure including, for example, grain size and long range order parameters. Thus, control over structure-sensitive superconducting properties such as critical current density is also inhibited.

The reason why stoichiometric, high-T_c Nb_3Al, Nb_3Ga and Nb_3Ge are not formed by direct reaction between constituent elements is related to their relative stability compared with competing compounds in the respective phase systems. In each case, one or more solute-rich compound is more stable, having higher melting point and is therefore inherently preferred. The stability of A15 type phases has been reviewed by Harsough [11]. The competing phases are b.c.c. and σ phases [12,13]. The stability of the A15 phase is found empirically to be influenced by several factors: (1) the atomic size ratio, (2) e/a ratio, (3) density of state near the Fermi surface N(o), and (4) thermodynamic factors. It

is suggested that the A15 type A_3B compounds is favored when the radius of the B atom is within 8% of the A radius and the range in e/a (total electrons/atom outside a closed shell) is about 4.0 to 7.0, as compared with whichever b.c.c. occurs in the range of 3.5 to 6.5 and σ 5.6 to 7.7 e/a [13]. It also appears that an A15 phase is favored at compositions which maximize N(0).

Stability of competing phases as temperature increases is determined by the balance between enthalpy and entropy. A15 phase is marked by its closed-packed crystal structure and high degree of order (14), therefore the entropy is low. Structures with high entropy, such as b.c.c. and σ, are favored over A15 at high temperatures. However, A15 phases with the highest bond strength (enthalpy) are stable enough to melt congruently.

The ability or inability of the bronze process to produce single-phase A15 compounds can only be understood by reference to the relevant Nb-Cu-X ternary phase diagram. Formation of phases by diffusion between elements or other phases is governed by thermodynamic considerations. In multicomponent systems, diffusion follows the two-phase tie-lines [15]. Except when two-phase interfacial energy becomes very low, then a two phase mixture will result [16]. Of the phases that can form, in a ternary diffusion couple, the ones most likely to form are those with the highest relative thermodynamic stability [16]. This tends to ensure that the more stable phases are most likely to be encountered on the diffusion path.

Three types of phase diagrams appropriate to the formation of superconducting A15 compounds by the bronze process may be recognized [17] as following.

(1) Those in which the A15 phase is the relevant stable phase, other than the terminal Nb(V) and Cu-based solid solutions. Fig. IV-3 is an estimate of the 700°C section of Cu-Sn-Nb isotherm deduced from the 1100°C section reported by Hopkins et al. [18]. This diagram shows that the diffusion path from the Cu-Sn solid solution to the Nb terminal element passes through the A15 Nb_3Sn phase field. The V-Cu-Ga phase diagram should be similar to that of Nb-Cu-Sn [19] and V_3Ga is formed with the same readiness as Nb_3Sn.

(2) Those in which the most stable phase is one in the Nb(V)-X binary, with a leaner content of Nb(V) than the A15 phase. There is no direct tie-line to the A15 phase from the Cu solid solution phase field, and the A15 may not lie on the direct tie-line route from the most stable phase to the Nb solid solution. An example of this type is the Nb-Ge-Cu diagram, an estimated section of which is shown in Fig. IV-4a. There are, in fact, two stable phases: Nb_5Ge_3 and Nb_3Ge_2. Two possible diffusion paths are indicated, depending upon the initial concentration of bronze. In both cases the resultant reacted layer is found to be Nb_5Ge_3 [16,18].

(3) In the third type of system, the most stable phase is a new, ternary phase that bears no relation to, and whose existence cannot be predicted from the constituent binary systems. The example here is Nb-Al-Cu [20]. An estimated 1000°C isothermal section is shown in Figure IV-5. Two ternary compounds CHI phase and a Laves phase $Nb(Al_xCu_{1-x})_2$ [16], block the diffusion path between Cu-Al bronze and the Nb-Al solid solution. Which one of these actually forms will depend on the starting bronze composition.

The forthgoing explains why Nb_3Ge and Nb_3Al cannot be formed by the bronze process. The Nb_3Ga ternary diagram has not been investigated, but it is probably of a type intermediate between (a) and (c) [17]. An attempt to form $Nb_3(Al,Ge)$ by diffusion between pure Nb and Cu(Al,Ge) ternary bronzes produced only Nb_3Ge_2 [16].

The isothermal section of V-Cu-Si system is estimated by Livingston [21] and is depicted in Figure IV-4b. It was found that V_3Si and V_5Si_3 are normally observed in bronze diffusion couples heat treated at ~700°C. After initial compound formation by an appropriate heat treatment, Livingston diluted Si in the bronze by cladding the samples with pure Cu. The resulting alloy was thus depleted in Si content and reduced the thermodynamic activity of Si accordingly. This has an effect of reducing the volume fraction of the 5:3 phase while increasing the layer thickness of the 3:1 A15 phase. This approach to A15 compound formation should also work in some other systems. In the Nb-Cu-Ga system, this attempt was found to be futile because the kinetic factors inhibited layer growth when the Ga concentration of the bronze was lowered [22].

In summary, it appears that the six high-T_c A15 compounds can be listed according to decreasing stability as Nb_3Sn, V_3Ga, V_3Si, Nb_3Al, Nb_3Ga and Nb_3Ge. Generally, the first three compounds can easily be made at the stoichiometric composition by arc melting and aging reaction. These three compounds are formed via the bronze diffusion method, V_3Si forming with an additional compound V_5Si_3.

Compound instability is reflected in Nb_3Al by the equilibrium composition being off the 3:1 stoichiometry, toward Nb-rich compositions for all temperatures below ~1750°C. In order to prepare high-T_c

stoichiometric Nb_3Al, anneals at high temperature are required in combination with rapid quenching and ordering heat treatments. Nb_3Al does not form when solid state bronze technique is employed. Fabricating conductors of Nb_3Al has been limited to powder, thin foil, and physical vapor deposition techniques (PVD) [23]26]. Although reasonably good T_c and J_c values have been obtained, filament integrity has always been inferior to Nb_3Sn and V_3Ga produced by the bronze process.

High-T_c Nb_3Ga can only be prepared by PVD or rapid quenching. It is virtually impossible to make bulk samples of high-T_c (>21K) Nb_3Ge by a combination of melting and quenching. Nb_3Ge is metastable at the stoichiometric composition and has only been produced with T_cs greater than 21K by chemical or physical vapor deposition under stringent experimental conditions [27-29]. CVD and PVD techniques offer promising means to produce these materials in tape form, such as that used in AC superconducting power transmission. Considerably more technical development is required to adapt them to the fabrication of multifilamentary wires, although single strands of a W-1 w/o ThO_2 wire have been successfully coated with Nb_3Ge using CVD [30].

C. ADVANTAGES AND DISADVANTAGES OF VARIOUS FABRICATION TECHNIQUES FOR CONTINUOUS FILAMENT CONDUCTORS.

The most important advance in high-field superconductor technology is the discovery of the 'bronze-process' [5-7]. This process has been developed extensively in the past decade for Nb_3Sn and V_3Ga multifilamentary conductors. Conductors in great length (several kilometers) with high current-carrying capacity and good stability, as required for

large magnet productions, are now available commercially. However, this processing technique is not without disadvantages.

Various modifications or processes based on different metallurgical principles have been sought extensively. These processes have both advantages and disadvantages with respect to the bronze process. The new processing technology is becoming extensive and important. It is my purpose to point out the important fabrication techniques and discuss their advantages and disadvantages. However, it should be noted that some of the points discussed here are not fully understood and their roles in being advantageous or disadvantageous could change with more study. In this section, the fabrication methods for continuous filament conductors are discussed.

1. Conventional (Internal) Bronze Process. The process of this method is depicted schematically in Figure IV-6a, after Suenaga et al. [31]. The deformation procedure starting from the initial billet of more than 20 cm diameter to a wire of less than 1mm diameter, with filament diameters of the order of several μm, is a treated sequence of two steps, i.e., extrusion and wire drawing. The extrusion temperature is determined by the Cu-Sn phase diagram and is restricted to values around 650°C. Further reduction of the extruded billets occurs by wire drawing at room temperature. Due to the rapid work-hardening of the bronze matrix, an annealing treatment at 450 to 550°C for 20 minutes to an hour is required for every 50 to 80% reduction of area. This leads to more than 10 intermediate annealings for a large billet.

The resultant composites are usually twisted in order to increase their electromagnetic stability and reduce the energy losses in time-varying magnetic fields [32]. For the production of high field magnets,

the conductor is first wound into a coil and then the Nb_3Sn phase is introduced by a diffusion reaction at the interface between the Nb filaments and the bronze matrix.

The advantages of the 'internal bronze' process can be stated as follows: (a) Nb filaments can be made with uniform size and continuous in a great length, thus eliminating or minimizing the current transfer through a resistive matrix. (b) The filament size and overall cross-sectional geometry can be varied without too much effort to optimize the properties of conductors for the particular application. (c) The use of Ta as a barrier for Sn diffusion to the Cu stabilizer from the bronze matrix, so that the high-conductivity Cu is adjacent to superconductors [33]. Also, instead of Ta for the diffusion barrier [34] it is possible to use Nb foils that are locally doped with P. (d) The 'wind-and-react' technique to fabricate high-field magnets is relatively easier to achieve for this self-stabilized conductor. Further, the heat treatment temperature (700° to $750^{o}C$) and time (in the order of a few days) are compatible with other steel components in the solenoid and the whole structure can reach equilibrium during heat treatment.

Two main disadvantages can be recognized for the internal bronze process. The first is the requirement for frequent intermediate annealing between deformation. This means that the processing procedure has to be interrupted and cannot form a continuous production, which not only increases the production cost but also makes quality control difficult, e.g., the pre-reaction Nb_3Sn [35] and the 'sausaging' effect of the Nb filaments [36]. The other disadvantage is concerning the bronze matrix. The tin concentration is restricted to below 13.5 wt.% in the bronze matrix due to the solubility limit of Cu. The consequence of the

composition restriction is two-fold: the percentage volume and microstructures of the A15 compound. The volume of A15 compound is restricted because the bronze to niobium ratio has to be close to or greater than 3 in order to have enough tin in the matrix to convert most or all of the Nb to superconducting phase. The effect of bronze composition on the microstructures of A15 is discussed in more detail in Chapters VI and VII. It can be mentioned that during diffusion reaction the tin composition in the matrix continuously decreases. This influences the nucleation of Nb_3Sn phase, which causes the change of morphology, and changes the composition of A15 near the bronze interface. It can demonstrated that if the bronze composition can be kept invariant, a more desirable microstructure will result.

Another point worth mentioning is that, as noted in Section III. 3, some selected ternary additions to the A15 phase should enhance its inherent properties. Therefore, it is generally desirable to dope the matrix and/or Nb filament with a small amount of third elements. The minor disadvantage associated with the 'internal bronze' method is that the processing will become more difficult with third element additions.

2. <u>The External Bronze Process.</u> The first modification, the external bronze process, was introduced by Suenaga and Sampson [37] soon after the discovery of the original bronze process following a suggestion to increase thickness of the layer in the bronze processed V_3Ga by Ga-plating the wire. This process is schematically depicted in Figure IV-6b. First, the Cu-Nb composite was extruded, bundled, and drawn to the final size. Then the wire was plated with a layer of tin before diffusion treatment to make a Cu-Sn matrix and then Nb_3Sn layers.

The main advantage of this process over the original one is that a Nb-Cu composite can be drawn to a small size without any intermediate annealing steps to remove work hardening of the matrix. Another advantage is that the overall tin concentration is not limited to ~13 wt.% as is that of the internal bronze process. Thus, changes in the phase boundary condition between the Nb_3Sn and bronze matrix interface and the inherent superconducting properties can be enhanced. Also, the matrix to Nb ratio is not restricted to ~3:1, therefore, the volume ratio of superconductor to normal can be increased. The other less significant advantage is that some ternary elements can be more readily added to the Sn layer without changing the process.

In this process, however, new problems have been encountered in the tin-plating process and subsequent heat treatment to diffuse the Sn into the Cu matrix to form a Cu-Sn solid solution and Nb_3Sn layers. The primary difficulty is delamination of the outer layer of the wire [38] when the plated Sn layer is greater than ~5μm [39]. Thus, the maximum wire size was limited to ~0.25mm in diameter. This problem is though to be caused by the volume expansion and the Kirkendal voids. Cogan et al. [40] suggested that an annealing step at ~500 to 750°C of the Cu-Nb composite before plating and heat treatment can largely suppress the formation of voids. It is believed this step eliminates heterogeneous nucleation sites for voids. Klein et al. [41] studied the effect of hydrostatic pressure during the reaction the treatment on the void formation. They found that above a critical pressure, the formation of the void can be suppressed. However, these processes cannot significantly increase the size of the wire without introducing the delamination problem or other difficulties such as beading of tin.

Other disadvantages associated with this process are: the A15 layers are less homogeneous radially in properties, and it cannot be used with the Ta-diffusion barrier and the Cu stabilizer at the outside portion of a wire. However, in some types of magnet design, these limitations may not be the major problems since wires for stabilization can be braided in the cable with the superconducting wires, and an optimum heat treatment can be found by microstructural study.

3 The Internal Tin Bronze Process. In 1974, a new modification to the bronze process was reported by Hashimoto et al. [42]. This process consists of assembling Cu-clad Nb-bars and a Cu-clad (Sn-20 w/o Cu) alloy rod in a Cu tubing such that the Cu-Sn rod will be at the center, the assembly is then cold drawn to final size for heat treatment to form the Nb_3Sn layer (See Fig. IV-7a). It was shown later that Sn-2 w/o Cu core can also be used for this purpose [43]. As in the case of the external bronze process, the main advantage of this process is the elimination of the intermediate annealing process and thus allowing the fabrication process to be continuous. However, unlike the external bronze process, the Ta diffusion barrier and the high-conductivity Cu stabilizer can be placed outside of the wire. Therefore, the conductor can be self-stabilized. Also, the 'wind-and-react' method can be utilized without contamination or loss of tin. As far as the microstructure is concerned, this process is very attractive because it permits high overall tin concentration of the matrix and the Nb/matrix ratio can be raised so as to increase the volume fraction of the A15 phase. Recently, short samples of the process have been reacted and tested [44]. It is found that not only the overall critical current density of the 'internal-tin bronze' is higher than that of the 'internal bronze',

but also the J_c of the original niobium area is higher, particularly in the lower field (<14T) range. The microstructural source of this improvement is discussed in section C.1.

The main disadvantages associated with this process can be recognized: the inhomogenity of the A15 phase microstructures that depend on the location of the filament. Even though by a low temperature homogenization process, tin can be distributed in the copper matrix prior to the A15 phase formation heat treatment. Due to the solubility limit of tin in copper, a continuous supply of tin from the central reservoir is required. This is also because the initial copper to Nb ratio is desirable to keep as small as possible. The diffusion length of tin from the reservoir to the outer region is much large than that of the local matrix to the nearby Nb. Therefore, there exists an optimum configuration and heat treatment procedure to yield a most homogeneous A15 microstructure and a maximum volume of A15 phase.

Another problem with the tin core is that during extrusion and preheat treatment, it is necessary to avoid its melting. This means that the extrusion has to be done in a highly controlled fashion and a long, low temperature (<200°C) has to apply before reaction for the diffusion of tin into the copper matrix to form higher melting point intermetallic compounds before the pre-reaction temperature can be raised. Therefore, it is obvious that the processing is much more complicated and the optimization of the process is a difficult task. It has been known for sometimes that the strain in the Nb_3Sn phase drastically decreases its superconducting properties. The degree of strain associated with the A15 layer should be much higher than the conventional bronze wire due to the much different thermal expansion of the constituent phases and the

multiple diffusion process. For example, the Kirkendal void will be much several. All these problems with the process do pose a very interesting and complicated metallurgical task and an intensive study of this subject is desirable both technologically and scientifically.

4. The Internal (Bronze and Tin) Tubing Process. In 1975, two similar modifications to the 'bronze process' were proposed [45,46]. Both of these employ Nb tubing instead of rods. The schematic representations of the process is depicted in Figures 7b and 7c. The difference in these two processes is that the internal bronze-Nb tubing [46] method uses a Cu-Sn solid solution while the internal Sn-Nb tubing utilizes a Sn-Cu eutectic alloy. Except for the geometrical difference, these two processes are closely analogous to the comparison of the internal bronze process and internal tin-bronze process. The common advantage in these former processes over the latter processes is that the Nb tube acts as a diffusion barrier for Sn, thus, the Ta diffusion barrier is not required. Furthermore, all of the Nb_3Sn phases will be very close to the copper stabilizer, while it is not always so for the other processes.

The drawbacks of these processes are that in the internal bronze Nb tubing method, frequent annealing is still needed while in the internal Sn-Nb tubing process, the extrusion and pre-heat treatment condition is stringent to avoid the melting of Sn-Cu eutectic alloy. Another problem in the fabrication is that the use of tubing increases cost. In the microstructural point of view, the filament size is limited to a much larger diameter, thus the advantage of fine-filament largely disappears. It also turned out that a large radial tensile strain exists due to the contraction of the bronze at the core area [47,48].

5. The ECN Powder Method. Recently, a new modification of wires containing Nb_3Sn following the powder method has been reported by a group in the Netherlands and is known as the ECN powder method [49-51]. In this method, $NbSn_2$ powder is encapsulated into niobium rods followed by bundling of rods into a copper tube and then deformed to the final size. A small amount of copper powder is added to the $NbSn_2$ powder to promote the Nb_3Sn phase formation. This catalytic copper plays an important role to ensure a low temperature reaction ($<700^oC$) is sufficient for the major diffusion layer, which is fine-grained Nb_3 Sn instead of non-superconducting Nb_6Sn_5 phase. The schematic processing is shown in Fig. IV-8(a).

The main advantage over the other modification methods is that this method does not rely on the diffusion interface between a Cu-Sn soliso-lution and Nb. Thus eliminating a large volume of resistant matrix and increases the volume of Nb_3Sn. Very high J_c has been reported [50], and this should be partly due to the fact that the Nb_3Sn phase is free to relax without the diffusional strain induced by the matrix. Other advantages associated with the tubing process in fabrication and stabilization are preserved (Section IV.C.3).

While enjoying the above advantages, the similar advantages that are encountered in the tubing process are also presented. There is one important point that remains to be understood--the strain associated in the Nb_3Sn layer. It can be speculated that the Nb_3Sn layer in this process is in a near zero strain. It follows that any applied strain will decrease its current carrying capacity. In all kinds of bronze processes, a reactional compressive strain is always present. By a compensating tensile strain, the J_c will increase. This will not be the

case for the present process. Then a degradation of J_c will always occur in the manufacture of magnets.

6. The Modified-Jelly-Roll (MJR) Method. The MJR method reported in the Applied Superconductivity Conference late last year is a very attractive modification of the original bronze process [52-54].

In this process, an already finely divided foaminous Nb fold mesh is interleaved with a ten-bronze foil and spirally wrapped in jelly-roll fashion to to produce a cylindrical billet which would be reduced in several steps to final size without rebundling. A schematic process is given in Fig. IV-8(b). The elimination of the rebundling process drastically reduces fabrication cost and represents the major advantage over the original internal bronze process. The disadvantage of this process is that a significant fraction of Nb_3Sn phase formed in a cross-linked fashion, which does not contribute to the transport current-carrying capacity. However, they do help in current transfer and against flux jumping. Also, the main disadvantages of the internal bronze process are still present (See section IV.C.1).

Another modification of the MJR method is to replace the Sn-bronze foil by pure copper, and the jelly roll is wrapped around a tin core [52]. This modification removes the intermediate annealing and the restriction on the limitation of Sn concentration in bronze. However, similar disadvantages shared with the 'internal tin' bronze process are encountered (See Section IV.C.3.).

D. A15 SUPERCONDUCTING WIRES PRODUCED BY DISCONTINUOUS FILAMENT.

Another promising route to fabricate high-field A15 superconducting wires, besides the continuous filament methods discussed in the last section, is by discontinuous fiber methods. The discontinuous fiber methods briefly described in this section include the in-situ method (or known as the Tsuei's method), powder metallurgy, the infiltration method, and the controlled precipitation process. All of these processes have a general advantage of being less costly in fabrication as compared with the continuous filament methods. However, since the filaments are discontinuous, a current-transfer induced voltage through the resistive matrix might be a drawn back in the manufacture of high-field magnets.

1. The 'in-situ' Method. In 1973, Tsuei [55] first realized that the dendritic Nb in an arc-melted Cu-rich Cu-Nb(or V) ingot could be deformed to fine fibers by drawing the ingot into a fine wire (Fig. IV-9). The metallurgical principle in the process is that Nb(V) and Cu are immiserible when cooled from melt. A composite of dendritic Nb(V) embedded in a copper matrix is ductile and can be deformed with a great area reduction without intermediate annealing. Tin (or gallium) can be added in the initial melt or added afterwards before the heat treatment to form Nb_3Sn or V_3Ga. As shown schematically in Fig. IV-7, an interesting aspect of this processing method is that the mechanical properties (yield strain and the strain tolerances of the wire) of this composite are greatly enhanced over the conventional multifilamentary Nb_3Sn or V_3 Ga wires due to the close proximity of finely divided (<1000 A) filaments. The processing technique is also favorable for yielding

Nb_3Sn and V_3Ga with better J_c, due to the elimination of the phase boundary between A15 and the bronze interface (Sn or Ga is very fast to consume) and very fine fiber. The reported J_c has a higher high-field property (>14T) than that of the bronze-processed wire. The main disadvantage of the process is that the radial inhomogenity of the A15 phase (i.e. depends upon the location of A15 from the Sn or Ga source). Another problem with this process is that the wind-and-react method for the production of magnets is difficult due to the short aging time and lack of stabilizing copper, and the final wire diameter generally is restricted to below small size (<0.5mm).

Recently, two new modifications have been proposed: the combination of MJR method [56] and the internal tin bronze method [57] with the in-situ process. These new modifications are mainly to overcome the size limitation of the external-tin diffused in-situ wire. Also, the conductor can now be self-stabilized. Preliminary studies showed that these modifications have promising results [56,57].

2. Powder Metallurgy. Powder processed Cu-Nb composites have been developed with ultrafine fiber multifilamentary geometries [58] incorporating external tin diffusion [59], a single internal tin core or multiple tin cores [60,61]. The first attempts to obtain multifilamentary composite wires by powder metallurgy (P/M) were undertaken in 1973 by Wessermann [59] who recognized that the required fine distribution of Nb and Cu could also be produced by mixing fine Cu and Nb powders together, followed by compacting and hot extrusion and finally, wire drawing to a fine wire which is then Sn coated and reacted. Non-equilibrium Nb-Al, which cannot be fabricated by the bronze-route, can also be produced by P/M [62,63]. The advantages are similar to that of the in-situ process,

including high strain tolerances and better critical current at high fields. The other advantage is that this process permits fabrication of superconducting materials with microgeometries not possible by the bronze route.

The disadvantages associated with this process are also similar to that of the in-situ process. In the case of Nb-Al P/M, the other intermetallic compounds also formed during reaction [62]. To minimize the undesirable compounds formation, higher temperature and shorter time reaction is required, which is not compatible with the wind-and-react technique.

3. Infiltration Process. The infiltration process has been reviewed in great detail and in a very descriptive text by Pickus, Holthuis and Rosen [64]. The idea of using a partially compacted, porous Nb rod infiltrated by tin was initially applied to the preparation of tapes [65]. In this process, Nb powders in the size range ~40 to 60μm are isostatically compacted into rods, followed by partially sintered at ~2250°C in vacuum. The volume fraction of voids is controlled, typically 15 to 20%, leaving an interconnected porous network in the Nb matrix. The rod is immersed in liquid tin at 350 to 400°C, removed and sheathed with monel and Ta diffusion burner. The rod is then reduced to the final dimension. Areal reductions of 4000 are possible without cracking, indicative of the great ductility of the selected Nb powders. A final heat treatment above 930°C produces the Nb_3Sn.

This method showed an exceptional high J_c at high fields but lower J_c at lower fields (<12T) as compared with the bronze-route wires. Total consumption of tin in porous brings the Nb_3Sn into contact, and a stoichiometric composition can be obtained. However, due to high

temperature reaction and the other intermetallic compounds formed before they eventually transformed into A15, the grain size of A15 is large. The resultant J_c characteristics caused by these two effects can be recognized. Good strain-tolerances are also found (same as the in-situ process).

The difficulties of the method are that the scale-up of production is more complicated and the heat treatment schedule is not compatible with the "wind-and-react" technique. Hot extrusion will not be suitable because the tin in the Nb matrix will melt and expand. Also, the volume fraction of the superconducting phase will be difficult to increase.

4. Controlled Precipitation Process. In some binary phase diagrams the stoichiometric composition A_3B exists at high temperature in the form of body-centered-cubic (BCC), which can be preserved at room temperature if the alloy is rapidly quenched. If the as-quenched solid solution is ductile enough, it can be fabricated into wires or tapes by conventional technology. Aging would then transform the metastable materials into the A15 phase. This process has been used with limited success for the V-Ga [66] system, but is of marginal interest since several alternative methods have been developed for this system. However, this approach is promising for systems such as Nb-Al. Another technique consists in quenching an off-stoichiometric metastable solid solution (A_{3+x} B_{1-x}) and to rely on precipitation after deformation to generate a multifilamentary composite. This method has been carried out on the V-Ga system [67]. Alloys of V-17 to 19 at.% Ga were arc-melted, homogenized, quenched, deformed at 750°C and aged to precipitate the A15 phase. A maximum T_c of 14.8K was measured after aging at 750°C.

This method has several drawbacks as far as high critical current is concerned: connectivity is not complete, volume fraction is low and there is no thermodynamic reason to ensure stoichiometric composition. However, this techniques is a metallurgically simple method, i.e., the A15 formed from BCC matrix is in an unconstrained state. Therefore, it is a good system for studying the nucleation and growth mechanism as well as the crystallographic orientation relationship between the A15 and BCC matrix [68].

Table 1. A15 compounds with promising superconducting properties.

Material	T_c(K)	H_{c2}(0^oK), T	H_{c2}(4.2^oK), T
V_3Ga	15.4	34.9	23.6
V_3Si	16.9	34.0	23.0
Nb_3Sn	18.3	29.6	26.0
Nb_3Al	19.1	32.7	29.5
Nb_3Ga	20.3	34.1	33.0
$Nb_3(Al_{0.8}Ge_{0.2})$	20.7	44.5	41.0
Nb_3Ge	23.0	38.0	37.0
NB - 48% Ti (BCC Alloy)	9.5	14.1	12.2

REFERENCES

1. B. W. Roberts, NBS Technical Note, 983, 1978.
2. J. E. Kungler, B. Zeitlin, R. E. Schwall, M. S. Walker and G. M. Ogeryansky,
3. D. L. Martin, M. G. Benz, C. A. Bruch and C. H. Rosner, Cryogenics, 3, 161, 1963.
4. M. G. Benz, D. L. Martin and C. A. Bruch, Cryogenics, 5, 248, 1965.
5. A. R. Kaufman, and J. J. Pickett, Bull. Am. Phys. Soc., 15, 833, 1970.
6. E. W. Howlett, U.S. Pat. 3728165 (filed October 19, 1970).
7. K. Tachikawa, Int. Cryo. Engr. Conf., Berlin, 1970, Iliffle Sci. Tech. Pub. 339, 1971.
8. See, for example, D. Dew-Hughes, Cryogenics 15, 435, 1975.
9. J. P. Charlesworth, I. MacPhail and P. E. Madsen, J. Mat. Sci. 51, 199, 1959.
10. K. Tachikawa, and Y. Iwasa, Appl. Phys. Lett. 16, 230, 1970.
11. L. D. Harsough, J. Phys. Chem. Solids, 35, 1691, 1974.
12. L. Brewer, in High Strength Materials, V. Zackay, ed., John Wiley and sons, New York, 1965, p. 12.
13. L. Brewer, in Phase Stability in Metals and Alloys, W. Hume-Rothery, ed., McGraw-Hill, New York, 1967, p. 350.
14. A. K. Sinha, Prog. in Mat. Sci., 15, 79, 1971.
15. J. B. Clark, and F. N. Rhines, Trans. Am. Soc. Met. 51, 199, 1959.

16. T. Luhman, O. Horigami, and D. Dew-Hughes, in Am. Chem. Soc. 29th Appl. Polym. Symp. Proc., J. Wiley and Sons, New York, 1976, p. 61.

17. D. Dew-Hughes, and T. S. Luhman, J. Mat. Sci. 13, 1868, 1978.

18. R. H. Hopkins, G. W. Roland, and R. Daniel, Metall. Trans., 8A, 91, 1977.

19. E. M. Saritskii, Y. V. Efimov, V. Y. Markiv, and O. I. Zrolinskii, Izv. Akad. Nak SSSR Metall., 199, 1976.

20. C. R. Hunt, and A. Gaman, Z. Metalk. 59, 707, 1968.

21. J. D. Livingston, J. Mat. Sci., 12, 1759, 1977.

22. T. Luhman, Treat. on Mat. Sci. & Tech., 14, 221, 1979.

23. R. H. Hammond, IEEE Trans Magn., MAG-11, 201, 1975.

24. S. D. Dahlgren, Metall. Trans. A, 7, 1375, 1976.

25. G. W. Webb, Appl. Phys. Lett., 32, 773, 1978.

26. J. M. Hong, I. W. Wu, J. T. Holthuis, M. Hong, and J. W. Morris, Jr., Adv. Cryo. Eng., 28, 483, 1982.

27. S. Ceresara, M. J. Ricci, N. Sacchet, and G. Sacerdoti, IEEE Trans. Magn. MAG-13, 311, 1975.

28. A. B. Hallek, R. H. Hammond, T. H. Geballe, and R. B. Zubeck, ibid, 311, 1975.

29. R. A. Sigsbee, ibid, MAG-13, 307, 1977.

30. I. Ahmad, W. J. Heffernan, and D. U. Gubser, ibid, MAG-13, 483, 1977.

31. M. Suenaga, W. B. Sampson, and T. S. Luhman, IEEE Trans. Magn., MAG-17, 646, 1981.

32. P. F. Smith, J. D. Lewin, C. R. Walter, M. N. Wilson and A. H. Spurway.J. Phys. D., 3, 1517, 1970.

33. D. C. Larbalestier, P. E. Madsen, J. A. Lee, M. N. Wilson, and J. P. Charlesworth, IEEE Trans. Magn., MAG-11, 247, 1975.

34. J. A. Lee, and C. A. Scott, in Filamentary A15 Superconductors, M. Suenaga and A.F. Clark, eds., Plenum Press, New York, 1980, p.35.

35. D. C. Larbalestier, and D. B. Smathers,IEEE Trans. Magn., to be published.

36. D. S. Holmes, IEEE Trans. Magn., to be published.

37. M. Suenaga, and W. B. Sampson, Appl. Phys. Lett. 20, 443, 1972.

38. W. A. Fietz, C. D. Henning, and R. M. Scanlan, IEEE Trans. Magn., MAG-11, 299, 1975.

39. D. W. Dies, ibid, MAG-13, 447, 1977.

40. S. F. Cogan, D. S. Holmes, and R. M. Rose, Appl. Phys. Lett., 35, 557, 1979.

41. J. D. Klein, G. Warshaw, N. Dudgiak, S. F. Cogan, and R. M. Rose, IEEE trans. Magn., MAG-17, 380, 1981.

42. Y. Hashimoto, K. Yoshizaki, and M. Tanaka, Proc. of 5th Internat'l Cryo. Eng. Conf., Kyoto, Japan, 1974, p. 332.

43. Y. Hashimoto, presented in the 2nd US-Japan workshop on Superconducting Materials for Fusion, San Diego, Calif. (May, 1983)

44. D. R. Dietderich, I. W. Wu, W. V. Hassenzahl, and J. W. Morris, Jr., unpublished.

45. Y. Koike, H. Shiraki, S. Murase, E. Suzuki, and M. Ichihara, Appl. Phys. Lett., 29, 384, 1976.

46. R. Randall, J. Wong, D. W. Dies, B. J. Shaw, and M. R. David, IEEE Trans. Magn., MAG-11, 291, 1975.

47. D. O. Welch, Adv. Cryo. Eng., 26, 48, 1979.

48. R. M. Scanlan, D. Cornish, J. Zbasnik, R. W. Hoard, J. Wong and R. Randal, Adv. Cryo. Eng., 26, 451(1979).

49. C. A. M. van Beijnen, and J. D. Elen, IEEE Trans. Magn., MAG-15, 87, 1979.

50. A. C. A. Van Wees, P. Hoogendam, and H. Veringa, ibid, to be published.

51. H. Veriga, P. Hoogendam, and A. C. A. Van Wees, ibid, to be published.

52. W. K. McDonald, and R. M. Scanlan, IEEE Trans. Magn., to be published.

53. M. B. Siddal, W. K. McDonald, and K. Efferson, ibid, to be published.

54. M. Suenaga, C. J. Klamut, and W. K. McDonald: ibid, to be published.

55. C. C. Tsuei, Science, 180, 57, 1973.

56. R. Aoki, R. Onodera, S. Wada, and K. Asayama, present in the U.S.-Japan workshop for High-Field Superconducting Materials for Fusion, May 23-27, San Diego, CA, 1983.

57. T. Kumano, M. Ichihara, E. Suzuki, H. Okuda, M. Kodera, T. Noguchi, N. Sudo, H. Okon, K. Yasohama, and K. Yasukochi, ibid.

58. S. Foner, ibid.

59. G. Wassermann, Z. Metallk., 64, 844, 1973.

60. H. Zhang, S. Pourrahimi, J. Otubo, C. L. H. Thieme, B. B. Schwartz, and S. Foner, IEEE Trans. Magn., to be published.

61. J. Otubo, S. Pourrahimi, C. L. H. Thieme, H. Zhang, B. B. Schwartz, and S. Foner, ibid.

62. J. M. Hong, I. W. Wu, J. T. Holthuis, and J. W. Morris, Jr., Adv. Cryo. Eng., 28, 483, 1982.

63. R. Akihama, R. J. Murphy, and S. Foner, IEEE Trans. Magn., MAG-17, 274, 1981.

64. M. R. Pickus, J. T. Holthuis, and M. Rosen, in Filamentary A15 Superconductors, M. Suenaga and A.F. Clark, eds., Plenum Press, New York, 1980, p. 331.

65. M. R. Pickus, V. F. Zackay, E. R. Parker, and J. T. Holthuis, Internat'l J. Powder Met., 9, 3, 1973.

66. J. W. Morris, Jr., Presented at the Workshop on Development of Superconductors for Fusion Power, D.O.E., Washington, D.C., January, 1978.

67. M. Hong, D. R. Dietderich, and J. W. Morris, Jr., J. Appl. Phys., 51, 2774, 1980.

68. I. W. Wu., M. Hong, and J. W. Morris, Jr., Appl. Phys. Lett., 39, 110, 1981.

V. EXPERIMENTAL PROCEDURE

A. MATERIALS PREPARATION AND HEAT TREATMENT

1. Direct Precipitated V_3Ga and Nb_3Al. The direct precipitation process has been developed by Pan et al. [1] in 1975 for the V-Ga system and subsequently studied by Hong et al. [2]. This method was also extended for the Nb-Al system [3]. In this process, the elements that form the A_3B A15 compound are arc melted in a proportion that permits the formation of an A-rich homogeneous solid solution at elevated temperatures. The homogenized solution is quenched to a low temperature at a cooling rate sufficiently rapid to prevent the formation of the A15 phase and then rolled at intermediate temperature into a tape. After deformation, the material is aged at an intermediate temperature to precipitate the A15 phase.

In this study, the V-15.5 at.% Ga samples were deformed at 700°C to 90% areal reduction. Several V-18at.% Ga samples were re-solution treated to compare the effect of deformation. The Nb-18 at.%Al samples were deformed at 750°C to 99% areal reduction.

The aging treatment was done at 700 and 750°C for V-Ga and Nb-Al samples, respectively. The aging temperatures were chosen such that these samples yield the best current carrying capacity among others. For both V-Ga and Nb-Al samples, the aging treatments were carried out by wrapping the samples in Ta foil bags and sealed in evacuated quartz tubes that were back-filled with argon. The purpose of wrapping the samples in the Ta foil was to prevent contamination from the reaction between the sample and quartz tube.

2. Conventional Bronze-Processed Nb_3Sn Multifilamentary Wire. The wire used in this study was manufactured by Airco Superconductors. It was a composite wire, 0.7mm in diameter, that contained an active core approximately $0.14mm^2$ in cross-sectional area. An etched section of the multifilamentary core is shown in Figure V-1, the core held 2869 niobium filaments grouped into sets of 19. The individual filaments were 3 to 5 microns in diameter. They were embedded in a Cu-13 wt.% Sn bronze matrix to give an overall bronze to niobium ratio of 3:1. The cores was wrapped with a tantalum foil diffusion barrier approximately 30 microns thick. For thermal and electric stabilization the wrapped core was encased in a pure copper shell, 0.15mm in thickness, which accounted for roughly two-thirds of the wire cross-section.

Samples of the wire were heat treated after encapsulation in sealed quartz tubes that were back-filled with argon. They were reacted at temperatures in the range 650 to 800°C for various periods of time. The maximum reaction time at each temperature was that which was necessary to achieve an essentially complete conversion of the niobium filaments to Nb_3Sn.

3. Bronze-Processed Multifilamentary Nb_3Sn Wires with Magnesium Addition to the Bronze. The multifilamentary wires used in this research were manufactured in the Materials and Molecular Research Division (MMRD) of the Lawrence Berkeley Laboratory from pure starting materials. They differed in composition of the bronze (Table V-1) which was varied to measure the influence of Mg at two Sn levels. The initial bronze ingots were melted in quartz tubes under argon atmosphere and cast into rods. The rods were doubly swaged and homogenized and were then machined into 10mm outer diameter and bored to form tubes of 5mm

inner diameter. Pure Nb rods were inserted into the tubes and the composite was drawn into wire. The monofilament wires were bundled into groups of seven, enclosed in a tube of the same bronze composition, and redrawn. The seven-filament wires were then rebundled into groups of nineteen (133 filaments) inside bronze tubes of identical composition and drawn to a final size of 0.5mm in diameter. During the drawing process, the wires were annealed at 450°C for approximately 40 minutes after each 50 to 80% reduction in area to anneal out the work-hardening of the bronze matrix. The annealing temperature and time were determined by the transition temperature measurement (no Nb_3Sn phase formed) and the workability. By this process, it is possible to fabricate multifilamentary wires without hydrostatic extrusion for small amounts of laboratory scale research purposes.

Sample cross-sections of two finished and partially reacted wires are shown in Figure V-2. The filaments are reasonably uniform, although those near the periphery of the wire are noticeably flattened. Small differences in the drawing properties of the wires due to the difference in composition of the bronze matrix caused the filament size to vary from wire to wire. However, for a particular wire the filament size was uniform within 10% along the length of the wire. The compositions and characteristcs of the wires are listed in Table I, where the composition of the bronze matrix is given in atomic percent (the balance is copper), D is the effective diameter of the filaments (determined from the cross-sectional area of the filament) and R is the volumetric ratio of the bronze to the Niobium.

After manufacture, the wires were sectioned into segments approximately 10cm in length and heat treated in sealed quartz tubes under

argon to form the A15 phase. The heat treatment temperatures were 650, 700, 730, 750 and 780°C and were chosen to bracket the optimum reaction temperature of the Mg-free wire [4,5]. The heat treatment times were a few hours to twenty days. The progress of the reaction during heat treatment was monitored by sectioning the wires after selected reaction times, taking scanning electron micrographs and measuring the area of the reacted layer with an image processing microcomputer. The consistency of measurements taken from serial sections confirmed that the reaction was uniform along the wire length.

B. MATERIALS CHARACTERIZATION.

The important materials' parameters include the overall extent of the reaction and the physical and chemical state of the superconducting phase formed. The methods of materials characterization to determine these parameters are the same for all the materials under investigation of this study.

1. Optical and Scanning Electron Microscopy. The extent of the reaction was determined by optical and scanning electron microscopic examination of etched surface of the heat-treated samples. For the direct precipitated V-Ga and Nb-Al samples, the A15 phase can be distinguished from the BCC matrix by the distinct appearance of the different etching behavior. Figure V-3 shows micrographs for V-15.6at.% Ga, 75% deformed, and aged at 700°C for 24 hours. It is clear that the V_3Ga phase formed along deformation textures. Due to this inhomogeneous nucleation and growth, an accurate determination of the volume percent is difficult in practice. Notice that in Figure V-3b, the A15 phase

region is a depression instead of an extrusion, this may be due to the etching acid attacks at the A15-BCC interface which is much faster than the phases themselves, and the A15 grains left the sample surface during cleaning.

For the bronze-processed wires, the Nb_3Sn layer is easily distinguished from both the bronze matrix and the unreacted Nb core by its intergranular brittle appearance in the broken wire sections and by its distinct etching behavior. Figure V-2 shows an example of the etching behavior of the laboratory scale mulfifilamentary wire and Figure V-4 is a scanning electron micrograph of a polished and etched section of the Airco wire.

The scanning electron microscopy also is useful to reveal the apparent grain size of the bronze-processed wires. The procedure of this experiment is to file or etch a small notch in the center of a small piece of wire and fracture it in liquid nitrogen to prevent plastic deformation, followed by dipping the fracture tip into acid to remove the bronze matrix. To enhance the contrast of the micrographs and minimize the build-up of charges on the surface, the specimens were sputtered with a few hundred Angstroms of gold.

2. Transmission Electron Microscopy (TEM). The physical and chemical state of the A15 phases were studied by transmission electron microscopy (TEM) on the thin sections. For direct precipitated V-Ga and Nb-Al, TEM specimens were prepared by mechanically grinding the as-deformed tape down to 4-5 mils, spark-cut into 3mm disks, heat treated at the desired condition, then followed by an ion-beam milling until perferated. Other thinning techniques are not suitable for preparation of foil due to the brittleness and preferential etching of the specimens

after aging. The same difficulties arise if the specimens were to be ground after heat treatment. The A15 grain size is typically less than 1 or 2 microns, which is much smaller than the specimen thickness before heat treatment (~100 microns), and the bulk behavior is believed to be preserved in TEM foils.

For the bronze-processed wires, samples for transmission electron microscopy began as longitudinal sections cut from the wire to reveal the multifilamentary material. The samples were ground mechanically to approximately 40 microns in thickness and glued on a copper disk holder by epoxy, and then milled in an ion-beam miller until perferated. For the study of grain morphology and the chemical state of the A15 layer, at least two whole Nb_3Sn layers have to be transparent to 100kV electrons. Close to 100% successful rate of sample preparation was achieved (after one year of trial and error) by first ion-milled at 7kV, 1mAmp and 22° impinging angle until perferated, then lower the voltage to 5kV, 0.4mAmp and 12° for 6-8 hours. The first step thinning is to establish a thin foil without preferential sputtering, and the second step is to smooth the damaged surface and make a uniformly thin area.

The TEM specimens were examined in a Siemens 102 and/or JEOL-100C electron microscope operated at 100kV, using a double tilt goniometer stage to achieve the desired diffraction conditions. The principal object of these examinations was to determine the A15 grain size. The grain size could be roughly estimated from scanning electron micrographs of the broken wire surfaces or the polished and etched cross-sections. However, since only some of the grain boundaries appear in the fracture surface, the transmission electron micrographs, at least 100 grains were

sampled for each datum point. Typically, the standard deviations of the measurement are within 10%.

3. Convergent Beam Electron Diffraction. The convergen beam electron diffraction (CBED) which is capable of forming a small electron probe and obtaining a 3-dimensional k-space information [6] was employed to determine the crystallographic orientation of submicron-sized A15 structure V_3Ga and Nb_3Al precipitates from supersaturated BCC solutions [7]. The thin foil specimens used in this study were the same samples for the TEM observations described above. The main facility was the JEOL 100C electron microscope capable of converging the electron beam to 1000 Angstrom probe size. The Philips-400 electron microscope with a scanning transmission attachment that is capable of converging down to 40 Angstroms was also used. The CBED technique was also used in determination of the misorientation between the fine grains (a few hundred Angstrom) of the bronze-processed wires. One hundred Angstrom probe of Philips 400 EM-operated at STEM mode was used in this study.

4. The STEM/EDXS Analysis. The chemical state of the reacted A15 phase was studied with a scanning transmission electron microscope (STEM). The specimens employed were TEM foils prepared as described above. They were examined with a 100kV, 100 Angstrom diameter electron probe in a Philips 400 electron microscope equipped with an energy dispersive x-ray spectrometer (EDXS). The x-ray spectrum was analyzed quantitatively using a KEVEX 7000 microcomputer. A beryllium low-background stage with a 30° tilting axis was used to minimize spurious excitations. For direct-precipitated V-Ga and Nb-Al samples, the spectrometer was set to 10keV and 20keV respectively, in order to use the more accurate k-lines excitations of the elements in question. For the

bronze-processed wires, the spectrometer was set at 40keV for the same reason. Quantitative results were obtained by counting the integrate peak intensities after background stripping. Each peak intensities were then analyzed by using a standardless approximation method [8] to convert into atomic composition which has a 10-20% maximum error in the absolute value. Residual niobium and in-hole configurations were examined to monitor the background shape and the peaks caused by inelastic scattering and spurious excitation. Non-uniformity in the specimen thickness is a further possible source of error. The spectra taken in this study were from the regions of approximately the same thickness as monitored by the transparency of the electron beam. The experimental set-up and integrated count number were kept as nearly constant as possible to minimize systematic errors.

5. The Electron Microprobe (EMP) Analysis. The samples for EMP analysis were the same as the optical microscopic specimens described above. The EMP analysis has a spatial resolution in the order of one micron and is incapable of resolving fine A15 layers. However, EMP has an advantage of high sensitivity for Mg in contrast to the low sensitivity of EDXS. Therefore, EMP was used to study the segregation of Mg in the MMRD wires. A commercial Mark-V electron microprobe was used in this study equipped with three x-ray wavelength dispersive spectrometer.

6. Scanning Auger Microprobe (SAM) Analysis. For the determination of the chemical difference of the grain boundary to that of the bulk, scanning Auger microprobe (SAM) analysis was employed for the bronze-processed wires. A Physical Electronics Super SAM was used in this study which is capable of forming a 1000 Angstrom probe with good signal to noise ratio, operated at 7kV and ultra-high vacuum condition. The

samples for the SAM Analysis were pre-etched out of the bronze matrix and mounted in the SAM stage. Fracture was performed right before the sample went into the high vacuum chamber to avoid contamination of the fracture surface. The difference in composition between the grain boundaries and the bulk is then the difference of spectra before and after sputtering since the fracture surface contains intergranular grain boundaries. The composition is determined by measuring the peak to peak height of each elements and their sensitivity factors. Quantitative results are not very accurate because of drastic differences in the sensitivity (compared with the EDXS and the EMP data). However, to study the location of the segregated Hg in the Nb_3Sn layer, this is the only method at present. This is due to the shallow escaping depth (~50 Angstrom) of the Auger electrons.

C. SUPERCONDUCTING PROPERTIES MEASUREMENT.

The superconducting properties that were determined included the transition temperature from the normal to the superconducting state, T_c, the critical current characteristics, $I_c(H)$, and the upper critical field, H_{c2} at 4.2K.

1. <u>Inductive-Transition Temperature Measurement</u>. The transition temperature was measured inductively as described in section II-B. Samples for direct-precipitated V-Ga and Nb-Al were irregular in shape but similar in volume since the inductive method has the advantage that it requires no electric contact with the sample and, thus, shapes of the sample could be irregular. Samples for bronze-processed wires were bent into a ring shape before the heat treatment and were etched to minimize

the shielding effect of the normal conductor. The onset and finish temperatures of the superconducting transition were taken to be the temperatures that gave 10% and 90% of the total inductive signal, respectively. the temperatures of the specimen were measured by a calibrated germanium thermometer.

2. Critical Current Characteristics Measurement. The critical current characterisitics were measured by using a standard four-point probe technique on samples placed in transverse magnetic fields that ranged in intensity from 6 to 19.5 tesla. The reported value of the critical current is that which produced an 0.5 microvolt potential between voltage taps 5mm apart except for the measurement of MMRD wire, which corresponded to 1 microvolt between taps of 5mm apart. The sensitivity of the measurement varies from field to field, as well as sample to sample. Typically, for the bronze-processed wires, the corresponding sensitivity at 10T is in the range of 5×10^{-13} to 1×10^{-12} ohm-cm and 2×10^{-22} to 1×10^{-11} ohm-cm at 15T (calculated for the cross-sectional area of the superconducting phase). All of the critical current measurements were done at the Francis Bitter National Magnet Laboratory, Cambridge, Massachusetts.

The critical current density, $J_c(H)$, within the tested samples was calculated from the overall critical current by dividing I_c by the cross-sectional area. For samples of direct-precipitated V-Ga or Nb-Al tapes, the $J_c(H)$ data reported here were divided by the overall cross-sectional area of the tape. For the Airco wires, $J_c(H)$ was determined by the cross-sectional area of the non-copper area, $0.14 mm^2$. The Nb_3Sn phase cross-sectional area was used in determining the $J_c(H)$ for the

MMRD wires to eliminate the variation that arises from the differences in filament size and shape.

3. <u>The Upper Critical Field, H_{c2}</u>. The upper critical field, H_{c2}, was obtained by extrapolating $J_c^{1/2}$ $H^{1/4}$ versus H to zero current [9]. The extrapolating was done by a least square fit of straight line from data points obtained from 16 to 19.5 tesla. The value of H_{c2} by this method is generally lower than that of direct measurement. However, a comparison between samples can be obtained.

Table 1. Chemical composition of the bronze matrix and average filament diameter (D) and bronze to Nb ratio (R) of laboratory scale multifilamentary Nb_3Sn wires.

Bronze matrix at.%, bal. Cu	average filament diameter D, μm	bronze/Nb ratio, R
6.7 Sn	11.4	14
6.7 Sn + 0.1 Mg	13.4	10
6.7 Sn + 0.2 Mg	10.9	15.3
6.7 Sn + 0.35 Mg	10.7	15.9
6.7 Sn + 0.62 Mg	12.5	12
7.8 Sn	8.3	27
7.8 Sn + 0.1 Mg	12.1	12

REFERENCES

1. V. M. Pan, Y. I. Beletskiy, V. S. Flis, S. A. Firstovand and G. F. Sarzhan: Fiz. Metal. Metalloved, 40, 281, 1975.

2. M. Hong, D. R. Dietderich, and J. W. Morris, Jr., J. Appl. Phys., 51, 2774, 1980.

3. M. Hong, D. R. Dietderich, I. W. Wu and J. W. Morris, Jr., IEEE Trans. Magn., MAG-17, 278, 1981.

4. I. W. Wu, W. V. Hassenzahl and J. W. Morris, Jr.: Proc. Inter-Nat'l Cryogenic Materials Conf., Kobe, Japan, Tachikawa, K. and Clark, A. (eds.) Butterworth's, London, 1982, p. 388.

5. I.W. Wu, et al., to be published in J. Appl. Phys., 1983.

6. J. W. Steeds: in **Introduction to Analytical Electron Microscopy**, Hren, J.J., Goldstein, J.I. and Joy, D.C. (eds.) Plenum Press, New York, 1980, p. 387.

7. I. W. Wu, M. Hong, and J. W. Morris, Apply. Phys. Lett., 39, 110, 1981.

8. J. I. Goldstein: in **Introduction to Analytical Electron Microscopy**, Hren, J.J., Goldstein, J.I. and Joy, D.C. (eds.) Plenum Press, New York, 1980, p. 83.

9. E. J. Kramer, J. Appl. Phys., 44, 1360, 1973.

VI. THE MICROSTRUCTURES OF DIRECT-PRECIPITATED V_3Ga AND Nb_3Al

A. INTRODUCTION

A15 compounds, like all the other ordered intermetallic compounds, are intrinsically brittle. Special processing techniques are required for the fabrication of these materials into useful conductors. Among the processing methods (described in Section IV-3) the direct-precipitation process has the advantage of being a simple monolithic tecnique from which the interpretation of its superconducting properties can be readily understood by the processing and microstructures.

The direct-precipitation process is simple to design in theory, and can be understood with reference to the V-Ga phase diagram [1-3]. The V_3Ga phase has a range of stability from 20 at.% to 30 at.% Ga and is characterized by a congruent transformation from the BCC solid solution at 1300°C,25 at.% Ga. A monolithic process can be designed in which a V-Ga ingot with its composition in the BCC + A15 phase region at lower temperatures (below the ordering temperature) is made homogeneous BCC solid solution by heat treatment at temperatures above the ordering temperature. If the ingot can be subsequently cooled at a rate sufficient to suppress the formation of the V_3Ga ordered compound, then a supersaturated solid solution can be made. The resultant solution is relatively ductile and amenable to process through wire drawing or extrusion. After deformation, the superconducting phase can then be introduced by an aging treatment for the precipitation of the V_3Ga phase. This monolithic processing was first proposed by the prior work

of Das et al. [2] and extended by Pan et al. [4] and Hong et al. [3] in the V-Ga system.

The same metallurgical principle can be applied to the Nb-Al system. Although the transformation of Nb_3Al phase is by a peritectic transformation the from BCC + Nb_2Al two phase field [5] instead of a congruent transformation as that of the V_3Ga, yet a range of composition can be found which lies in the two phase (A15 + BCC) region at lower temperatures but in the BCC solution at higher temperatures. Therefore, the same procedure can be applied to fabricate the Nb_3Al superconductor. This method was recognized by Webb et al. [6,7] and Pan et al. [8] and Hong et al. [9].

While the processing method described above is simple and appealing in theory, its practical implementation faces substantial difficulties. In Hong's thesis [10], which is devoted to the processing method and its superconducting property, several problems were described: sample preparation, quench cracking, brittleness, interstitial impurities, and non-stoichiometric starting ingot limitation. However, these problems are not intrinsic difficulties associated with this process, they can be largely overcome by modifications in materials and processing. It is my belief that there are at least several other more severe disadvantages which discourage the scale-up of this process for high-field applications. These difficulties are more intrinsic in nature and cannot be overcome by simple modification of processing.

The first difficulty is the fast quenching rate which is required for suppressing the formation of the brittle A15 phase. Even though small ingots has been successfully fabricated in laboratory, in the real application, however, this required process is prohibitive. It is

desirable to fabricate a large quantity of superconductor with controllable properties. This requires that a large ingot should be cooled at a very high rate homogeneously. Current technology is incapable of handling such a large ingot at the temperature around 1300°C and quenching it to room temperature without the problems of thermal stress and chemical segregation. This is a three fold problem of heat capacitance, thermal conductivity and thermal expansion. These parameters are all intrinsic materials properties and they can not be changed into more desirable values for the quenching process to be realized.

The other difficulty associated with this process may be even more prohibitive. It is the inferior current carrying capacity compared to other processing techniques. This point will become more apparent in the following discussion of results of microstructural studies. The critical current of a superconducting body is known to be determined by volume of the superconducting phase and the critical current density, J_c, within it. The critical current density is a function of the transverse magnetic field, H. The characteristic function, $J_c(H)$, depends on the effective cross-sectional area of the superconducting phase and on its microstructural state. The most important microstructural parameters are the composition and crystallographic order of the A15 crystal, the grain size, and the continuity.

The main reasons of the inferior current-carrying capacity of the direct-precipitation process are two-fold: the grain size and chemical composition of the A15 crystals. The grain size of the direct-precipitated A15 phase is approximately five times as large as that of a bronze-processed wire. This ratio is even larger as compared to a carefully processed powder or an in situ wire. The intrinsic problem here

is that the nucleation of the A15 occurs at a much slower rate than in the other processes. This might be due to the fact that the interface of different phases are very effective nucleation sites for the A15, e.g., the Nb and bronze or Nb and Al interfaces. In the direct-precipitation process, the nucleation sites are subgrain boundaries of the BCC phase which are much less effective. The grain size of the A15 phase is determined by the rate of nucleation, a smaller rate causes a larger grain size. The grain boundary is the primary flux pinning site for the A15 type superconductor,and a large grain size means a less strong pinning, and smaller critical current density.

The other problem of the microstructural state of the precipitated A15 phase is its composition. At equilibrium, the A15 phase formed will have a composition corresponding to the phase boundary of BCC + A15 and A15 phase field. This composition is always lean in the B element of the A_3B phase. An non-equilibrium composition will be shown later to exist, but the tendency is always toward off-stoichiometric composition. This effect further reduces the ability for the precipitation process to yield high-J_c conductors.

The other point that may also be an important influence in the current-carrying capacity of the direct-precipitated wire is a continuity (or connectivity) problem. Thin films of BCC phase between A15 grains are generally lean in B element due to the out-diffusion into the adjacent A15 grains. Therefore, the thermodynamical stability of the BCC phase is greatly enhanced (the microstructural evidence is given in the following text). The existence of the resistive films between superconducting grains induces a voltage drop and local heating effect which reduces the stability of the conductor.

The disadvantages discussed above, namely, the quenching problem and the inferior micro-physical and chemical state of the A15 phase, are believed to be intrinsic in nature, that is, they cannot be overcome by modification of the process. These points lead me to propose that this method is not promising to produce a practical conductor, against previous workers' suggestion.

Although the direct-precipitation process is not suitable for the fabrication of high-field conductors, this process employs a unique metallurgical principle which is different from all other processes. The A15 phase formed by this process is in a unconstrained state, i.e., precipitation from a supersaturated solution. All the other currently adopted processes rely on the formation of A15 phase at the interface of the other two phases. Therefore, the formation of the A15 phase is by a directional diffusion mechanism at some pre-determined spatial site. Because of this mechanism the A15 phases thus formed are constrained.

Therefore the microstructural study of the direct-precipitated A15 phase will provide vital information concerning the nucleation and growth kinetics, the orientation relationship with the BCC matrix, the compositions and kinetic effect, the stability of A15 and BCC phase, and the correlation of the microstructure to superconducting properties. In fact, discussion of the disadvantages associated with this process in the present section are largely dependent upon the results of the microstructural analyses. These points were not recognized before this study.

Research on the direct-precipitated V_3Ga and Nb_3Al reported here is mainly focussed on microstructural study and correlation with the superconducting properties. Based on this objective, V-15.6 at.% Ga and 18

at.% Ga and Nb-17.8 at.% Al compositions were selected. After homogenization, quench, and deformation, the specimens were given aging treatments at 700°C and 750°C for various periods of time. The aging temperatures were selected such that the highest J_c was obtained. Although this project is not complete due to lack of interest in the less superior properties, several points of interest can be described in the following sections.

B. SUPERCONDUCTING PROPERTIES

Measurements of superconducting properties included inductive T_c, four-point probe J_c under static transverse-magnetic field, and H_{c2} extrapolation from $J_c^{1/2}H^{1/4}$ versus H method for V-15.6 at.% Ga and -18 at.% Ga and Nb-17.8 at.% Al tape-shaped samples.

1. <u>The Transition Temperature Measurement</u>. The results of the transition temperature onset for the V-15.6 at.% Ga and 18 at.% Ga after homogenization followed by deformation at 700°C to 90% reduction in cross-sectional area, and aged at 700°C for various periods of time ranged from one to 300 hours are shown in Fig. VI-1. Those of precipitated Nb-17.8 at.% Al samples aged at 750°C are shown in Fig. VI-2. Also included in this figure are the results of the Nb-18.8 at.% Al samples for comparison. The data show that the onset of the critical transition temperature generally increases with aging time. However, the characteristics of each composition is quite different. The data of V-15.6 at.% Ga has a maximum T_c at 14K for samples aged for 4 days, then decreases with prolonged aging. While, the T_c of the V-18 at.% Ga samples increases monotonically to 15K which is close to that of the

stoichiometric composition [1,2]. The data of Nb-17.8 at.% Al samples showed a much less drastic change with respect to the aging time: approximately 2K difference with aging time changes from one to seven hundred hours. The data of Nb-18.8 at.% Al samples showed a similar trend and were about one degree Kelvin higher than that of the Nb-17.8 at.% Al. However, the highest T_c onset is only about 15K, which is about 3K lower than that of the stoichiometric Nb_3Al [11].

2. The Upper Critical Field H_{c2}. The upper critical fields, H_{c2}, were estimated by extrapolating the critical current characteristic as suggested by Kramer [12]. Examples of the upper critical fields of precipitated V-Ga and Nb-Al are shown in Figs. VI-3 and VI-4, respectively. Comparing the upper critical field data to the critical transition temperature (Figs. VI-1 and 2), it is found that they have a close correlation between them though not identical. Assuming that the precipitated crystallites have a range of composition, the inductive T_c measurement will tend to measure the properties of the most nearly stoichiometric (highest T_c) particles, provided these particles are larger than approximately twice the penetration depth, while the H_{c2} will reflect a composition closer to the mean. Hence, it is not surprising that these characteristic property curves have slightly different shapes.

3. Critical Current Characteristics. The variation of overall critical current with applied magnetic field was measured for a number of V-Ga and Nb-Al specimens. The overall critical current density, J_c, is obtained by dividing the I_c by the cross-sectional area of the tape shape specimen. The sensitivity of this measurement is not very high even though a 1μV/cm criterion is used, which is approximately in the

order of 10^{-10} ohm-cm range. Examples of the data are given in Figs. VI-5, 6 and 7 showing the variation of properties with heat treatment time for different composition.

In the V-Ga case represented in Figs. VI-5 and 6, the current-carrying properties improve over the whole range of fields studied as the heat treatment time is increased to 48 hours but deteriorate thereafter. In the Nb-Al case represented in Fig. VI-7, the low field properties improve for heat treatment time up to 12 hours and deteriorate thereafter, while the properties at the highest fields studied continue to improve.

The correlation of the superconducting properties with the microstructure and microchemical state of the A15 phases will be discussed in the following sections. Particular attention is giving to understanding the critical current characteristic from the intrinsic properties of the A15 particles.

C. RESULTS

1. The Recovery of Deformation. Samples of V-15.6 at.% Ga and 18 at.% Ga BCC solution were deformed at 700°C to 90% reduction of thickness. The microstructure of the as-deformed specimens consisted of a high density of dislocations as well as the prior-deformation grains. Fig. VI-8 shows a sample TEM microstructure of an as-deformed specimen. The dislocations are severely tangled, but there is no evidence of dynamic recovery. Also, there is no A15 precipitation found in the as-deformed specimen, indicating both the quenching and deformation process are successful in suppressing the formation of A15 crystal.

During aging heat treatment at 700°C, the dislocations annihilated and polygonized into dislocation walls and gradually reduced in density. Two sample TEM micrographs of the polygonized wall structures are shown in Figs. VI-9 and 10, of V-15.6 at.% Ga sample aged at 700°C for 2 days. The density of dislocation is significantly reduced from that of the as-deformed specimen.

Figure VI-11 shows a TEM micrograph of V-18 at.% Ga sample aged at 700°C for one day. The polygonized dislocation wall structure is also evident.

The quenched Nb-17.8 at.% Al solid solution was deformed 99% and aged at 750°C. The as-deformed specimens show a high density of dislocations. There is no evidence of dynamic recovery or the A15 phase. Fig. VI-12 shows a TEM micrograph of a sample aged at 750°C for 12 hours. Notice that the recovery process has driven the dislocations to form bands of high dislocation density, but very little well-developed dislocation cells has occurred. This behavior, which is different from that of V-Ga samples, may be due to a higher density of dislocations and/or a slower polygonization process.

2. <u>The Microstructures of Precipitated V-15.6 at.% Ga</u>. The TEM study in this research is focussed on the physical state of the precipitated A15 phase nucleation and growth of crystal, defects in the precipitates, and its grain size. This section describes the result of microstructural study of the V-15.6 at.% Ga after 90% deformation and aged at 700°C for various periods of time.

Figure VI-13 shows a sample V_3Ga precipitate at the intersections of prior-grain boundaries of a sample aged for one day. The nucleation of the precipitates is rather inhomogeneous, as a result, only a small

number of precipitates were found in the thin foil TEM samples. These precipitates generally were found at the grain boundaries, especially the intersection of grain boundaries as the one shown in the figure. It can also be observed that the growth of the precipitates follows some definite crystallographic orientation. In Fig. VI-13, the precipitate grew into different grains along different orientations which formed an interesting morphology. Due to the rather small nucleation sites of the grain boundaries, it is not surprising that the number of precipitates is small.

For samples aged at 700°C for 2 days, the morphology of A15 precipitation is quite different from that of the samples aged for one day. The volume fraction of precipitates increases significantly, and can be found to nucleate and grow from dislocation walls also. This can be attributed to the fact that the kinetics of nucleation on dislocation walls is sufficiently high for 2 days aging for the precipitates to be observed.

The difference of nucleation kinetics between the prior-grain boundaries and dislocation walls is one important reason for the large variation in grain size observed. The grain size of precipitates nucleated on the prior-deformation grain boundaries is larger than that of the dislocation walls. Also, the nucleation of A15 precipitates does not occur on all dislocation walls. Some of the dislocation wall sites are more favorable than others. Examples of this phenomenon can be demonstrated by referring to Figs. VI-9 and 10. The dislocation walls are very stable compared to the formation of A15 phase. This inhomogeneous nature of nucleation is quite common for all V-Ga samples, irrespective of the overall composition or aging time.

Another common phenomenon is that the nucleated V_3Ga precipitates are generally free of defects in the grains' interior. Only some in-grown dislocations were observed. An example of the in-grown dislocation dipole is shown in Fig. VI-14 of a sample aged at 700°C for 2 days. The insert of this figure shows the diffraction condition of the micrograph. The A15 grain in the center is near the (111) zone-axis and the BCC film to the left of the figure shows a strong reflection of [011] spots. The in-grown dislocation has been identified by a contrast analysis [13-15] to be edge in character with Burgers vector of the type ⟨100⟩ and lies on a ⟨001⟩ direction. This result is consistent with that reported by Pande [16]. The A15 grains were elongated with aspect ratios between 2 to 5. A film of BCC phase with a high density of dislocations usually exists between two adjacent A15 grains.

Figures VI-15 and 16 show two typical TEM micrographs of samples aged for 69 hours. The elongation of the A15 grains and the BCC films between A15 grains are very distinct. Under a suitable diffraction condition, e.g., Fig. VI-15, it can be seen that A15 grains are highly correlated crystallographically, even though they were separated physically. This is an indication that a definite crystallographic orientation exists between the A15 grains and BCC matrix.

For samples aged for 4.5 days, similar features have been observed. Figs. VI-17 and 18 showed two micrographs of clustered A15 grains with BCC films between them. The grain size is noticeably larger than that of shorter aging times, while the aspect ratio remained similar. An example of the nucleation of V_3Ga grains on a dislocation cell boundary is shown in Fig. VI-19, and the diffraction pattern of the A15 grain is given in the insert. It is clear that the two elongated A15 grains in

this figure lie on the dislocation cell wall, and that a film of BCC matrix is stable in between A15 grains. These kinds of micrographs established that the dislocation cell walls are the nucleation sites for the precipitation of A15 phase.

Figure VI-20 is a TEM micrograph of a sample aged for 7 days and Figs. VI-21 and 22 show two micrographs of samples aged for 11.5 days. It can be seen that the general features are similar, but the average grain size increases with aging time. The cluster of A15 grains in Fig. 6.22 all have the same crystallographic orientation (see the inserted diffraction pattern) such that all the grains exhibit a similar contrast. Fig. VI-23 is a dark field micrograph taken from a diffraction maximum of the A15 phase, and the BCC matrix is dark. Thickness contours are very distinct in the A15 grains. Also, the BCC films between A15 grains can be seen to be very stable, even with this long aging time (11.5 days).

3. <u>The Microstructures of Precipitated V-18 at.% Ga After 90% Deformation</u>. The precipitation and recovery process of V-18 at.% Ga after 90% reduction in cross-sectional area are very similar to that of V-15.6 at.% Ga discussed in the previous section. The range of aging time for V-18 at.% Ga samples is between 3 hours to 2 days, instead of 1 to 11.5 days aging time for 15.6 at.% Ga samples. This is because the precipitation kinetics are much faster in the case of 18 at.% Ga (Fig. VI-6).

Figure VI-24 shows a sample TEM micrograph of samples aged at 700°C for 6 hours. The corresponding diffraction pattern of the V_3Ga precipitates are shown in the insert. Even with such a short aging time, a large number of V_3Ga precipitates are observed. The recovery process

causes dislocations to form bands of high dislocation density, and V_3Ga phase nucleates and grows from thse bands. Therefore, an increase of the gallium content from 15.6 to 18 enhances the nucleation kinetics: a comparison can be made of the same nucleation sites for 6 hours and 48 hours aging at 700°C, respectively. The precipitated V_3Ga grains are elongated as that of the V-15.6 at.% Ga sample.

Figure VI-25 shows a typical TEM micrograph of a sample aged at 700°C for 12 hours. The elongated shape of the V_3Ga grains is evident. Also, even though the A15 precipitates have a closely correlated crystal orientation (the insert of the figure), coalescence of grains to form a larger grain does not happen, or at least in a very small amount. It is clear that a film of BCC phase is stable against coalescence of the adjacent grains.

Figure VI-26 is an example of the microstructure of samples aged for one day. The region in this figure was almost fully occupied by the precipitated V_3Ga phase. However, films of the BCC phase still persist between the A15 grains.

The microstructure of the samples aged at 700°C for 2 days is quite different from the others. Figure VI-27 shows a typical bright field micrograph and corresponding diffraction pattern. The main difference here is that the film of BCC matrix phase that persisted between A15 grains underwent spheroidization in this sample. The driving force of spheroidization is the reduction of surface energy between BCC and A15 phase. This spheroidized BCC phase is still stable against further shrinkage and contains a high density of dislocations. The A15 phase is strained, as can be seen by the strain contrast near the BCC phase. Also, it is clear that the A15 grains are in a very close crystallo-

graphic orientation such that when different grains coalesce, there is no grain boundary in between them. This can only be due to the A15 phase that precipitates from the BCC matrix following a definite crystallographic orientation relationship.

4. Microstructures of Nb-17.8 at.% Al Aged at 750°C After 99% Deformation. Samples for microstructural analysis were aged from 1.5 to 12 hours at 750°C after 99% reduction in thickness. The precipitation kinetics are faster than the V-Ga samples, this may be due to: (1) diffusion of Al in Nb is faster than Ga in V through a higher density of dislocation cores produced by larger reduction and higher temperature aging, (2) the dislocation cell walls are more effective nucleation sites for precipitation of Nb_3Al, and (3) 17.8 at.% Al is closer to the A15 phase boundary on the phase diagram [5] than that of 18 at.% Ga [1-3], so that the chemical driving force is larger. Because of these reasons, the aging times for the Nb-Al samples are shorter than V-Ga samples.

Figures VI-28 and 29 show two typical TEM micrographs of samples aged at 750°C for 3 hours. It can be seen that the precipitated Nb_3Al crystals are equiaxed in shape and preferentially precipitated on the dislocation cell walls. Another important feature that can be seen from these types of micrographs is that BCC matrix phase is still quite stable between A15 grains. These BCC matrix films, instead of having a plate shape in the case of V-Ga specimen, has a hyperbolic shape because their adjacent A15 grains are equiaxed.

Figure VI-30 shows a TEM micrograph of specimen aged for 6 hours. The BCC matrix films are more distinct and the A15 grain size is noticeably larger than that of the samples aged for 6 hours. Figs. 6.31 and

32 are micrographs and the corresponding diffraction patterns of samples aged at 750°C for 12 hours. The grain size is progressively larger and equiaxed in shape. From the diffraction patterns inserted in the figures, it can be noted that the Nb_3Al grains are closely related in crystallographic orientation, similar to that of V_3Ga. Complex contrast is associated with Nb_3Al grains, this may be due to either bending contours of thin foil sample buckling or the Nb_3Al grains were strained. The complex contrast is more severe in the precipitated Nb_3Al than in V_3Ga.

5. Grain Sizes of Precipitated A15 Phase. The grain size of the precipitated A15 phase was determined by direct measurement of TEM micrographs. At least 50 grains were sampled for each datum. Both the width and length of each grain of the V_3Ga phase were measured due to their elongated shape. For equiaxed Nb_3Al grains, the grain diameters were measured.

Figure VI-33 shows the result of V-15.6 at.% Ga. It was plotted as the logarithm of grain size in micron meter versus that of the aging time in hours. The grain size of samples aged for one day was not given in the figure. Because of too small a number of grains were observed and the statistic error is large. The standard deviation of each datum point is marked by the error bar.

The average aspect ratio for V-15.6 at.% Ga aged at 700°C increases slightly with aging time: from 2.2 for the sample aged for 2 days to 3.5 for the sample aged for 11 days. The grain size versus aging time relation in the log-log plot fits very nicely with a straight line. The slopes of these two lines were determined by a least square fit method

and found to have the values of 0.24 and 0.42 for width and length of A15 grains, respectively.

The results of grain size measurements for V-18 at.% Ga deformed to 90% area reduction are shown in Figure 6.34. The statistical standard deviation is given as the error bar for each datum. The least square fit straight lines are also shown in the figure. The width and length of the V_3Ga grains increased following a power relation with aging time. The power coefficients are 0.36 and 0.13 for the length and width, respectively.

Figure VI-35 shows the results of grain size measurement for Nb-17.8 at.% Al samples. The power coefficient of the relation between grain size and aging time is 0.49. The average grain sizes fall into the least square fit line almost precisely. The error bar represents the statistical standard deviation for each datum.

6. <u>The Crystallographic Orientation Relationship</u>. Microstructural analysis of the precipitated V_3Ga and Nb_3Al in the previous sections reveals that there is a common orientation between the A15 crystals. This section presents the results of an investigation to determine the common crystallographic relations which govern the orientation of A15 precipitates in supersaturated BCC solutions. Convergent-beam electron microscopy [17-19] was used in this study in order to deal with sub-micron sized A15 precipitates. A JEOL-100C microscope operated at 100 kV and capable of converging an electron beam to a probe 1000A in diameter was the primary facility employed. The Philips 400 scanning transmission electron microscope which has the ability to further converge the electron beam down to 100A was employed for confirmation.

The analysis of the V-15.6 at.% Ga samples is illustrated in Fig. VI-36(a,b). The TEM micrograph presented in Fig. 6.36(a) shows the precipitates formed in a deformed V-15.6 at.% Ga sample after aging at 700°C for 4.5 days. The V_3Ga precipitates are lenticular in shape and have an average size of 1.1 um length by 0.4 um width. A typical convergent beam electron diffraction pattern from this region is shown in Fig. VI-36(b). The disc-shape of the diffraction spots is due to the angular convergence of the incident electron beam [17-19]. It is clear that the $(\underline{2}11)$ plane of the precipitated A15 phase of the [111] zone axis is parallel to the $(0\underline{11})$ planes of the BCC matrix. Since the corresponding diffraction spots are almost parallel to each other and lie on a direction parallel to the electron beam. Therefore, the set of parallel planes between BCC and A15 phase must also satisfy the relation: $(\underline{2}11)_{BCC}//(0\underline{11})_{A15}$. However, this type of analysis reveals a necessary condition for the complete orientation relationship, but it does not give a sufficient condition. It has been known [20,21] that parallel planes and directions are both needed to determine the crystallographic orientation relationship between two crystal structures. The above mentioned condition can be satisifed by a large number of different relationships. Therefore, it is necessary to find an experimental condition such that the parallel planes and directions can be determined simultaneously.

Such an analysis of the V_3Ga precipitate is illustrated in Fig. VI-37(a-c). The TEM micrograph presented in Fig. VI-37 (a) shows the precipitates present in a deformed V-18 at.% Ga after aging at 700°C for 12 hours. The V_3Ga precipitates are again lenticular in shape and have an average size of 3000A length by 1300A width. The corresponding

convergent diffraction pattern from this sample is shown in Fig. VI-37(b). The diffraction pattern is indexed in Fig. VI-37(c). The zone axis of the BCC matrix and the A15 precipitates are [111] and [001], respectively. The rows of parallel matrix and precipitate spots in the diffraction pattern indicate parallel planes (within $\pm 5^{o}$) since the corresponding reflecting planes are almost parallel to the electron beam (Bragg angle $< 1^{o}$) [21]. It follows that the (100) plane of the A15 precipitate is essentially parallel to the $(1\underline{1}0)$ plane of the BCC matrix. The complete orientation relation is hence given by the appealingly simple correspondence:

$$[001]_{A15}//[111]_{BCC}, \text{ and } (100)_{A15}//(1\underline{1}0)_{BCC} \qquad (1)$$

The analysis of the Nb-Al system is illustrated in Fig. VI-38(a,b). The TEM micrograph presented in Fig. 6.38(a) shows that the Nb_3Al precipitates formed from Nb-18 at.% Al on aging at 750°C for 3 hours. It can be noted that the morphology of the Nb_3Al precipitates are quite different from that of V_3Ga (see previous sections). Nevertheless, selected-area convergent-beam diffraction patterns (Fig. VI-38(b)) reveal an A15-BCC lattice correspondence identical to that found in the V_3Ga case and given by equation (1).

7. <u>Microstructures of the Fully-Annealed V-18 at.% Ga</u>. To understand the effect of deformation on the microstructure and transition temperature, V-18 at.% Ga solution were annealed at 1400°C for 10 minutes and quenched before aging treatment to fully anneal the deformation history

Inductive measurements showed that the as-annealed sample has a T_c close to 9°K which corresponds to the pure Nb. After aged at 700°C for 2 days, T_c increases to 12K, and further increases to 13.5K and 14.2K

for 4 and 8 days aging. The T_c measurement results are quite different from the deformed specimens (Fig. VI-1), showing that the precipitation kinetics were significantly influenced by the thermal-mechanical history.

The precipitated V_3Ga grain morphology of samples aged for two days is illustrated in Fig. VI-39. The corresponding crystallographic orientation is shown in the figure. It can be seen that the V_3Ga precipitates along a definite crystallographic direction: $[100]_{A15}$ and $[1\underline{1}0]_{BCC}$. The V_3Ga phase forms clusters of precipitates that concentrated at the grain boundaries of BCC matrix. The prior grain boundaries are not visible due to precipitation, they are still recognizable from the changes of the precipitation directions. Fig. VI-40(a-c) shows a set of bright-field, dark-field micrographs and the corresponding selected-area-diffraction pattern of the same heat treatment as that of Fig. VI-39. The diffraction pattern (c) reveals that the A15 phase is near the [001] zone axis and the BCC phase is near [111]. The dark-field micrograph (b) was taken from the fundamental reflection of BCC phase, as indicated in (c). It is clear that the BCC phase formed a stable film against coalescence of A15 grains. This phenomenon is the same as that in the deformed samples.

The microstructure of a precipitated V_3Ga phase cluster is shown in Fig. VI-41 for a sample with 4 days aging. The same features as that of the 2 days sample is observed. It is interesting to note that the precipitates grew into one another and stopped, but usually did not coalesce, even though they have a closely correlated orientation relationship. The lenticular shape of the V_3Ga precipitates is most distinct in Fig. VI-42(a-c). The selected-area-diffraction pattern (c)

shows that the zone axis of the thin foil was in the direction of [111] for A15 phase, and that the ($\underline{2}$11) of A15 phase is parallel to the (110) of BCC phase. The dark-field micrograph (b) was taken from a fundamental reflection of the A15 phase.

Figure VI-43 shows a lattice image of the precipitated V_3Ga formed by aging the specimen at 700°C for 4 days. The diffraction condition of this particular image is taken from the two $\pm$ (100) reflection at $S_g = \pm$ 0.5 condition. The image shown in this figure covered roughly 0.01 um^2 area of a precipitate. From optical interference technique, it can be concluded that the lattice planes have a uniform spacing, 4.82A. This is an implication that the composition within a grain is quite homogeneous [2].

D. DISCUSSION

The discussion of this work is divisible into two parts: the formation mechanisms and microstructures, and the correlation of superconducting properties with microstructures. The former discusses nucleation sites and microstructures of A15 precipitates, the orientation relationship, the stability of BCC films, effects of deformation and some implications of chemical composition. The latter will discuss the T_c, H_{c2} and J_c characteristics and correlate them to the physical and chemical state of A15 precipitates.

1. Formation Mechanisms and Microstructures.

a. Nucleation of A15 precipitates: The nucleation sites of the A15 precipitates are the prior-deformation BCC grain boundaries and the dislocation cell walls or sub-grain boundaries. The precipitates are

most easily nucleated on the prior-deformation BCC grain boundaries, especially at the sites of grains intersections. For example, V-15.6 at.% Ga samples aged at 700°C for 1 day presented V_3Ga precipitates mostly on the grain intersections (Fig. VI-13). Fig. VI-44 shows optical micrographs of the same sample. From the difference in etching behavior, the positions of the likely V_3Ga precipitates were revealed. It is clear that the precipitates are formed on the prior-deformation grain boundaries. In this short heat treatment, the dislocation cell walls are free of precipitates.

The dislocation cell walls became preferred nucleation sites for longer aging treatments for both the V-Ga and Nb-Al samples. However, the nucleation process is different for V-Ga and Nb-Al. In Nb-Al samples, the Nb_3Al precipitates were distributed more homogeneously on most of the sub-grain boundaries, while in V-Ga case, the precipitates tended to form clusters from some dislocation cell walls (i.e., some regions were precipitation free while the others had a high density of precipitates). This may arise from the gettering effectiveness of the sub-grain boundaries are more effective nucleation sites for the Nb_3Al precipitates than the dislocation cell walls are for V_3Ga. The dislocation cores can decrease the activation energy of nucleation and act as fast-diffusing paths for solute atoms. Therefore, the heterogeneous nucleation of V_3Ga and Nb_3Al always occurs with a high density of dislocations.

It has been mentioned that the polygonization of dislocations has to be formed first if finely dispersed A15 precipitates are desired. Even with a high desity dislocation wall structure, the nucleation of A15 precipitates still requires a random thermal activation process.

Therefore, it is not surprising that the grain sizes of the A15 precipitates reported here are several times larger than that of other processing methods. All the other processing methods described in Chapter IV rely on the reaction between two different phases, e.g., the Nb and Cu-Sn interface of the bronze process, and the Nb-Al interface of the powder wires. The nucleation of an intermetallic compound between two terminal phases at the interface will have a much higher nucleation rate than a random thermal activation process. Also, at the same temperature, the diffusion will be faster down a pre-existing composition gradient than a random composition fluctuation. A higher nucleation rate implies finer grain size, therefore, the grain size of the direct-precipitated A15 phase will be larger than the other processes.

b. The nature of dislocations in the A15 phase. The precipitated A15 grains are generally defect-free, but some of them have in-grown dislocations. Contrast analysis reveals that they are edge dislocations with Burgers vector of the type 1/a ⟨100⟩ and lie on ⟨001⟩ directions. This result is intrinsically plausible because the A15 crystal structure is an ordered phase, and the only way to preserve the three-orthogonal linear chains is to have a Burgers vector of 1/a ⟨100⟩. The other types of Burgers vector will cause the linear chains to connect with B sites (Fig. IV-1) and create anti-phase boundaries. This will be an energetically unfavorable situation since the overlapping of the d-shell electrons of A-atoms is responsible for the stability of the A15 phase [22,23].

c. The morphology and grain size of V_3Ga and Nb_3Al: After nucleation of the A15 precipitates, grain growth followed to bring the system toward equilibrium by diffusion of B-atoms toward nuclei. The growth of

A15 precipitates also obeys a minimum energy requirement that determines its shape and size. The results of microstructural analyses of the V_3Ga and Nb_3Al precipitates were shown in the previous sections. It is found that there are significant differences between the patterns of precipitation in the two materials. V_3Ga precipitates as a set of discrete particles which grow in a lenticular shape away from the boundaries into the interior of the grains following a low index direction, e.g., $[100]_{A15}$ and $[1\underline{1}0]_{BCC}$. Alternatively, Nb_3Al precipitates as small, nearly equiaxed particles at an early stage of the reaction and grows along the sub-grain boundaries.

It is well known that the shape and habit plane of precipitates are determined by the minimization of the sum of elastic strain and interfacial energy [24-27]. The lenticular shape and directional growth of the V_3Ga precipitates indicates that the transformation is strain energy dominated. On the other hand, the Nb_3Al precipitates as equiaxed grains showing that it is surface energy dominated.

The growth of the precipitated A15 grains is determined by the diffusion kinetics. The results of grain size measurement were shown in Figs. VI-33, 34 and 35. It can be seen that the growth rate follows a power relation: $D = kt^n$ [28], where coefficients k and n are functions of aging temperature and composition, but independent of grain size. It can be observed from the two V-Ga samples that the higher the Ga concentration, the smaller the grain size. Also, the exponent, n, decreases with increasing Ga concentration. This may be due to the higher nucleation rate of the higher Ga-contenting specimen, such that the growth rate decreases due to the depletion of solute atoms at the vicinity of each grain.

The exponent, n, of Nb-18 at.% Al is very close to the diffusion controlled layer growth exponent 0.5, and it is higher than the V-Ga samples. This effect can be attributed to the higher deformation and higher nucleation rate. High nucleation rate means the transformation rate is growth controlled. Therefore, it is not surprising that the average grain size is small but the growth exponent is high.

d. The orientation relationship: The results of convergent beam electron diffraction analysis of the crystallographic orientation relationship between the A15 precipitates and BCC matrix were described in Section VI.C.6. The A15-BCC lattice correspondence found in this study (eq. (1)) is illustrated in Fig. VI-45. It is an intuitively plausible correspondence since it insures that the most closely packed planes and directions of the A15 and BCC structures are parallel to one another, and in this sense resembles the familiar Kurdjumov-Sachs [20] relation between the FCC and BCC structures. This relation does, however, differ from that previously suggested by Togano et al. [29] from an analysis of surface diffused V_3Ga on a V tape: $[110]_{A15}//[120]_{BCC}$, $(001)_{A15}//(001)_{BCC}$. The Togano correspondence was never found in this work. Using X-ray and reflection electron diffraction (RED) techniques, Diadiuk et al. [30] studied the preferred orientations of Nb_3Sn diffusion layers grown by Sn-vapour reaction with single-crystal Nb substrates. The preferred parallel planes were given: $(100)_{BCC}//(110)_{A15}$, $(110)_{BCC}//(100)_{A15}$, $(211)_{BCC}//(110)_{A15}$, and $(111)_{BCC}//(111)_{A15}$ for the four preselected BCC orientations. The respective parallel directions, however, could not be determined by their techniques. Since the parallel planes and directions are both necessary to describe crystallographic orientation relationship between two crystal structures, this type

of analyses is incomplete. It should also be noted that for a Sn diffusion reaction on a bulk Nb substrate, the growth direction of the A15 Nb_3Sn layers is restricted by the orientation of the BCC Nb substrate, rather than being permitted to take a path to minimize the free energy. The same restriction will be found in the multifilamentary wires. The preferred parallel planes reported by Diadiuk et al. [30] were also consistent with that found in this work.

The habit planes of the V_3Ga precipitates found in this work followed the relation: $(100)_{A15}//(1\underline{1}0)_{BCC}$, which is consistent with the parallel planes of A15 and BCC structures. Since the shape of the V_3Ga phase is strain energy dominated, it is not surprising that the habit plane coincides with the plane of parallel orientation, since both the habit plane and orientation relationship obeys the same law of minimizing energy. For the Nb_3Al phase, surface energy dominates the shape of the precipitates but the same orientation relationship is still obeyed. In this sense, the orientation relationship found in this study might be a general one, which governs the transformation of A15 from BCC structure.

e. <u>Stability of BCC films</u>: Microstructural observations showed that the precipitated A15 crystals within one prior-deformation BCC grain usually have a common crystallographic orientation. However, they do not coalesce into large crystals during growth. A BCC matrix film, typically with a thickness of only a few hundred angstroms, can be frequently found in between two adjacent A15 precipitates. This type of matrix film has a remarkably high stability against the high interfacial energy they created. In the V-15.6 at.% Ga samples, these BCC matrix films were stable and showed some form of partial coalescence only after

aging at 700°C for 11.5 days (Figs. VI-22 and 23). The spheroidization of the BCC films is very distinctive in the V-18 at.% Ga, 700°C for 48 hours aged sample (Fig. VI-27). But for shorter aging times (6 hours to 24 hours) these BCC films showed no sign of instability. This kind of morphology is not so clear for the Nb-Al samples, mainly due to the shape of the Nb_3Al precipitates. However, by careful examination of a large number of micrographs, it is found that the similar phenomenon exists in the Nb-Al system. For example, the high stablity of the BCC films for the samples aged at 750°C for 12 hours can be seen in Fig. VI-32.

This phenomenon is quite remarkable, since the high interfacial energy and the identical orientation of the adjacent A15 precipitates should tend to spheroidize the BCC films in order to reduce the surface energy. The same situation can be found, for example, in the spheroidization of carbides in carbon steel. Also, the films are quite thin compared to that of the precipitates, consequently, this small amount of BCC lattice contains a large surface area. The high stability of the BCC films was therefore not anticipated.

This phenomenon can be explained by consideration of the compositions of the BCC phase. The films of BCC phase between A15 precipitates are lean in solute atoms (Ga or Al), due to the short diffusion distance to the adjacent A15 grains. Therefore, the BCC phase stability is greatly enhanced which must be sufficiently high to oppose the instability set forth by surface tension. The metastable BCC films can be pushed into spheroidized particles only at a slow kinetics rate, at the expense of increasing A15 grain size.

The existence of resistive films between superconducting grains induces a voltage drop and local heating. The reduce the stability of the conductor against flux-jump and thermal instability. Also, it has been established that the A15 precipitates in a specimen are grouped into several sets of crystallographic orientations determined by the minimum energy path of the transformation. As a result, the effective grain size will be much larger than the average of individual grains. In this sense, the surface pinning between BCC films and A15 precipitates might be responsible for a large fraction of the J_c obtained. The conductivity is provided by the proximity effect [31] and current transfer [32] in the normal metal. As a consequence, the intrinsic stability of the conductor is very limited.

f. Effect of deformation on microstructure. To understand the effect of deformation on the precipitation kinetics and microstructure, V-18 at.% Ga solutions were fully annealed before aging treatment and the experimental results are compared with samples of the same composition with heavy deformation. The precipitation process is very slow in the annealed samples. Microstructural observation found no A15 precipitates until aged at 700°C for two days, while the corresponding deformed samples have a significant amount of precipitates after three hours aging. This observation is supported by inductive T_c measurement where the annealed sample aged at 700 °C between three and 24 hours has only a T_c corresponding to the pure Nb. Therefore, it can be concluded that the deformation significantly enhances the precipitation.

The morphology and orientation relationship between the A15 precipitates and BCC matrix were identical irrespective of the prior-deformation. The A15 precipitate forms clusters at the grain boundaries or

grain intersections for the annealed specimens aged at 700°C from two to eight days. Therefore, it can be concluded that the A15 precipitates nucleate heterogeneously on dislocations. Also, the precipitation of a few nuclei may create a solute diffusion toward that region by dislocation cores, which will further enhance the nucleation rate in the region. This effect may be responsible for the clustering of precipitates.

g. Chemical compositions. The compositions of the A15 phase were studied by a scanning transmission electron microscope equipped with energy dispersive x-ray spectroscope (STEM/EDXS) on the thin foil of TEM specimens. Although the results of STEM/EDXS studies were not conclusive, several points are worth discussing. The A15 precipitates usually have a range of compositions between ~18 to 24 at.% Ga within each V-Ga specimen. Similar situations were found for the Nb-Al specimens. It should be noted from the phase diagrams (1-3,5) that the equilibrium composition of precipitates should be bout 18-20 at.% of B atom for both Nb_3Al and V_3Ga. The existence of ~24 at.% composition in the precipitates indicates that the process is not an equilibrium one. Hong, Dietderich and Morris [3] suggested that the precipitation of small particles is not governed by Gibbs' free energy. Instead another thermodynamic function, based on the assumption of incompressibility of the parent and precipitated particle, is relevant. By this argument, a higher composition than that of the equilibrium phase boundary can be obtained to explain the higher T_c data than that of the equilibrium condition. Another possibility is that the boundary conditions of the chemical potential changed due to the existence of dislocations so that higher concentration of B atom in the precipitates is more stable when

the precipitates were small. For longer aging treatments, the boundary condition slowly changes back to the equilibrium values, then the precipitates will have a composition close to that of the equilibrium phase diagram.

This plausible explanation can account for the range of composition of precipitates in one sample: the local configuration of dislocations and the duration of precipitate formation were different from region to region. Therefore, the composition of each precipitate will be different. It has also been found that the composition within each A15 grain seems to be homogeneous from the STEM/EDXS probes across each grain and from lattice images (e.g. Fig. VI-43). These results imply that the redistribution of B atoms inside a single grain is fast compared to the growth of the precipitates.

2. Correlations of Superconducting Properties and the Physical and Chemical State of Precipitates.

a. T_c and H_{c2}. The T_c and H_{c2} of a superconducting material are strong functions of the chemical composition, long range order parameter, state of strain, and less sensitive to microstructure, as discussed in Chapter II. Since the long range order and state of strain should be similar for the A15 precipitates formed at the same temperature [35], therefore, T_c and H_{c2} have been used as a rough measure of composition.

Examples of the critical temperature and upper critical field of precipitated V-Ga are given in Figures VI-1 and VI-3. Those of precipitated Nb-Al are shown in Figures VI-2 and VI-4. The critical temperatures were measured by an inductive method with a calibrated germanium resistance thermometer. The upper critical fields were estimated by extrapolating the critical current characterisitic, suggested by Kramer

[36]. Because the precipitates have a range of compositions, the former technique will tend to measure the properties of the most nearly stoichiometric (highest T_c) particles, while the latter will reflect a composition closer to the mean. Hence, it is not surprising that the characteristic results as a function of aging time have slightly different shapes. Experimental results do suggest, however, that the T_c measurement gives a reasonable indication of composition when the particles are well-developed. Also, the transition widths of the inductive signals always show an extraordinarily broad transition, compared to all the other processing methods, revealing that the compositions of V_3Ga and Nb_3Al precipitates have a range of compositions.

In V-Ga aged at 700°C both the critical temperature and critical field increases with the Ga content of the starting alloys. They tend to reach a maximum, then decrease after long aging times, a behavior pattern which suggests an eventual decrease in the Ga content toward the equilibrium phase boundary of the A15 phase. The initial increase of T_c and H_{c2} probably do not suggest a simple increase in Ga content in the V_3Ga precipitates but a complicated effect arising from the interplay of particle sizes, their composition distribution, and the proximity effect between particles. For example, when the particles diameter of the particles are less than approximately twice the magnetic penetration, the magnetic fluxes can penetrate the particles and there will be no inductive signal shown. Also, the proximity effect, which is responsible for the tunneling of copper pairs through normal metal, will depend on the thickness of normal metal and its composition. The shape of the T_c measurement results can then be qualitatively understood. The maximum T_c of V-18Ga, 15K, corresponds to a nearly stoichiometric A15

phase. The maximum critical field also suggests a Ga content near 25 at.%.

The critical temperature and critical field increase with the starting content of Al, and also slightly increase with aging for times up to 500 hours. The data suggest that the kinetics toward the equilibrium phase boundary of the compositions of Nb_3Al precipitates is much slower than that of V_3Ga. However, the compositions of the Nb_3Al precipitates apparently remains lean in Al since the highest values of T_c and H_{c2} are significantly below their values for stoichiometric Nb_3Al [37,38].

b. Critical current characteristics. The variation of overall critical current with applied magnetic field was measured for a number of V-Ga and Nb-Al specimens. Examples of the data are given in Figs. IV-5, 6 and 7. Figures IV-5 and 6 show the variation of critical current characteristics with heat treatment time for samples of V-15.6 at.% Ga and V-18.0 at.% Ga, respectively. Those of Nb-17.8 at.% Ga were shown in Fig. IV-7.

From the perspective of establishing a microstructure conducive to good current-carrying properties, the Nb_3Al precipitation pattern revealed in this study is clearly preferable to that of V_3Ga. The Nb_3Al reaction establishes precipitates with fine equi-axed grains which are uniformly nucleated on the network of dislocation cell walls at a reasonable volume fraction. The V_3Ga pattern yields particles which tend to be isolated from one another by buffer films of the matrix solution and which grow to relatively large size and nucleate in a severe heterogeneous manner on certain dislocation networks. On the other hand, the inherent superconducting properties are better in the V_3Ga case. The

A15 phase in V-Ga achieves a critical temperature and upper critical field reasonably close to the best obtainable in V_3Ga, while the Nb-Al A15 phase has a critical temperature and field well below the best found in Nb_3Al. The two materials hence have different behaviors including one having a basically good A15 phase in an undesirable morphology and one having a less attractive A15 in a much superior morphology. These features are reflected in their relative critical current characteristics.

In the V-15.6 at.% Ga case represented in Fig. IV-5, the critical current improves over the whole range of fields studied as the heat treatment time is increased to 48 hours but deteriorates thereafter. The improvement apparently reflects both the better intrinsic characteristics of the A15 precipitates, which particularly determine high-field properties, and the increasing volume fraction of the A15 phase. The subsequent deterioration presumably reflects the lowering of intrinsic properties coupled with the increasing grain size of the A15. The critical current is relatively low at all fields compared with multifilamentary V_3Ga conductors formed by the bronze-process [39]. The critical current characteristics of a V-18 at.% Ga sample represented in Fig. IV-6, show the same response of current-carrying capacity with heat treatment time. Compared to that of V-15.6 at.% Ga, the J_c shows a marginal increase. The improvement might be reflecting the increase in volume fractions of A15 precipitates which is governed by the precipitation kinetics and the level-rule.

In the Nb-Al case represented in Fig. IV-7, the low field properties improve for heat treatment times up to 12 hours and deteriorate thereafter, while the properties of the highest fields continue to

improve. The latter effect may be due to the improvement of the intrinsic superconducting properties at longer aging times documented in Fig. IV-2. The former probably reflects the competition between increasing volume fraction and continuity, which cause the critical current to increase, and grain growth of the A15 precipitates, which causes the J_c to decline. The very rapid increase in the overall critical current of the 12 hour specimen for decreasing fields below H_{c2} suggests a very good balance between A15 grain size, continuity and volume fraction. The relatively slow increase in J_c of the 1.5 hr specimen presumably reflects the poor continuity of the A15 phase at this stage of the precipitation process. The highest obtained J_c at all fields is far lower than the Nb_3Al conductors by powder metallurgy [40,41]. This inferior current-carrying capacity can be attributed to the low intrinsic superconducting properties, much larger grain size and poor continuity.

E. SUMMARY

The research of direct-precipitated V_3Ga and Nb_3Al reported in this chapter demonstrates a connection between the processing and the resultant superconducting properties through the microstructural analyses of the A15 phases. The microstructural considerations discussed in this chapter suggest that the overall critical current characteristics of V-Ga and Nb-Al will be improved by either increasing the deformation of the samples prior to aging, which should refine the size of the subgrain dislocation cell on which the precipitates form, or by increasing solute

content of the starting alloy, which should improve the intrinsic properties of the A15 phase.

However, the microstructural analyses also revealed that there are some intrinsic disadvantages of this process for producing a high current-carrying-capacity conductor (besides the problem of quenching a big ingot suggested in Section A). The grain size of the precipitated A15 phase is much larger than that can be obtained by other processes. The reason for this disadvantage is that the nucleation of the A15 phase is much faster at a two-phase boundary reaction than a thermally activated nucleation reaction by the composition fluctuation. Faster nucleation rate yields a finer grain size and a higher J_c. Also, the diffusion of solute atoms down a pre-existing composition gradient is faster than through the composition fluctuation. A faster reaction will permit fully reaction at shorter aging time, resulting in a higher volume fraction. The other microstructural problem of the process is the continuity. The BCC films between A15 precipitates have been found to have high stability due to lowering of the chemical potention by a locally lower solute concentration. The existence of the resistive films between superconducting grains induces a voltage drop and a local heating effect which greatly reduce the intrinsic stability of the conductor.

The micro-chemical state of the A15 precipitates also is unfavorable. Even though near stoichiometric-precipitates exist, due to the configuration and chemical effect of dislocations, the majority of the precipitates are lean in solute atom. This effect is revealed also by the T_c and H_{c2} characteristics. The larger A15 grains have a tendency toward off-stoichiometric composition (equilibrium condition). The

other processing methods have different boundary conditions, thus will have different chemical states, a point will become clearer in the next chapter. Therefore, both the physical and chemical state of the A15 precipitates are not favorable for application of high-field conductors.

On the other hand, this method permits the formation of A15 phase in a non-restricted manner which allows the study of the precipitation process without other influences. For example, the mechanisms of nucleation and growth of precipitates, the nature of dislocations in A15 phase, the morphology and orientation relationship, and the effects of deformation can be studied in great detail. The microstructures can be related to the processing variables through the apparent mechanisms of the reaction forming the A15 phase. These mechanisms are inferred from the results of high resolution studies of the development of the microstructure. The relation between the microstructure and the critical current is consistent with current understanding of the role of grain size and stoichiometry in determining superconducting properties.

REFERENCES

1. J. H. N. van Vucht, H. A. C. M. Bruning, H. C. Donkersloot and A. H. G. de Mesquita, Philips. Res. Rep., 19, 407 (1964).
2. B. N. Das. J. E. Cox, R. W. Huber and R. A. Meussner, Met. Trans. 8A, 541 (1977).
3. M. Hong, D. Dietderich and J. W. Morris, Jr., J. Appl. Phys., 51, 2774 (1980).
4. V. M. Pan, Y. I. Beletskiy, V. S. Flis, S. A. Firstov and G. F. Sarzhan, Fiz. Metal. Metalloved, 40, 706 (1980).
5. V. M. Pan and V. I. Latysheva, Metallofizika, 33, 38 (1971).
6. G. W. Webb, Appl. Phys. Lett., 32, 773 (1978).
7. J. A. Woolam, S. A. Alterovitz, E. Haugland, and G. W. Webb, Appl. Phys. Lett., 36, 706 (1980).
8. V. M. Pan, V. I. Latysheva, Y. N. Khusid, V. N. Minakov and Y. V. Turtsevich, Fiz. Metal. Metalloved., 40, 412 (1975).
9. M. H. Hong, D. R. Dietderich, I. W. Wu, and J. W. Morris, Jr., IEEE Trans. Magn., MAG-17, 278 (1981).
10. M. Hong, Ph.D. Thesis, University of California at Berkeley (1980).
11. S. Mehleuke, Ph.D. Thesis, University of Estudial de Campians, Brazil (1977).
12. E. J. Kramer, J. Appl. Phys., 44, 1360 (1973).
13. L. J. Chen and I.-W. Wu, J. Appl. Phys., 52, 3310 (1981).
14. L. J. Chen, Y. J. Wu and I. W. Wu, Ibid, 3520 (1981).
15. I. W. Wu and L. J. Chen, Ibid, to be published.
16. C. S. Pande, Treatise on Mats. Sci. and Tech., 14, 171 (1979).
17. J. W. Steeds, in Introd. Analytical Electron Microscopy, p. 387, J.

J. Hren, J. I. Goldstein and D. C. Joy, eds., Plenum Press, New York (1979).

18. K. E. Easterling, J. Mat. Sci., 12, 851 (1977).

19. I. W. Wu, M. Hong and J. W. Morris, Jr., Appl. Phys. Lett., 39, 110 (1981).

20. Z. Nishiyama, in Martensitic Transformation, M. E. Fine, M. Meshii and C. M. Wayman, eds., Academic Press, New York (1978).

21. T. Maki and C. M. Wayman, Acta Met., 25, 681 (1977).

22. G. Barak, I. B. Goldberg and M. Weger, J. Phys. Chem. Solids, 36, 847 (1975).

23. A. T. Van Kessel, H. W. Myron and F. M. Mueller, J. Less Common Metals, 62, 49 (1978).

24. A. G. Khachaturyan, Sov. Phys. Solid State, 8, 2163 (1967).

25. A. G. Khachaturyan and V. N. Hairapetyan, Phys. Stat. Sol. (b), 57, 801 (1973).

26. J. W. Morris, Jr., A. G. Khachaturyan and S. H. Wen, presented at the ASM International Conference on Solid State Phase Transformations, Pittsburgh, PA, Aug. 1981, LBL Report No. 9800.

27. D. E. Wedge, M.S. Thesis, University of California, Berkeley (1980).

28. P. Cotterill and P. R. Mould, Recrystallization and Grain Growth in Metal, John Wiley β Sons, New York (1976).

29. K. Togano, K. Tachikawa and R. M. Rose, J. Appl. Phys., 49, 5218 (1978).

30. V. Diadiuk, J. Bostok and M. L. A. MacVicar, IEEE Trans. Magn., MAG-15, 610 (1979).

31. P. G. de Gennes and E. Guyon, Phys. Lett., 3, 168 (1963).

32. L. F. Goodrich, J. W. Ekin and F. R. Fickett, Adv. Cryo. Eng., 28, 571 (1981).

33. J. W. Ekin, J. Appl. Phys., 49, 3406 (1978).

34. E. C. Van Reuth and R. M. Waterstrat, Acta Cryst., 24, 186 (1968).

35. R. Flukiger and J. L. Standenmann, J. Less Common Metals, 50, 253 (1976).

36. E. J. Kramer, J. Appl. Phys., 44, 1360 (1973).

37. R. H. Willens, T. H. Geballe, A. C. Gossard, J. P. Maita, A. Menth, G. W. Hull, Jr., and R. R. Soden, Solid State Commun., 7, 837 (1969).

38. S. Foner, E. J. McNiff, Jr., T. H. Geballe, R. H. Willens and E. Buehler, Physica, 55, 534 (1971).

39. D. U. Gubser, T. L. Francavilla, D. G. Howe and R. A. Muessner, IEEE Trans. Magn., MAG-15, 385 (1979).

40. J. M. Hong, I. W. Wu, J. T. Holthuis, M. Hong and J. W. Morris, Jr., Adv. Cryo. Eng., 28, 483 (1982).

41. S. Foner, presented at the Second Workshop of US-Japan Superconducting Materials for Fusion, San Diego, CA, May 1983.

VII. THE INFLUENCE OF HEAT TREATMENT ON THE STRUCTURE AND PROPERTIES OF BRONZE-PROCESSED MULTIFILAMENTARY NB_3SN SUPERCONDUCTING WIRE

A. INTRODUCTION

The most common method for producing high field Nb_3Sn superconducting wires is the "internal bronze" process [1,2]. In this method niobium rods are inserted into a Cu-Sn bronze billet and drawn into a fine, multifilamentary wire. The wire is then heat treated to form the A15 Nb_3Sn superconducting phase through reaction at the niobium-bronze interface.

The maximum superconducting current, I_c, that can be carried by the reacted wire at a given temperature is determined by the wire diameter and the critical current density, J_c, within it. The critical current density is a function of the transverse magnetic field, H; the characteristic function, $J_c(H)$, depends on the area of the superconducting phase and on its microstructural state. The most important microstructural parameters are three: the composition and crystallographic order of the A15 crystal, the grain size, and the state of strain. The composition and order of the crystal determine its inherent superconducting properties [3-5]. It should be noted that the maximum effect of the crystallographic oder is relatively small compared to that of composition [6]. The grain size controls the density of the most efficient flux line pinning sites [7-11] that prevent the loss of superconductivity at high current. The state of strain modifies the inherent superconducting properties, and is in part an internal strain that reflects the macrostructure of the superconducting composite [12].

The microstructural state of the superconducting wire cannot be controlled directly, it is determined indirectly by the starting geometry and the heat treatment. The relation between heat treatment and microstructure is not well understood, but must be identified and utilized if bronze-processed wires are to be engineered for maximum critical current. The present work was undertaken to characterize the microstructure of a typical wire with a fixed internal geometry, to establish the connection between the microstructure and the heat treatment the wire had received, and to correlate the microstructure and the superconducting properties. This work led into an effort to design heat treatments that would improve the microstructure so as to enhance the critical current. The success of the modified heat treatments has obvious engineering implications, but also gives credence to the qualitative relations between processing, microstructure and properties that emerge from the characterization studies.

Specific aspects of the work reported here have been published previously [13,14]. The present chapter provides a comprehensive presentation of the results and their implications. It should be noted that the research samples were commercial Airco wire with a fixed macrostructure and bronze/niobium ratio. The research concerned the nature and development of microstructure in this wire and its influence on the critical current characteristic in the relaxed condition; the influence of the elastic strain was not specifically considered. Okuda, et al. [15] have recently studied the consequences of varying filament size and the bronze/niobium ratio in similar multifilamentary superconducting wire. Their report includes a discussion of the influence of residual strain on the critical current in the relaxed condition. The maximum

effect of the residual strain is small relative to that associated with significant changes in the microstructure.

B.EXPERIMENTAL PROCEDURE

1. Sample Geometry and Heat Treatment. The wire used in this investigation was manufactured by Airco Superconductors. It was a composite wire, 0.7mm in diameter, that contained an active core approximately 0.4mm in diameter. An etched section of the multifilamentary core is shown in Fig. VII-1. The core held 2869 niobium filaments grouped into sets of 19. The individual filaments were 3 to 5 microns in diameter. They were embedded in a Cu-13 wt.%Sn bronze matrix to give an overall bronze to niobium ratio of 3:1. The core was wrapped with a tantalum foil diffusion barrier approximately 30 microns thick. For thermal and electrical stabilization the wrapped core was encased in a pure copper shell, 0.15mm in thickness, that accounted for roughly two-thirds of the wire cross section.

Samples of the wire were heat treated after encapsulation in sealed quartz tubes that were back-filled with argon. They were reacted at temperatures in the range 650-800°C for various times. The maximum reaction time at each temperature was that necessary to achieve an essentially complete conversion of the niobium filaments to Nb_3Sn.

2. Materials Characterization. The important materials parameters include the overall extent of the reaction at the Nb-bronze interface and the physical and chemical state of the superconducting layer formed.

The extent of reaction was determined by optical and scanning electron microscopic examination of etched cross sections of the heat

treated wires. The A15 layer is easily distinguished from both the bronze matrix and the unreacted Nb core by its brittle appearance in broken wire sections and by its distinct etching behavior. A sample scanning electron micrograph of a polished and etched section is shown in Fig. VII-2. The data obtained from such micrographs varies by ~10% due to the inhomogeneity of the reacted filaments.

The physical state of the reacted layer was studied by scanning electron microscopy (SEM) on broken and etched sections and by high resolution transmission electron microscopy (TEM) on thin sections. Samples for transmission electron microscopy began as longitudinal sections cut from the wire to reveal the multifilamentary material. The samples were ground to approximately 40 microns thickness, and then milled in an ion beam until perforated. They were examined in a Siemens 102 or JEOL-100C electron microscope at 100kV, using a 45° double tilt goniometer stage to achieve the desired diffraction conditions. The principal object of these examinations was to determine the A15 grain size. The grain size could be roughly estimated from scanning electron micrographs of the broken wire surfaces. However, since only some of the grain boundaries appear in the fracture surface, the transmission electron microscopic analysis was essential to an accurate determination of the grain size. The values of the average grain size reported here were determined by the line intercept method on transmission electron micrographs. At least 100 grains were sampled for each datum point. The standard deviation in the grain size measurements is less than 80A.

The chemical state of the reacted layer was studied with scanning transmission electron microscopy (STEM). The specimens employed were TEM foils prepared as described above. They were examined with a 100kV,

100A diameter electron probe in a Philips 400 electron microscope equipped with an energy dispersive x-ray spectrometer. The x-ray spectrum was analyzed quantitatively using a KEVEX 7000 microcomputer. The tin concentration within the reacted layer was determined from the x-ray spectra using a standardless approximation method [16] that has a 10-20% maximum error in the absolute value. A beryllium low-background stage with a 30° tilting axis was used to minimize spurious excitations. Residual niobium and 'in hole' configurations were examined to monitor the background shape and the peaks caused by inelastic scattering and spurious excitation. Nonuniformity in the specimen thickness is a further possible source of error; a specific investigation suggests that this error is less than 1 atom percent. The experimental arrangement and integrated count number were kept as nearly constant as possible to minimize systematic errors.

3. Superconducting Property Measurements. The superconducting properties that were determined included the overall critical current characteristic, $I_c(H)$ at 4.2K, and the transition temperature from the normal to the superconducting state, T_c. The transition temperature was measured inductively using a ring shaped sample of the wire with the copper stabilizer removed to minimize the shielding. The onset and finish temperatures of the superconducting transition were taken to be the temperatures that gave 10% and 90% of the total inductive signal, respectively. The critical current characteristic was measured by using a four-point probe technique on samples placed in transverse magnetic fields that ranged in intensity from 8 to 19.5 tesla. To minimize the displacement of short samples by Lorentz force, supporting block made of commercial grade G-10 fibre re-enforced glass which has a similiar

thermo-expansion coefficient with the samples were mounted on the sample probes [17-19]. The direction of Lorentz force was calibrated such that the specimens were immobile during test. The reported value of the critical current is that which produced an 0.5 microvolt potential between voltage taps 5mm apart. The estimated error in the critical current measurement is $\pm 10\%$. All of the critical current measurements were done at the Francis Bitter National Magnet Laboratory. The sensitivity of this measurement ranged from 5×10^{-13} to 1×10^{-12} ohm-cm.

The overall critical current density, $J_c(H)$, within the multifilamentary core of the wire was calculated from the critical current by dividing I_c by the cross-sectional area of the core, $0.14 mm^2$. Volume pinning force, $J_c XB$, was plotted against the reduced applied magnetic field, $h = H/H_{c2}$, where the upper critical field H_{c2} was determined by extrapolating $J_c^{1/2} H^{1/4}$ versus H to zero current [20].

C.RESULTS AND DISCUSSION

Two sets of experiments were done. They differed in the type of heat treatment given the wires to form the A15 phase. Samples in the first set of wires were reacted at constant temperature in the range 650°C to 800°C. The superconducting properties of these wires were measured as a function of the reaction time and temperature and correlated with the microstructural state of the A15 layer. The results suggested that the microstructure of the A15 layer was far from optimal, even in the wires that had the highest critical current. The results were then used to guide the design of new, double-aging heat treatments to improve the microstructure and enhance the critical current. A

second set of wires was prepared and tested to evaluate the new heat treatments.

1. Conventional Heat Treatments.

a. Superconducting Properties.

i. The critical current characteristic. Samples of multifilamentary wire were reacted at one of five temperatures, 650, 700, 730, 750 or 800°C, for various times up to those necessary to achieve an essentially complete conversion of the Nb filaments to Nb_3Sn. The critical current of the wires was then measured at 4.2K in magnetic fields of 8-16 Tesla. Examples of the results are given in Table I and in Figures VII-3 and 4. The measured properties are in reasonable agreement with those found by Sanger, et al. [16] for similar wires.

The dependence of the critical current on the heat treatment time and temperature varied with the magnetic field. Figure VII-3, for example, is the $J_c(H)$ characteristics of samples aged at 650°. The J_c at higher fields increases with increasing aging time, but has a marginal increase at lower fields. Figure VII-4 shows the change in $J_c(H)$ with the time of heat treatment at 700°C. The best low-field properties (8-12T) are achieved with the shorter aging times (2-6 days). Increasing the aging time to 8 days decreases the critical current at the lower fields even though it increases the areal fraction of A15 within the wire core (Table II). At higher field (16T), on the other hand, J_c increases monotonically with the aging time.

The critical current characteristics of wires that had been reacted nearly to completion are plotted in Figure VII-5. The critical current is a strong function of reaction temperature only at the lowest (8-10T) and highest (15-16T) fields. Good low-field properties are associated

with low reaction temperatures (650°C) and short reaction times (730°C/2 days). Good high-field properties seem to require a reaction temperature above 700°C and a relatively long reaction time (Fig. VII-4).

ii. The upper critical field. The upper critical field H_{c2} was determined by Kramer's extrapolation [20] at 4.2K and up to 19.5 tesla applied field. Examples of H_{c2} data of several isothermal-aged specimens were listed in Table I. The data fell within a small range (21.3 to 21.9 tesla) for almost all the heat treatment conditions even though their J_c characteristic varies significantly. The H_{c2} for sample heat treated at 800°C for 2 days has a somewhat high value, 23T, which may be reflecting a difference in the chemical state of the Nb_3Sn layer.

iii. The superconducting transition temperature. The superconducting transition temperature was measured for all heat treatment conditions. The results, which include an estimate of the width of the transition, are given in Table I. The variation of T_c with aging time is plotted for three representative heat treatment temperatures in Figure 5, which also shows the average T_c for the as-received wire. The data show that the critical temperature increases with aging time to an asymptote near 18K. The apparent width of the transition decreases with aging time.

b. The Microstructure of the Reacted Wire.

i. The fraction of A15 phase. The micrographs presented in Figures VII-1 and 2 show that the filaments within the active core of the superconducting wire are somewhat irregular. The filaments differ slightly in shape, and a given filament has small variations in its cross section from point to point along its length. The variation in shape and diameter has the consequence that the reaction that forms the

A15 layer is not strictly uniform. Figyre VII-7 shows another scanning electron micrograph of the Cu stablizer, Ta diffusion barrier, and the active core. Noticed that the Ta diffusion barrier and the Cu stablizer constrained the volume expansion of the active core during the diffusion reaction. The volume expansion arises not only by thermal expansion but also from the vacancy flux into the matrix and Kirkendall force of the bronze-A15 interfaces. Without this restrictive layer, the bronze matrix would be able to expand plastically (relatively low yield strength during aging) and not exert as much stress on the Nb_3Sn layer.

Two parameters were used to measure the overall extent of the reaction: the mean thickness of the A15 layer on a filament, and the areal fraction of the A15 phase relative to the cross-sectional area of the unreacted filament. Both were determined from measurements on scanning electron micrographs of polished metallographic sections of the active core. The average thickness is plotted as a function of the reaction temperature and time in Figure VII-8. The areal fractions are given in Table II. The data are in qualitative agreement with those reported previously [8,15,21,22].

As expected, the reaction rate increased dramatically with the aging temperature. An essentially complete reaction was defined as the conversion of more than 90% of the initial niobium to the A15 phase, and was achieved after 16 days at 650°C, 8 days at 700°C and 730°C, 2 days at 750°C, and 1 to 2 days at 800°C (Table II).

ii. <u>The substructure of the A15 layer. The three-shell substructure</u>. The microstructure of the A15 layer is clearly revealed only in transmission electron microscopic images. The analysis of a number of such images shows that the layer typically has the composite structure

that is drawn schematically in Fig. VII-9. The layer consists of three morphologically distinct shells. The innermost shell is made up of columnar grains that radiate out from the residual niobium core. A sample micrograph of this shell is given in Fig. VII-10. The grains are roughly equiaxed in cross section and have a long axis approximately five times their diameter. Figure VII-11 shows a selected area diffraction pattern(a), and the correspondent micrograph of the boundary region between A15 and the residual Nb. The identical crystallographic orientation relationship of K-S type as that found in the direct-precipitated V-Ga and Nb-Al (Chapt.VI) were observed.The intermediate shell is made up of fine, equiaxed grains whose mean diameter (d) is approximately equal to the short, transverse diameter of the columnar grains in the inner shell. The outer shell, near the bronze matrix, is made up of large, irregular grains with diameters in the range 5-10d. Two sample transmission electron micrographs are presented in Figs. VII-12 and 13, showing the fine-grained intermediate shell, the coarse outer shell, and the transition between them.

The general features of the microstructure are also apparent in scanning electron micrographs of broken filaments, such as those shown in Figure VII-14, but are not so clearly revealed. In particular, the fine-grained intermediate shell is rarely seen. Its absence is due to the fact that the SEM fractograph shows the fracture surface rather than the grain surface itself. Those grain boundaries that provide the easiest intergranular fracture path dominate the fracture surface. A detailed examination of the grain boundaries in the fine-grained layer (Fig. VII-15) shows that these are most frequently low-angle grain boundaries that would not be expected to appear in intergranular

fracture surfaces, and would not even be obvious in the transgranular segments of the fracture surface.

The overall morphology of the A15 layer is the same for all reaction times and temperatures studied. However, the microstructure of the layer is sensitive to the reaction conditions. The reaction temperature and time affect both the areal fractions of the three shells and the grain sizes within them.

The areal fractions of shells within the layer. The thickness of each shell was measured as a function of reaction time and temperature from transmission electron micrographs. The areal cross sections were then estimated from the thickness of the shell and its inner or outer radius. The results are tabulated as a function of the heat treatment time and temperature in Table II. The area fractions given in this table are relative to the initial cross-sectional area of the Nb filament.

The data presented in Table II reveal systematic changes with the reaction time and temperature. The fraction of columnar grains tends to decrease as the reaction temperature is raised, while the areal fraction of the coarse-grained shell increases with either the temperature or the reaction time. These two trends have the consequence that the highest fraction of fine-grained material is achieved by aging at intermediate temperature (700-730°C) for times that are sufficient to bring the reaction to about 90% completion. The maximum areal fraction of the fine-grained shell is plotted as a function of the reaction temperature in Fig. VII-16.

The grain size within the fine-grained shell. The mean grain size within the fine-grained shell increases monotonically with the reaction

time and temperature as shown in Table II. The mean grain size in the fine-grained shell of the almost fully-reacted wire increases exponentially with the reaction temperature, as shown in Figure VII-17.

The grain size data previously reported by Scanlan et al. [7] and by Shaw [8] are also plotted in Fig. 12. The data agree on the functional dependence of the grain size on the reaction temperature, but disagree on the magnitude of the grain size. Both Scanlan, et al. [7] and Livingston [9] used samples with much larger filament sizes than those employed here and found larger grains after a given heat treatment. Okuda, et al. [15] lso report an increase in the grain size with the filament diameter. The filaments in the samples studied by Shaw [8] were comparable to ours, as were those in the wires examined by West and Rawlings [24 and by Schelb [25], but were in an uncertain state of reaction at the time the measurements were made. These authors report data that are roughly comparable to ours, but scatter significantly at the lower reaction temperatures.

<u>The mechanism of reaction</u>. The essential features of the reactions that establish the three-shell structure of the A15 layer seem clear from the micrographs, although further work will be required to test them in detail. The key observations include the columnar grain structure at the Nb interface, the presence of arrays of dislocations within these grains, particularly near their outer boundaries (Figs.VII-12 and 13), the prevalence of low-angle grain boundaries in the fine-grained layer (Fig. VII-10) and the frequency of dislocation arrays and pileups near the outer periphery of the columnar shell (Figs. VII-18 to 20).

Both the morphology of the reacted layer and the absence of Kirkendall voids within the Nb core suggest that the reaction occurs by the

diffusion of Sn to the Nb/Nb_3Sn interface. The reaction at the interface causes the growth of columnar grains that penetrate into the niobium. As the grains grow, they develop internal strains due to the volume and crystallographic changes associated with the transformation. The strains impel the formation and migration of dislocations that presumably originate from the columnar grain boundaries. The dislocation density builds up near the outer radius of the columnar region. The dislocations polygonize and effectively recrystallize the columnar grains into the fine-grained layer, in a reaction common to many crystalline materials. The fine-grained morphology is initially rather stable, but the continued reorganization of the grain boundary structure increases the mobility of the grain boundaries. The fine grains then coarsen to establish the coarse, outer shell.

This model is consistent with all of the microstructural observations of the reacted filaments, but does not easily explain the occasional appearance of exceptionally large grains on the periphery of the filament. It is possible that these are the product of A15 grains that nucleated during wire processing and were present in the pre-reacted wire. The measurable critical temperature of the unreacted wire (Fig. VII-5) establishes that some A15 phase formed during processing.

In addition to agreeing with the microstructural observations of the reacted layer, this model is also consistent with the time and temperature dependence of the microstructure. At low temperature dislocations are relatively immobile. They should be generated in comparatively large numbers to relieve the strain, but their polygonization will be retarded. The columnar shell should hence be relatively thick, and eventually break up into very fine grains. At high temperature the

dislocation mobility is higher, so the initial grain size in the fine-grained shell should be larger. But high temperature also increases the grain coarsening rate, so the coarse-grained shell should be thicker. It is therefore expected that the areal fraction of fine-grained material will pass through a maximum at an intermediate aging temperature while the grain size within the fine-grained shell increases monotonically with temperature. The microstructure should hence change with the reaction time and temperature very much as it is shown to change by the data given in Table II.

iii. The chemical state of the A15 layer. The important chemical properties of the A15 layer are its composition and state of order. Previous work [6,28,29] suggests that the crystalline order of Nb_3Sn is nearly ideal, irrespective of heat treatment. The composition profile of the layer was determined by STEM/EDXS analysis of the concentration of tin relative to that of niobium. While the analysis is subject to quantitative errors that were discussed above, the data that were obtained are mutually consistent and appear to be informative. Examples of the data are shown in Fig. VII-21, which presents the measured Sn concentration profile as a function of reaction time at 700°C, and in Fig. VII-22, which presents the concentration profile as a function of the reaction temperature for wires that have reached an essentially complete reaction. The data show that there is a gradient in the Sn concentration within the layer. The mean concentration gradient through the fine-grained shell is listed in Table II for all samples studied. Both the shape of the composition profile and its variation with time and temperature are of interest.

The shape of the Sn concentration profile. The Sn concentration decreases monotonically through the layer from an apparently Sn-rich composition at the bronze interface to a Sn-poor composition at the Nb interface. The compositions at the Nb interface are qualitatively consistent with the binary Nb-Sn phase diagram, in that they are lean in Sn by an amount that decreases with temperature (Fig. VII-22). The phase relations at the Nb_3Sn-bronze interface are not known, but the measured composition at that interface is Sn-rich and becomes increasingly so as the temperature decreases. The composition profile through the layer is not smooth; it has a nearly flat central portion with steep concentration gradients near the two interfaces.

The shape of the concentration profile is consistent with current views on the mechanism of Sn diffusion. An idealized profile is shown in Fig. VII-23 as an overlay on the microstructure of the reacted layer. It is widely accepted [22,26,27] that the principal Sn diffusion path through the A15 layer is along the Nb_3Sn grain boundaries. The Sn concentrations at the terminal points of the profile are fixed by the local equilibria between Nb and Nb_3Sn at the inner surface of the A15 layer and between Nb_3Sn and bronze at the outer surface. If the composition is different at the two interfaces, as it generally will be, then there must be a concentration gradient through the layer. But the much higher density of grain boundaries in the fine-grained central shell has the consequence that, if grain boundary diffusion dominates, the Sn composition can be homogenized within the intermediate shell at a much faster rate than it can diffuse into or out of it. The expected result is a flattening of the composition profile in the fine-grained layer

with a concomitant steepening of the gradient near the two interfaces, just as is found experimentally.

The change in the Sn profile with time and temperature. The Sn composition profile becomes flatter and more nearly stoichiometric as either the reaction time or the reaction temperature is increased (Figs. VII-21 and 22μ Table II). There are three independent factors that lead to a flatter profile after long reaction times: homogenization within the fine-grained layer by grain boundary diffusion, the increase in the thickness of the fine-grained layer, and the depletion of Sn from the bronze, which decreases the Sn concentration at the outer boundary. Raising the reaction temperature also tends to flatten the profile, since it decreases the overall concentration change across the layer and increases the diffusivity. The temperature is a more potent variable than the time in this regardμ the most constant, and, apparently, most nearly stoichiometric composition is obtained at the highest reaction temperature.

c. The influence of microstructure on superconducting properties Two superconducting properties were measured: the superconducting transition temperature and, more importantly, the critical current characteristic. Both show the influence of the microstructure.

i. The critical current characteristic. The variation in the critical current characteristic, $J_c(H)$, with heat treatment has a reasonably straightforward and consistent explanation in terms of the composition and grain size of the A15 layer. The relative influences of the composition and the grain size should change with the magnetic field.

The critical current at low field. When the applied field is comparatively low, that is, below about 14T, virtually all of the A15

layer is superconducting and capable of carrying current. The critical current is then expected to vary roughly with the grain size. For samples with comparable grain size, the critical current should depend on the areal cross section of fine-grained material. It follows that the material reacted at the lower temperatures will have higher critical current, and that this current will be determined by some balance between the grain size in the fine-grained shell and its areal fraction. The smallest grain size results from the lowest reaction temperature (650°C). The highest volume fraction of fine-grained material is obtained at a slightly higher reaction temperature (700-730°C) and has a grain size that is only slightly larger. It is, therefore, not surprising that the best low-field properties are found after treatment at low to intermediate temperatures (Fig. VII-5, Table I).

There is also an optimum reaction time for low-field properties. A specific example is given in Fig. VII-4, where an increase in the reaction time at 700°C from 2 to 6 to 8 days decreases the low-field critical current. The data presented in Table II offer a simple explanation for this phenomenon. Increasing the reaction time from 2 to 6 days increases the grain size within the fine-grained shell. However, there is a concommitant increase in the area of the shell. The net effect is a slight decrease in the low-field critical current. Extending the aging time to 8 days causes a substantial increase in grain size without a corresponding expansion in the area of the shell. The result is a substantial decrease in J_c.

<u>The critical current at high field</u>. At higher field the critical current is sensitive to the composition of the layer as well as to its grain size. The upper critical field is known to be a strong function

of composition. Only that subvolume of the reacted layer that is nearly stoichiometric should be able to support a high critical current density at fields of 16T or higher. The STEM/EDXS analyses suggest that there is at least some nearly stoichiometric material within the fine-grained shell at all reaction temperatures. But the fraction of nearly stoichiometric material depends on the magnitude of the Sn gradient, and the gradient decreases with both the reaction time and temperature (Table II). It follows that the best high field conductors will be those that are treated for long times or at high temperatures, in agreement with the data shown in Fig. VII-5. The best high field properties were obtained after long heat treatments at intermediate temperatures, for example, 700°C for 8 days. The data presented in Table II show that these heat treatments result in a nearly uniform composition through an intermediate shell that retains a relatively small grain size.

The arguments presented here are qualitative. It should be possible to phrase them in a quantitative form. Research toward that end is now in progress. But a qualitative appreciation of the coupling between microstructure and critical current is sufficient to provide guidelines for process development. An apparently successful application of this understanding is described in the following section.

ii. <u>The upper critical field.</u> The variation of the upper critical field with heat treatment is a strong function of the composition profile across the A15 layer and does not depend on its microstructural state. Since the composition profiles for various heat treatments have a common simple shape (Figs. VII-21 and 23), it is not surprising that H_{c2} data are more or less independent upon heat treatment conditions. From the theory of flux pinning (Chapt.III), if Nb_3Sn follows the scaling

law of flux pinning [20] then the upper critical field obtained by Kramer's law will reflect the average of H_{c2} of state of order, composition, and lattice strain of the superconducting volume which is determined by the sensitivity of I_c measurement. In theory, the sensitivity of measurement can be varied such that to change the volume of superconducting phase in question, therefore some information can be obtained on the detail composition profile of the Nb_3Sn phase. However, the complex interplay of flux flow, current transfer, and thermal effects near critical current transition offen make this information obscure. Therefore, some predetermined measurement sensitivity, which in turn fix the volume of the superconducting phase in interest, is gererally employed to obtain a meaningful comparison.

Since the state of order, composition variation and lattice strain of the Nb_3Sn phase within a small volume (centered in the position of stoichiometric composition) of the A15 layer were about the same, then the corresponding H_{c2} will fall within a small range. One expection is the H_{c2} of sample heat treated at 800°C for two days which has a value of 23T. This may due to the composition profile of the sample is exceptionally flat around 25 at.%. Therefore, the H_{c2} will have the value of stoichiomtric composition. It is interested to discuss the difference of H_{c2} in the direct-precipitated case (previous chapter), where the A15 crystals are randomly nucleated on the dislocation cell walls. A common superconducting path must exist to allow supercurrent toflow. Even though the same measurement criteria was used to determine I_c, the sensitivity is much lower than that of the Bronze-wires. Lower sensitivity means a larger volume is contributing the result of H_{c2}.

Therefore, in the direct-precipitation case, H_{c2} will reflect the average composition.

iii. The superconducting transition temperature. Measurements of the superconducting transition temperature (Table I) revealed two phenomena. As the reaction nears completion, the transition temperature increases monotonically toward 18K and the width of the transition decreases. Both phenomena are plausibly related to the state of the reacted layer.

The STEM/EDXS analysis suggests that as long as the Sn is not depleted from the matrix and the Nb is not fully reacted there will be at least a thin shell of nearly stoichiometric Nb_3Sn within the reacted layer. But the inductive T_c measures the transition temperature of a volume that is sufficient to expel the flux lines. Given the small values of the amplitude and frequency of the applied ripple field in a typical apparatus, the required volume is contained in a shell about 1 micron in thickness [30]. The particular subvolume of the layer that has the highest transition temperature is responsible for the experimental result. When the A15 layer is thinner than about 1 micron the inductive signal is not finished until virtually all the A15 phase is superconducting. Given the composition gradient through the layer, a thin layer will therefore show a broad transition with a center below 18K. This phenomenon can be understood by the M-H curve shown in Fig. III-1. When the layer is thick enough to have a region of nearly stoichiometric material that is of the order of one micron in thickness, the transition will be sharper and centered near 18K. Since the further increase of magnetization does not influence the average slope of the M-H curve within the region of the applied field amplitude. The variation

of the critical temperature and the transition width with heat treatment (Table I) is hence reasonable in light of the variation of microstructure with heat treatment (Table II).

The results presented here are generally consistent with those previously reported by Smathers and Larbalestier [30], by Evetts, et al. [31], by Suenaga [32], and by Okuda, et al. [15]. It is clear, however, that small variations in the critical temperature and transition width reflect the interplay between the strain, the variation of composition within the penetration depth, and the long range order parameter. Therefore, a small variation of transition width and/or onset can not be attributed to the chemical state of the Nb_3Sn layer. An exact analysis of the superconducting transition in a multifilamentary composite would require an elaborate theoretical treatment.

2. Double-Aging Treatments.

a. Selection of a Double-Aging Treatment. Studies of the singly aged wires show that there are advantages to both low and high reaction temperatures. A low reaction temperature leads to a fine-grained microstructure and good low-field properties while a high reaction temperature leads to a better chemical distribution within the reacted layer and to an improved critical current at high fields. It is desirable to find an alternative heat treatment that combines the best features of both microstructures.

The simplest aging treatment that may combine the benefits of low and high temperature aging is a sequential, double-aging treatment in which a low temperature reaction is completed at higher temperature. Examples of the heat treatment schedule of this type of modification is shown in Fig. VII-24. In such a sequence the low temperature treatment

is intended to establish a fine grain size while the high temperature treatment is included to improve the chemical distribution within the layer. The sequential treatment is at least superficially capable of improving the microstructure since chemical redistribution via grain boundary diffusion should occur more rapidly than grain growth. It is hence plausible that the fine grain size established at low temperature can be retained during a high temperature reaction that improves the stoichiometry of the layer.

Several combinations of double-aging time and temperature were used to test this hypothesis. These included: 650°C, 14-16 days + 730, 750 or 800°C, 0.5hr. to 2 days, and 700°C, 2-6 days + 730 or 750°C, 1-2 days. In each case the initial aging time was long enough to establish the general microstructure appropriate to the lower aging temperature. The 650°C/16 days + 800°C/0.5 hr. treatment was included for comparison with the earlier work of Schauer and Schelb [28].

b. The Double-Aged Microstructure. The A15 layer thickness is plotted as a function of the total reaction time of the double-aging treatments in Figure VII-25. The second, high temperature aging causes a rapid increase in the reaction rate and substantially shortens the time required to achieve an essentially complete reaction.

The distribution of grain size within the reacted layer is tabulated in Table III and illustrated in Fig. VII-26. Those treatments that were finished at 730°C yielded a high areal fraction of fine-grained material with a small final grain size. The treatments that were finished at 750 or 800°C, on the other hand, produced a relatively thin intermediate shell with a rather coarse grain size. A 700°C initial aging was preferable to one at 650°C, primarily because of the

greater thickness of the coarse-grained outer layer after the 650°C treatment.

Interestingly, as illustrated in Fig. 17, the combined 700/730°C treatment produced a greater areal fraction of fine-grained material than was achieved by single aging at either temperature. It is not entirely clear why this beneficial effect happens. The reason may be that the relatively high defect density developed at the lower temperature (700°C) is rapidly polygonized at 730°C, but is partly lost if the reaction is continued to completion at 700°C because the long aging time permits some recovery. This explanation is supported by high resolution studies of the microstructure of the reacted layer in the double-aged condition. The overall morphology is similar to that of the reacted layer in the isothermally aged specimens, but the dislocation density appears to be greater both near the outer boundary of the columnar shell and within the fine-grained shell, as illustrated in Figure VII-27. A comparison of the apparent grains morpfology is shown in Fig. VII-28. It is interesting to see to see the drastic difference in the grain size that can be achieved by heat treatment.

The Sn gradient through the reacted layer is tabulated in Table III. Examples of the measured Sn profiles are plotted in Fig. 19. The 700/730°C treatments appear to give a more nearly constant and stoichiometric distribution of Sn than either the single aging treatments or the double-aging treatments that are finished at 800°C. The reason for the small gradient is probably the combination of the small grain size and high areal fraction of the fine-grained layer, whose composition homogenizes at the higher reaction temperature. The 650/800°C treatment yields a very irregular Sn distribution. This is tentatively ascribed

to the relatively short aging time at 800°C, which is not adequate to homogenize the layer.

The microstructural analyses show that the 700/730°C heat treatments establish an attractive combination of grain size, grain distribution, and chemical distribution within the reacted layer. The best of the treatments tested appears to be 700°C, 4 days + 730°C, 2 days.

c. The Superconducting Properties of Doubly-Aged Wires. The superconducting transition temperatures and critical currents of the doubly-aged wires are tabulated in Table IV. The $J_c(H)$ characteristics of double-aged specimens starting with 650°C and followed by various higher temperatures treatments are shown in Fig. VII-30. These doubly aged specimens has higher J_c especially at higher fields, as compared to that of 650°C for 16 days. Lower field J_c of sample aged at 650°C, 14 days +730°C, 2days shows an increase mainly through an increase of fine-equiaxed layer while the the other two double-aged samples have a small deterioration due to the increase of grain size (Table III). Figure VII-31 is the $J_c(H)$ characteristics of several double-aged specimens with 700°C as the starting heat treatment temperature. The $J^o(H)$ of the 700°C, 6 days aged sample is also included for comparison representing the best obtained by isothermal aging treatment. In Fig. 32 the critical current characteristic of the best of the double-aged wires is compared to those of the two best of the isothermally aged group.

It is clear from this data that a proper double-aging leads to a substantial improvement in the critical current characteristic over the best attained with single aging treatments. The wire given the heat treatment 700°C, 4days + 730°C, 2 days has a critical current that is approximately fifty percent higher at all fields tested than the maximum

measured after single aging. On the other hand, the double-aging treatments that were finished at 800°C, including that proposed by Schaur and Schelb [28], did not improve the critical current and caused an actual deterioration in the critical current at lower fields.

It also seems clear that the increase in J_c is due to the improvement in the microstructure of the reacted layer. The best double-aging treatments yield a reacted layer that contains a high areal fraction of fine-grained material with a reasonably constant Sn concentration. The smaller composition gradient is reflected in the high H_{c2} (Table IV). The H_{c2} data of double-aged specimens fall in a small reange close to 22.5T, which is higher than that of isothermally aged samples (21.3 to 21.9T). The H_{c2} of sample aged at 800°C for 2 days has the highest value, 23T, may be due to both the flatest composition profile and the relaxation of lattice strain associated in the Nb_3Sn layer at the aging temperature. The microstructure combines the best features of low temperature and high temperature aging. The best double-aging treatments were finished at 730°C. Double-aging treatments that were finished at 800°C were ineffective because of the rapid grain growth at this temperature. Fig. VII-33 shows the volume pinning force, $F_p = J_c \times H$, versus the reduced magnetic field, $h = H/H_{c2}$ for two double-aged and three isothermal samples. The maximum pinning force, F_p, can be seen will occur at h lower than ~0.35, and smaller for the double-aged specimens. From the theory of flux pinning (Chapter III, Fig. 3), it can be assumed that the pinning strength of pinning centers has been increased by double-aging treatments.

In evaluating the specific heat treatments used in this work, however, it should be kept in mind that the microstructure that results

from a given heat treatment is influenced by several variables that affect the rate and morphology of the reaction. These include, at least, the size and geometry of the filament, the composition of the bronze, and the bronze/niobium ratio. A change in any of these geometric variables may alter the relation between microstructure and processing and hence change the optimum heat treatment. The present work demonstrates the sequential connection between heat treatment, microstructure and critical current. It suggests that the heat treatment can be systematically varied to engineer the microstructure and achieve better properties. But the optimal heat treatment will vary with the overall characteristics of the wire, and the successful heat treatments identified in this work cannot just be incorporated into the processing of other types of wire.

D. CONCLUSION

The research reported here appears to demonstrate a simple and necessary connection between the heat treatment and the critical current characteristic of bronze-process multifilamentary Nb_3Sn superconducting wire. The connection is made through the microstructure of the superconducting phase. Both the physical and the chemical states of the A15 layer that forms around the Nb filament are relevant to the superconducting properties. The most striking physical feature of the reacted layer is its three-shell composite structure. The critical current density is apparently determined by the areal fraction, grain size and composition of the central, fine-grained shell.

The detail behavior of the inductive T_c measurement and the upper critical field have been examined. Both of the measurements were found to be relatively independent of the composition profile of Nb_3Sn layer, because of the geometry and the characteristic of the Nb_3Sn layer. Inductive T_c and the extrapolated H_{c2} results reflect the average properties of a small volume of the superconducting phase, determined by the oscillating amplitude of field and the sensitivity of I_c measurement, respectively. The only way to study the composition profile of the reacted layer which in term will determine the critical current is by direct microscopic measurement.

The areal fraction and the microstructure of the fine-grained shell depend on heat treatment. Isothermal reaction at lower temperatures (650°C) creates a fine grain size, but yields a low fraction of fine-grained material that has a relatively poor composition. Isothermal reaction at high temperature (800°C) establishes a good composition profile, but yields a large grain size and low critical current. Isothermal aging at intermediate temperature (700-730°C) gives the best combination of microstructural features and the highest critical current. Both the microstructure and the critical current can be improved further by double-aging treatments that start the reaction at 700°C and finish it at 730°C. This treatment produces a large areal fraction of fine-grained material with a nearly constant composition, and enhances the critical current density by approximately 50%.

The microstructure can be plausibly related to the heat treatment through the apparent mechanisms of the reaction forming the A15 phase. These mechanisms are inferred from the results of high resolution studies of the development of the microstructure. The critical current

varies with the microstructure, and specifically with grain size and stoichiometry, as current understanding suggests it should.

TABLE I. The results of superconducting properties measurements: J_c data at 10, 14 and 15 tesla and inductive T_c onset and transition width and upper critical field for various isothermal treated specimens.

Aging Condition	Overall J_c, 10^3Amp/cm^2 10T	14T	15T	T_c(K) Onset (ΔT_c)	H_{c2} (T)
650°C/4D	33.3	8.9	6.4	17.5 (0.6)	--
8D	37.9	11.0	8.0	17.7 (0.3)	21.6
16D	40.5	15.7	10.8	17.9 (<0.1)	21.3
700°C/2D	46.0	15.7	10.4	17.5 (0.5)	21.8
6D	44.3	17.1	12.2	17.7 (0.2)	--
8D	36.3	17.9	13.8	17.9 (0.1)	21.9
730°C/4hr	34.3	9.0	6.1	17.4 (0.4)	--
1D	38.7	11.1	11.8	17.9 (0.1)	--
2D	46.7	16.4	13.1	17.9 (<0.1)	21.8
8D	44.0	14.5	12.7	18.0 (<0.1)	21.8
750°C/2D	44.6	16.3	12.7	17.9 (0.4)	--
800°C/12hr	18.6	8.1	6.2	17.9 (0.3)	21.9
2D	31.4	15.7	12.7	18.0 (<0.1)	23.0

TABLE II. The results of microstructural analyses of the A15 layer for isothermal treated samples.

Aging Condition	Volume Fraction Columnar Grain	Equiaxed Grain	Coarsened Grain	Total	Grain Size, d (Å)	Sn Gradient At.% Sn/μm
650°C/4D	0.31	0.32	--	0.63	530	--
8D	0.25	0.33	0.29	0.87	600	--
16D	0.27	0.34	0.32	0.93	630	4.7
700°C/2D	0.13	0.37	0.23	0.76	640	8.5
4D	0.17	0.43	0.26	0.86	720	--
6D	0.17	0.46	0.28	0.91	740	5.4
8D	0.8	0.47	0.29	0.94	770	5.2
730°C/20min	0.11	0.15	0.07	0.33	540	--
1hr	0.14	0.17	0.08	0.39	590	--
1D	0.15	0.37	0.29	0.81	690	--
2D	0.13	0.42	0.33	0.88	720	5.3
8D	0.10	0.39	0.46	0.95	800	5.1
750°C/2D	0.14	0.34	0.46	0.93	840	--
800°C/4hr	0.16	0.28	0.31	0.75	--	--
12hr	0.22	0.24	0.44	0.90	1090	6.2
2D	0.14	0.31	0.52	0.97	1190	2.1

TABLE III. The results of microstructural analyses of the A15 layer for several doubly-aged specimens.

Aging Condition	Volume Fraction Columnar Grain	Equiaxed Grain	Coarsened Grain	Total Grain	Grain Size, d (Å)	Sn Gradient At.% Sn/μm
650°C/14D + 730°C/2D	0.16	0.40	0.42	0.98	650	--
650°C/16D + 800°C/4hr	0.22	0.28	0.46	0.96	930	10.8
700°C/2D + 730°C/2D	0.15	0.48	0.31	0.94	730	2.0
700°C/4D + 730°C/2D	0.11	0.58	0.29	0.98	760	2.3
700°C./6D + 730°C/1D	0.12	0.56	0.30	0.98	770	2.5
700°C/2D + 750°C/2D	0.12	0.43	0.43	0.98	830	2.6

TAELE IV. The results of superconducting properties measurements (J_c, T_c and H_{c2}) for several doubly-aged samples.

Aging Condition	Overall J_c, 10^3 Amp/cm^2 10T	14T	15T	T_c(K) Onset (ΔT_c)	H_{c2} (T)
650°C/14D + 730°C/2D	56.5	17.8	12.5	17.6 (0.3)	--
650°C/14D + 750°C/2D	48.5	16.0	11.8	17.8 (0.2)	--
650°C/16D + 800°C/0.5hr	45.8	14.8	10.0	17.8 (0.2)	--
700°C/2D + 730°C/2D	57.1	22.9	17.9	17.6 (0.3)	22.5
700°C/4D + 730°C/2D	61.4	25.1	20.7	18.0 (0.5)	--
700°C/6D + 730°C/1D	58.2	23.5	17.5	17.8 (<0.1)	22.6
700°C/2D + 750°C/2D	55.5	21.2	15.3	17.9 (0.2)	22.5

REFERENCES

1. A. R. Kaufmann and J. J. Pickett, Bull. Am. Phys. Soc., 15, 833, 1970.
2. E. W. Howlett, U.S. Pat. 3,728,165 (filed 10/19/1970)μ Great Britain Pat. 52,623/69 (filed 10/17/69).
3. B. E. Jacobson, R. H. Hammond, T. H. Geballe and J. R. Salem, J. Less Common Metals, 62, 59, 1978.
4. T. P. Orlando, J. A. Alexander, S. J. Bending, J. Kwo, S. J. Poon, R. H. Hammond, M. R. Beasley, E. J. McNiff and S. Foner, IEEE Trans. Mag., MAG-17, 368, 1981.
5. D. B. Smathers and D. C. Larbalestier, Filamentary A15 Superconductors, edited by M. Suenaga and A. F. Clark (Plenum Press, New York, 1980).
6. E. C. van Reuth and R. M. Waterstrat, Acta Cryst., B24, 186 (1968).
7. R. M. Scanlan, W. A. Fietz and E. F. Koch, J. Appl. Phys., 46, 2244, 1975.
8. B. J. Shaw, J. Appl. Phys., 47, 2143, 1976.
9. J. D. Livingston, Phys. Stat. Sol. (a), 44, 295, 1977.
10. G. Zerweck, J. Low Temp. Phys., 42, 1, 1981.
11. E. J. Kramer, Adv. Cryo. Eng., 28, 307, 1982.
12. J. W. Ekin, Cryogenics, 20, 611, 1980.
13. I. W. Wu, W. V. Hassenzahl and J. W. Morris, Jr., Proc. International Cryogenic Materials Conf., Kobe, Japan, edited by K. Tachikawa and A. Clark, (Butterworths, London, 1982), p. 388.
14. I. W. Wu, D. R. Dietderich, W. V. Hassenzahl, M. Hong and J. W. Morris, Jr., J. Appl. Phys., in press.

15. S. Okuda, M. Suenaga and R. L. Sabatini, J. Appl. Phys., 54, 289, 1983.

16. J. I. Goldstein, Introduction to Analytical Electron Microscopy, edited by J. J. Hren, J. I. Goldstein and D. C. Joy (Plenum Press, New York, 1979).

17. J. W. Ekin, Appl. Phys. Lett., 29, 218 (1976).

18. G. Fujii, J. W. Ekin, R. Redebaugh and A. F. Clare, Adv. Cryo. Eng., 26, 589 (1980).

19. L. F. Goodrich, J. W. Ekin and F. R. Fickett, Adv. Cryo. Eng., 28, 571 (1982).

20. E. J. Kramer, J. Appl. Phys., 44, 1360 (1973).

21. P. A. Sanger, E. Adam, E. Ioriatti and S. Richards, IEEE Trans. Mag., MAG-27, 666, (1981).

22. K. Togano, T. Asano and K. Tachikawa, J. Less Common Metals, 68, 15 (1979).

23. M. Suenaga, K. Aihara, K. Kaiho and T. S. Luhman, Adv. Cryo. Eng., 26, 442 (1980).

24. A. W. West and R. Rawlings, J. Mat. Sci., 12, 1862 (1977).

25. W. Schelb, J. Mat. Sci., 16, 2575 (1981).

26. H. H. Farrell, G. H. Gilmar and M. Suenaga, J. Appl. Phys., 45, 4025 (1974).

27. A. A. Bochvar, V. S. Sergeev, V. G. Kuznetsova, A. D. Nikulin, E. A. Klepatskaya and M. A. Fomishkin, Metallovedenie i Termicheskaya Obrabotka Metallov., 12, 44 (1980).

28. R. Flukiger, Adv. Cryo. Eng., 28, 399 (1982).

29. J. L. Standenmann, Solid State Phys., 23, 121 (1977): 26, 461

(1978).

30. D. B. Smathers and D. C. Larbalestier, Adv. Cryo. Eng., 28, 415, (1982).

31. J. E. Evetts, J. R. Cave, R. E. Somekh, J. P. Stanton, and A. M. Campbell, IEEE Trans. Mag., MAG-17, 360 (1981).

32. M. Suenaga, Superconductor Materials Science, edited by S. Foner and B. B. Schwartz, (Plenum Press, New York, 1981).

33. W. Schaur and W. Schelb, IEEE Trans. Mag., MAG-17, 374 (1981)

VIII. THE INFLUENCE OF MAGNESIUM ADDITION TO THE BRONZE ON THE CRITICAL CURRENT OF BRONZE-PROCESSED MULTIFILAMENTARY NB_3SN SUPERCONDUCTING WIRES

A. INTRODUCTION

Composite-Processed multifilamentary Nb_3Sn conductors are been intensively pursuited for high-field applications, particularly in the magnetic confinement for fusion reactors operated at fields from 10 to 15T, and the 10T dipole magnets for high energy accelerators. The requirements for these applications are very stringent, and the improvement of critical current density, J_c, is required before large scale applications can be realized. Three parallel efforts have been dedicated to fulfill this task: (1) by modifying the existent processing methods, as described in the Chapter IV, (2) by designing a novel heat treatment such that the microstructural state of the Nb_3Sn phase can be improved and hence J_c, Chapter VII [12,13], and (3) by alloying additions to the niobium core, or to the bronze matrix, or to both [1-11]. This chapter reports the experimental effort of doping Mg to the bronze matrix, and the microstructurers and J_c of laboratory scale multifilamentary wires.

Prior work by Tachikawa and coworkers [5,9] has shown that the addition of magnesium to the bronze matrix prior to the formation of bronze-processed Nb_3Sn tape causes a significant increase in the critical superconducting current density at 6.5 tesla, and that this increase is associated with a decrease in the apparent A15 grain size. The present work was undertaken to determine whether a similar improvement

in J_c would follow the addition of Mg to multifilamentary Nb_3Sn wires at 10-15T field range and to identify the microstructural and mechanistic sources of any beneficial effects. To accomplish this, multifilamentary wires were drawn in the laboratory. They contained 133 filaments of pure Nb embedded in bronze with various concentrations of Sn and Mg. Their critical current densities were measured as a function of bronze composition, heat treatment, and transverse magnetic field at 4.2K. The reacted A15 layers were subsequently examined using a variety of microscopic and microanalytic techniques. An important result of this research was obtained by comparing the J_c of wires with various Mg concentration in the Sn-bronze matrix which were heat treated to the same, nearly completely reacted state. This result leads to an obvious implication of further improvement of J_c through the mechanistic influence of Mg.

B. EXPERIMENTAL

1. Wire Manufacture. The multifilamentary wires used in this research were manufactured in the laboratory from pure starting materials. They differed in composition of the bronze (Table 1) which was varied to measure the influence of Mg at two Sn levels. The initial bronze ingots were melted in quartz tubes under argon and cast into rods. The rods were doubly swaged and homogenized, and were then machined to 10mm outer diameter and bored to form tubes of 5mm inner diameter. Pure Nb rods were inserted into the tubes and the composite was drawn into wire. The monofilament wires were bundled in groups of seven, enclosed in a tube of the same bronze composition, and redrawn.

The seven-filament wires were then rebundled in groups of nineteen (133 filaments) inside bronze tubes of identical composition and drawn to a final diameter of 0.5 mm. During drawing the wires were annealed at 450°C for 40 minutes after approximately each 50-80% reduction in area. The Mg-doped wires have higher work-hardeniong rate, and more frequent annealing are needed. Sample cross-sections of two finished and partially reacted wires are shown in Fig. VIII-1. The filaments are reasonably uniform, though those near the periphery of the wire are noticeably flattened. Small differences in the drawing properties of the wires and the manufacturing procedure caused the final filament size to vary from wire to wire. The compositions and characteristics of the wires are listed in Table 1, where the composition of the bronze is given in atomic percent (the balance is Cu), D is the effective diameter of the filaments (determined from the cross-sectional area of the filament) and R is the volumetric ratio of bronze to Nb. Seven different types of wires were successfully manufactured, they differed in the composition of the bronze matrix. In the forgoing, the samples will be nomenated by four digit numbers which signify the composition of the bronze matrix, e.g., 6720 representing the wire with bronze matrix contenting 6.7 at.% Sn and 0.20 at.% Mg (Table 1).

2. Heat Treatment. After manufacture the wires were sectioned into segments approximately 10 cm in length and heat treated in sealed quartz tubes under argon to form the A15 phase. The heat treatment temperatures were 650, 700, 730, 750 and 780°C, and were chosen to bracket the optimum reaction temperature of the Mg-free wire [11,12]. The heat treatment times were a few hours to twenty days. The progress of the reaction during heat treatment was monitored by sectioning the wires

after selected reaction times, taking scanning electron micrographs and measuring the area of the reacted layer with an image processing microcomputer. The consistency of measurements taken from serial sections showed that the reaction was uniform along the wire length.

3. Measurement of the Critical Current Density. The critical current (I_c) of the wires was measured at 4.2K in transverse magnetic fields of 8-15T at the National Magnet Laboratory. The tests employed a four-point probe technique on specimens 30mm long. The critical current was defined to be that giving a potential difference of 1 microvolt between voltage taps placed 5mm apart. The sensitivity of the I_c measurement is approximatly 10^{-11} and 10^{-10} ohm-cm at 10 and 15 tesla, respectively. The critical current density (J_c) was determined by dividing the critical current by the measured area of A15 phase in the wire cross-section. At least three specimens were tested for each combination of composition and heat treatment.

4. Materials Characterization. The characterization of the A15 phase employed microstructural and microchemical analyses in addition to the overall stereological examination of the reacted layer described above. The grain size of Nb_3Sn was estimated from scanning electron fractographs of broken wire specimens (the A15 phase always fractured in an intergranular mode) and measured more precisely from transmission electron micrographs of thin foil samples prepared by ion milling. The peripheral surfaces of the reacted filaments were examined by SEM after the matrix is removed by etch to study the effect of Mg addition on grain coarsening. The composition within the A15 layer was studied by electron microprobe analysis, which readily reveals the Mg, by scanning transmission electron microscopy, which offers greater spatial

resolution but a less sensitive analysis of Mg, and by high resolution scanning Auger analysis, which was used to assess the degree of segregation of Mg to the Nb_3Sn grain boundaries.

C. RESULTS AND DISCUSSION

1. The Influence of Mg on Wire Drawing and Reaction Rate. The wires containing Mg-bronze were noticeably more difficult to draw, presumably because of solution hardening by the Mg. However, the change in drawing response was minor, and was accommodated by slight alterations in the wire-drawing technique and annealing schedule. The Mg-bronze wires tended to have larger filament sizes after the completion of drawing to 0.5mm final diameter (Table 1), but it is not yet clear whether this difference reflects changes in the drawing properties of the wire or minor variations in the manufacturing procedure. The rate of the reaction forming A15 at the Nb-bronze interface also varied from wire to wire. However, the reaction rate depends on the filament size and shape as well as on the composition and temperature. Samples of the cross-sectional areas of the reacted A15 phase versus aging time for samples heat treated at 650 and 700°C were shown in Figures VIII-2 and 3, respectively. The growth of the reacted layers follows a power law which is the characteristics of a diffusion-controlled reaction. From this experimental results, it is clear that 6700 and 6762 samples has the slowest reaction rate. This may due to that although moderated amount of Mg enhances growth of the A15 phase, too high a concentration deterioates it. It is also clear that the variation of the state of reaction is significant form wire to wire for any given heat treatment

condition. The result of this effect is that the comparison of microstructure and critical current density can be made valid only when the wires are compared at same stage of reaction. Table 2. lists the times for all wires aged to almost fully reaction (approximately 95% of Nb to Nb_3Sn conversion) at aging temperatures from 700 to 780°C. The data for 650°C aging are also included for comparison.

2. The Influence of Mg on the Critical Current Density. The addition of Mg to the bronze-processed wire increased its maximum critical current density over the range 8-15T for all values of the reaction temperature. The increment in J_c increased with the magnesium concentration. Samples of the results are presented in Figs. VIII-4 and 5. Figure VIII-4 shows the critical current characteristic, $J_c(H)$, for wires heat treated to 4 days at 730°C. The increase in J_c following an addition of 0.6Mg to the bronze is much greater than that caused by the addition of 1.1Sn, and persists over the tested range of applied fields. Fig. VIII-5 compares the J_c of the 6.7Sn-0.6Mg wire at 10T to those of the 6.7Sn and 7.8Sn wires in the same heat treatment conditions which have a decreasing aging time with increasing aging temperature to achieve a similar degree of reaction. The data agrees with that of Tachikawa and coworkers [5,9] in showing an optimum temperature for the Mg effect, but suggests that the optimum temperature is lower for the multifilamentary wires (700-730°C) than it is for the tapes they studied (800°C). The net improvement due to Mg is substantial. The addition of 0.6 Mg to the 6.7Sn bronze increases the maximum J_c by nearly 100%. The resulting current density is 60% higher than the maximum achieved in 7.8Sn.

Since the reaction rates for different wires varies significantly, the comparison of J_c at the same heat treatment conditions is not a very good one. A better comparison can be obtained by selecting the similar stage of reaction at each temperatures. The J_c per unit Nb_3Sn area of the nearly fully reacted samples should then represent the inherent current-carrying capacity of the superconducting phase. Figures VIII-6 presents the $J_c(H)$ characteristics of wires aged at 730°C to ~95% the reacted state (Table 2.). These results confirm qualitatively with that of Fig. VIII-4, where the comparison was made for all samples aged for 4 days. However, the detailed characteristics are very different. For example, the previous 7810 sample showed little improvement in J_c as compared to its Mg-free counterpart, 7800 sample. This result is only because that the 7810 sample is being over-aged after 4 days treatment, while in the Fig. VIII-6, the 7810 sample, which was reacted to 94% after 2 days treatment, shows an ~ 50% and 200% improvement in J_c at 12 and 15 tesla, respectively. The discrepancy here proves that the importance of a valid comparison.

The J_c of the wires for different aging temperatures with 6.7% Sn and various Mg concentrations in the bronze matrix at 10T in their most fully reacted condition (~95%, Table 2.) is shown in Fig. VIII-7. The 650°C-treated samples were reacted to ~65%, and their J_c were included for comparison. It is clear from this figure that the improvement in J_c increases with the Mg content in the bronze matrix monotonically. The highest J_c is achieved by the wire with 0.62% Mg (6762) and aged at 700 to 730°C, which represents an ~200% increase over what is obtained with the Mg-free sample, 6700. A similar J_c comparison at 10T for wires with 7.8% Sn-bronze matrix is shown in Fig. VIII-8. It can be seen that by

doping only 0.1% Mg to the matrix increases the critical current density for ~50%. Figure VIII-9 combines the highest J_c sample, 6762, and the two Mg-free wires. It is found that the J_c of 6762 wire is higher than for the Mg-free samples, 7800 and 6700, by approximately 100 and 200%, respectively. The second highest J_c is achieved by the 7810 sample, and it J_c is roughly 30% lower than that of the highest, 6762 sample.

The influence of Mg addition on J_c at 15T is shown in Fig. VIII-10. The 700°C treatments, which correspond to the best aging temperature at 10T field, results in much lower J_c than the 730°C treatments. This can be attributed to the higher temperature treatments yielding a better composition of the A15 layer which results in a better J_c at higher fields [12-13]. The same increment of J_c on the Mg content as that of 10T field is found, but the amount of increase is even higher, e.g., the maximum J_c of the 6762 sample is almost four times as high than the Mg-free wires.

3. <u>The Distribution of Mg in the Reacted Wire</u>. The available evidence shows that Mg segregates strongly to the A15 layer during the reaction, and suggests that it incorporates primarily in the bulk Nb_3Sn rather than in the grain boundaries. Fig. VIII-11 presents sample data taken from electron microprobe studies of the reacted layer and gives the distribution of Mg in fully reacted 6.7Sn-0.6Mg aged at 750°C. Essentially all of the Mg has accumulated in the reacted layer. The measured Mg concentration profile through the reacted layer is nearly flat at a concentration of slightly more than 3%. The location of the Mg within the reacted layer was studied by high resolution Auger spectroscopy on fresh fracture surfaces, which reveal the Nb_3Sn grain boundaries, and on sputtered surfaces which represent the grain interior.

The quantitative results of the Auger analysis are unreliable, since Mg does not have strong Auger peaks. However, the qualitative results are reasonably clear. No strong Mg peaks arise from fresh fracture surfaces and the peak height does not change consistently when the surface is sputtered away from the grain boundary, hence Mg does not segregate strongly to the grain boundary.

4. The Influence of Mg on the Grain Size. Previous work [12,13] on the grain size of reacted layers of Nb_3Sn has shown that the layer is divisible into three morphologically distinct regions: an inner layer of columnar grains growing out from the Nb interface, an intermediate layer of fine-grained material, and an outer layer of large, coarsened grains. It is hence important to consider the influence of Mg on both the minimum grain size and on the distribution of grain size. The grain size is best measured from TEM micrographs of the reacted layer. These measurements are in progress, and the preliminary results suggest that Mg does induce a consistent decrease in the minimum grain size, However, the most striking effect of the Mg addition is on the grain size distribution. As illustrated in Fig. VIII-12 to 14, for example, the addition of Mg suppresses the growth of large grains in the periphery of the reacted layer, giving a much more uniform and fine-grained structure. This effect is most pronounced at intermediate reaction temperatures. It is likely that the suppression of grain coarsening is responsible for much of the improvement in J_c. In a Mg-free wire aged at intermediate temperature, 30-50% of the total volume of the A15 phase is coarse-grained. Since the critical current density is a strong inverse function of the grain size, the grain refinement of this material is expected to yield a substantial improvement in J_c. Figure VIII-15 shows

two scanning electron micrographs the surface of the fliaments periphery of 6700 samples (a) before aging, and (b) after aged at 750°C for 1 day with the bronze matrix removed. The unreacted filaments showed only some drawing marks and a few small voids, and there is no pre-reacted Nb_3Sn found. The absence of the pre-reacted A15 grains has also been proved by T_c measurement and SEM/EDXS spectra taken from the periphery surfaces of filaments. For the reacted filaments, extraneous large coarsened grains are observed at the bronze-A15 interfaces. These grains have large regular facets and are polyhedron in shape. The A15 grains of the inner layer have a much smaller size and are equiaxial in shape. This observation is consistent with that found in the commercial Nb_3Sn multifilamentary wire, Chapt.VII [12,13]. I believed that this is the first clear illustration of the three dimentional view of the A15 grains. A distinctive prove of the Mg effects on the coarsening of grains was shown in Figure VIII-16, where the deep-etched peripheral view of (a) 6700 sample aged at 730°C for 12 days and (b) 6762 sample aged at 730°C for 9 days were demonstrated. The ability of Mg to suppress the grain coarseing and yield an uniformly fine-grained product is very striking. From these micrographs, it can be seen that Nb_3Sn grain boundaries are preferentally etched for both the Mg-free and Mg-bronze wires. This may be due to the high concentration of Cu in the grain boundaries [14] and hence the grain morphology can be revealed.

5. <u>The Influence of Mg on the Composition of the Reacted Layer.</u> In previous work [11,12] scanning transmission electron microscopy was used to study the concentration profile of Sn within Nb_3Sn reacted layers. The results showed a gradient of Sn from a Sn-rich value at the bronze interface to a Sn-poor value at the Nb interface, with a band of

nearly stoichiometric material near the center of the reacted layer. The initial results of similar studies of Mg-bearing material are presented in Fig. VIII-17. The STEM analyses suggest that the Sn profile within the Mg-bearing layer is very flat relative to that in Mg-free wire [11,12]. Quantitative STEM analysis is difficult, and the results presented in Fig. VIII-17 must be confirmed by further work before they can be accepted as true. Preliminary results of T_c and H_{c2} measurements show that the T_c midpoint of the Mg-doped and Mg-free wires are similar, and that the H_{c2} increases slightly with Mg addition. However, the increase of H_{c2} is far too small to account for any significant part of the improvement in J_c. Therefore, it can be concluded that the effects of Mg addition is mainly microstructural rather than simultaneously affecting the intrinsic properties of Nb_3Sn. The significant effect of grain size on J_c at higher fields has been recently suggested by Suenaga [14]. The decrease in grain size and the more uniform Sn distribution by the Mg addition are responsible for the large increase in J_c at 15T.

D. SUMMARY

The research reported here confirms the original work of Tachikawa and coworkers on the beneficial influence of Mg on the critical current density of bronze-processed Nb_3Sn. The results show that Mg may be used to improve J_c in multifilamentary wire. The critical current density improves significantly: at 10T, there is 100 to 200% increase from adding 0.62% Mg to the bronze matrix. The next best improvement in J_c is achieved for the 7.8% Sn-bronze wire doped with 0.1% Mg. The J_c of this small amount of Mg addition is only approximately 30% lower than

the best. The increase of J_c is large enough to be technologically interesting. Chemical analysis reveals that the Mg segregates to the reacted layer, and resides principally in the bulk Nb_3Sn, and it does not affect the intrinsical properties of the A15 phase in any significant way. The microstructural analyses suggest that its principal effect is to suppress coarsening of the Nb_3Sn grains and establish a uniformly fine-grained layer. Preliminary data also suggests that Mg decreases the minimum Nb_3Sn grain size and improves the overall stoichiometry of the reacted layer.

It should finally be recalled that, while the results obtained in this work are technologically interesting, the samples used had very high bronze to Nb ratios (R). Since the increase in J_c apparently depends on the concentration of Mg in the reacted layer, and since virtually all the Mg accumulates there, it may prove difficult to achieve comparable results at lower R values without substantially raising the Mg content of the bronze, or changing to an 'external bronze' process. However, by simultaneously adding with other elements which has the effect of improving the intrinsic properties, e.g., the H_{c2}, may be resulting a even higher J_c conductor. This program is now under investigation.

Table 1. Composition, nomenation, filament size (D), and bronze to Nb ratio (R) of the bronze processed multifilamentary wires.

Composition (at%) bal. Cu	Nomenation	D	R
6.7 Sn	6700	11.4	14
6.7 Sn + 0.1 Mg	6710	13.4	10
6.7 Sn + 0.2 Mg	6720	10.9	15.3
6.7 Sn + 0.35 Mg	6735	10.7	15.9
6.7 Sn + 0.62 Mg	6762	12.5	12
7.8 Sn	7800	8.3	27
7.8 Sn + 0.1 Mg	7810	12.1	12

Table 2. The heat treatment time, in day, and percent conversion of Nb to Nb_3Sn, in parenthesis, of wires at their most fully reacted state for J_c comparison

	650°C	700°C	730°C	750°C	780°C
6700	20 (63)	20 (93)	12 (92)	8 (90)	4 (90)
6710	14 (57)	4 (99)	2 (99)	1 (95)	1 (99)
6720	8 (67)	8 (95)	2 (97)	1 (95)	0.5 (95)
6735	8 (62)	10 (99)	3 (96)	1 (95)	0.75 (96)
6762	20 (62)	12 (95)	9 (99)	2 (94)	1.75 (99)
7800	8 (67)	8 (95)	4 (94)	2 (96)	2 (96)
7818	4 (68)	6 (95)	2 (98)	1 (98)	0.5 (97)

REFERENCES

1. M. Suenaga, T. S. Luhman and W. B. Sampson, J. Appl. Phys., 45, 4049 (1974)

2. O. Horigami, T. S. Luhman, C. S. Pande and M. Suenaga, Appl. Phys. Lett., 27, 738 (1976).

3. D Dew-Hughes, IEEE Trans. Magn., Mag-13, 651 (1977).

4. H. Sekine, K. Tachikawa and Y. Iwasa, Appl. Phys. Lett., 35, 472 (1979).

5. K. Togano, T. Asano and K. Tachikawa, J. Less-Common Metals, 68, 15 (1979).

6. M. Suenaga, K. Aihara, K. Kaiho and T. S. Luhman, Adv. Cryo. Eng., 26, 442 (1980).

7. H. Sekine, T. Takeuchi and K. Tachikawa, IEEE Trans. Magn., MAG-17, 383 (1981).

8. M. Suenaga, W. B. Sampson and T. S. Luhman, Ibid, P. 646.

9. K. Tachikawa, Adv. Cryo. Eng., 26, 378 (1980).

10. I. W. Wu, D. R. Dietderich, J. T. Houlthusi, W. V. Hassenzahl and J. W. Morris, Jr., IEEE Trans. Magn., in press.

11. I. W. Wu, D. R. Dietderich, J. T. Holthuis, P. E. Johnson-Walls, J. Glazer, W. V. Hassenzahl and J. W. Morris, Jr., Adv. Cryo. Eng., in press.

12. I. W. Wu, M. Hong, W. V. Hassenzahl and J. W. Morris, Jr., Proc., ICEC9-ICMC, Kobe, Japan, 1982, Butterworth β Co., England, p. 388 (1982).

13. I. W. Wu, D. R. Dietderich, J. T. Holthuis, M. Hong, W. V. Hassenzahl and J. W. Morris, Jr., J. Appl. Phys., in press.

14. M. Suenaga, Brookheaven National Laboratory, L. I., N. Y., private communication.

IX. CONCLUSIONS

The main body of my thesis work is devoted to the understanding of superconducting properties in terms of the micro-physical and chemical states of high-field A15-type materials. Higher critical current is achieved through microstructural control which is based on the knowledge of the relationships between properties, microstructures and processing. The A15 materials under investigation are divisible into two parts: the V_3Ga and Nb_3Al phases formed by a direct-precipitation process, and the multifilamentary Nb_3Sn conductors formed by the bronze-process. The microstructures can be related to the processes and heat treatments through the apparent mechanisms of the reaction which form the A15 phases. These mechanisms are inferred from the results of high resolution studies of the microstructures. As current understanding suggests it should, the critical current varies with the microstructure, specifically with grain size and stoichiometry.

The theories of superconductivity, flux pinning, and metallurgy of A15 conductors are critically reviewed. The advantages and disadvantages of various processing methods were discussed based on knowledge of metallurgical principles and microstructures. A mathematical model for calculating the net free energy increase of a superconducting body by the passage of an external electric current is proposed, based on the increase in kinetic energy of the electrons. A new interpretation of inductive T_c measurement and H_{c2} estimation was also discussed. These results can be summarized as follows.

A. THEORETICAL CONSIDERATION OF FREE ENERGY

The change in the internal energy of a superconducting body by the passage of a supercurrent has not been understood, except estimated by a phenomenological two-fluid model. However, by using the BCS microscopic theory and a quantum mechanics description of electrons in momentum space, a mechanistic treatment can be found. This model requires knowledge of the Fermi surface, density of state, population and energy gap to calculate the total energy change of the electrons. The work done by the outside environment and hence the free energy change can be calculated by the kinetic energy of electrons and the density of Cooper pairs. The goat of the calculation is to express the intensive and extensive thermodynamical variables by measurable physical quantities.

B. THE DIRECT PRECIPITATED V_3Ga and Nb_3Sn

Superconducting V_3Ga and Nb_3Al were made by quenching supersaturated solutions, deformation, and then precipitation of the A15 phase by aging treatment. The critical current characteristics of the product materials depend both on the inherent properties of the A15 phase and on the details of the precipitation process, which determines the grain size, continuity, volume fraction and composition of precipitates. These metallurgical parameters were examined to study the critical current characteristics. The lattice correspondence between the A15 crystals and BCC matrix was found to follow the K-S relationship: the closed packed planes and directions of the precipitates are parallel to those of the matrix. The lattice correspondence is shown in Fig. IX-1.

A15 precipitates preferentially nucleate on the prior-deformation BCC grain boundaries and the dislocation cell walls. The nucleation of Nb_3Al precipitates is more homogeneous than that of V_3Ga. The V_3Ga precipitates grow into elongated grains which have their habit planes coincident with the orientation relationship, while the Nb_3Al precipitates are equiaxial in shape. An typical example is shown in Fig. IX-2. However, in both cases, thin films of BCC phase between two adjacent A15 grains have high stability against spheroidization. These films of normal metal may provide part of the current-carrying capacity through a surface pinning mechanism. Since the A15 grains in a cluster usually have an identical orientation, the A15 grain boundary pinning mechanism will be relatively weak (the effective grain size is larger than the average of individual grains). However, the normal-state films lower the stability of the conductors. The formation and growth of A15 precipitates have been shown to be controlled by the overall composition, prior deformation, and heat treatment. The resultant microstructure and chemical composition then determines the superconducting properties.

C. CONVENTIONAL BRONZE PROCESSED Nb_3Sn MULTIFILAMENTARY WIRE

Microscopic analyses appear to demonstrate a simple and necessary connection between the heat treatment and the critical current characteristic of bronze-process multifilamentary Nb_3Sn superconducting wire. Both the physical and the chemical state of the A15 layer that forms around the Nb filament determine its intrinsic superconducting properties. The most striking physical feature of the reacted layer is its three-shell composite structure. The schematic representation of this

three-shell structure and the Sn concentration profile are illustrated in Fig. IX-3. A mechanism to account for the formation of this structure is proposed which includes dislocation generation and polygonization and grain coarsening. The polygonized dislocation cell walls in the columnar grains are shown in Fig. IX-4. The critical current density is apparently determined by the areal fraction, grain size and composition of the central, fine-grained layer. The areal fraction and the microstructure of the fine-grained shell depend on heat treatment. Isothermal reaction at lower temperatures creates a fine grain size, but yields a low volume fraction of fine-grained material which has a relatively poor composition. Isothermal reaction at high temperatures establishes a good composition profile, but yields a large grain size and low critical current. Isothermal aging at intermediate temperatures gives the best combination of microstructural features and the highest critical current. Both the microstructure and the critical current can be improved further by double-aging treatments that start the reaction at 700°C and finish it at 730°C. This treatment produces a large areal fraction of fine-grained material with a nearly constant composition, and enhances the critical current density by approximately 50% at fields between 10 and 15T. The $J_c(H)$ characteristic of such a treatment is shown in Fig. IX-5, where the best obtained J_c of isothermal aged samples were also included for comparison.

D. BRONZE PROCESED MULTIFILAMENTARY Nb_3Sn WIRES WITH MAGNESIUM ADDITION TO THE MATRIX

Magnesium addition to the bronze matrix increases the attainable critical current density (100-300%) in bronze-processed multifilamentary Nb_3Sn wires at all fields tested (8-15T). An example of J_c at 10T of the wire doped with 0.62% Mg and the Mg-free wires is shown in Fig. IX-6. The increase is large enough to be of technological interest. The magnesium segregates almost completely to the Nb_3Sn layer during the reaction. Mg resides predominately within the A15 matrix, it is not a strong grain boundary surfactant. The most obvious effect of the Mg addition is to retard grain coarsening during growth of the A15 layer, yielding a uniformly fine-grained product. The peripheral surfaces of filaments without Mg addition is shown in Fig. IX-7. This effect accounts for much (if not most) of the improvement in critical current density. Preliminary experimental results also suggest that Mg decreases the minimum A15 grain size, and that it also improves the Sn distribution within the reacted layer to establish a more uniformly stoichiometric phase.

E. INDUCTIVE T_c AND EXTRAPOLATED H_{c2} MEASUREMENTS

The detailed behavior of the inductive T_c measurement and the upper critical field by Kramer's extrapolation have been examined. Both of the measurements were found to be rlatively independent of the composition profile in the Nb_3Sn layer due to the geometry and the intrinsic nature of the bronze process. These measurements reflect the average

properties of a small volume of the superconducting phase, and were determined by the oscillating field amplitude of the inductive apparatus, and the sensitivity of the critical current measurement. Therefore, the results of these measurements cannot be directly related to the composition profiles of the bronze-processed Nb_3Sn layer.

FIGURES AND CAPTIONS

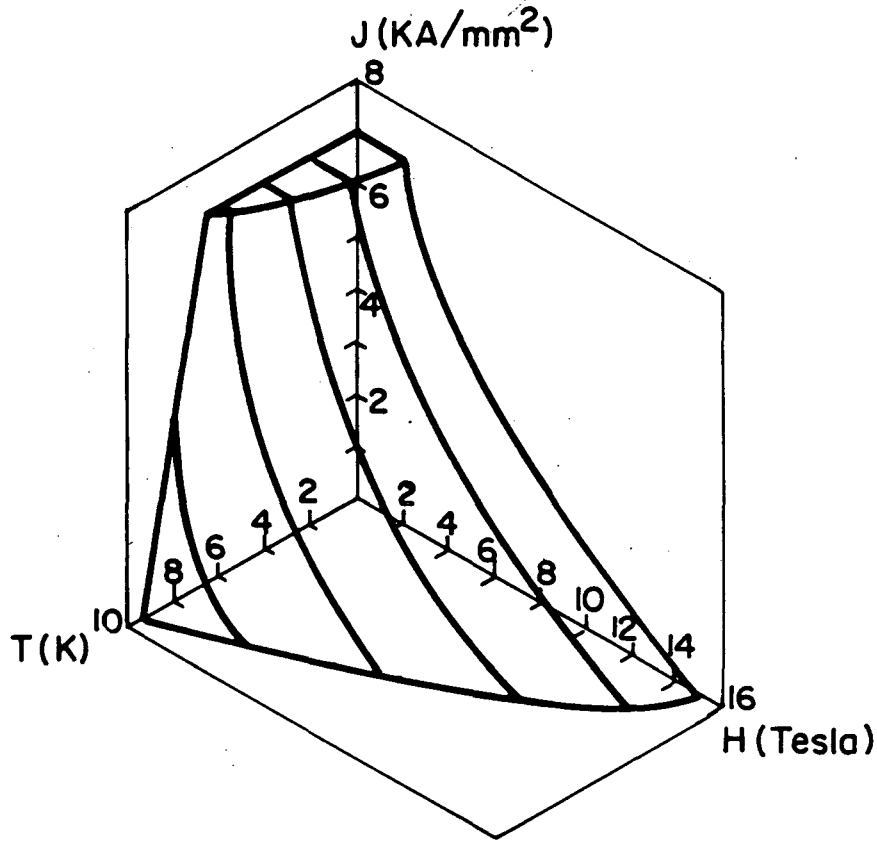

THE CRITICAL SURFACE OF Nb-Ti

XBL 833-5412

Fig. I-1. The critical surface of a typical Nb-Ti superconductor.

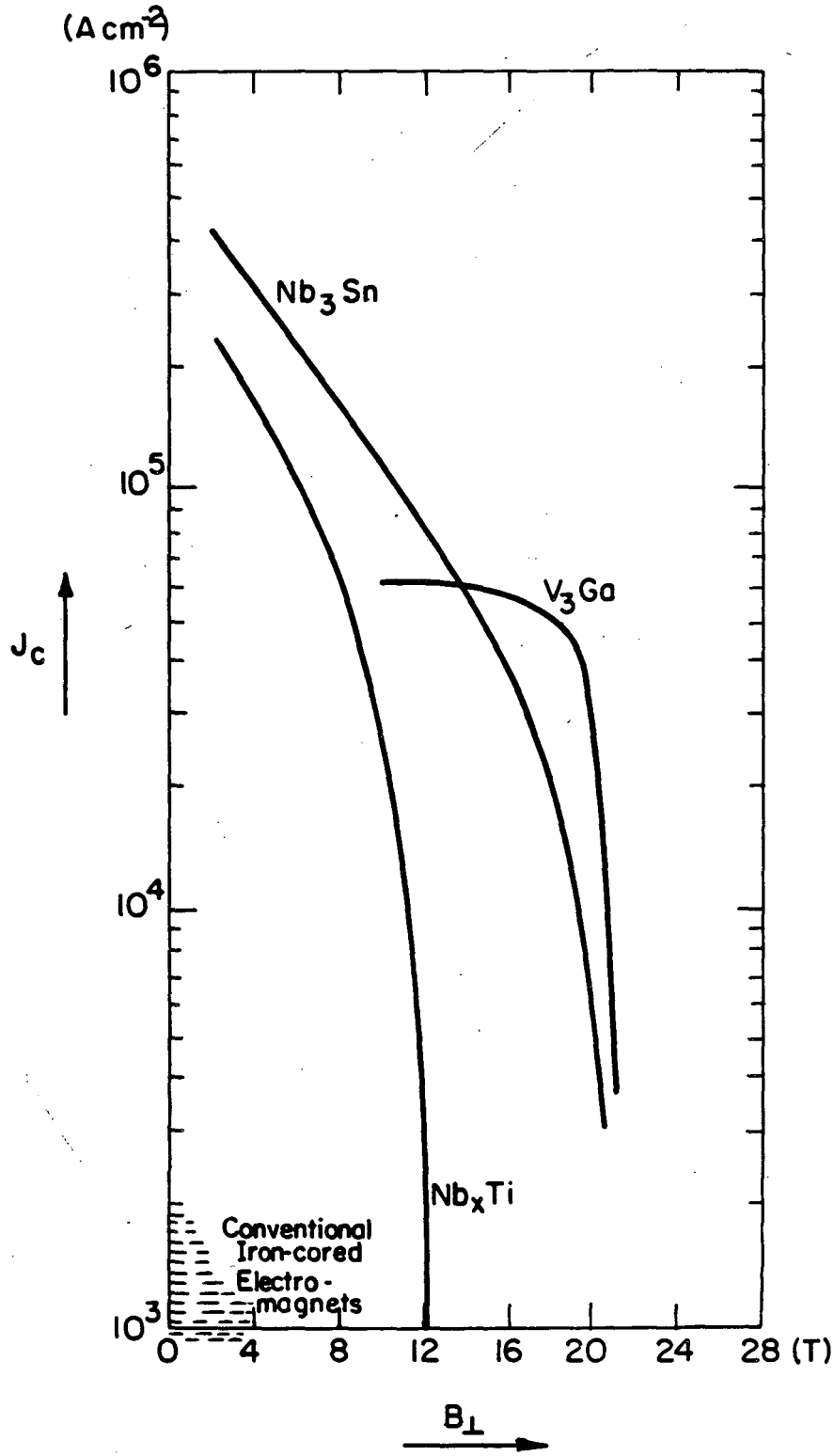

XBL 833-5416

Fig. I-2. The $J_c(H)$ characteristics of commercially available type-II superconductors. Nb_xTi is used in the field ranges up to 8T, Nb_3Sn up to 16T, and V_3Ga in the range of 13-18T. The current density of conventional iron-cored electro-magnets is shown in the shaded area.

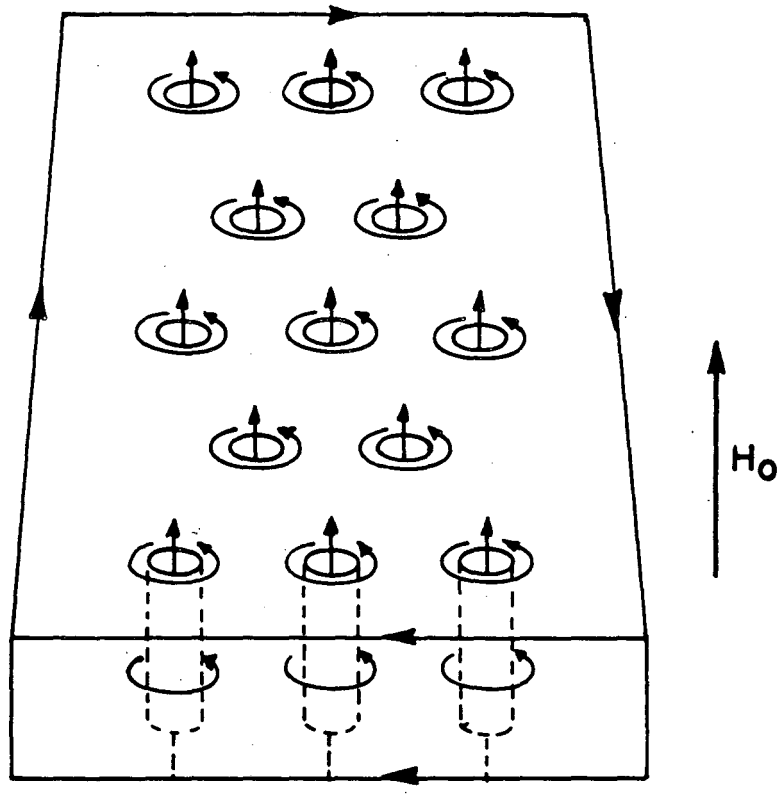

FLUX-LINE-LATTICE OF TYPE-II SUPERCONDUCTOR
IN EXTERNAL FIELD

XBL 833-5413

Fig. II-1. A schematic representation of the flux-line-lattice (FLL) of Type-II superconductor in external field. The direction of supercurrent is shown by arrows.

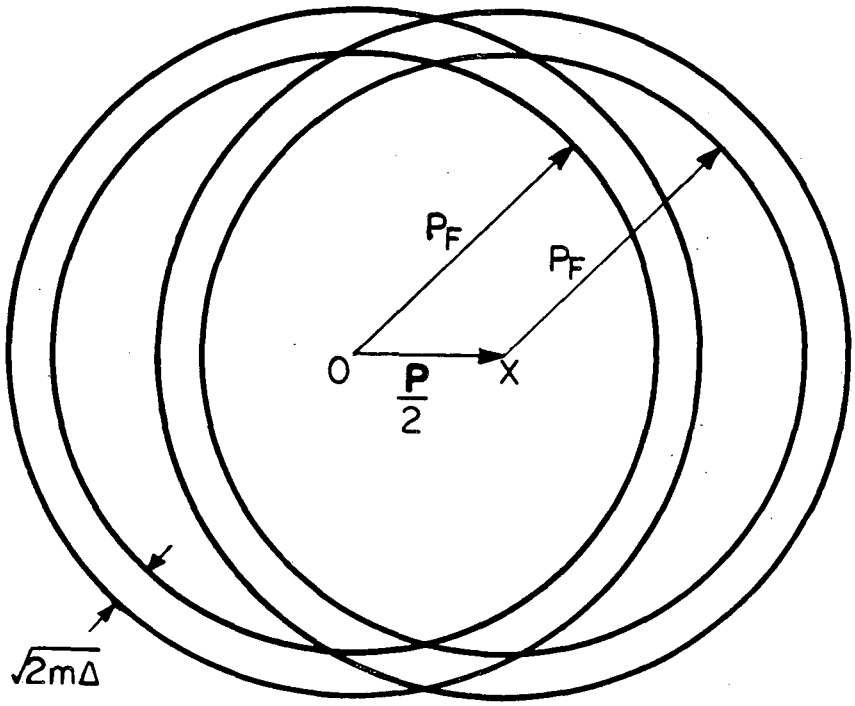

XBL834-5498

Fig. II-2. The Fermi-surface of a superconductor with a net total momentum **P**/2 due to current flow. The shell of superconducting state has the width of $(2m\Delta)^{1/2}$ above the Fermi momentum P_F.

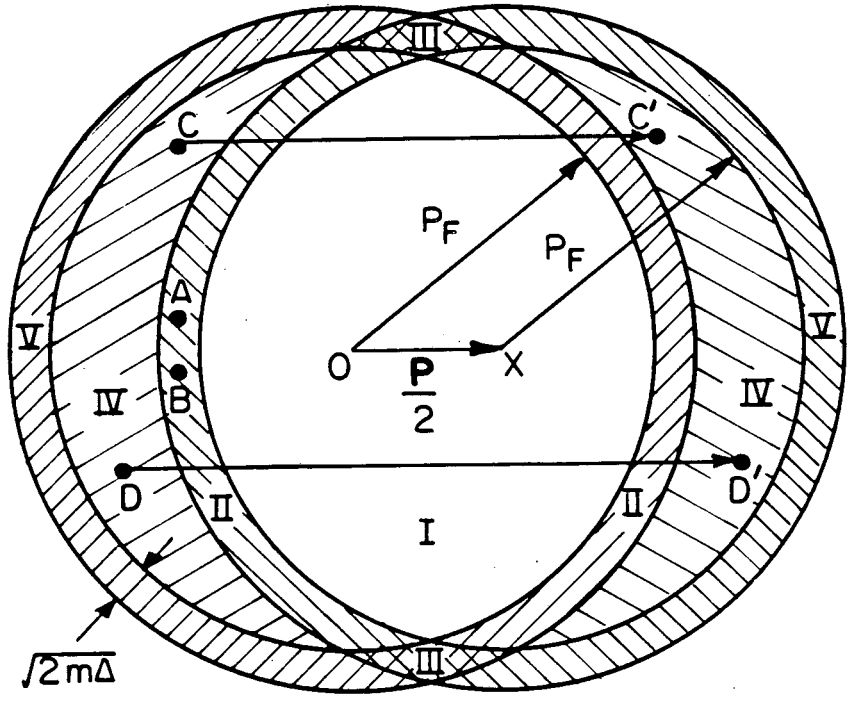

XBL834-5499

Fig. II-3. The calculation of total energy change of a superconductor with an external currentμ potential energy (pairing and depairing of Cooper pairs) remains constant and the net energy increase corresponding to the increase of kinetic energy of regions IV and V.

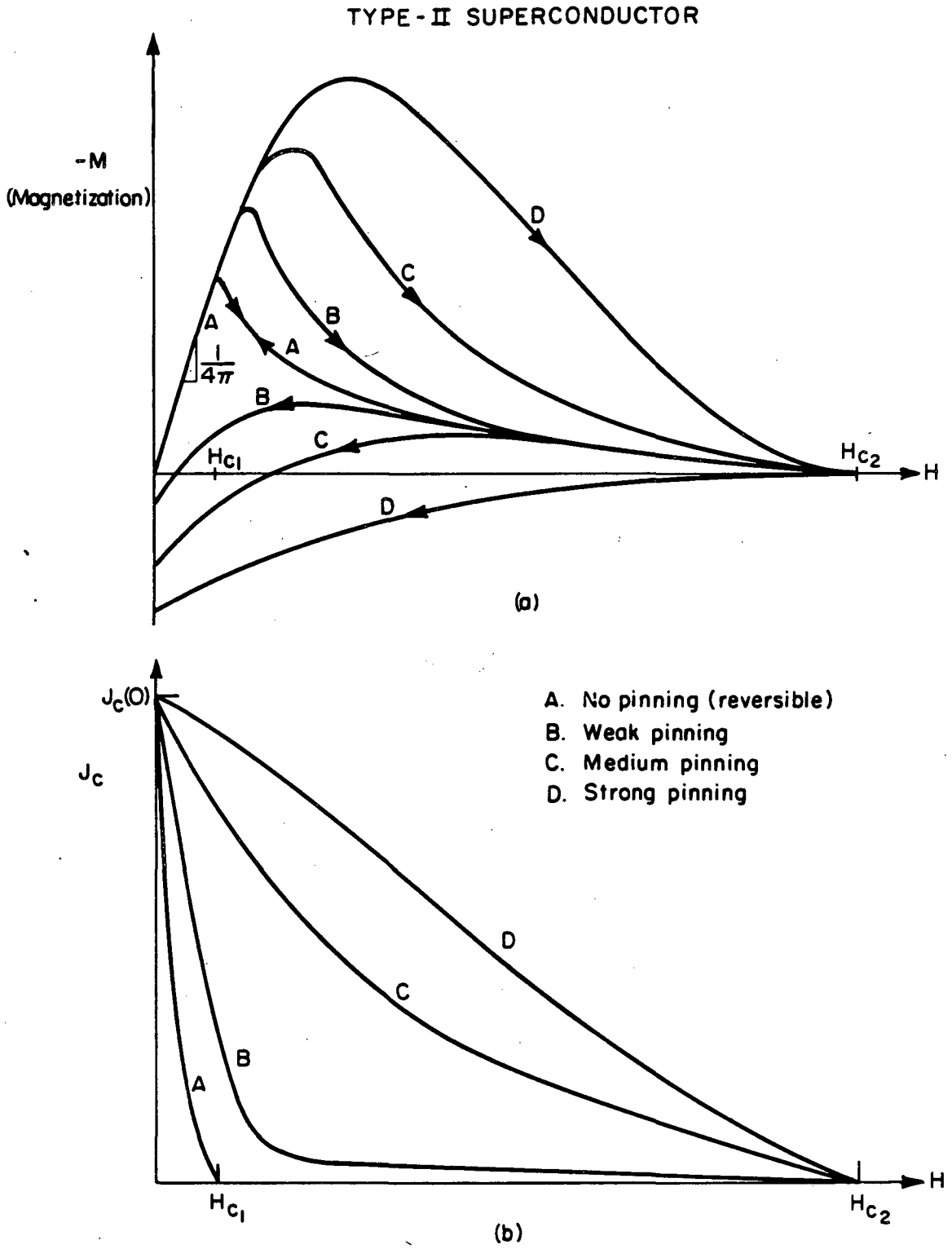

Fig. III-1. The characteristics of (a) magnetization and (b) critical current density, versus applied magnetic field of a Type-II superconductor with different pinning strength.

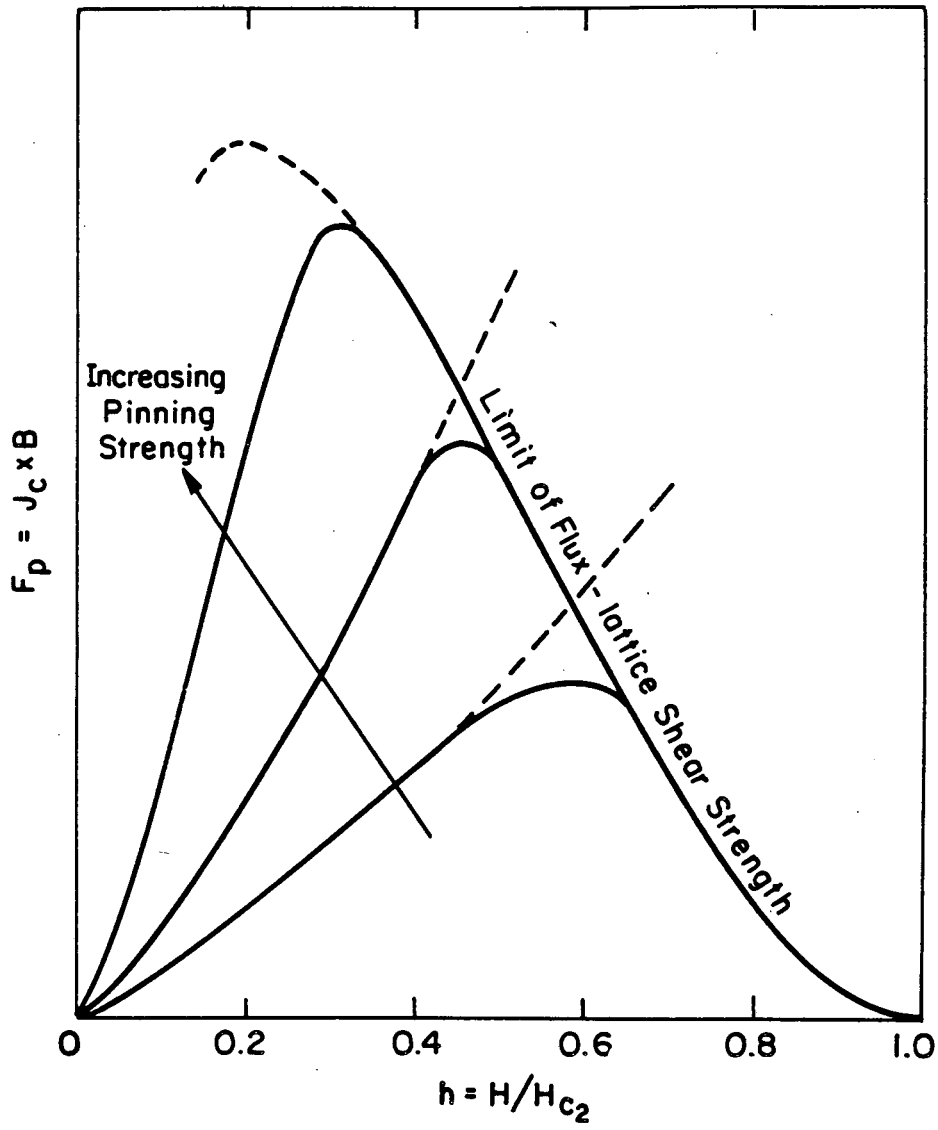

XBL 834-5541

Fig. III-2. Schematic representation of Kramer's flux-shear model. The flux-lattice shear strength decreases with increasing external reduced field as $h^{1/2}(1 - h)^2$. The flux-pinning interaction initially increases with h, at a rate depending upon the detailks of the pinning mechanism. The actual Lorentz force curve is the lower combination of these two curves. As the pinning strength is increased, the lattice shear

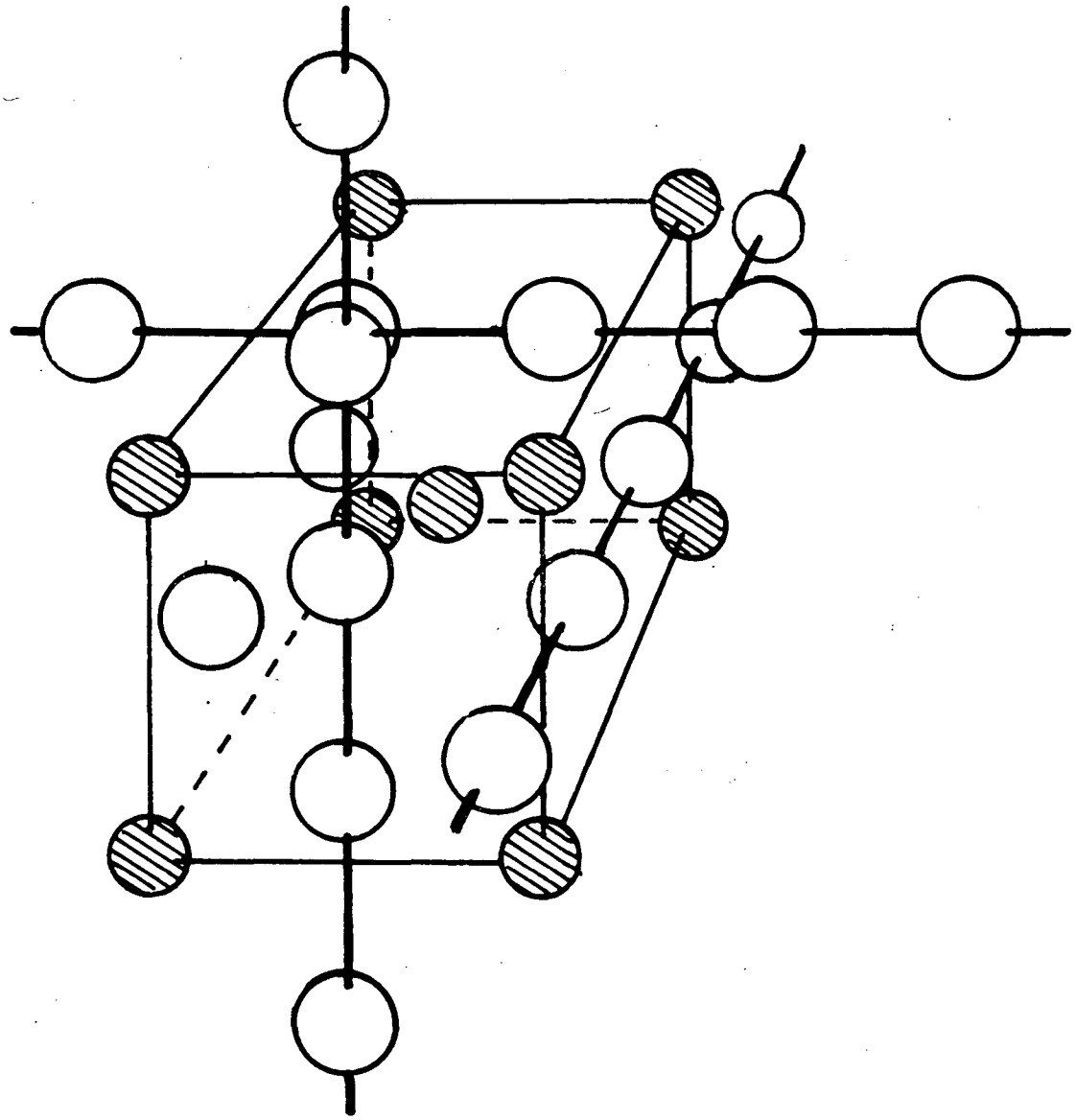

XBL 833-5437

Fig. IV-1. The crystal structure of A15 phase. Three orthogonal linear chains of transition elements which lie on the surfaces of conventional unit cell were shown by solid lines.

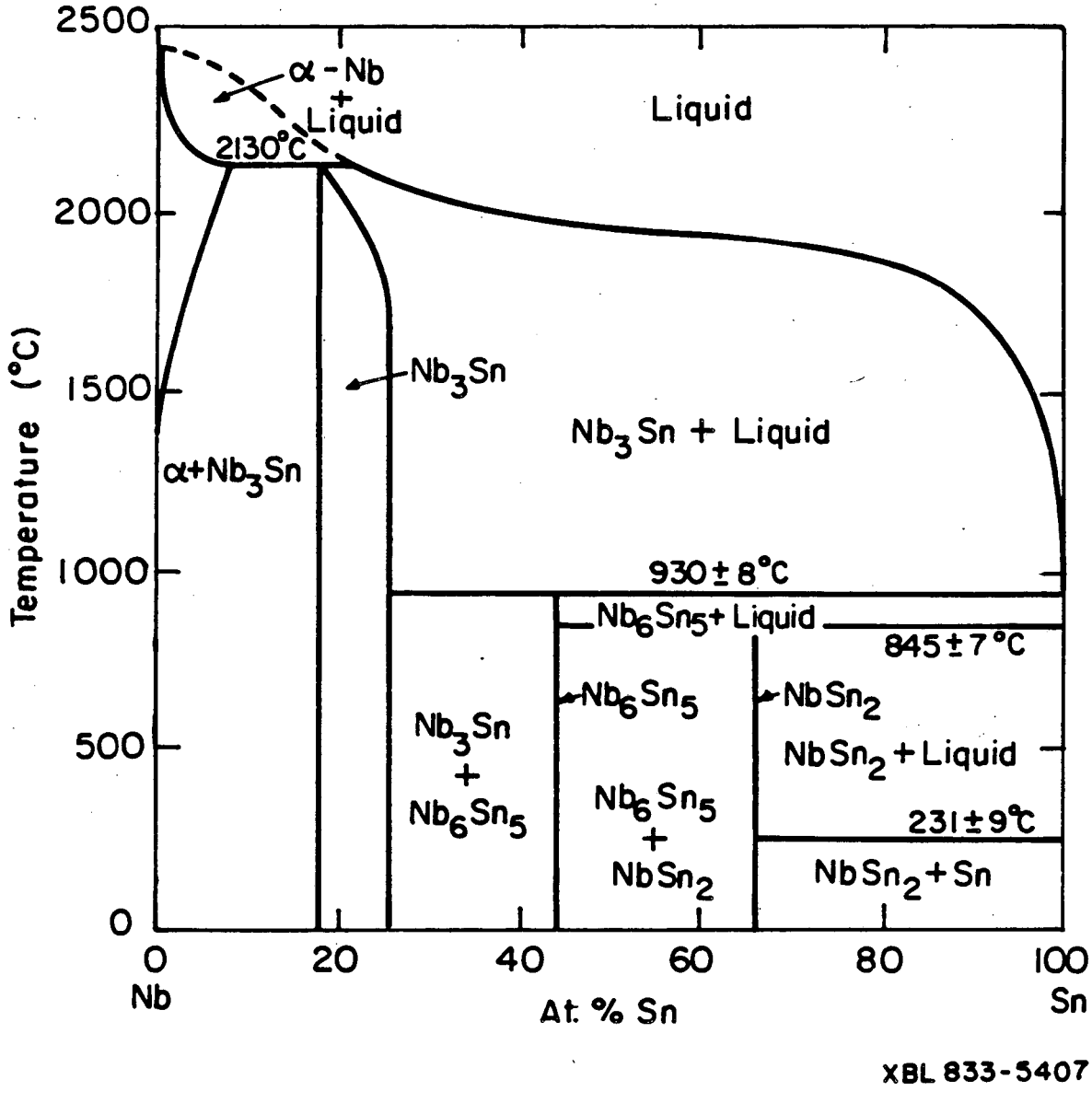

Fig. IV-2. The equilibrium Nb-Sn phase diagram.

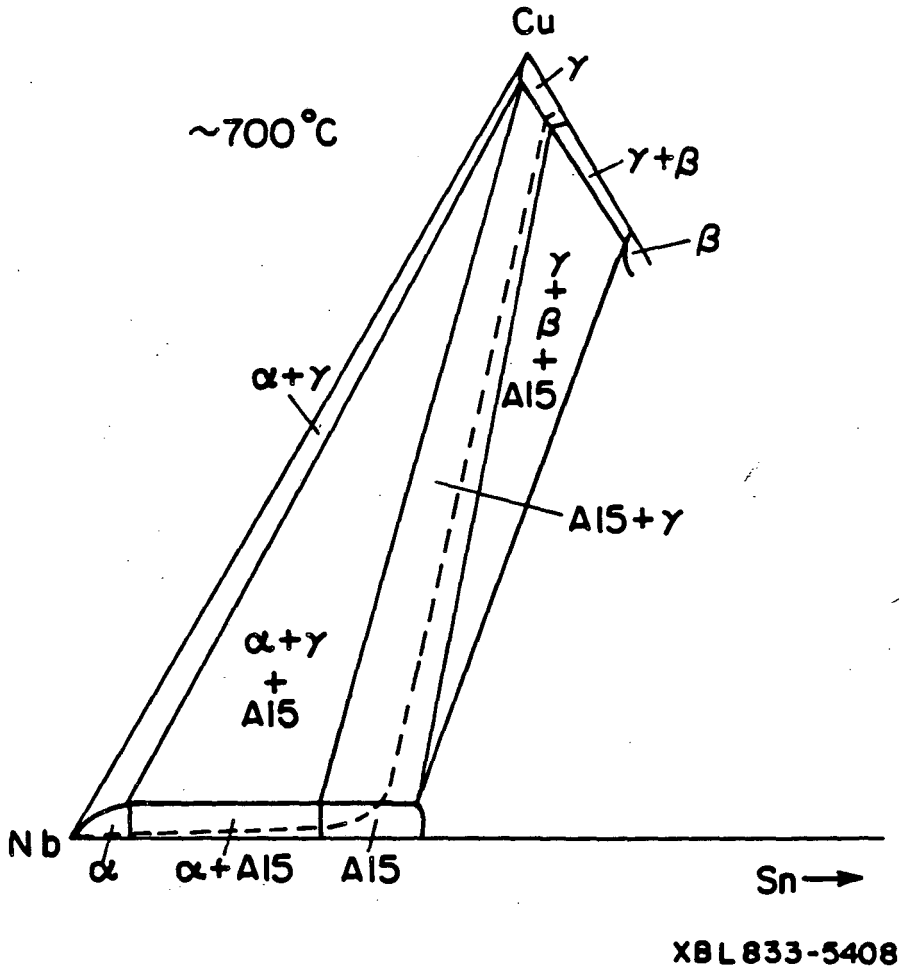

Fig. IV-3. The schematic representation of a portion of Nb-Cu-Sn ternary Gibbs triangle at 700°C. The diffusion path of bronze-process is shown by dotted line.

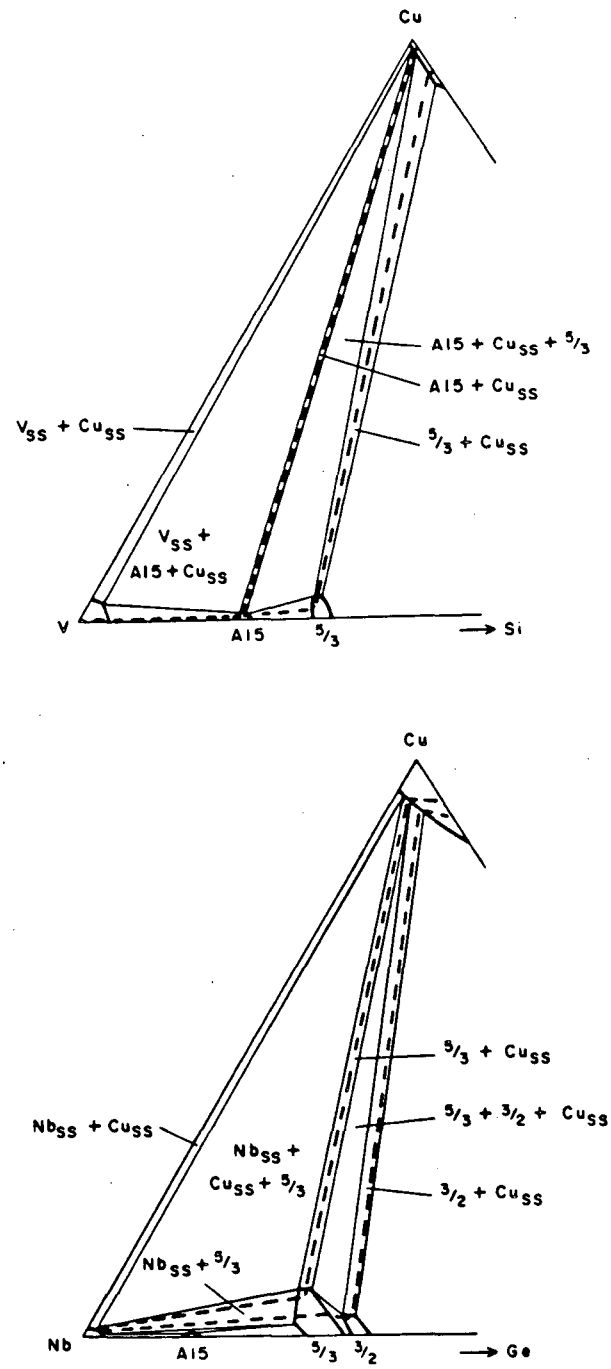

XBL 834-9016

Fig. IV-4. The schematic phase diagrams of (a) V-Cu-Si, and (b) Nb-Cu-Ge ternary Gibbs triangle at 700°C. The diffusion paths of two bronze compositions to V (Nb) were shown by dotted lines.

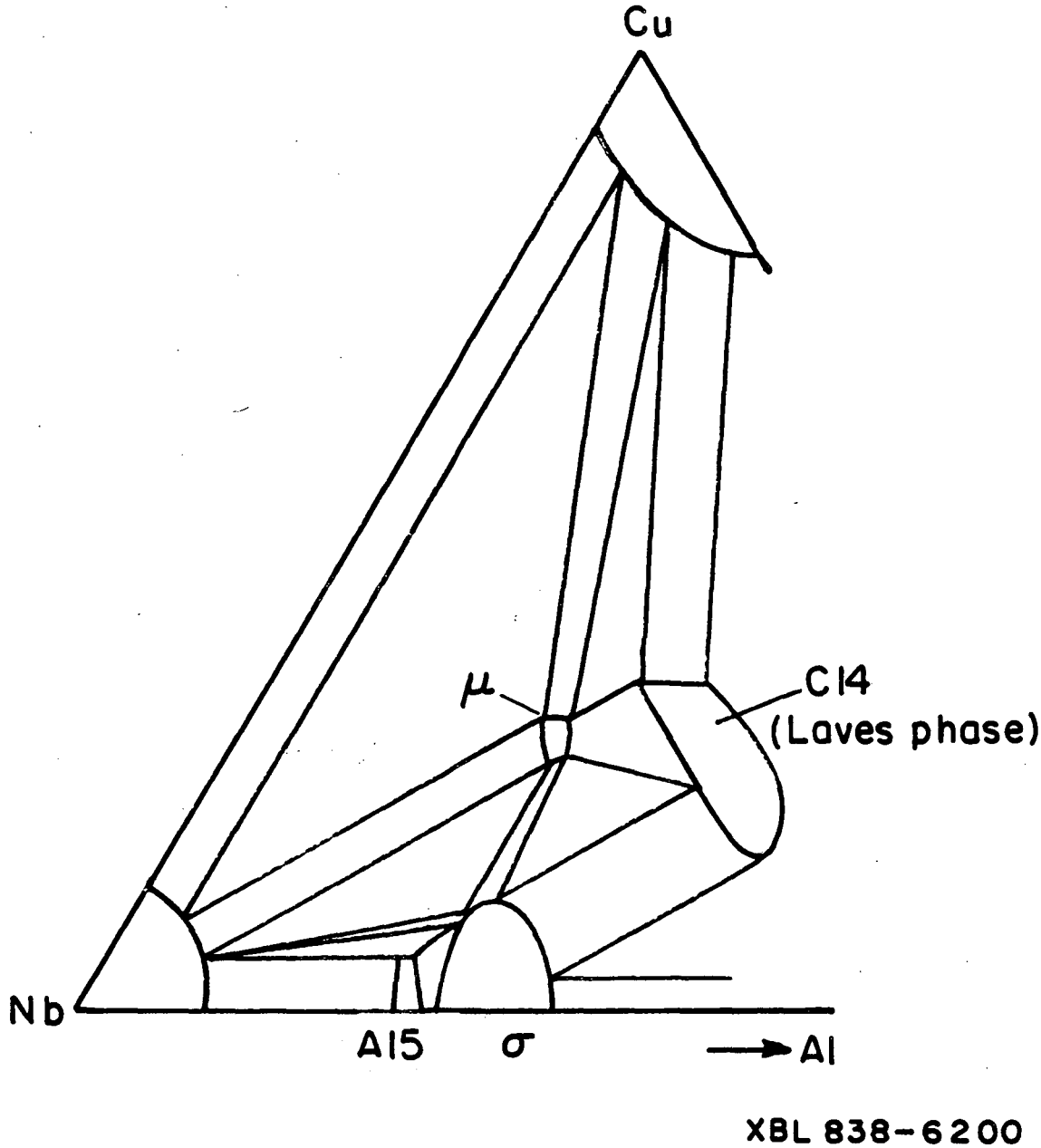

Fig. IV-5. The equilibrium isotherm at 1000°C of the Nb-Cu-Al phase diagram.

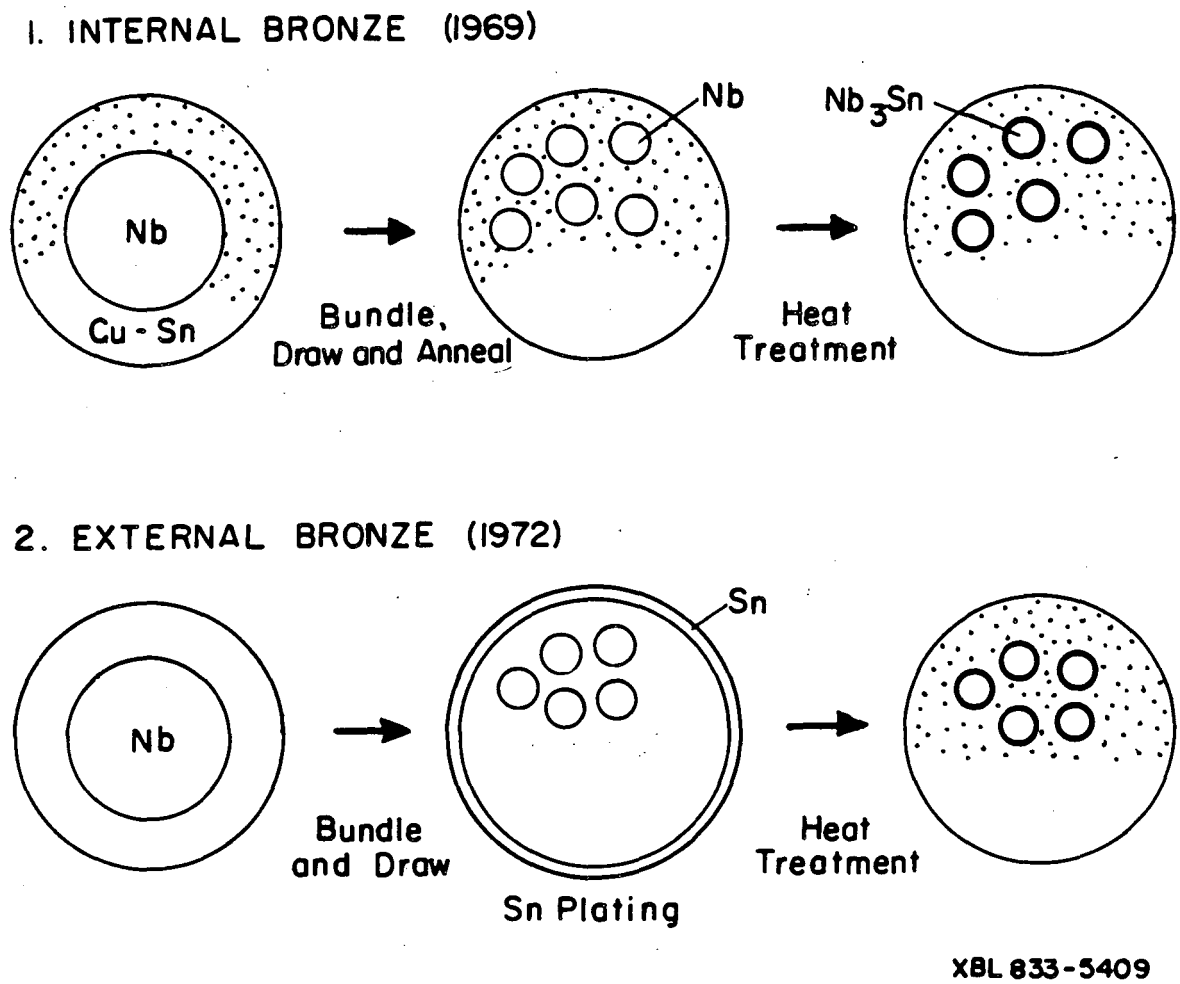

Fig. IV-6. Schematic diagrams for (1) the internal bronze and (2) the external bronze proceses for multifilamentary Nb_3Sn wires.

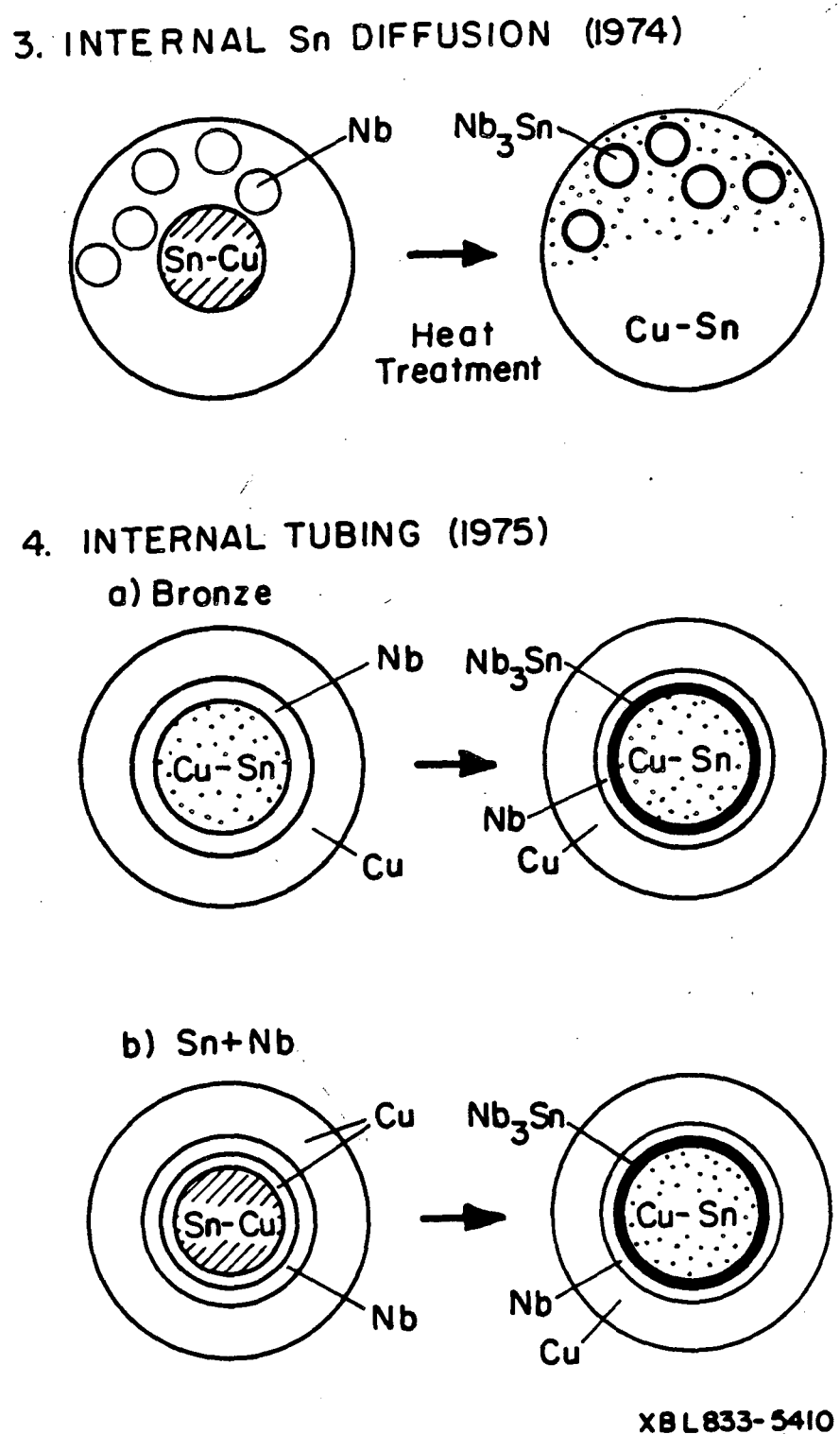

Fig. IV-7. Schematic diagrams for modified bronze processes; (3) the internal tin diffusion, (4a) the internal bronze tubing, and (4b) the internal tin-Nb tubing processes. The dotted and the shaded areas represent the bronze and Sn-Cu alloys, respectively.

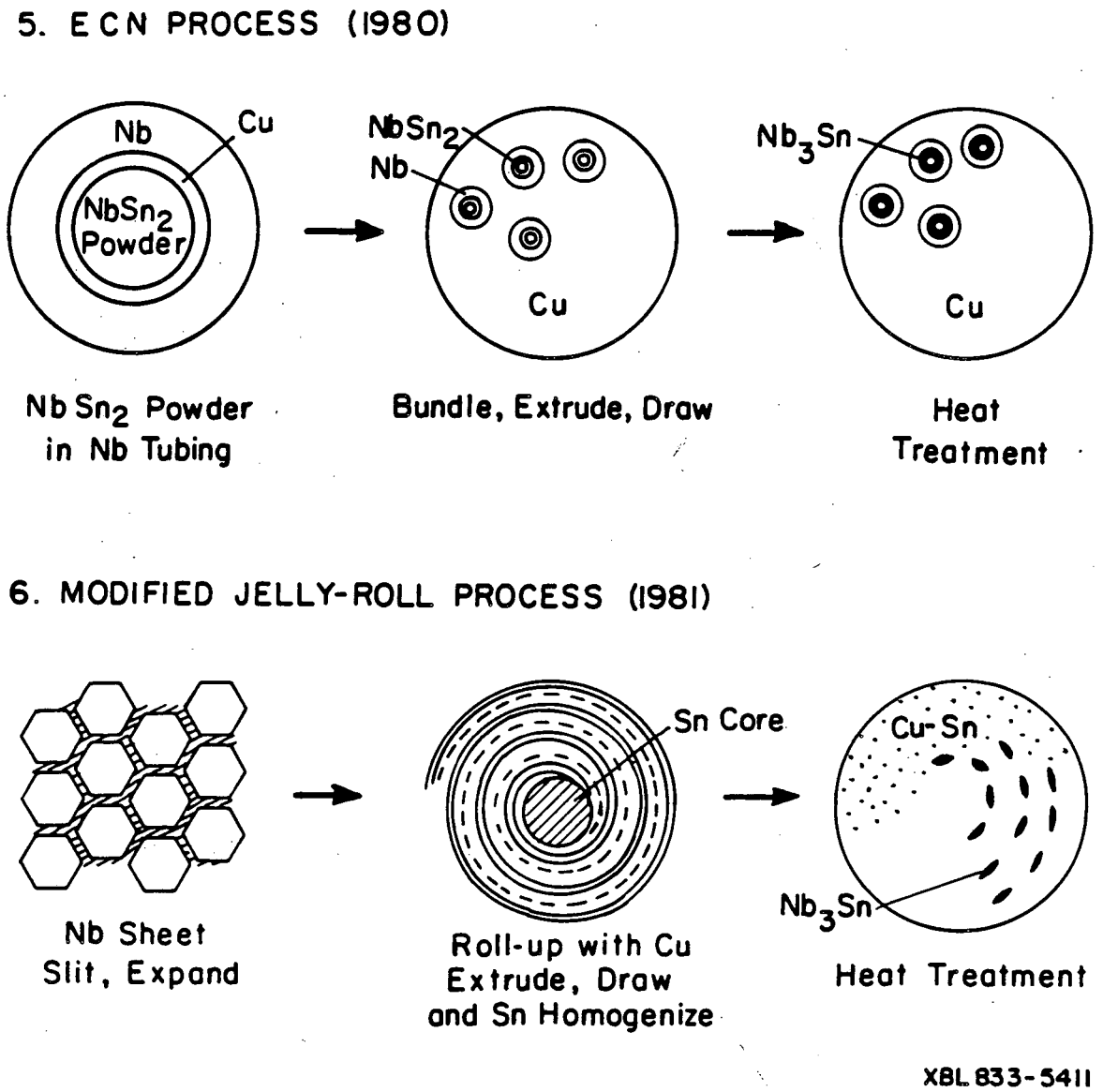

Fig. IV-8. Schematic diagrams for modification of bronze processes: (5) ECN powder process, and (6) modified Jelly-Roll process.

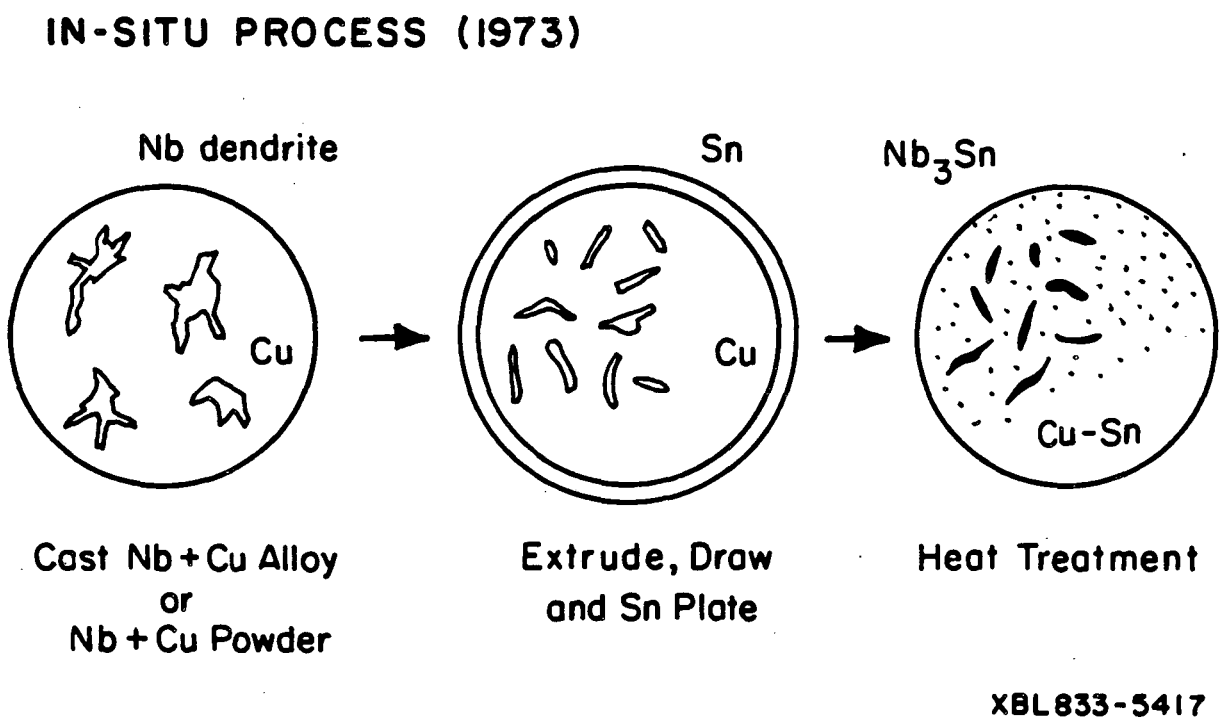

Fig. IV-9. Schematic diagram of the in situ process.

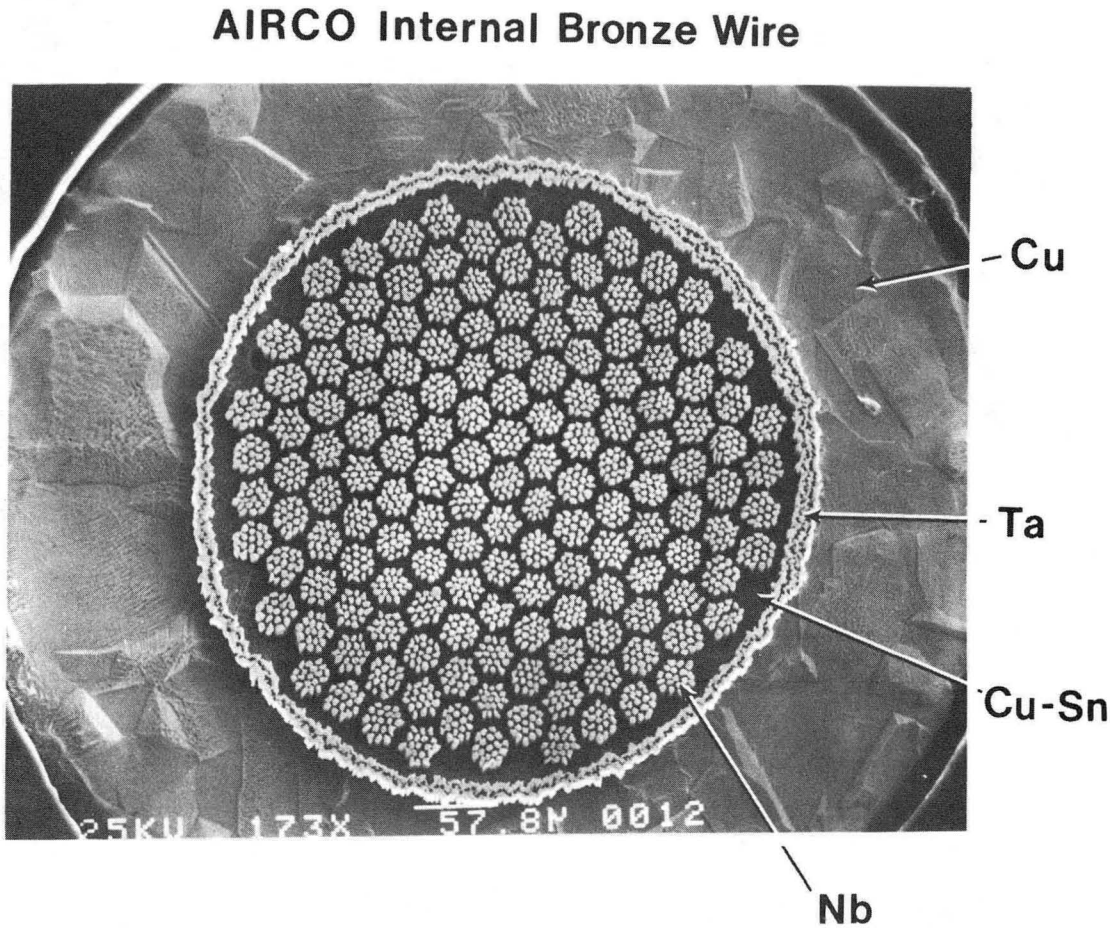

XBB 831-546A

Fig. V-1. Scanning electron micrograph showing the overall configuration of bronze-processed multifilamentary Nb_3Sn wire used in this study.

6.7 SN

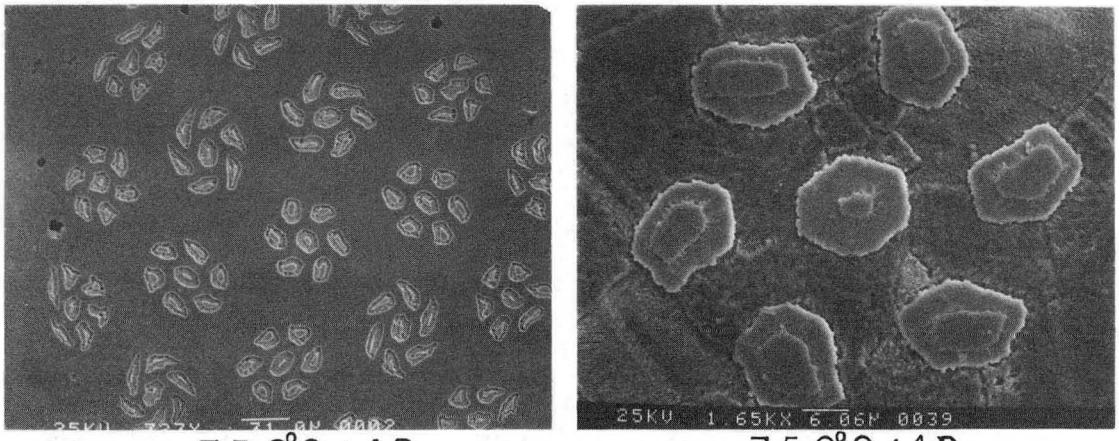

730°C/4D 750°C/4D

XBB 820-10448

Fig. V-2. Sections of two partially reacted laboratory scale bronze-processed Nb_3Sn multifilamentary wire.

V– 15.6% Ga, 75% Def., 700°C/ 1 D

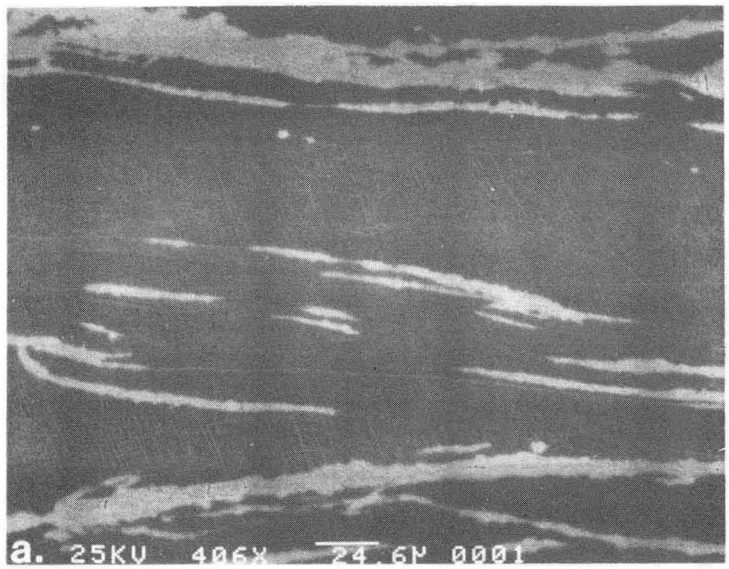

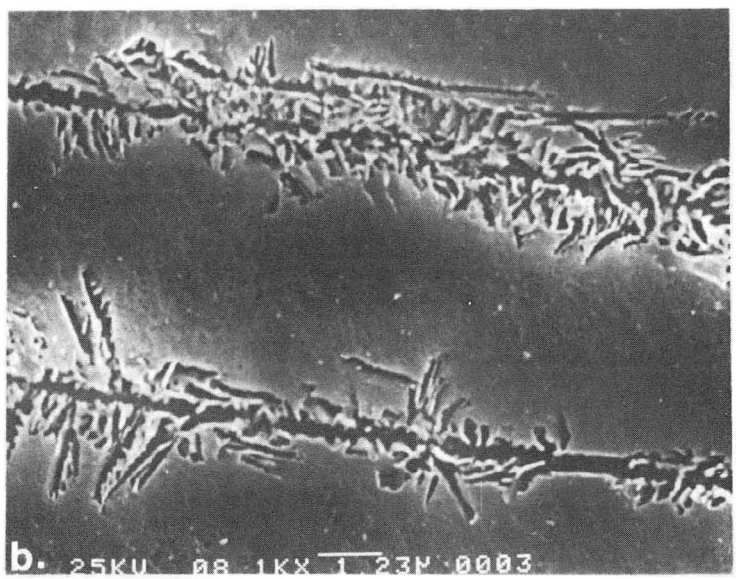

XBB 836-5391

Fig. V-3. Scanning electron micrographs of etched section of V-15.6 at.% Ga deformed 75% and aged at 700°C for 1 day.

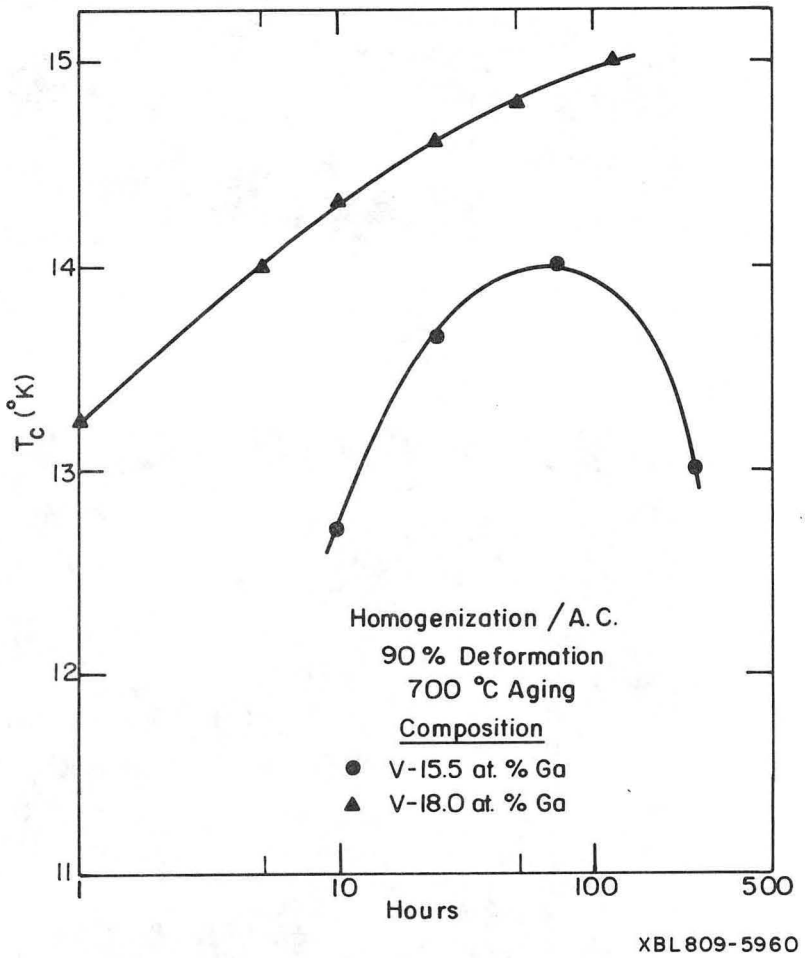

Fig. VI-1. Critical temperature versus aging time for V-15.5 at.% Ga and V-18 at.% Ga samples.

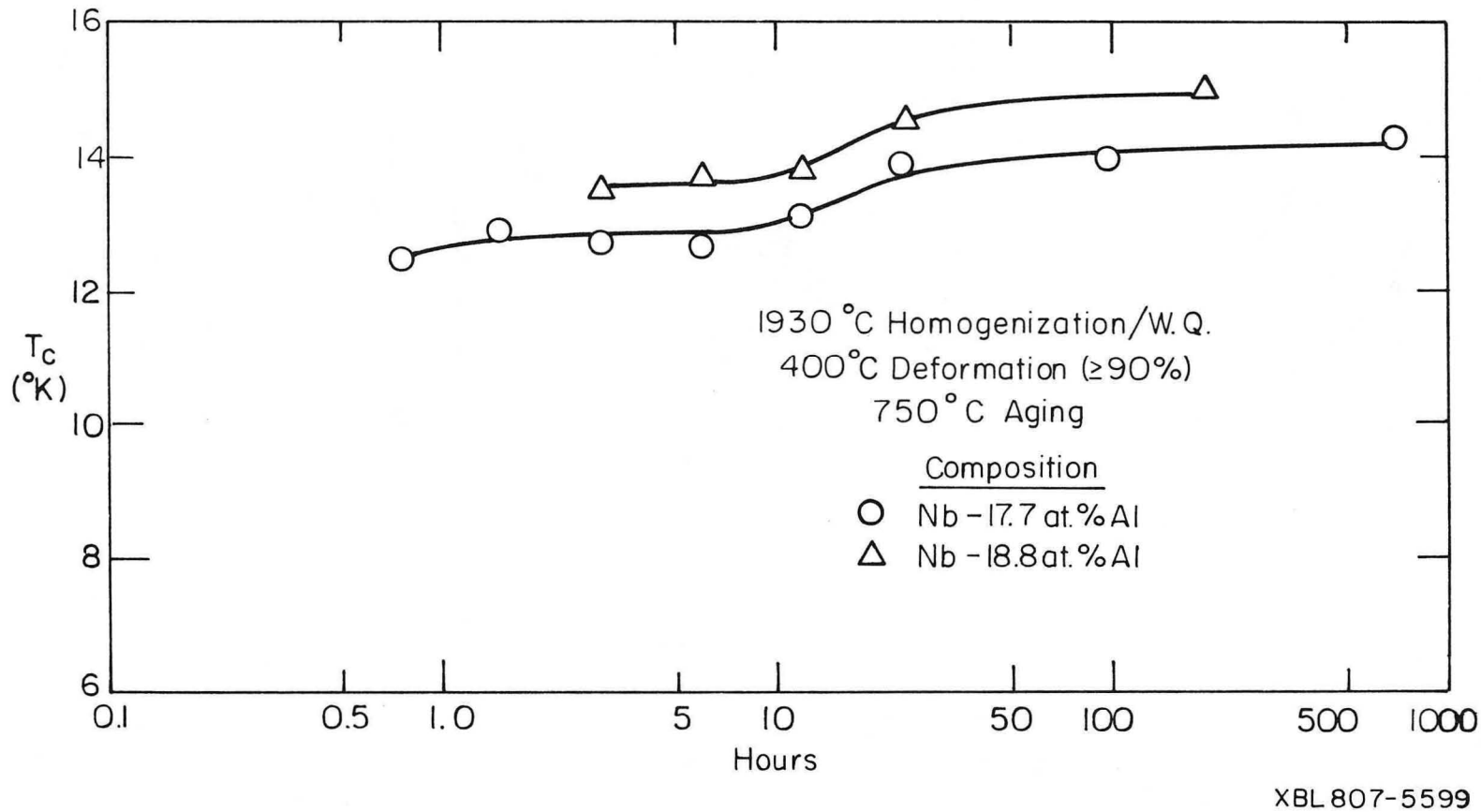

Fig. VI-2. Critical temperature versus aging time for Nb-17.7 at.% Al and Nb-18.8 at.% Al specimens.

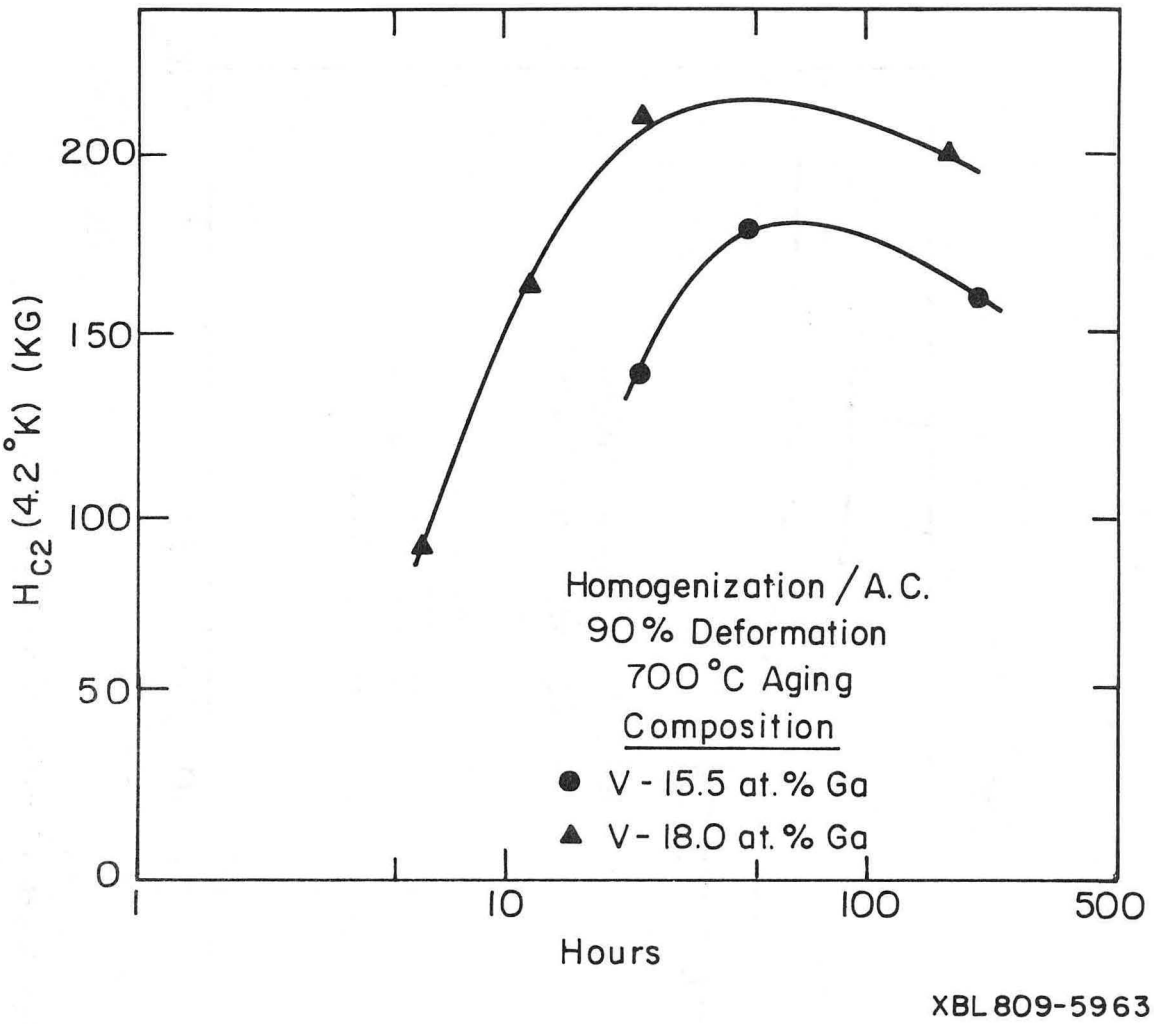

Fig. VI-3. Critical field at 4.2K versus aging time for V-15.5 at.% Ga and V-18 at.% Ga samples.

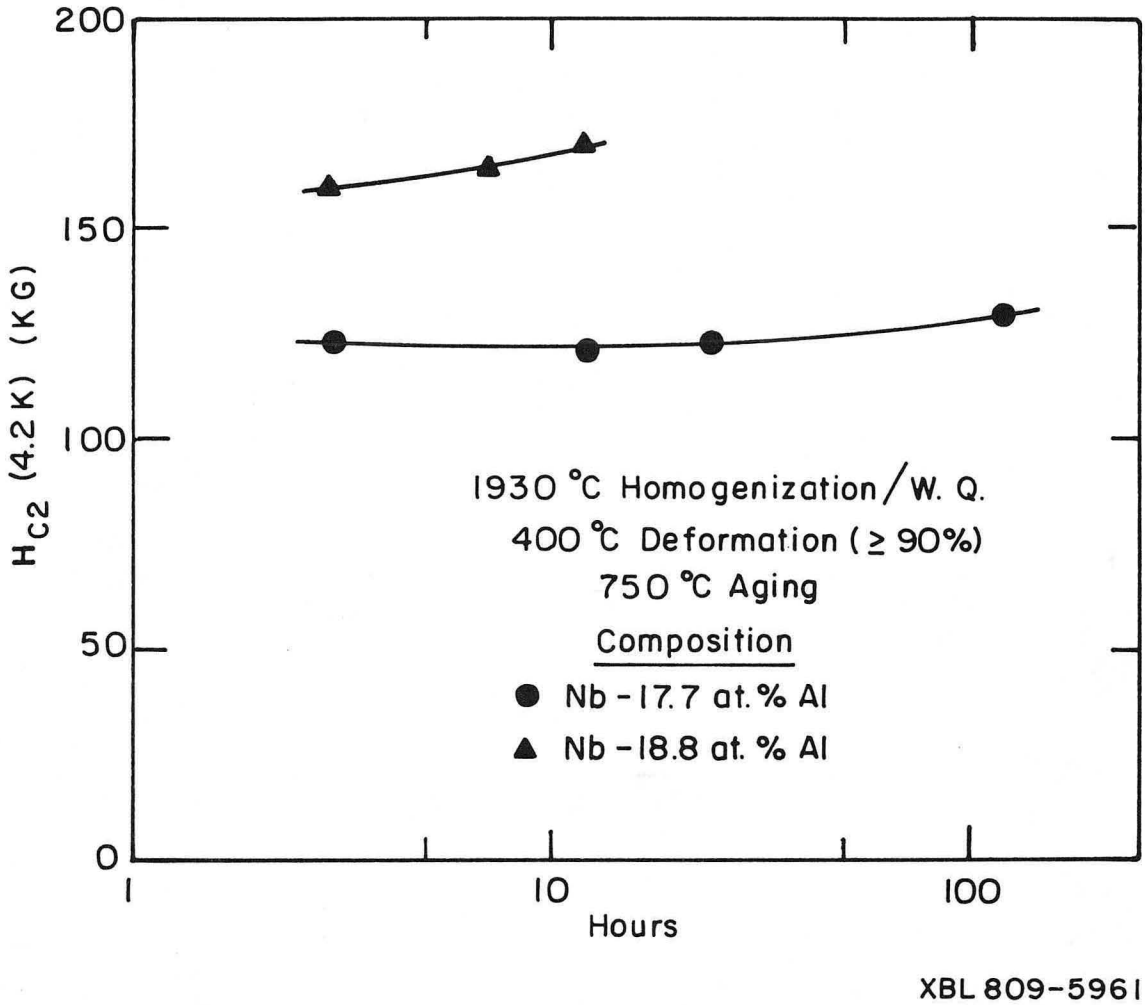

Fig. VI-4. Critical field at 4.2K versus aging time for Nb-17.7 at.% Al and Nb-18.8 at.% Al specimens.

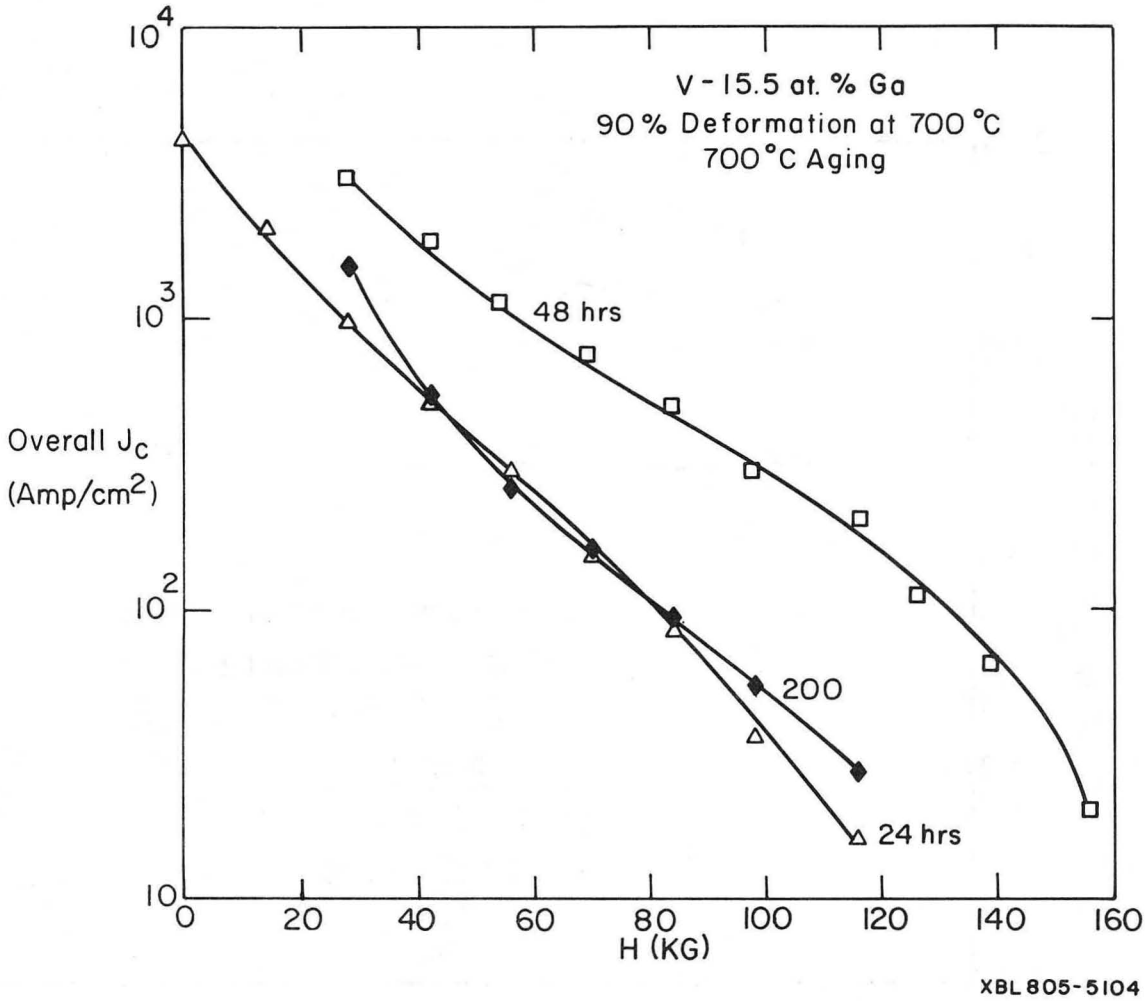

Fig. VI-5. Critical current versus applied magnetic field for V-15.5 at.% Ga samples with different aging times.

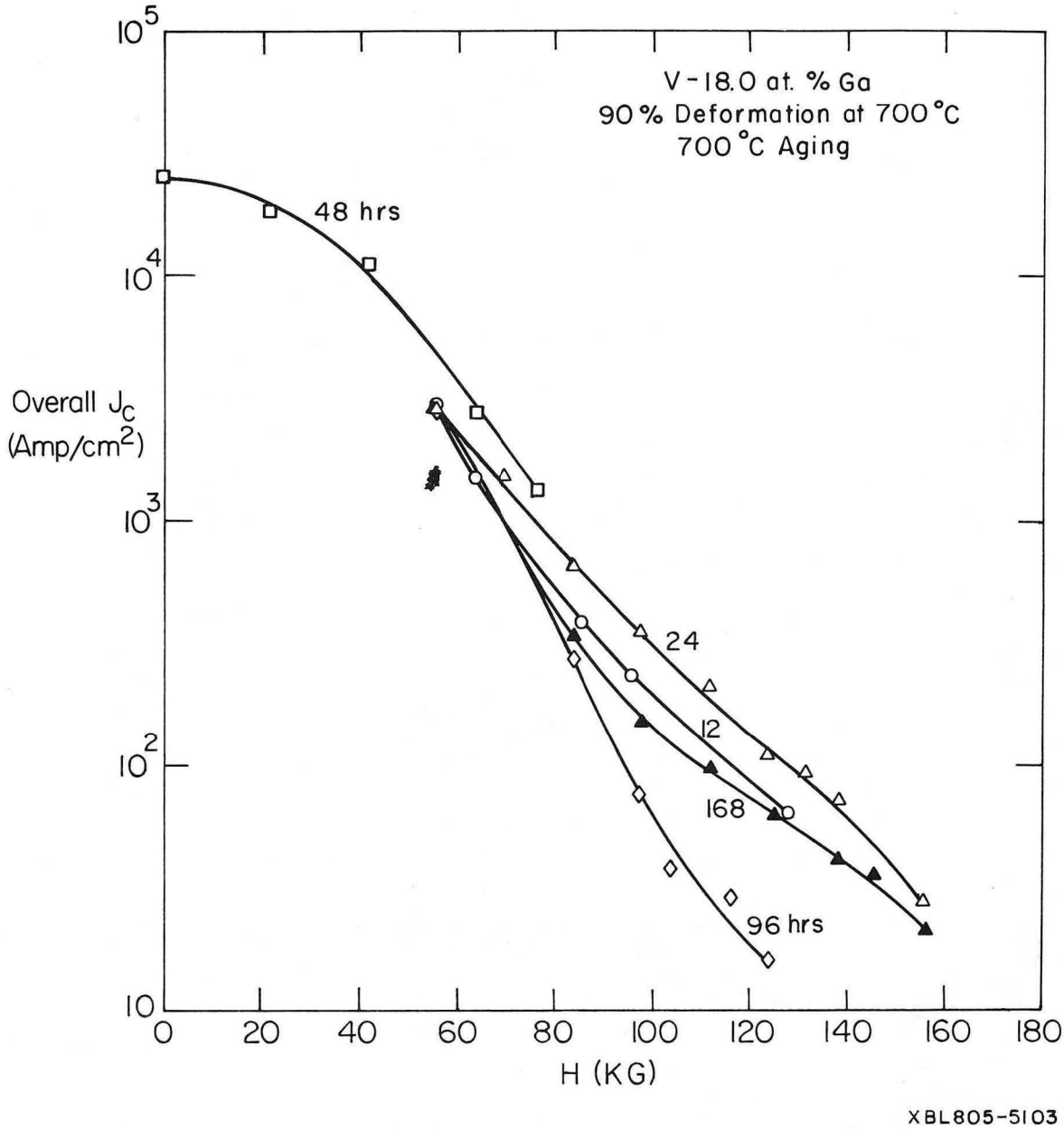

Fig. VI-6. Critical current characteristics, $J_c(H)$, of V-18.0 at.% Ga with different aging times.

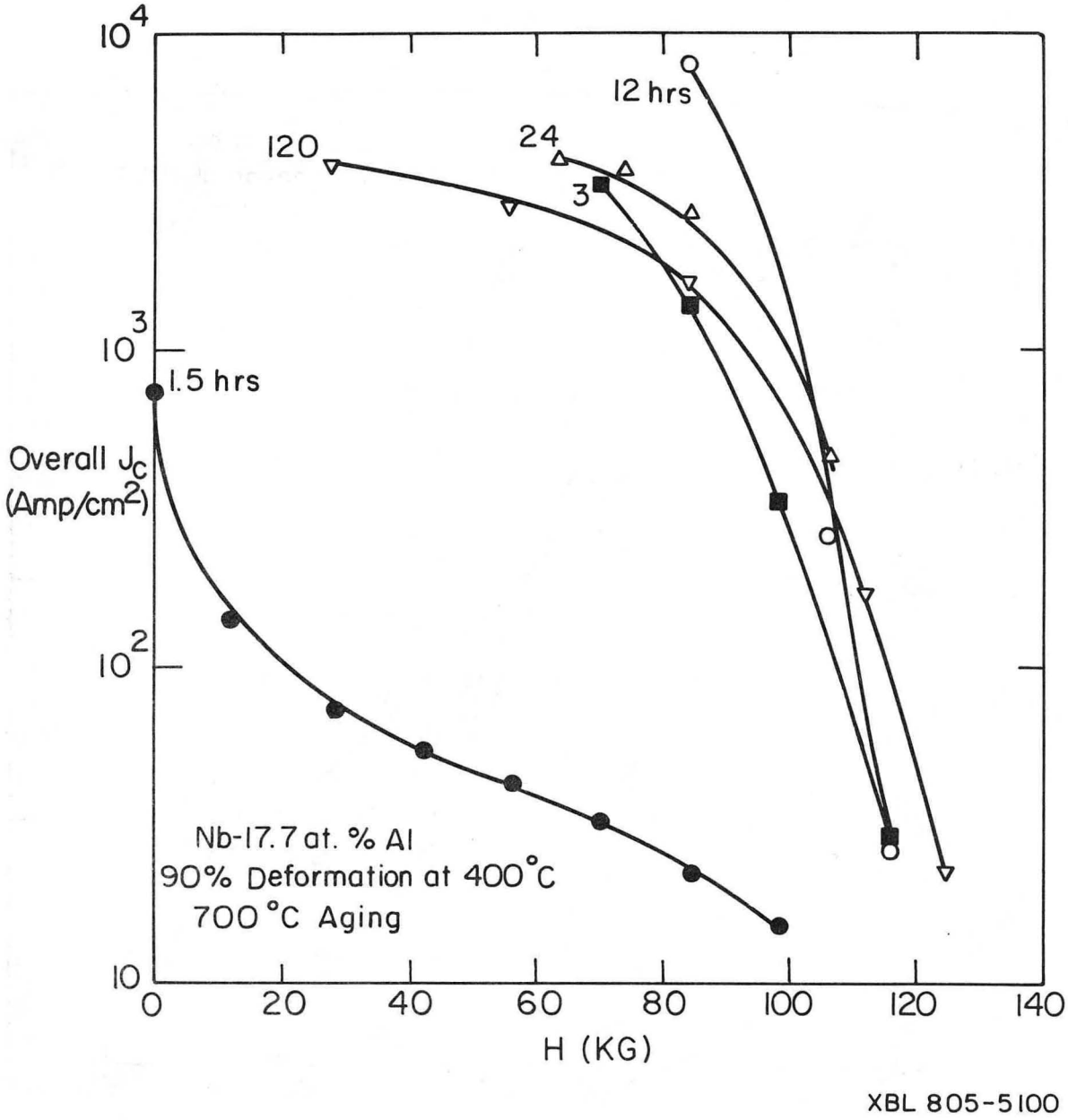

Fig. VI-7. Critical current characteristics, $J_c(H)$, of Nb-17.7 at.% Al with different aging times.

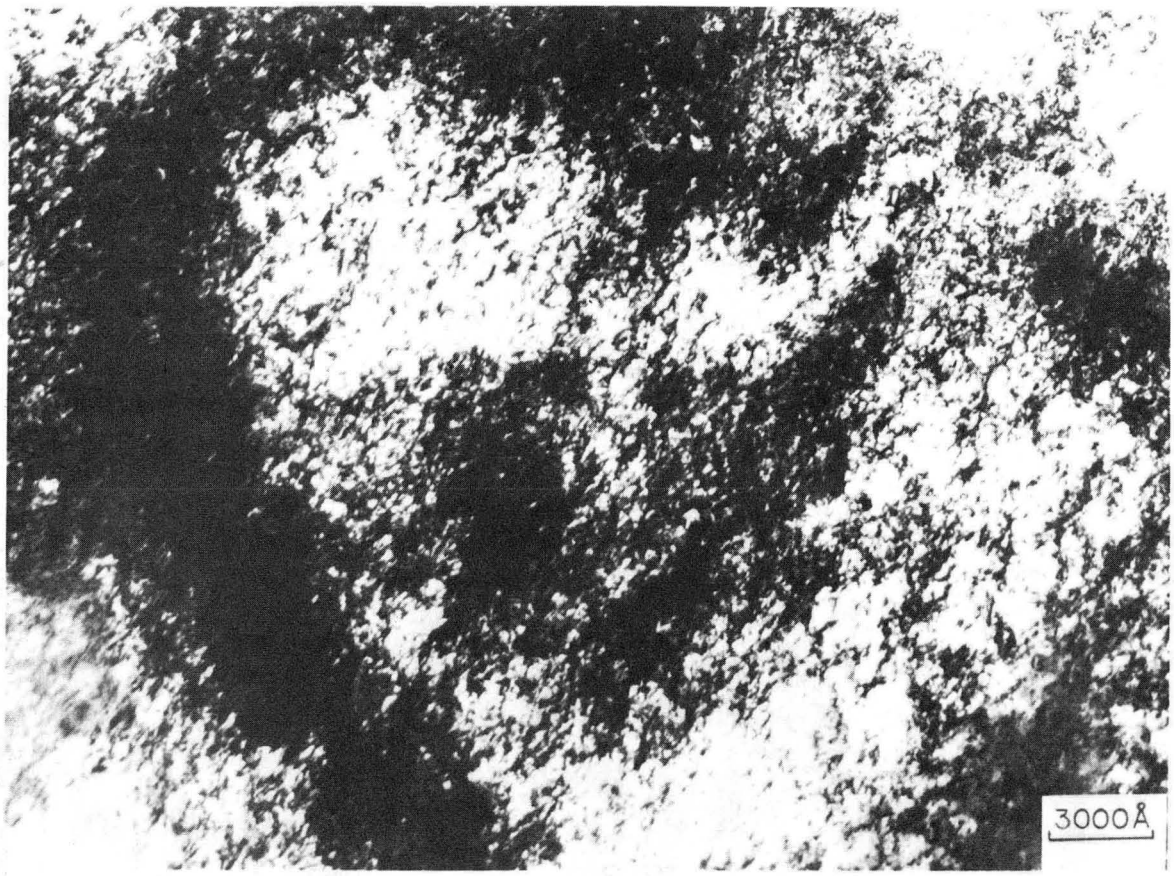

XBB 800-13513

Fig. VI-8. Transmission electron micrograph (TEM) of as-deformed V-15.6 at.% Ga specimen.

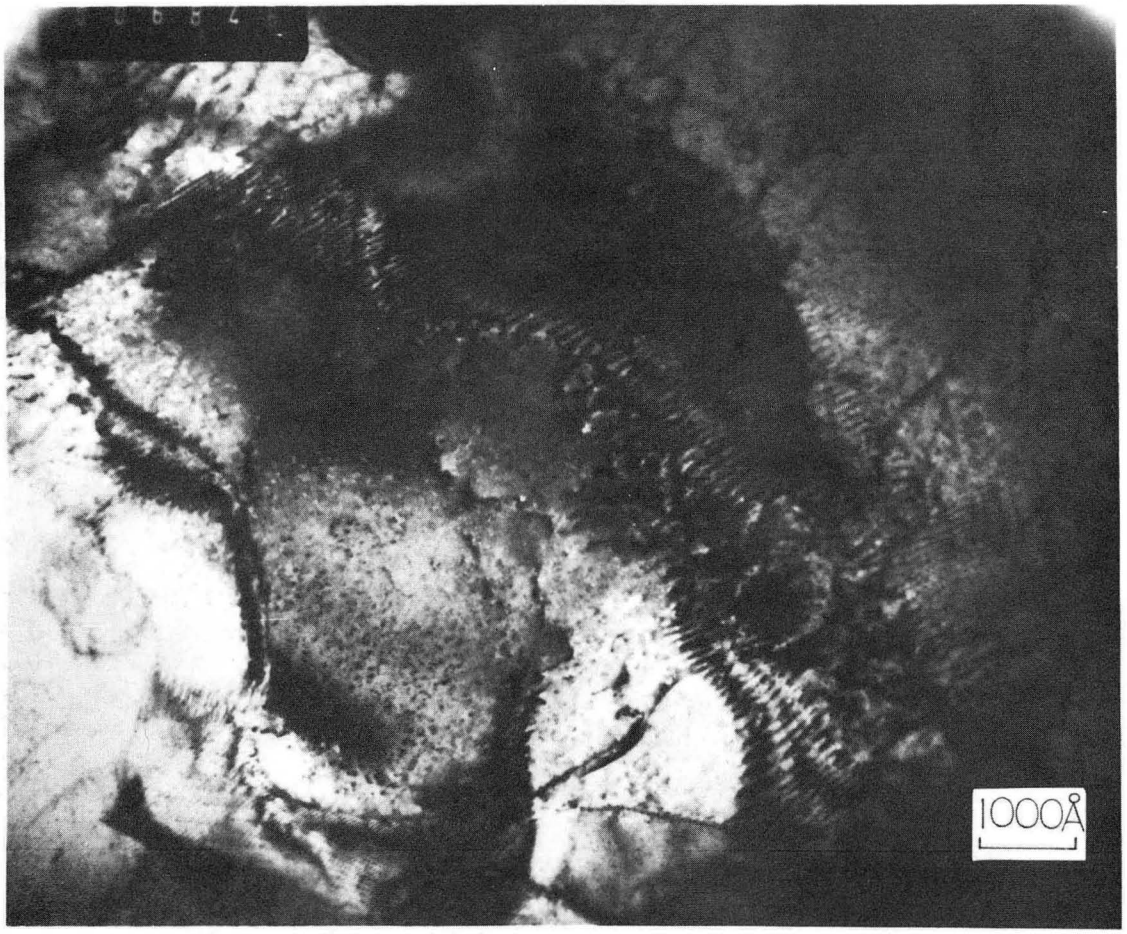

XBB 823-2681

Fig. VI-9. TEM micrograph of dislocation cell wall structure of V-15.6 at.% Ga sample aged at 700°C for 1 day.

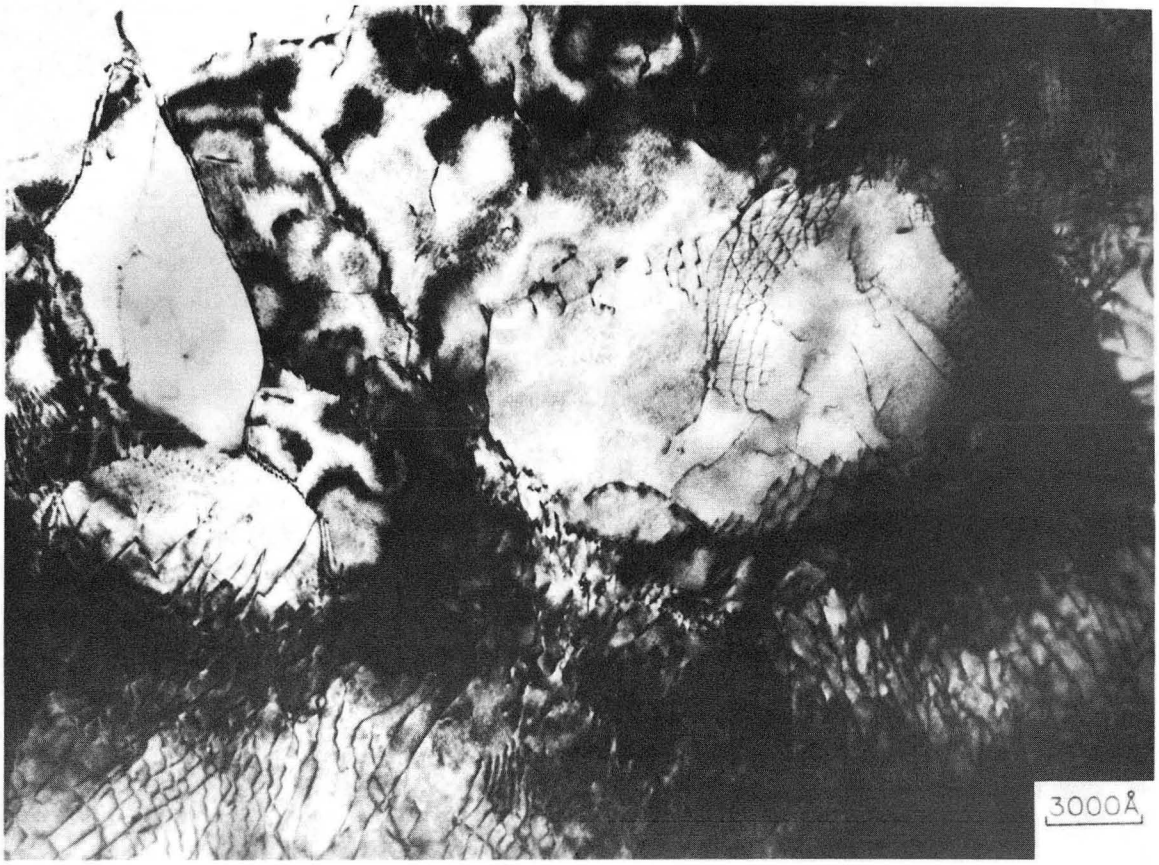

XBB 800-13511

Fig. VI-10. TEM micrograph of dislocation cell wall structure of V-15.6 at.% Ga sample aged at 700°C for 2 days.

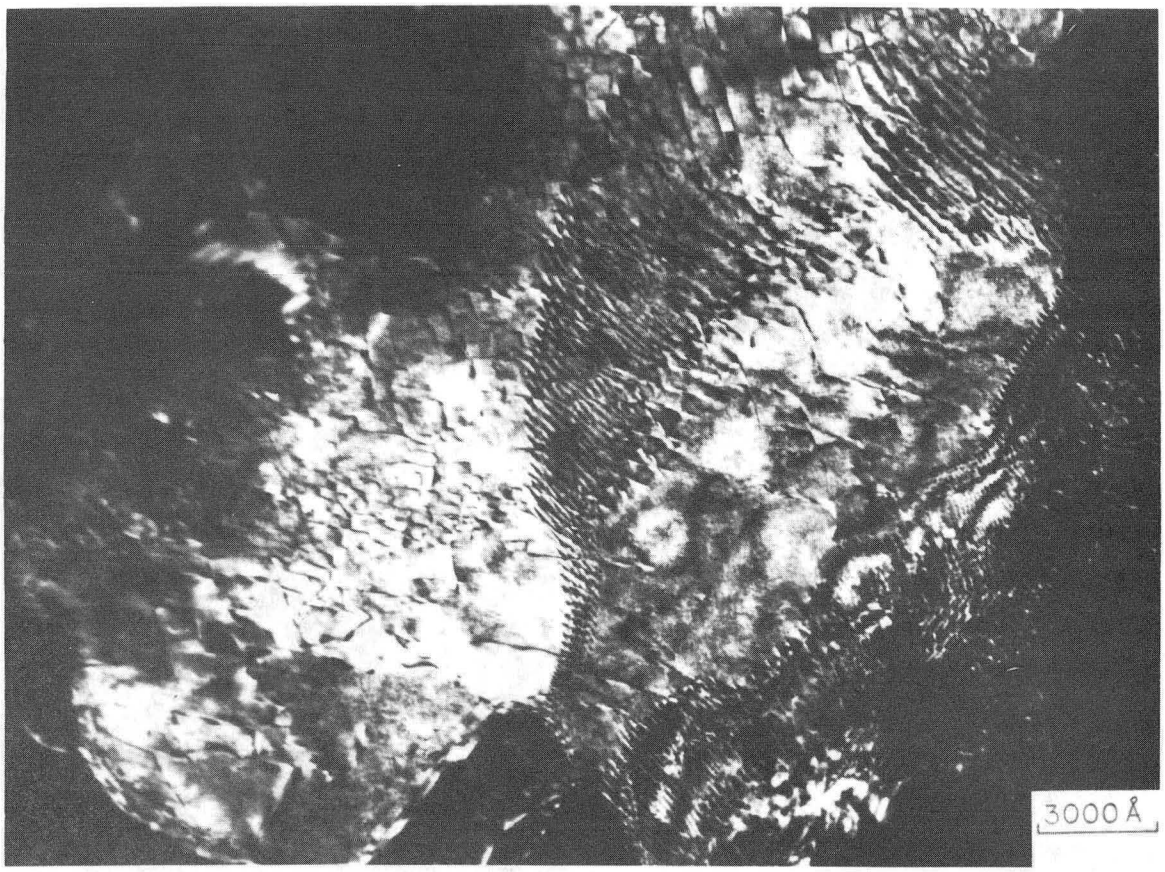

XBB 800-13516

Fig. VI-11. TEM dark-field micrograph of dislocation cell wall structure of V-18 at.% Ga sample aged at 700°C for 1 day.

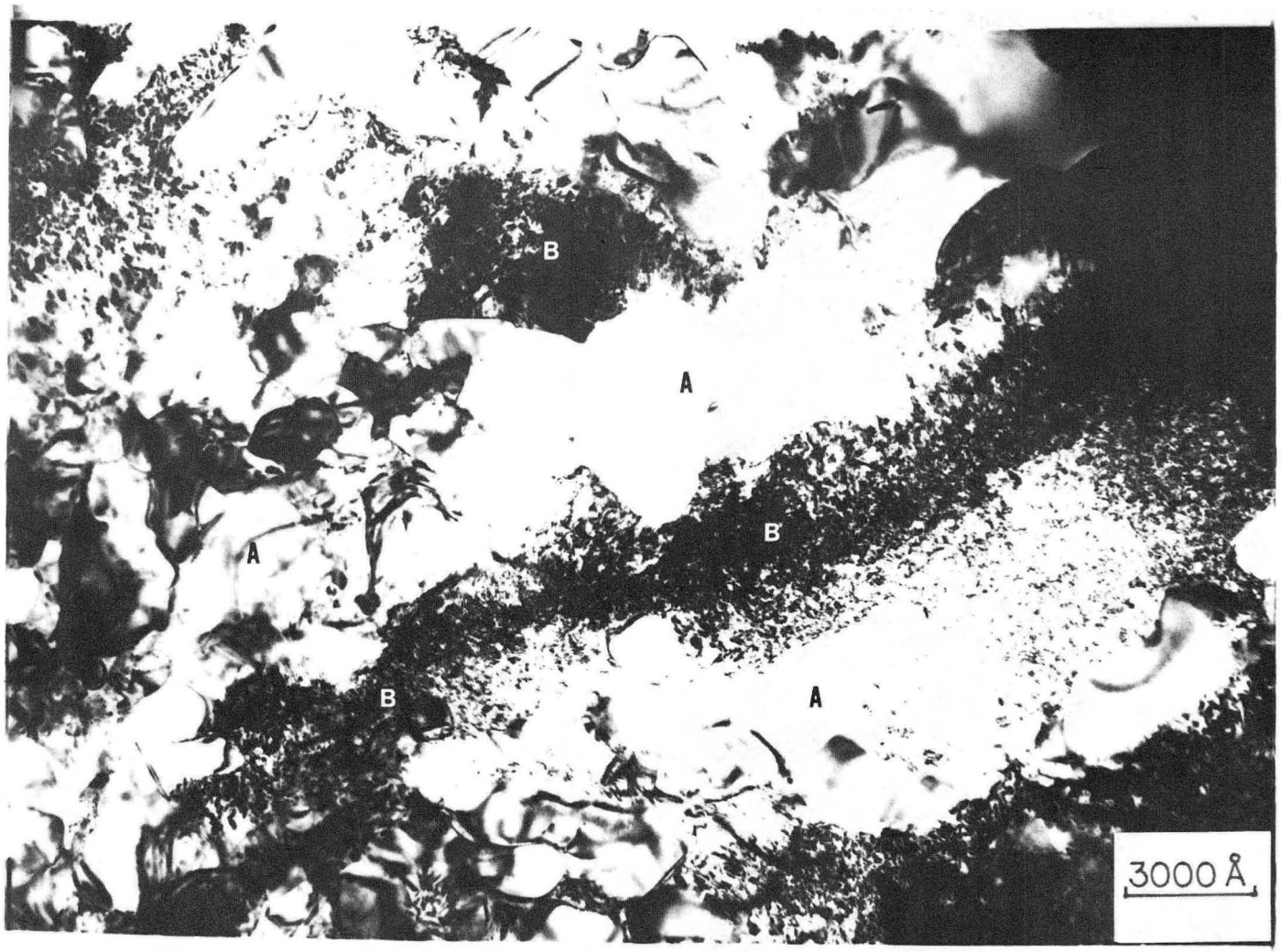

XBB 800-14547A

Fig. VI-12. TEM micrograph of dislocation subgrain boundaries of Nb-17.8 at.% Al sample aged at 750°C for 12 hours.

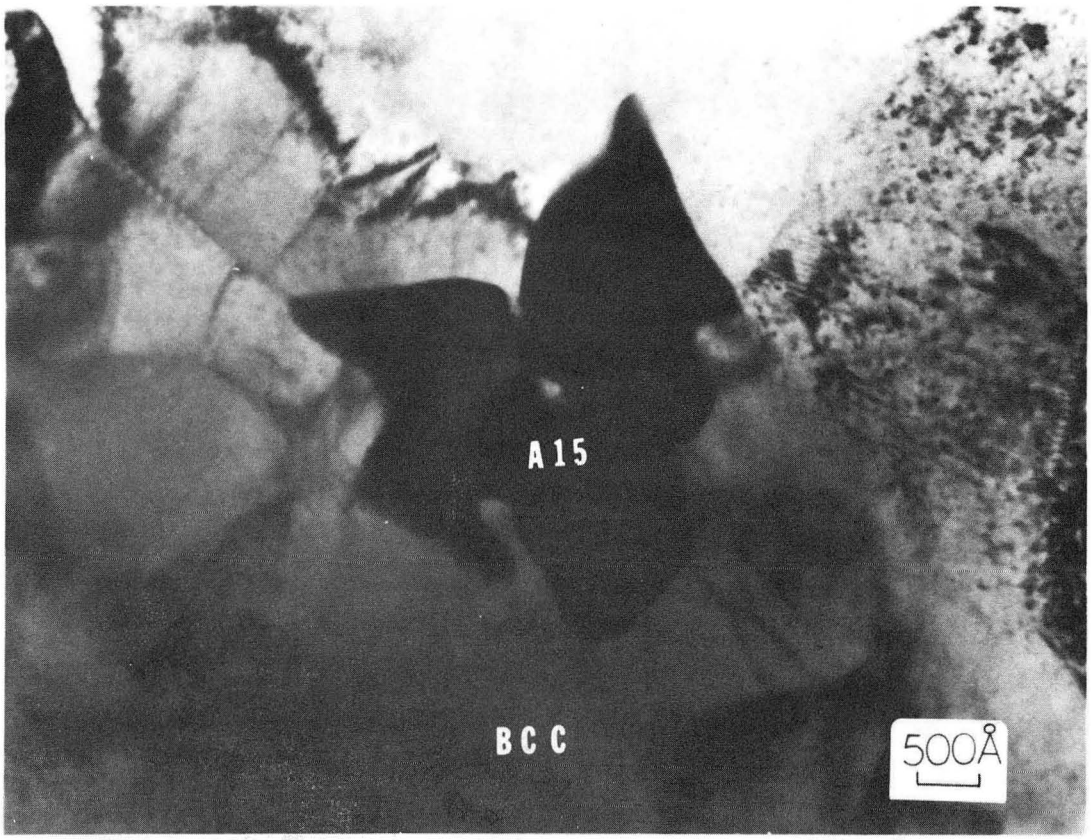

XBB 800-2680

Fig. VI-13. TEM micrograph showing a V_3Ga precipitate at the intersection of prior-deformation grain boundaries of sample aged at 700°C for 1 day.

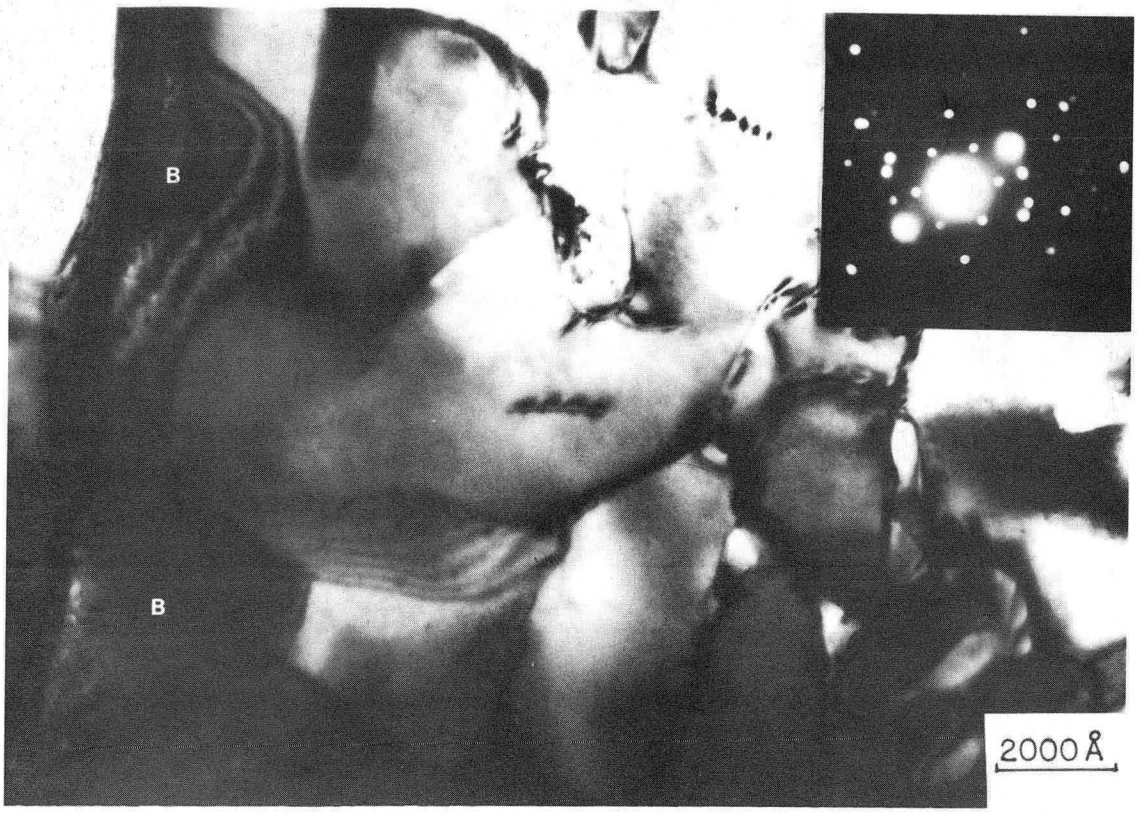

XBB 800-14542A

Fig. VI-14. TEM micrograph and the corresponding diffraction pattern (insert) of V-15.6 at.% Ga sample aged at 700°C for 48 hours. The in-grown dislocation was clearly visible at the center of the micrograph.

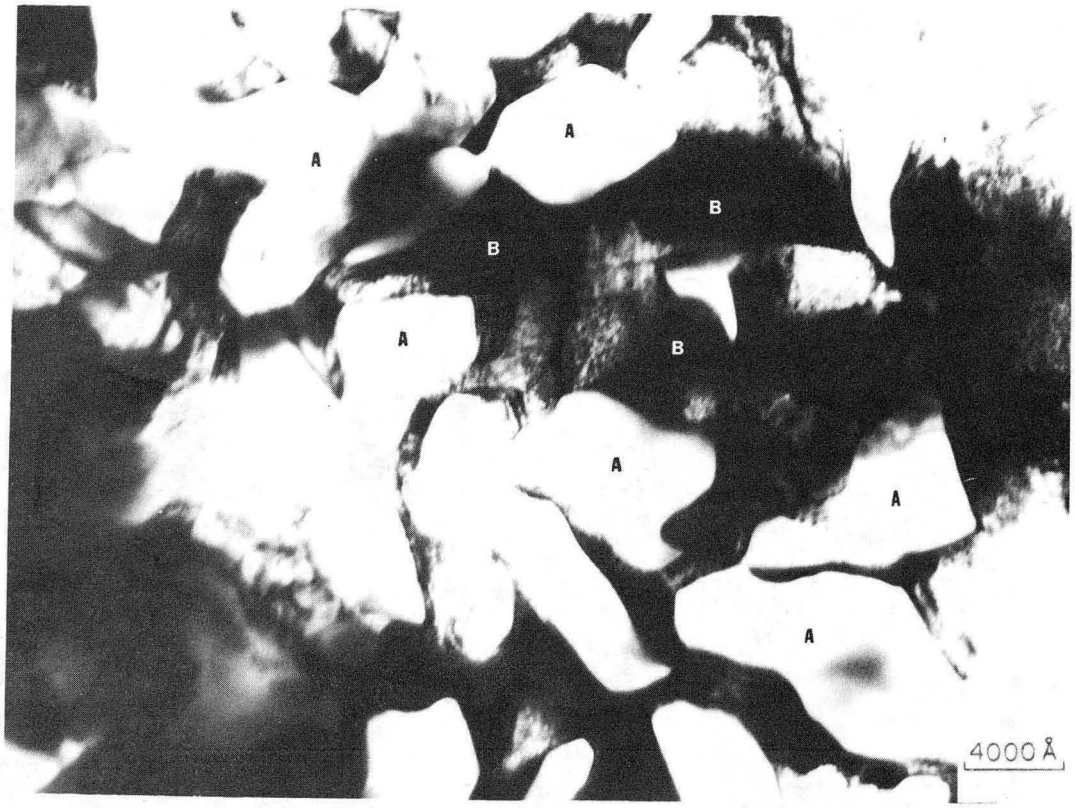

XBB 800-13517

Fig. VI-15. TEM micrograph of V-15.6 at.% Ga sample aged at 700°C for 69 hours.

XBB 800-14550A

Fig. VI-16. Another example of TEM micrograph of the same specimen as that of VI-15.

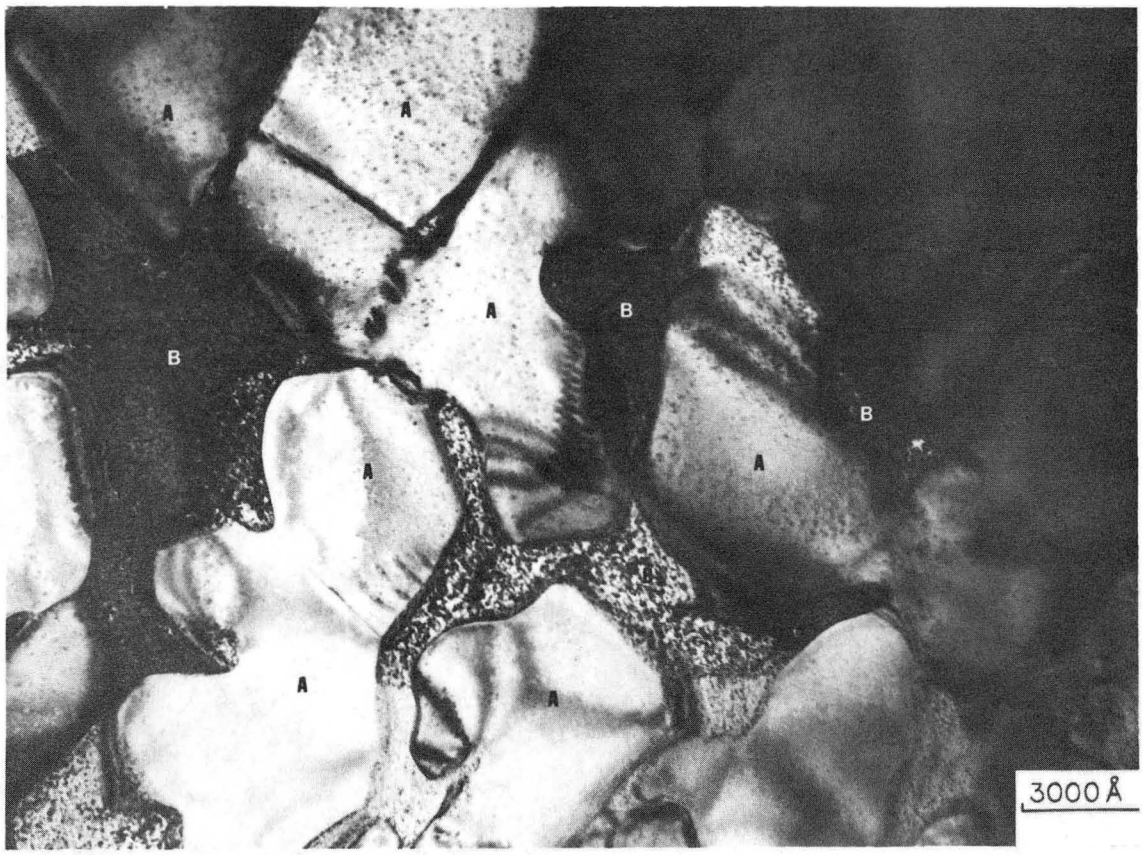

XBB 800-13514

Fig. VI-17. TEM micrograph of V-15.6 at.% Ga sample aged at 700°C for 4.5 days. Regions A and B are A15 and BCC phases, respectively.

XBB 800-13519

Fig. VI-18. Another TEM example of the same condition specimen as VI-17.

Notice the elongated shape of A15 precipitates.

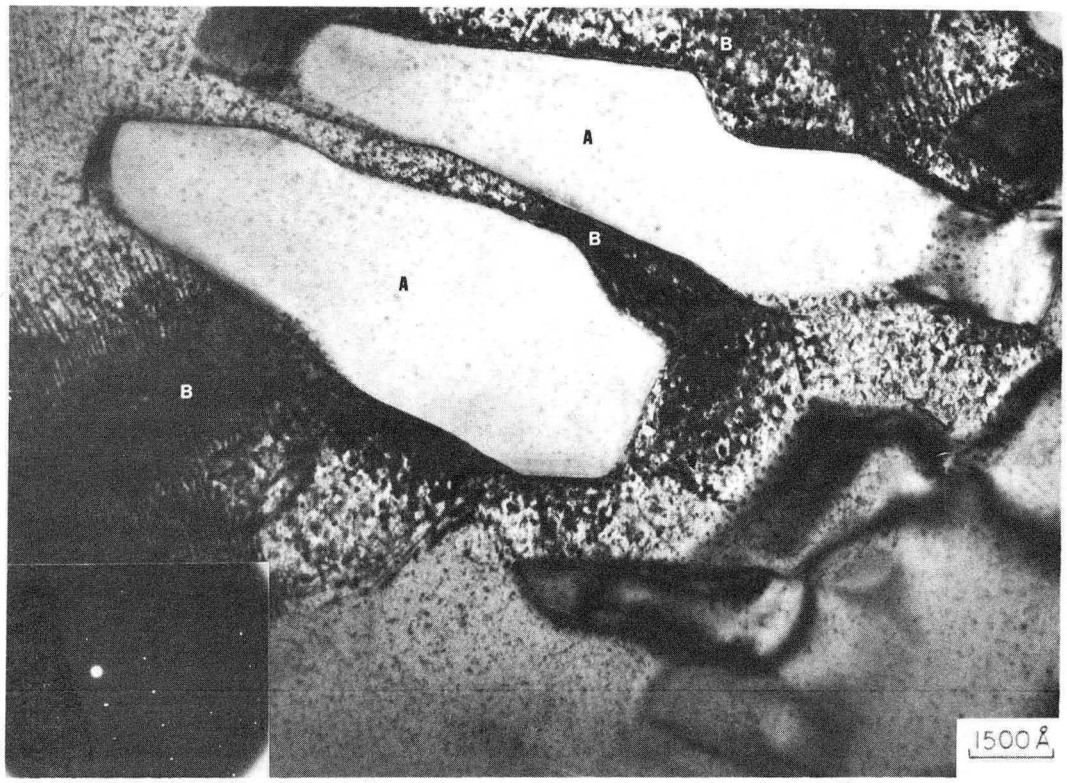

XBB 800-13515

Fig. VI-19. TEM micrograph and the corresponding diffraction pattern of A15 precipitates on dislocation cell walls of the sample aged at 700°C for 4.5 days.

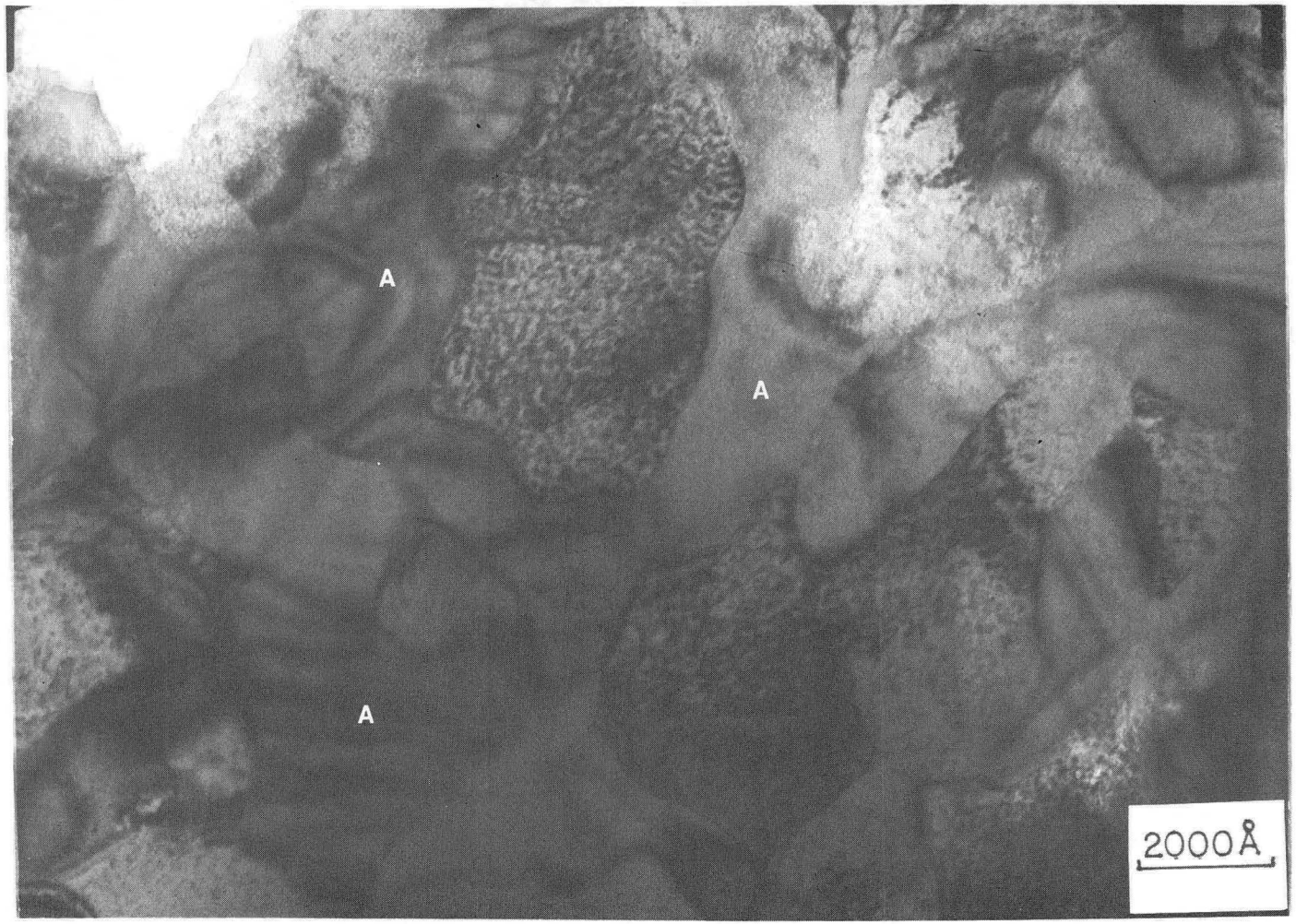

Fig. VI-20. TEM micrograph of V-15.6 at.% Ga aged at 700°C for 7 days. XBB 800-14545A

XBB 800-13524

Fig. VI-21. TEM micrograph and the corresponding diffraction pattern of sample aged for 11.5 days.

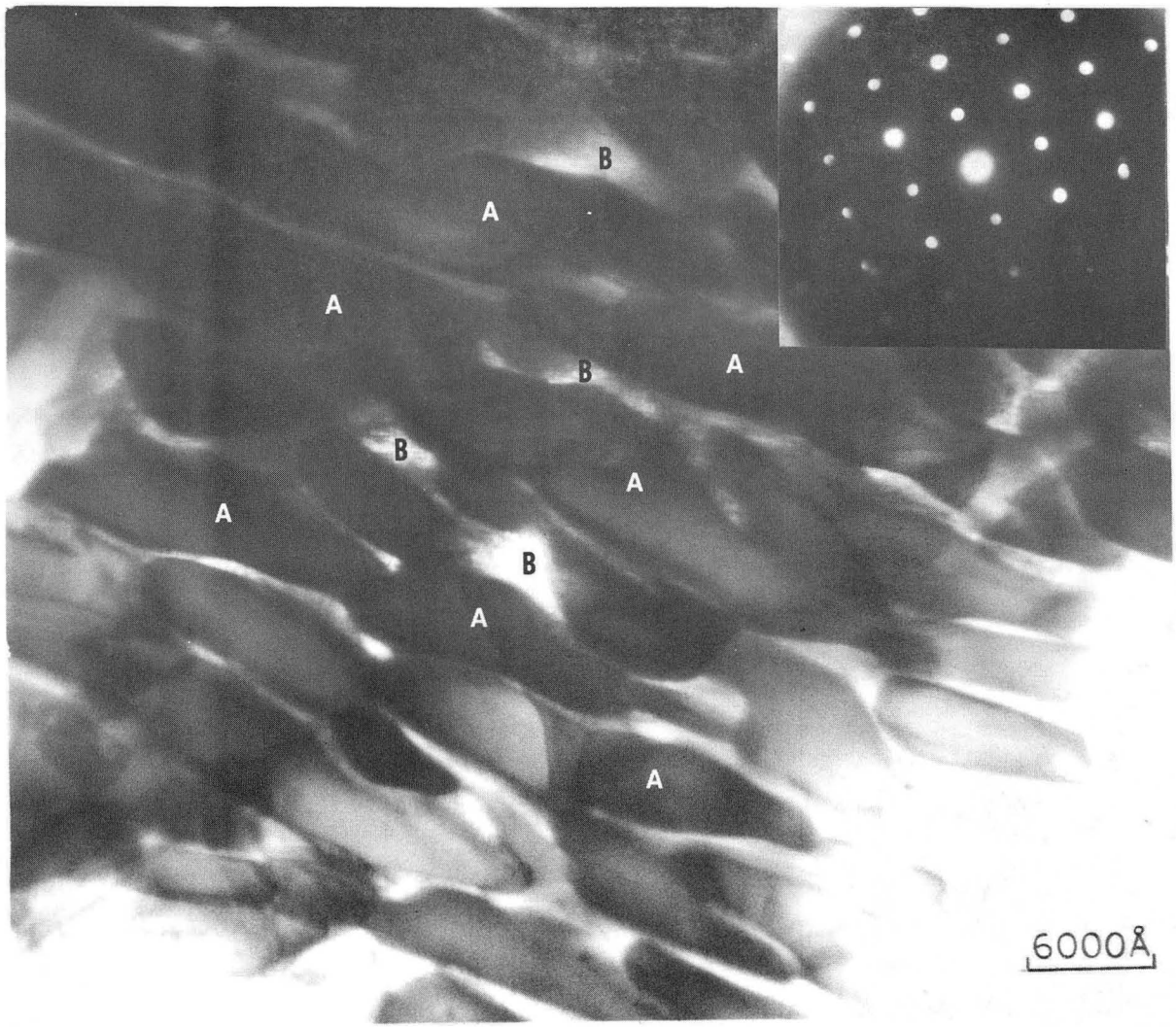

Fig. VI-22. TEM micrograph and the corresponding diffraction pattern of A15 (011) zone axis showing the A15 precipitates having similar orientation. The sample was aged at 700°C for 11.5 days.

XBB 800-13522

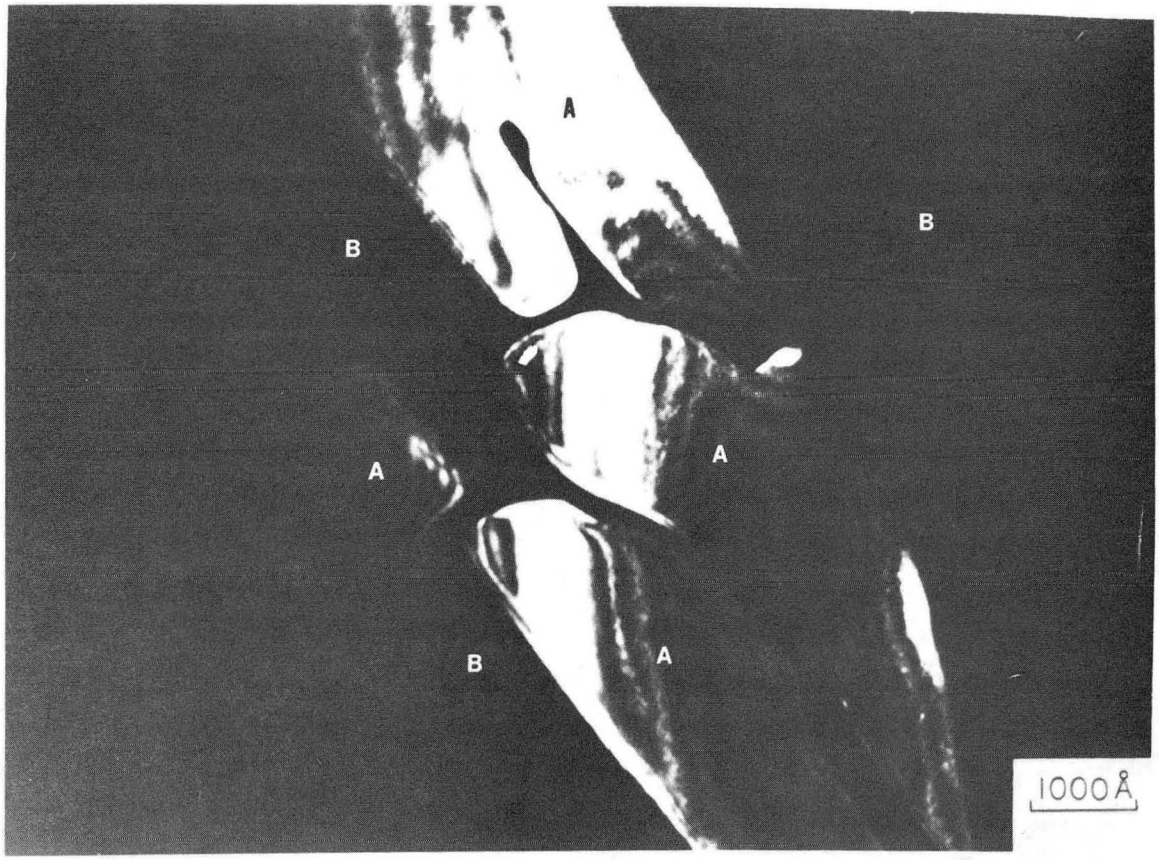

XBB 800-13521

Fig. VI-23. Dark-field micrograph of V_3Ga precipitates showing stable BCC films between A15 phase. The sample was heat treated at 700°C for 11.5 days.

XBB 800-13525

Fig. VI-24. TEM micrograph and the corresponding diffraction pattern of V-18.0 at.% Ga aged at 700°C for 6 hours.

XBB 800-14543A

Fig. VI-25. TEM micrograph showing the V_3Ga precipitates of samples aged for 12 hours.

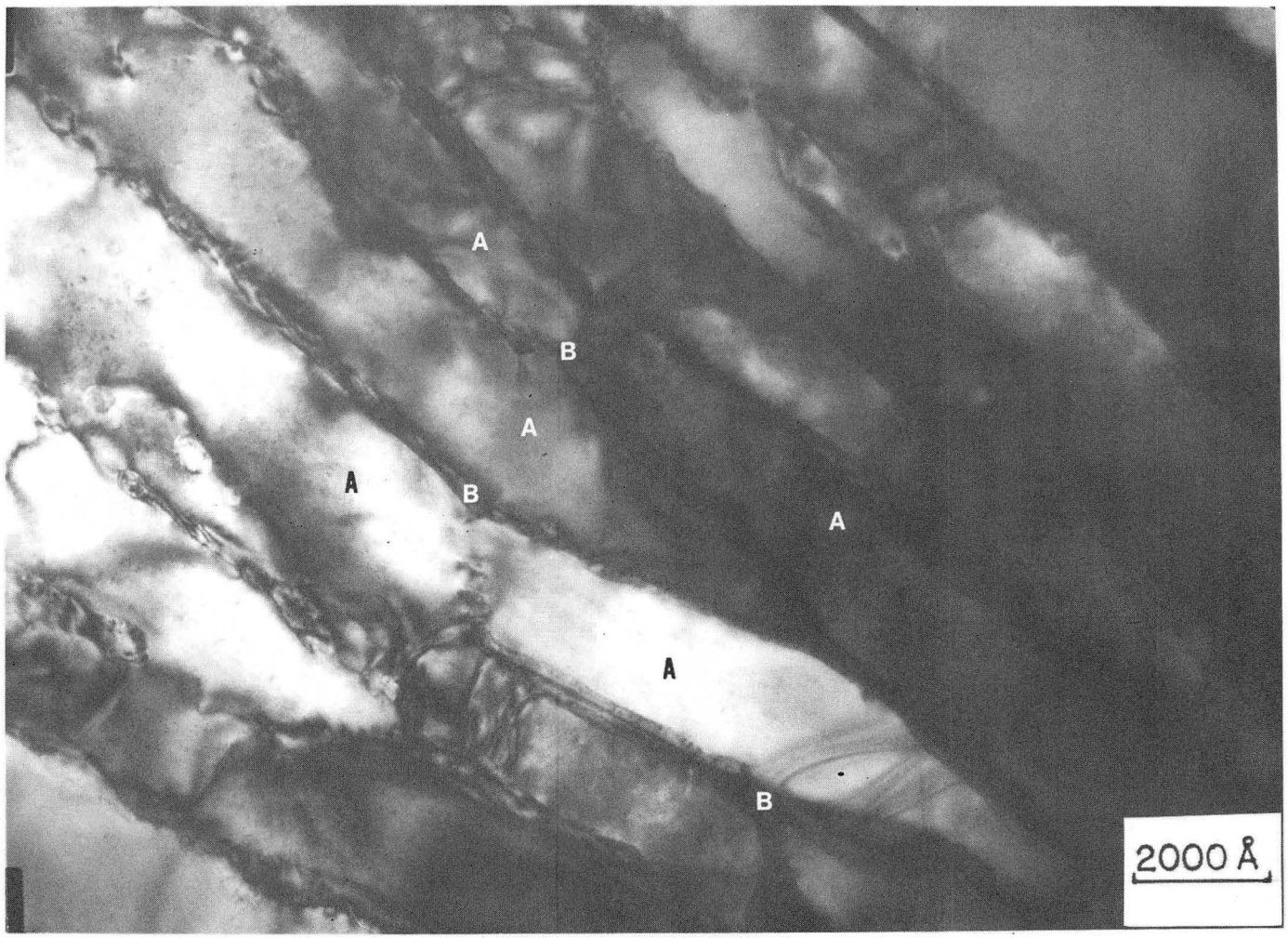

Fig. VI-26. TEM micrograph showing the V_3Ga precipitates and the stable BCC films of V-18 at.% Ga sample aged at 700°C for 24 hours.

XBB 800-14548A

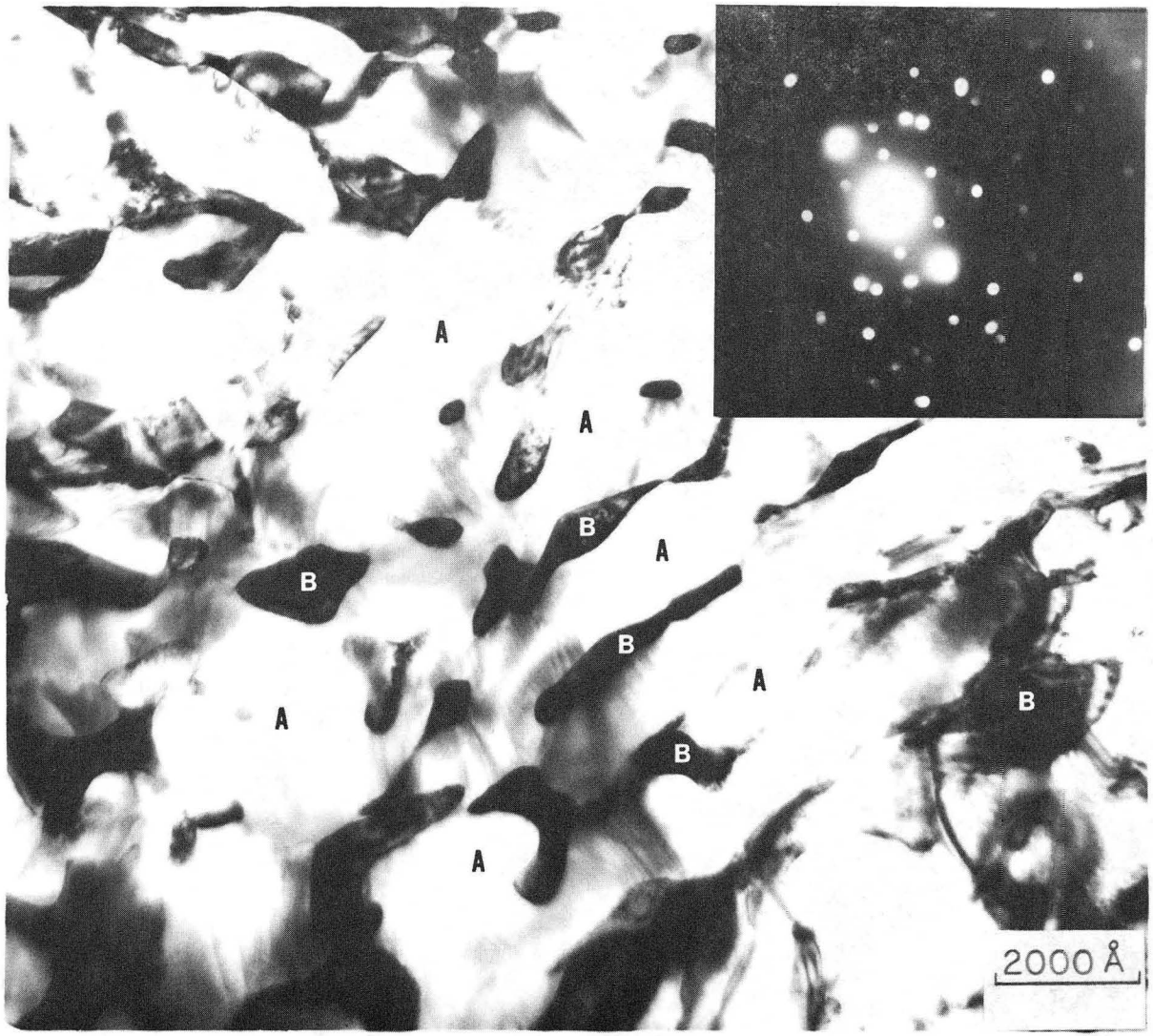

Fig. VI-27. TEM micrograph and the corresponding diffraction pattern showing the coalescence of V_3Ga precipitation and the spheroidization of BCC phase of V-18 at.% Ga sample aged at 700°C for 48 hours. XBB 800-13523

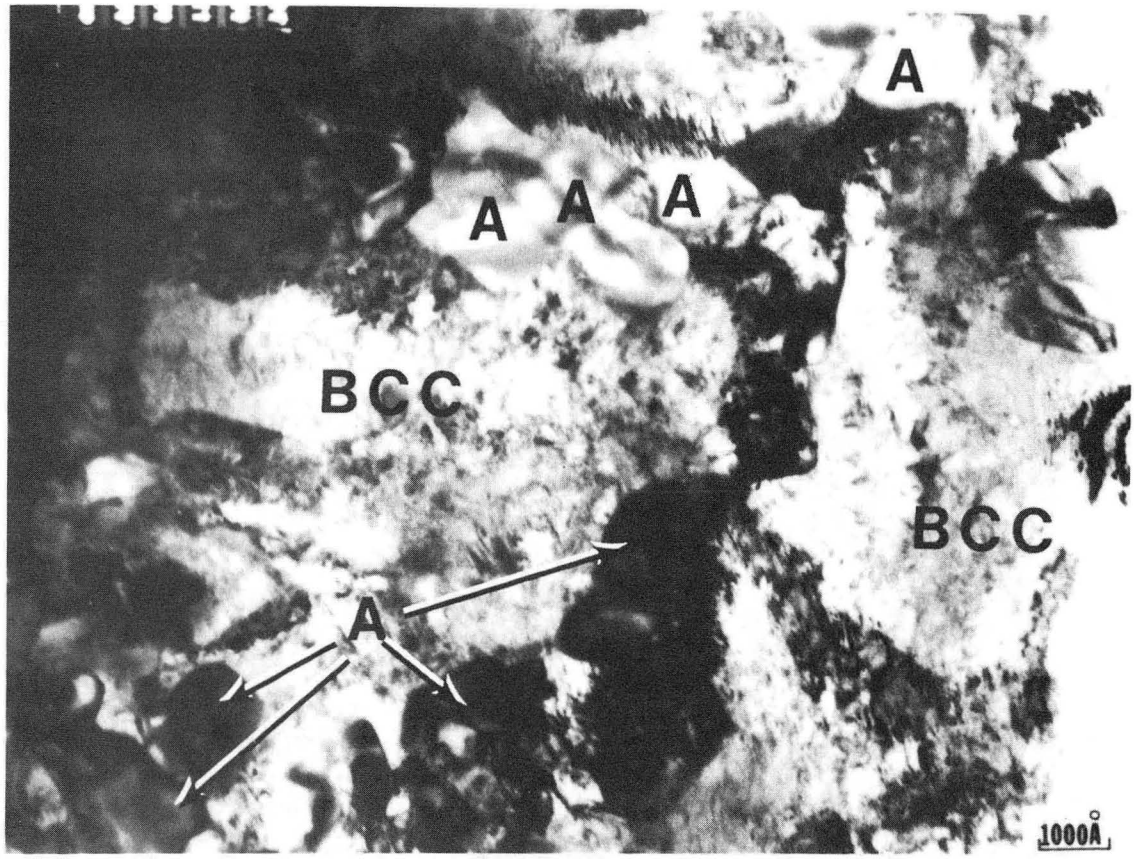

Fig. VI-28. TEM micrograph of Nb-18 at.% Al sample aged at 750°C for 3 hours. The Nb_3Al precipitates nucleated preferentially on the sub-grain boundaries.

XBB 800-2119

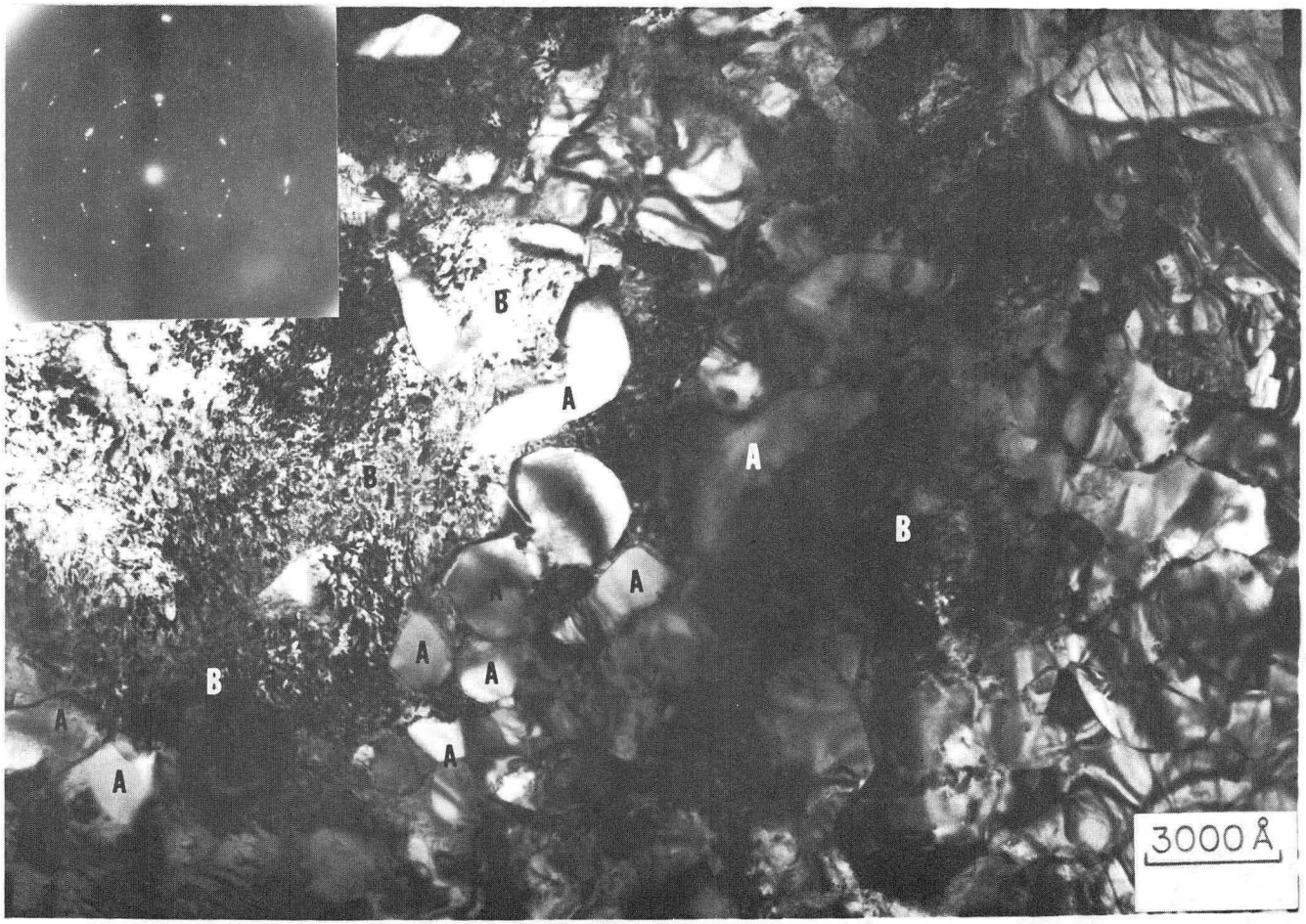

XBB 800-13536

Fig. VI-29. TEM micrograph and the corresponding diffraction pattern of Nb-18 at.% Al sample aged at 750°C for 3 hours.

XBB 800-13537

Fig. VI-30. TEM micrograph and the corresponding diffraction pattern of Nb-18 at.% Al sample aged at 750°C for 6 hours.

Fig. VI-31. TEM micrograph and the corresponding diffraction pattern of sample aged at 750°C for 12 hours. Notice that the precipitates showing complex bending contours indicate the strain of A15 phase.

XBB 800-13541

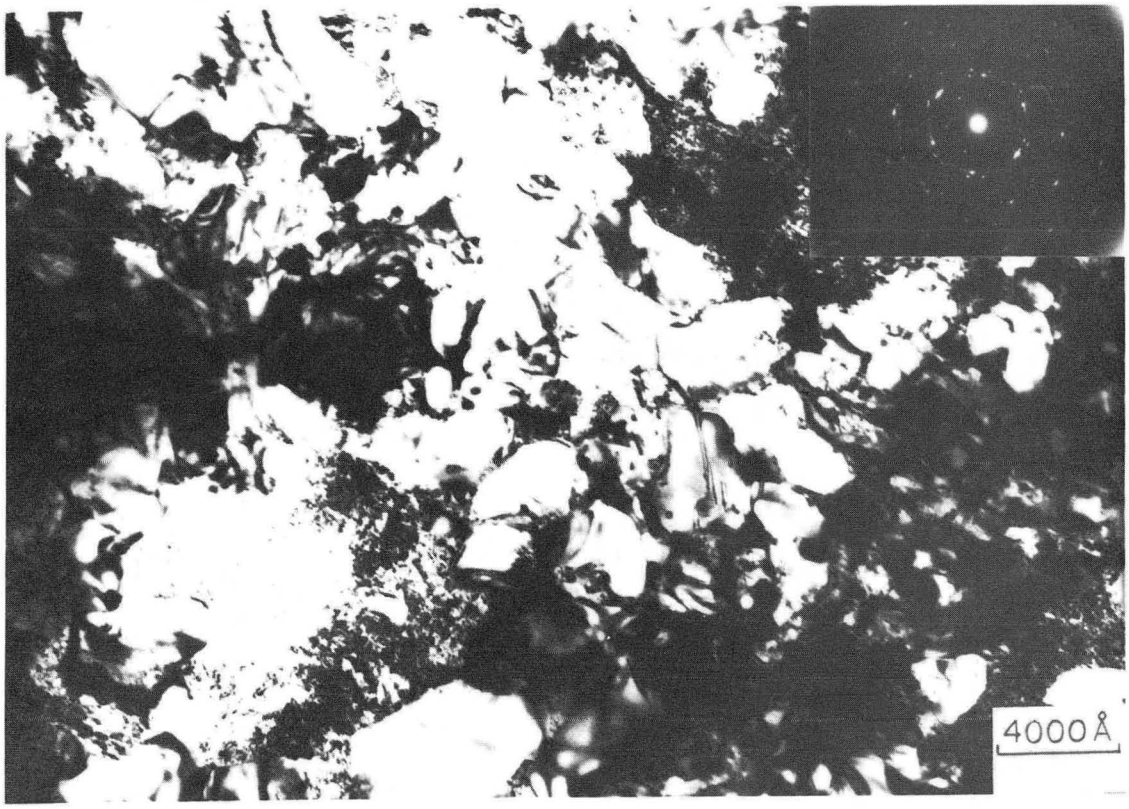

XBB 800-13540A

Fig. VI-32. TEM micrograph of Nb-18 at.% Al sample aged at 750°C for 12 hours.

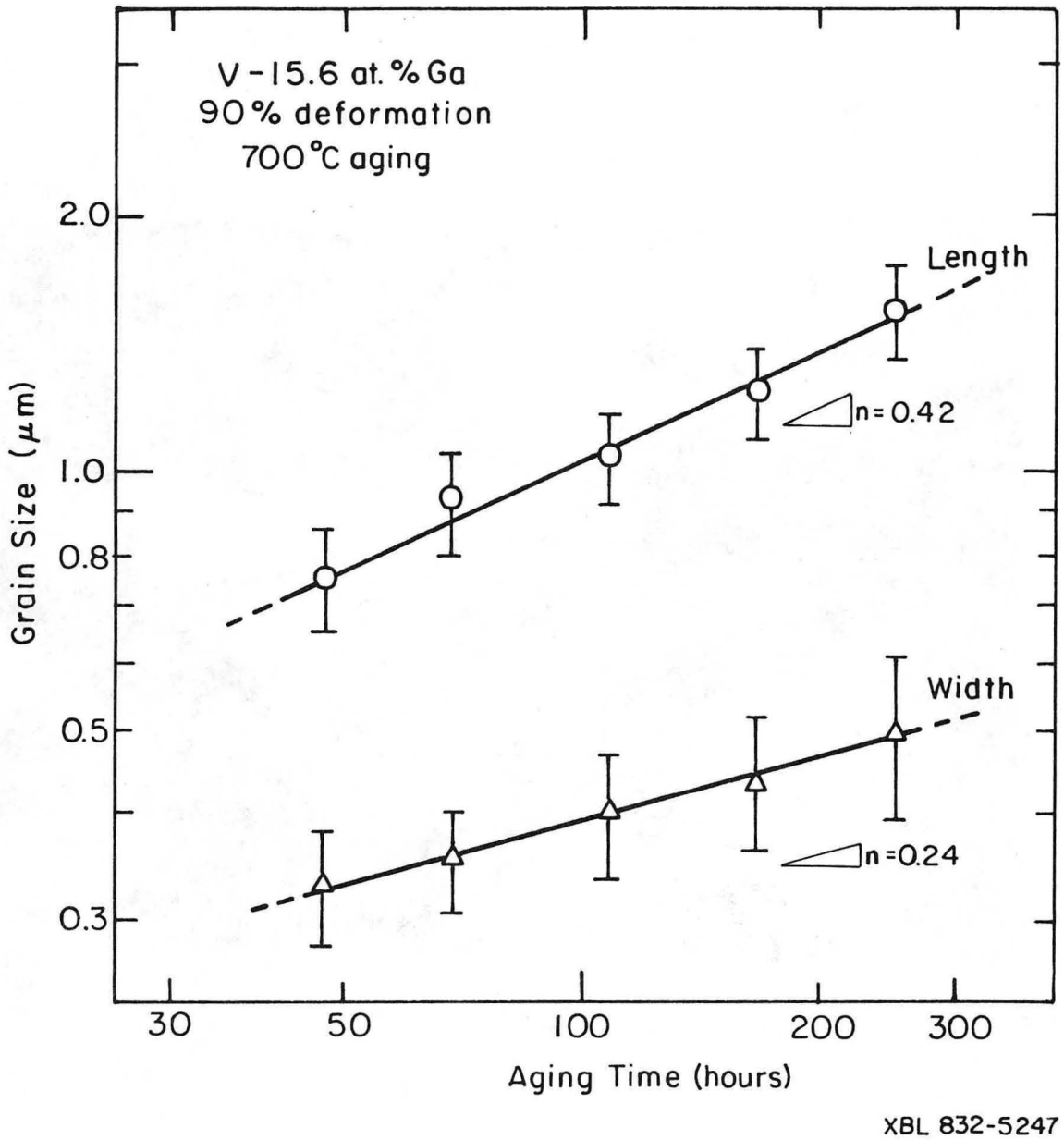

Fig. VI-33. Grain size versus aging time for V-15.6 at.% Ga samples aged at 700°C.

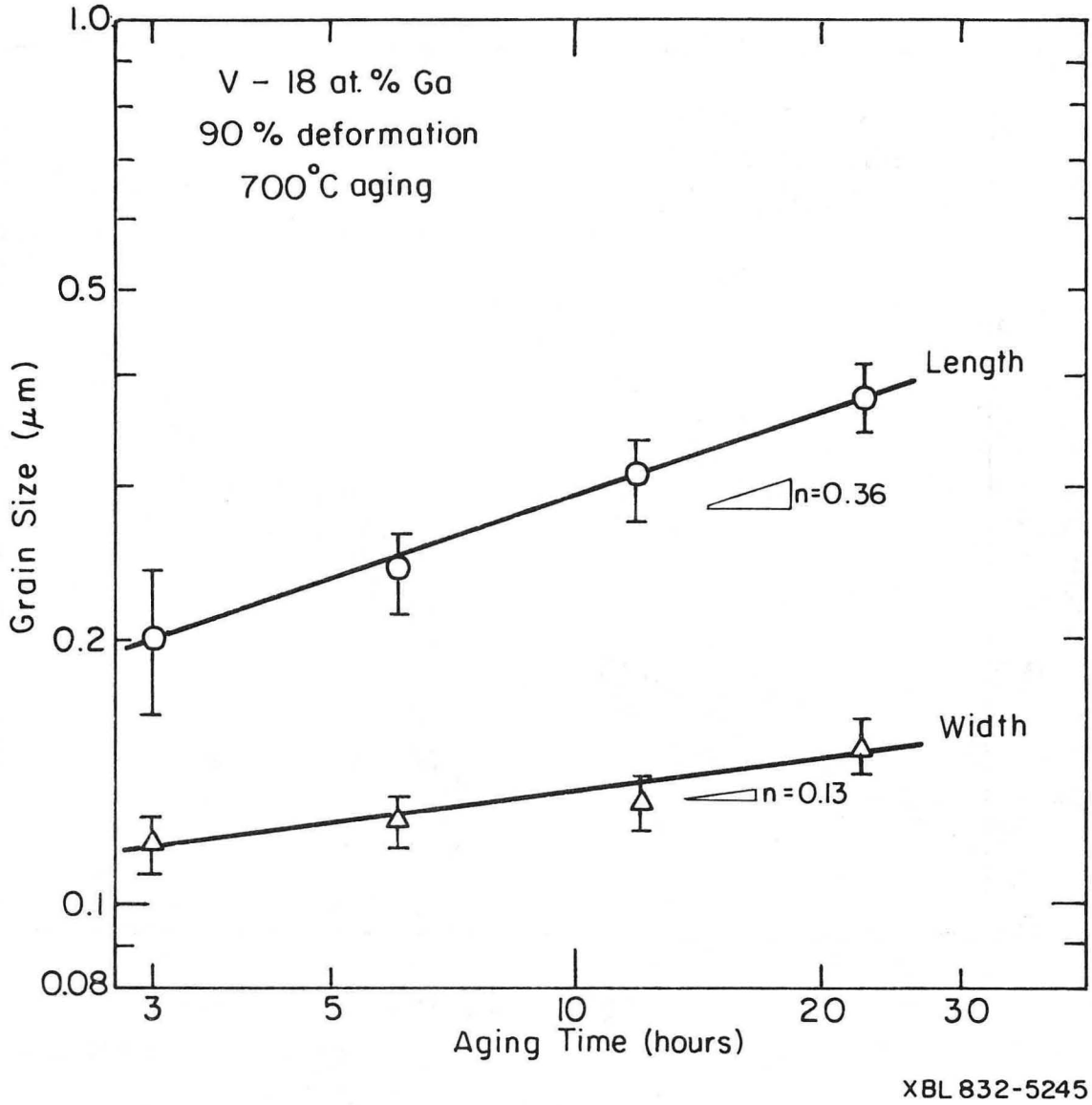

Fig. VI-34. Grain size versus aging time for V-18.0 at.% Ga samples aged at 700°C.

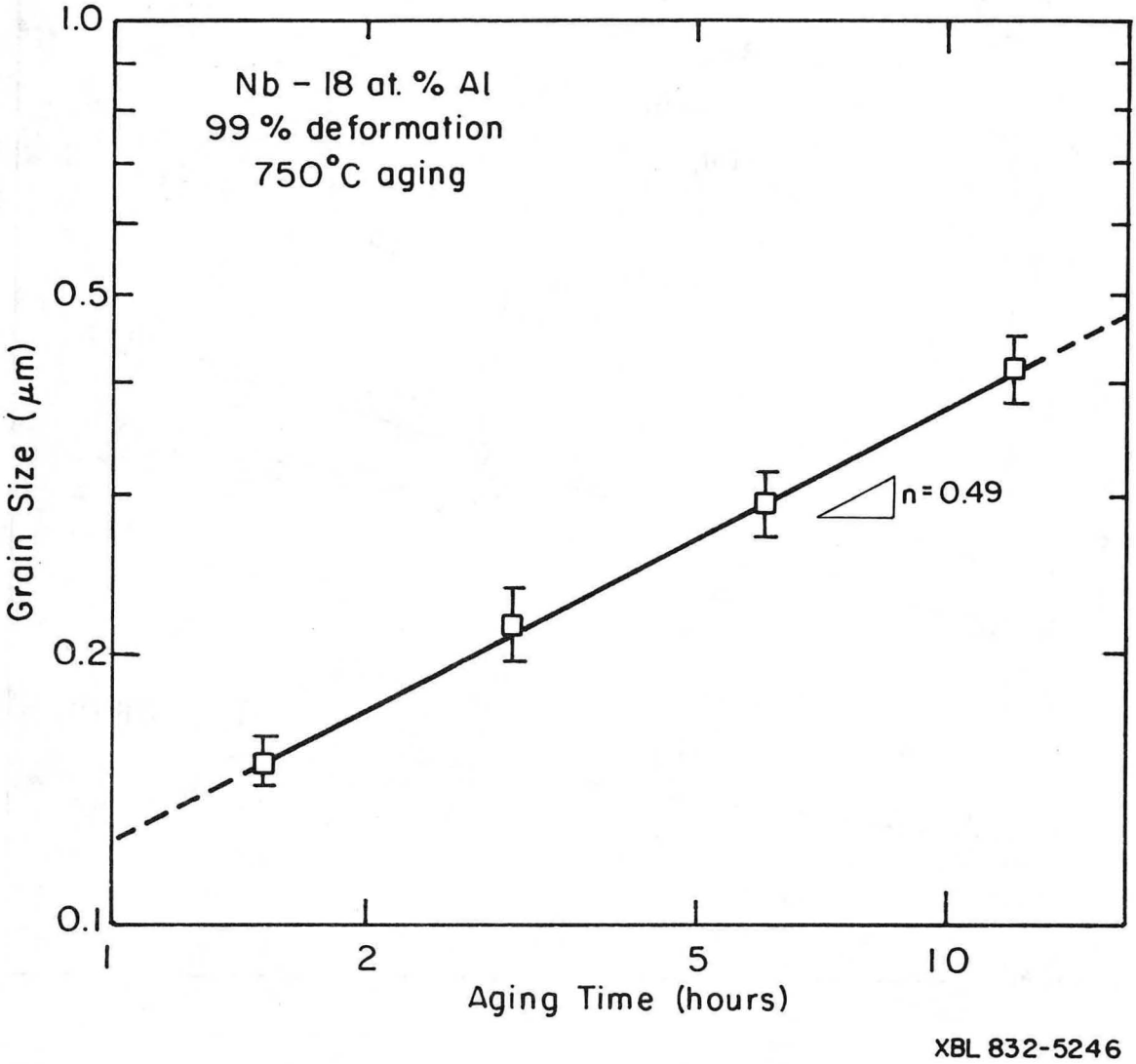

Fig. VI-35. Grain size versus aging time for Nb-18 at.% Al samples aged at 750°C.

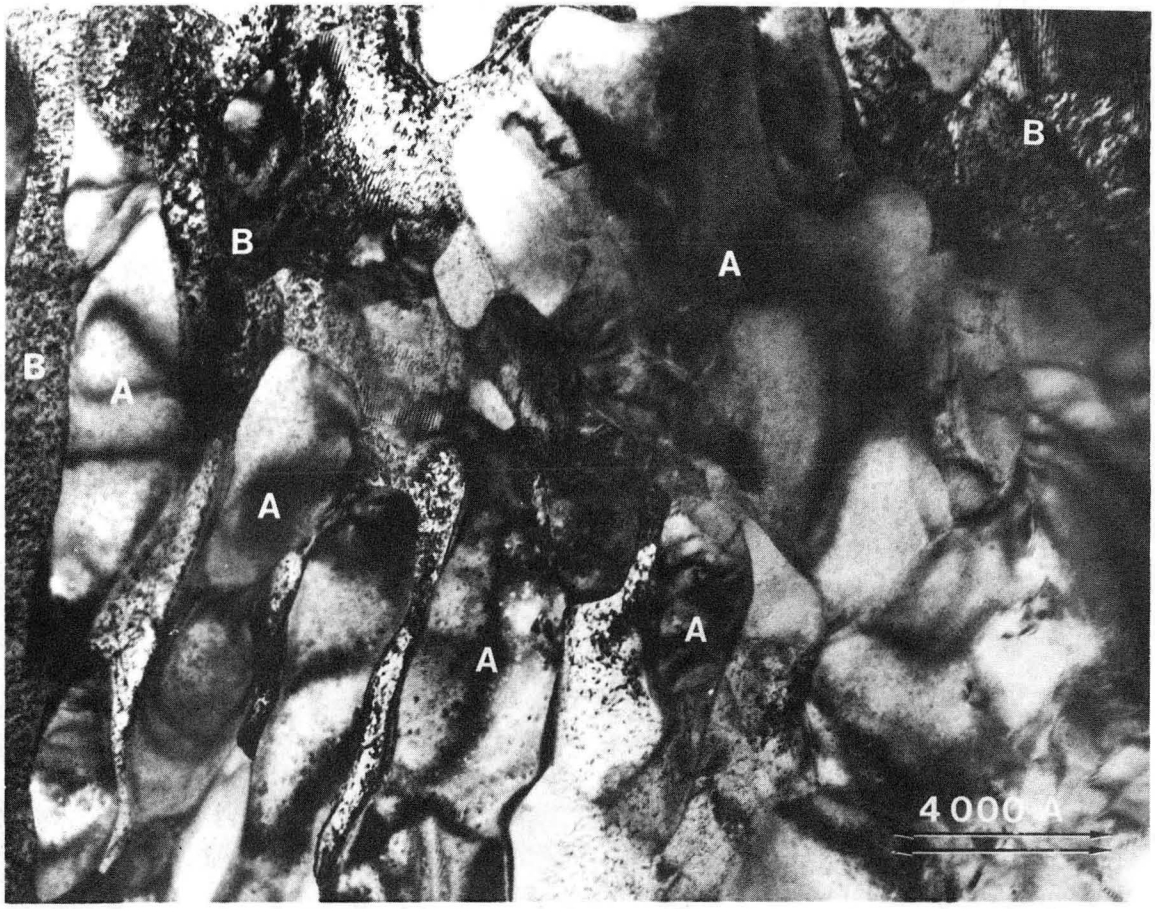

Fig. VI-36(a)

XBB 837-5993

Fig. VI-36. TEM micrograph (a) and the corresponding convergent beam electron diffraction pattern (b) of V-15.6 at.% Ga sample aged at 700°C for 4.5 days.

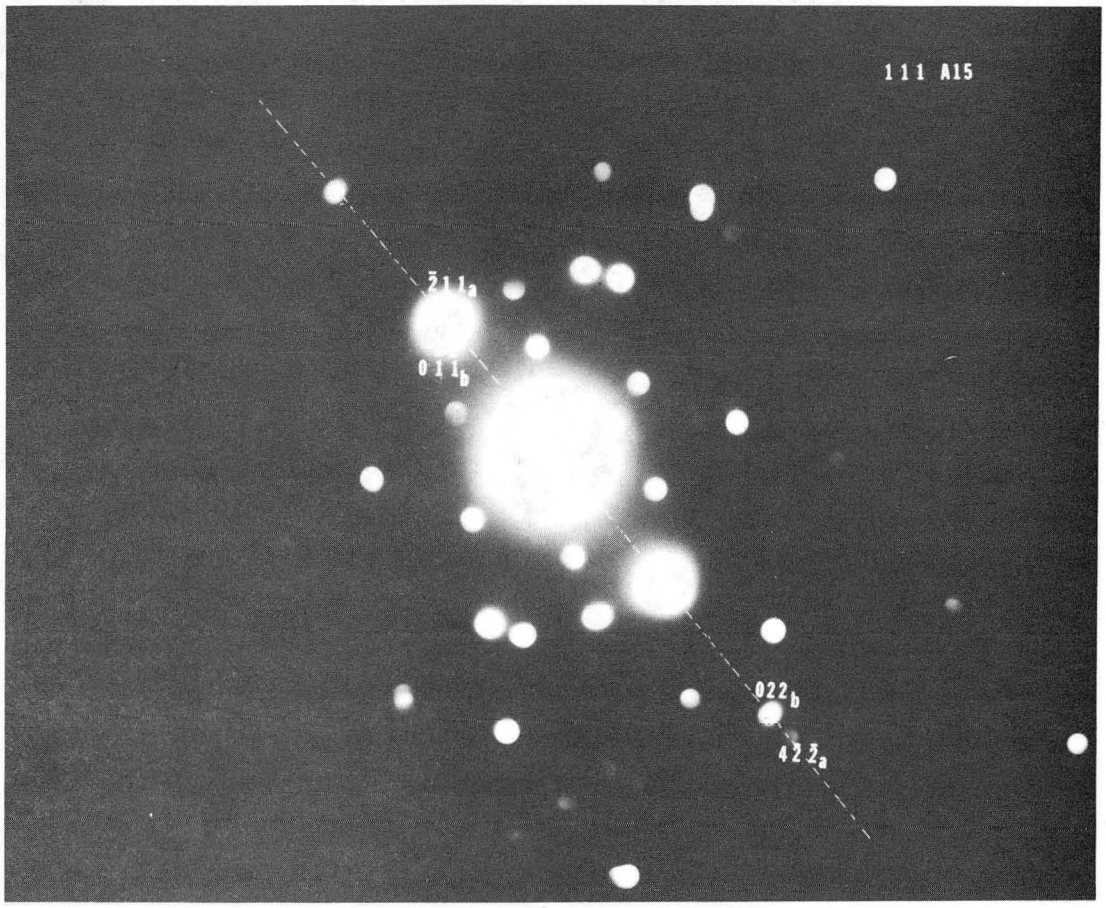

Fig. VI-36(b)

XBB 800-14820

Fig. VI-37(a) XBB 800-14543A

Fig. VI-37. (a) TEM micrograph of V-18 at.% Ga deformed 90% and aged at 700°C for 12 hours. Regions A and B are A15 and BCC phases, respectively. (b) The corresponding convergent beam electron diffraction pattern. (c) Index pattern of (b).

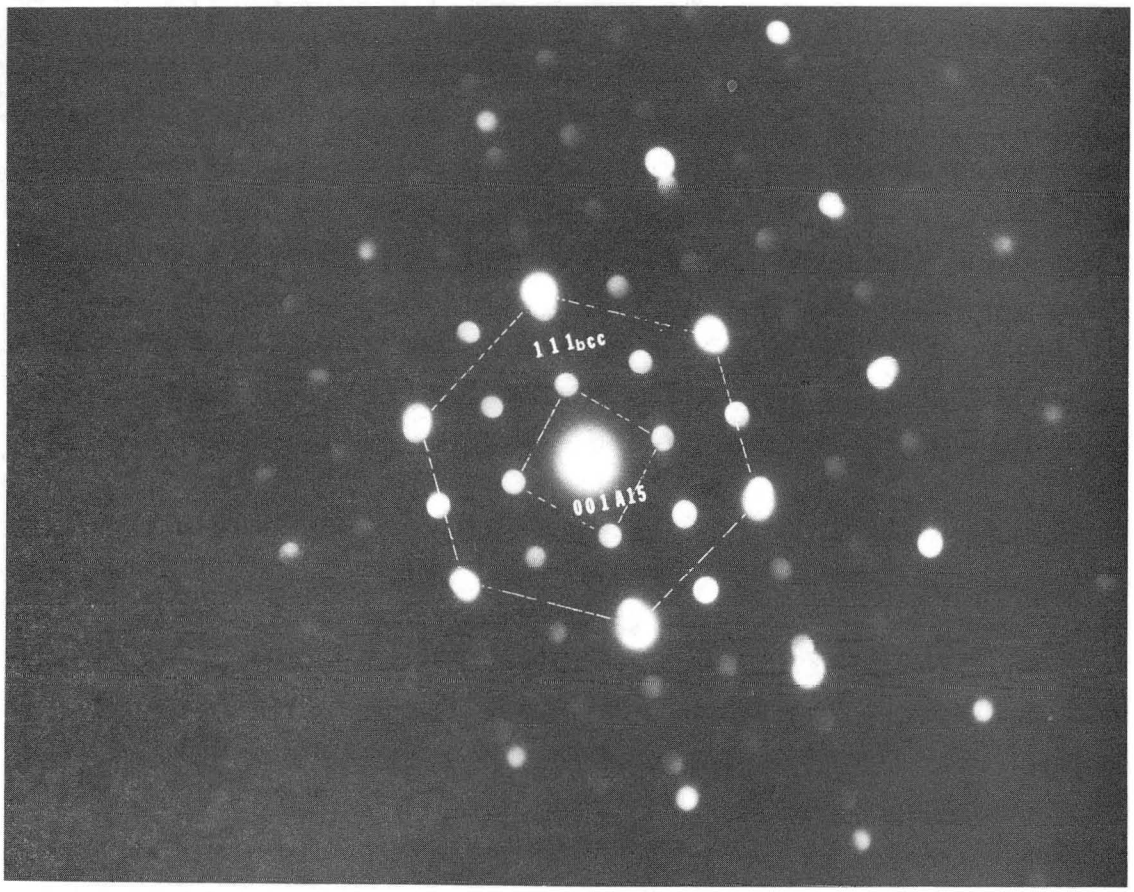

Fig. VI-37(b)

XBB 800-14821

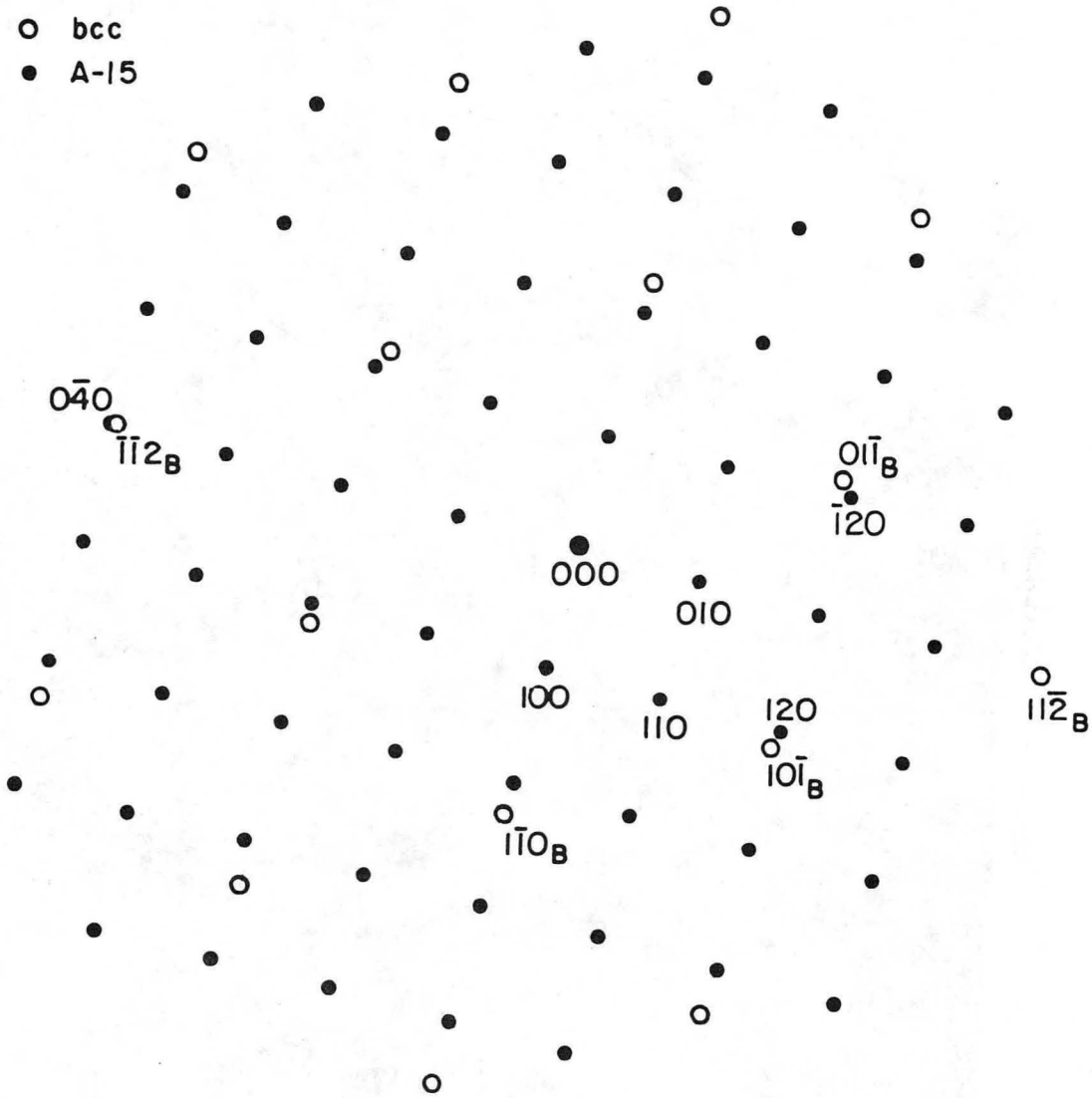

Fig. VI-37(c)

XBL 811-5123

Fig. Vi-38 (a)

XBB 800-13538A

Fig. VI-38. (a) TEM micrograph of Nb-18 at.% Al deformed 99% and aged at 750°C for 3 hours. (b) The corresponding convergent beam electron diffraction pattern.

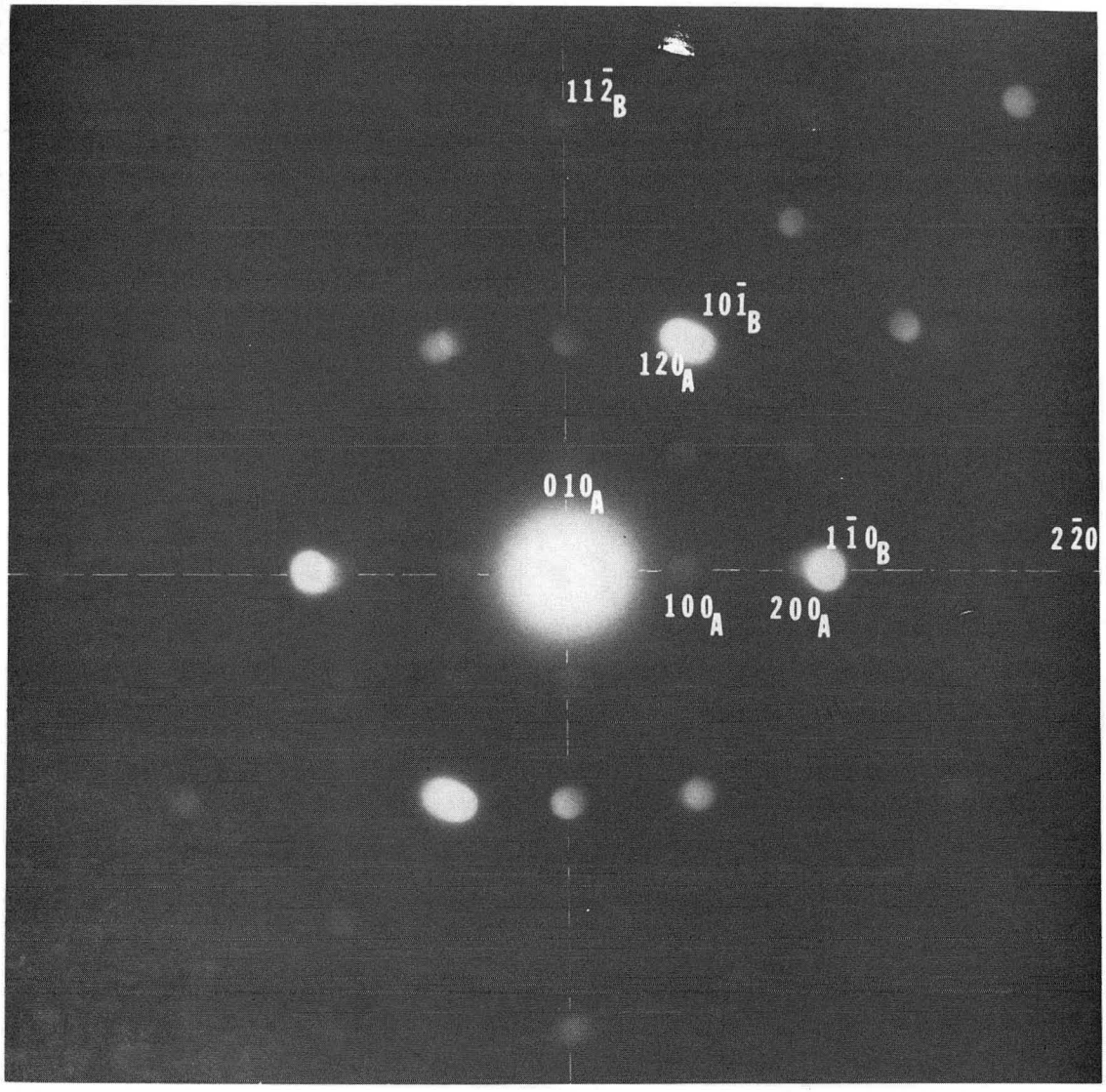

Fig. VI-38 (b) XBB 811-796

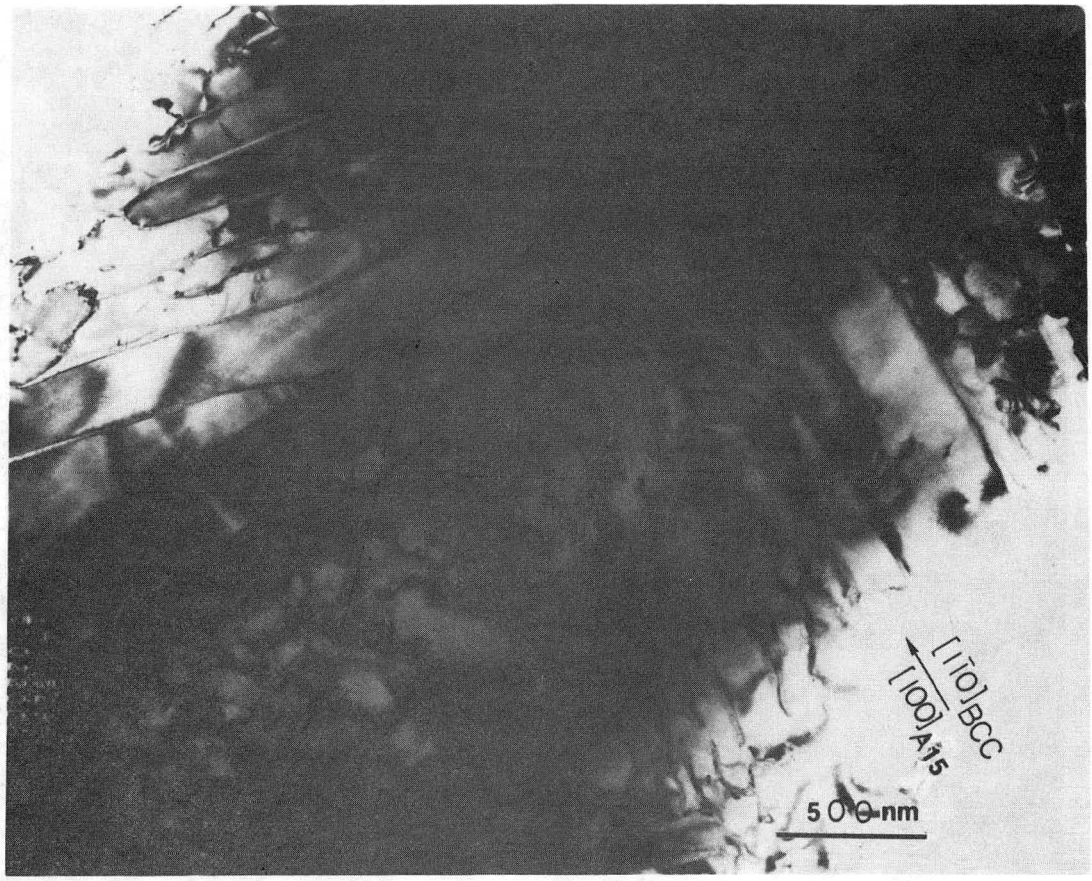

XBB 823-2690

Fig. VI-39. TEM micrograph of the annealed V-18 at.% Ga sample aged at 700°C for 2 days. The crystallographic orientation of precipitates' habit plane is shown in the figure.

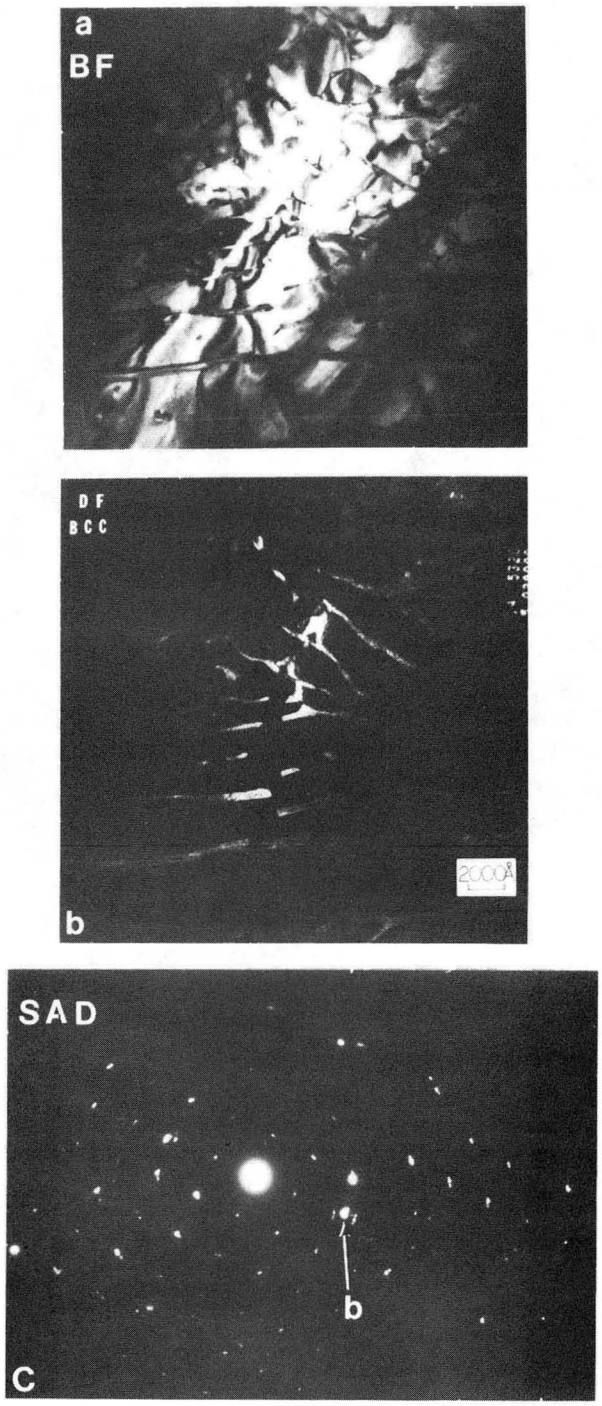

XBB 823-2695A

Fig. VI-40. (a) Bright-field TEM micrograph, (b) dark-field of BCC reflection, and (c) the corresponding diffraction pattern of the annealed V-18 at.% Ga aged at 700°C for 2 days.

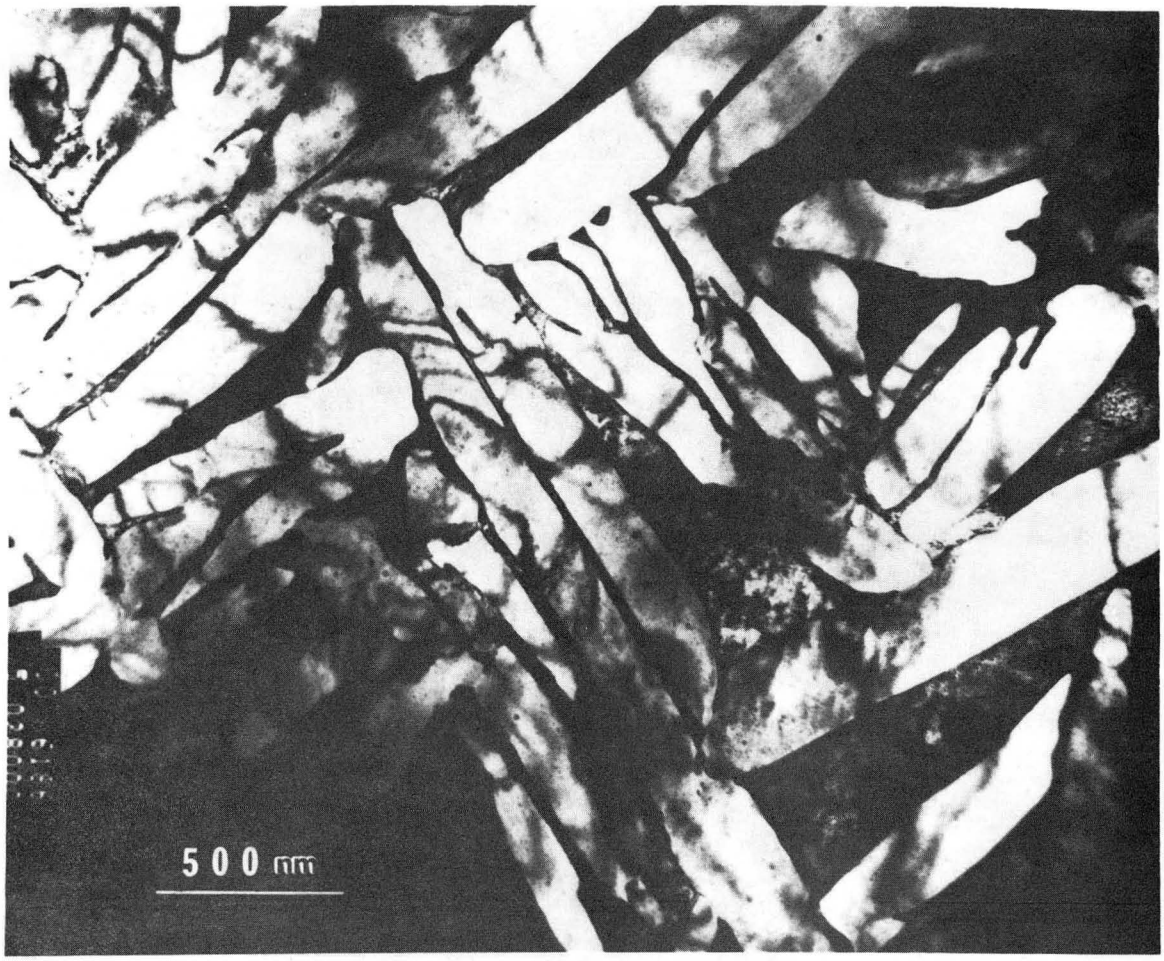

XBB 823-2685

Fig. VI-41. TEM micrograph of annealed V-18 at.% Ga sample aged at 700°C for 4 days.

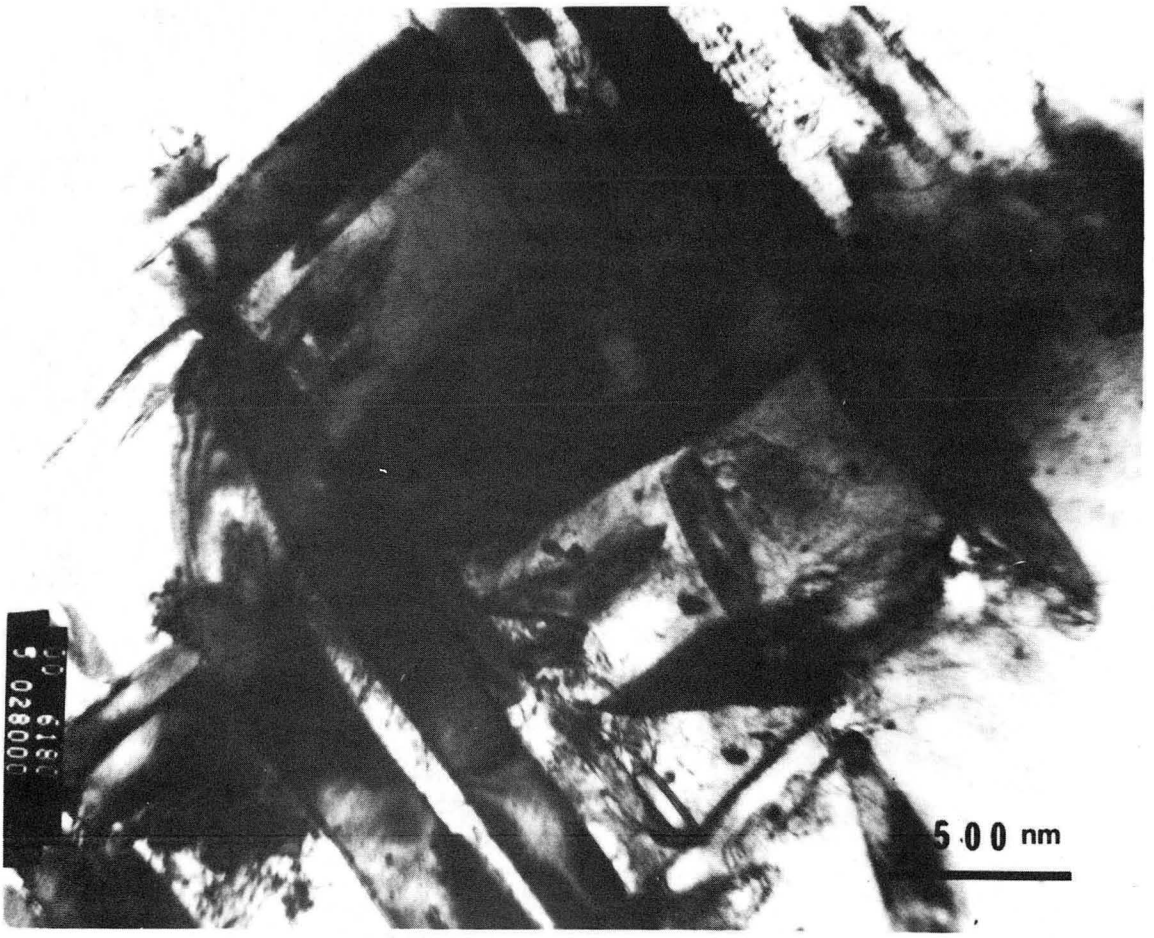

Fig. VI-42(a)

XBB 823-2687

Fig. VI-42. (a) Bright-field TEM micrograph, (b) dark-field of A15 reflection, and (c) the corresponding diffraction pattern, of annealed V-18 at.% Ga sample aged at 700°C for 4 days.

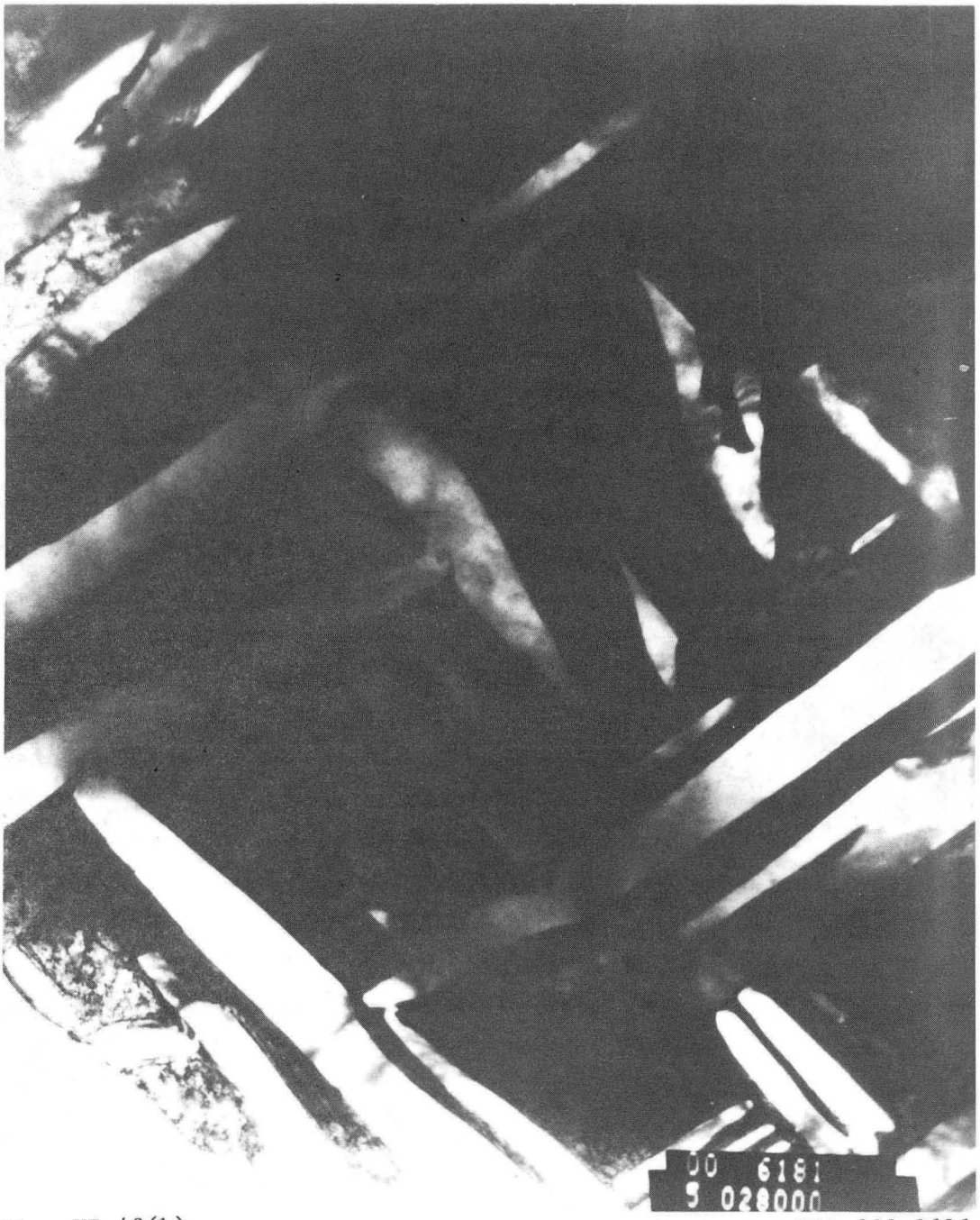

Fig. VI-42(b) XBB 823=2686

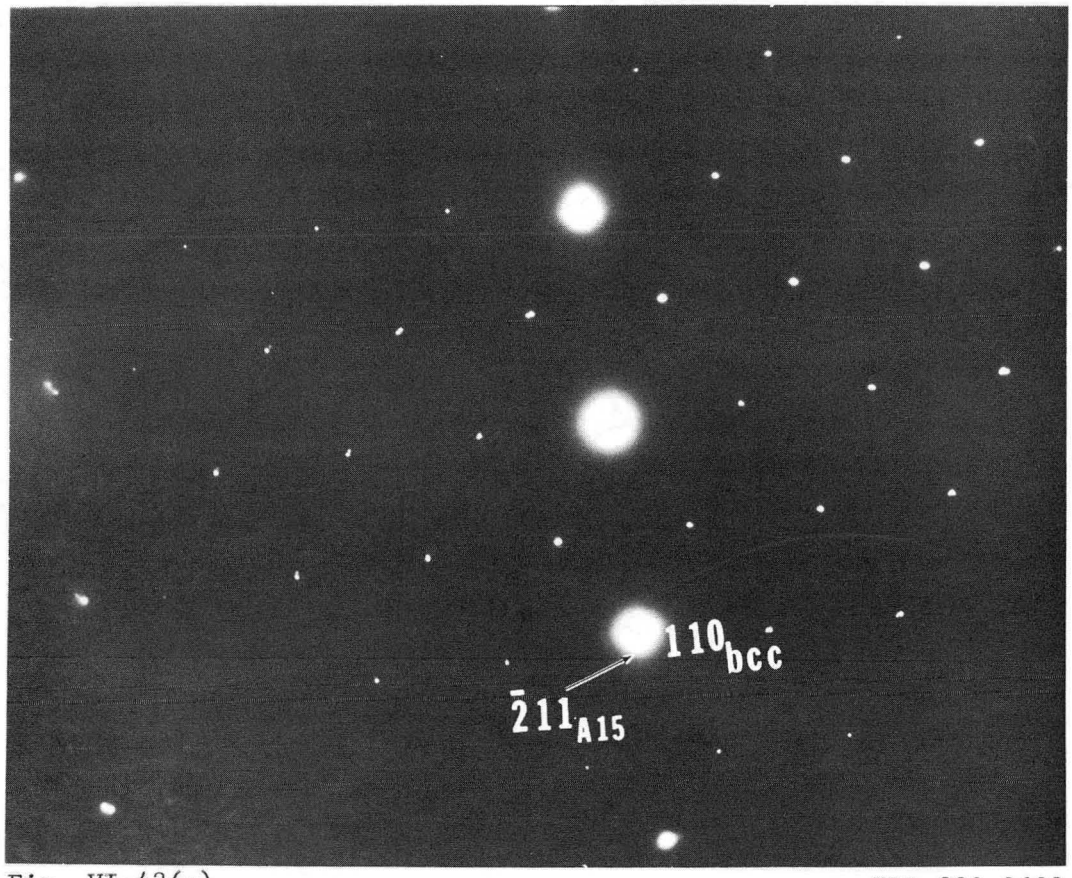

Fig. VI-42(c) XBB 823-2688

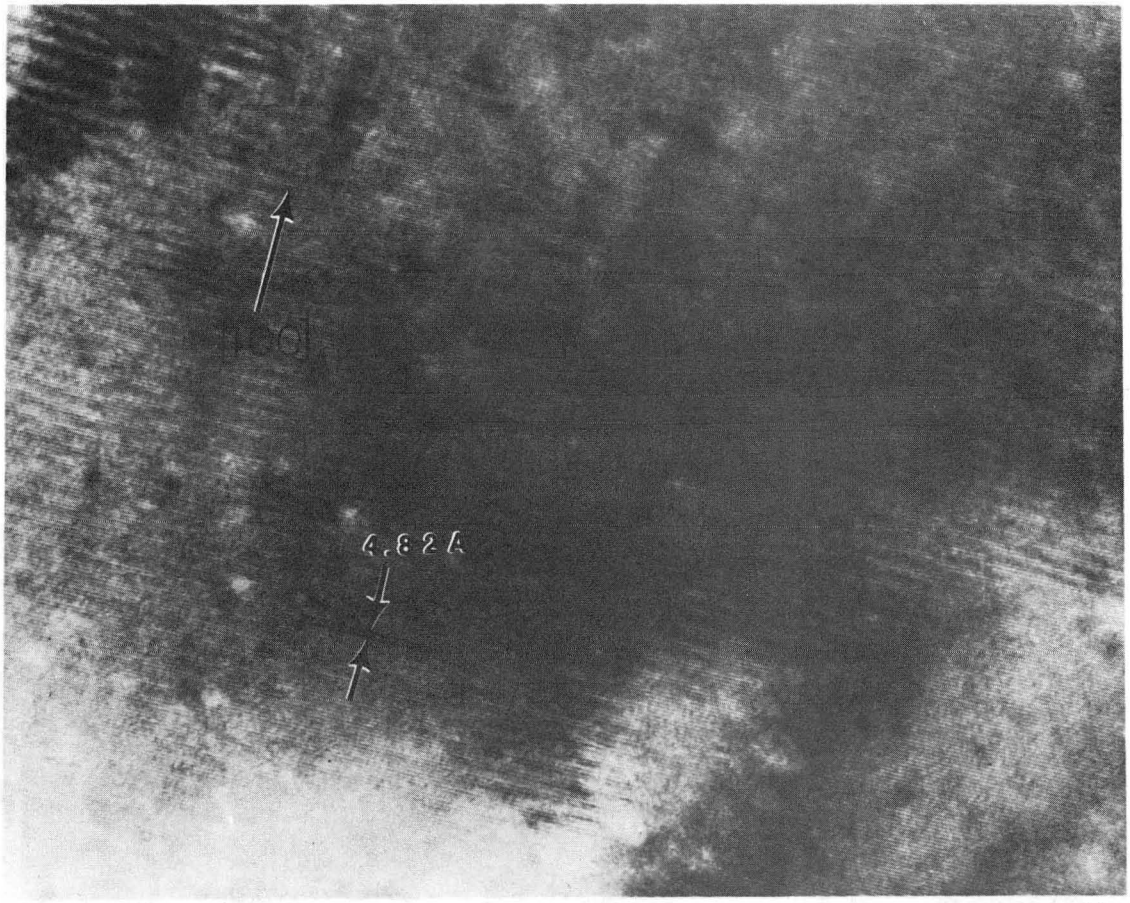

XBB 823-2689

Fig. VI-43. Lattice image of a precipitated V_3Ga in the annealed V-18 at.% Ga sample aged at 700°C for 4 days.

V– 15.6% Ga, 75% Def., 700°C/ 1 D

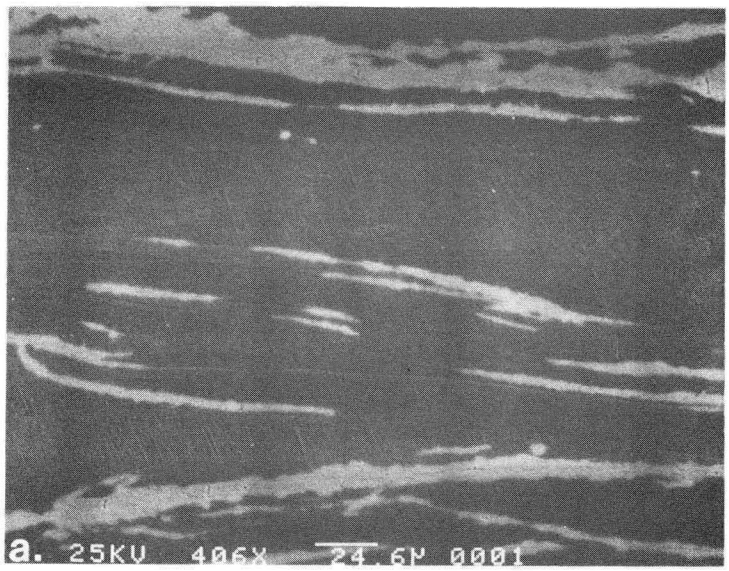

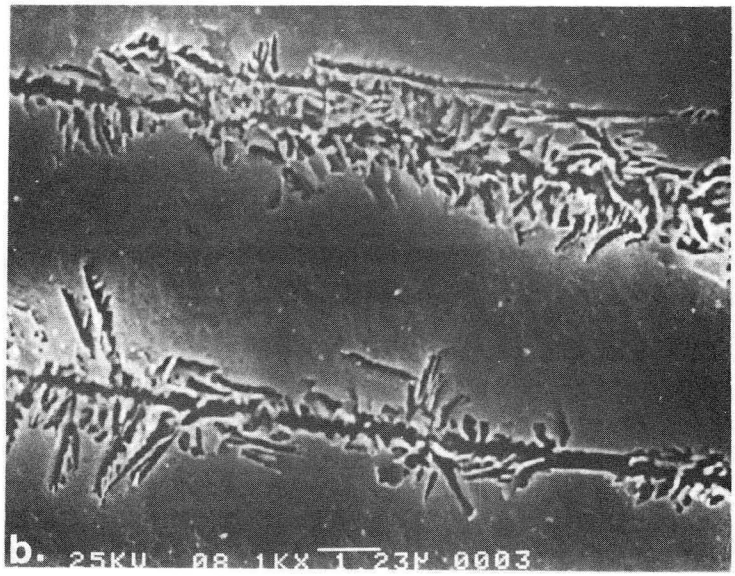

Fig. VI-44. Scanning electron micrographs of V-15.6 at.% Ga deformed 75% and aged at 700°C for 1 day showing the heterogeneous nature of V_3Ga precipitation.

XBB 836-5391

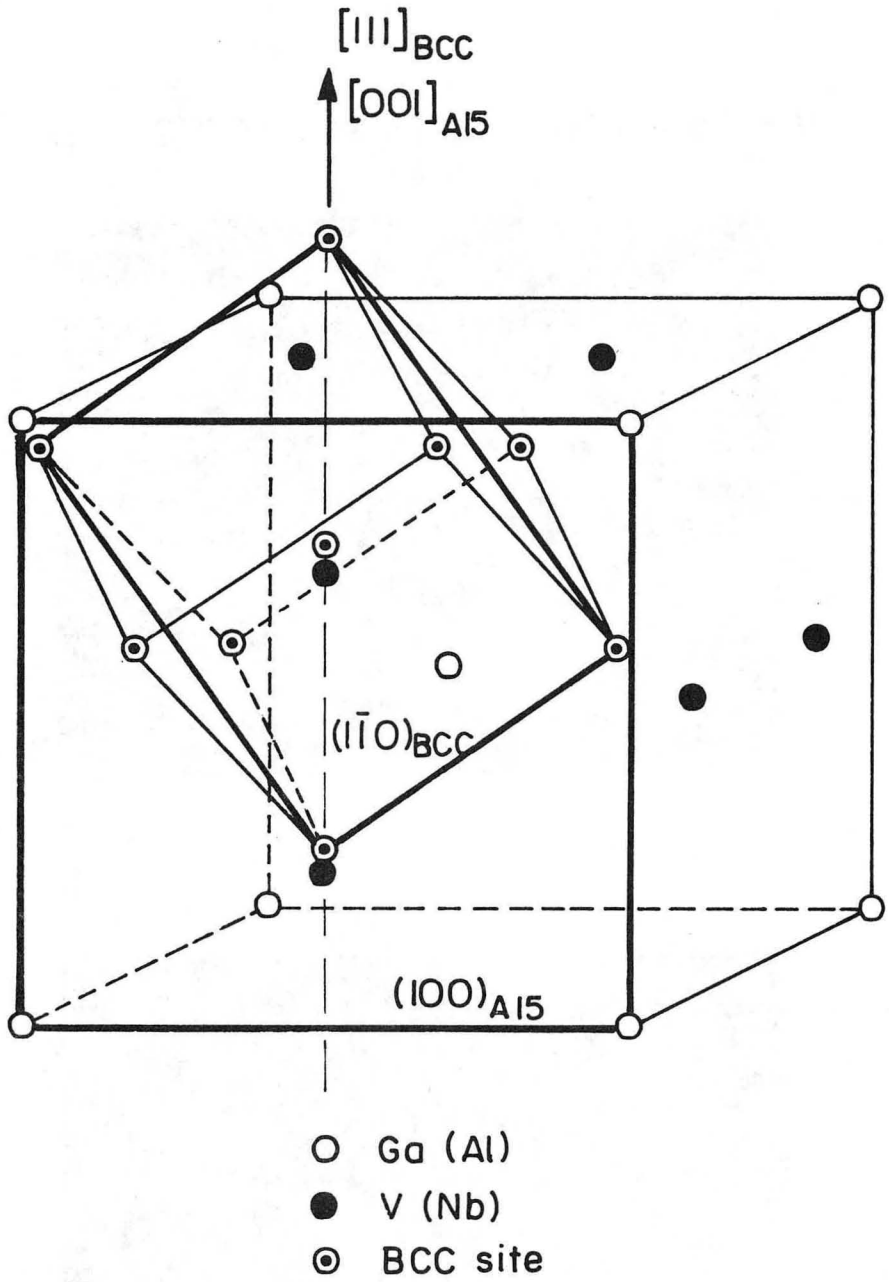

XBL 812-5194

Fig. VI-45. The superimposed conventional unit cells of BCC and A15 structures with the parallel planes (heavy lines) and direction (large dashed line) indicated.

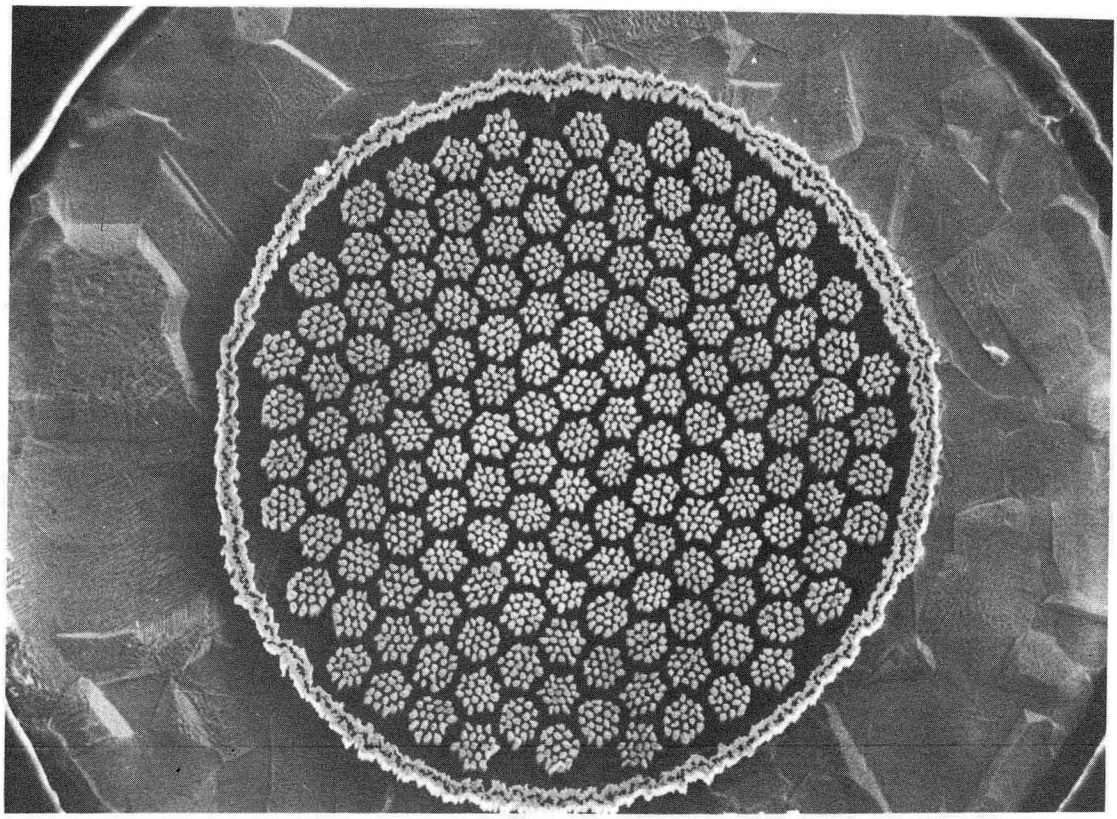

25 KV 173× 57.8 μm XBB 831-546

Fig. VII-1. A scanning electron micrograph of the cross section of a typical multifilamentary Nb_3Sn wire sample.

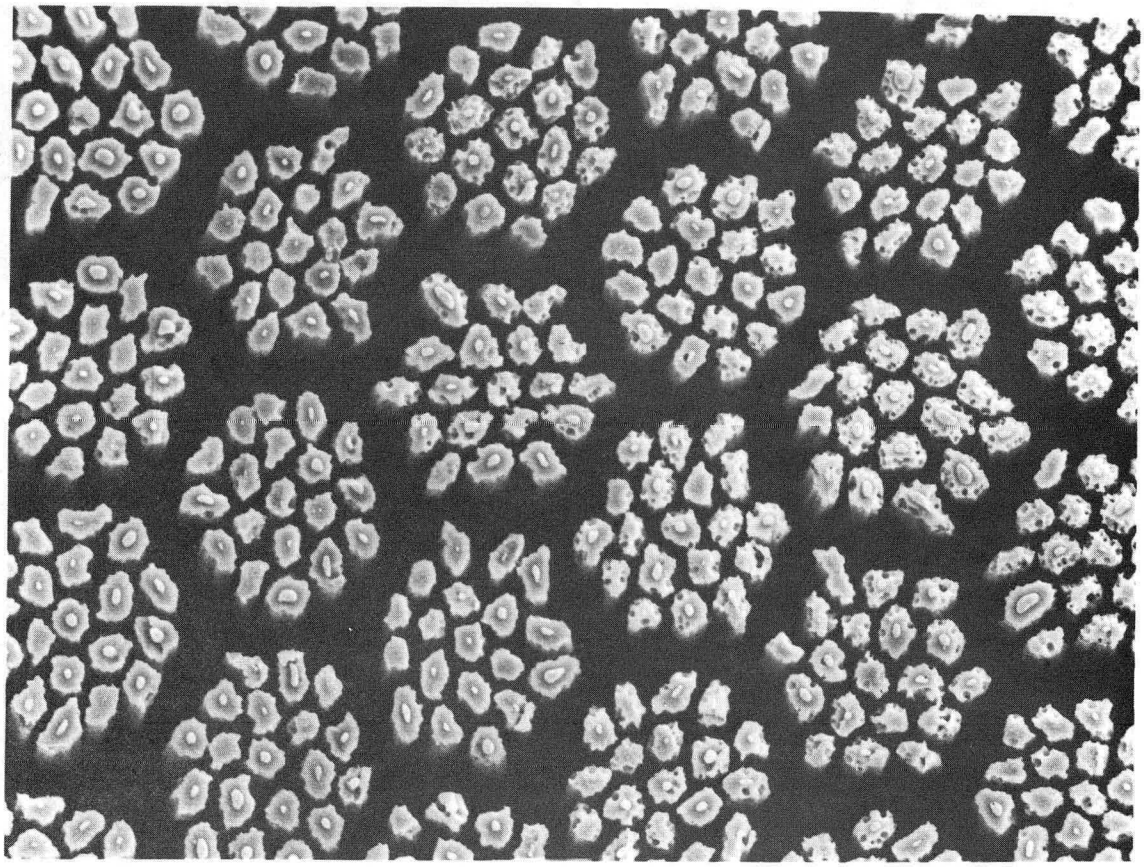

25 KV 860× 11.6μm XBB 831-957

Fig. VII-2. A scanning electron micrograph showing the reacted A15 layer around the filaments. The sample was heat treated at 700°C for 6 days.

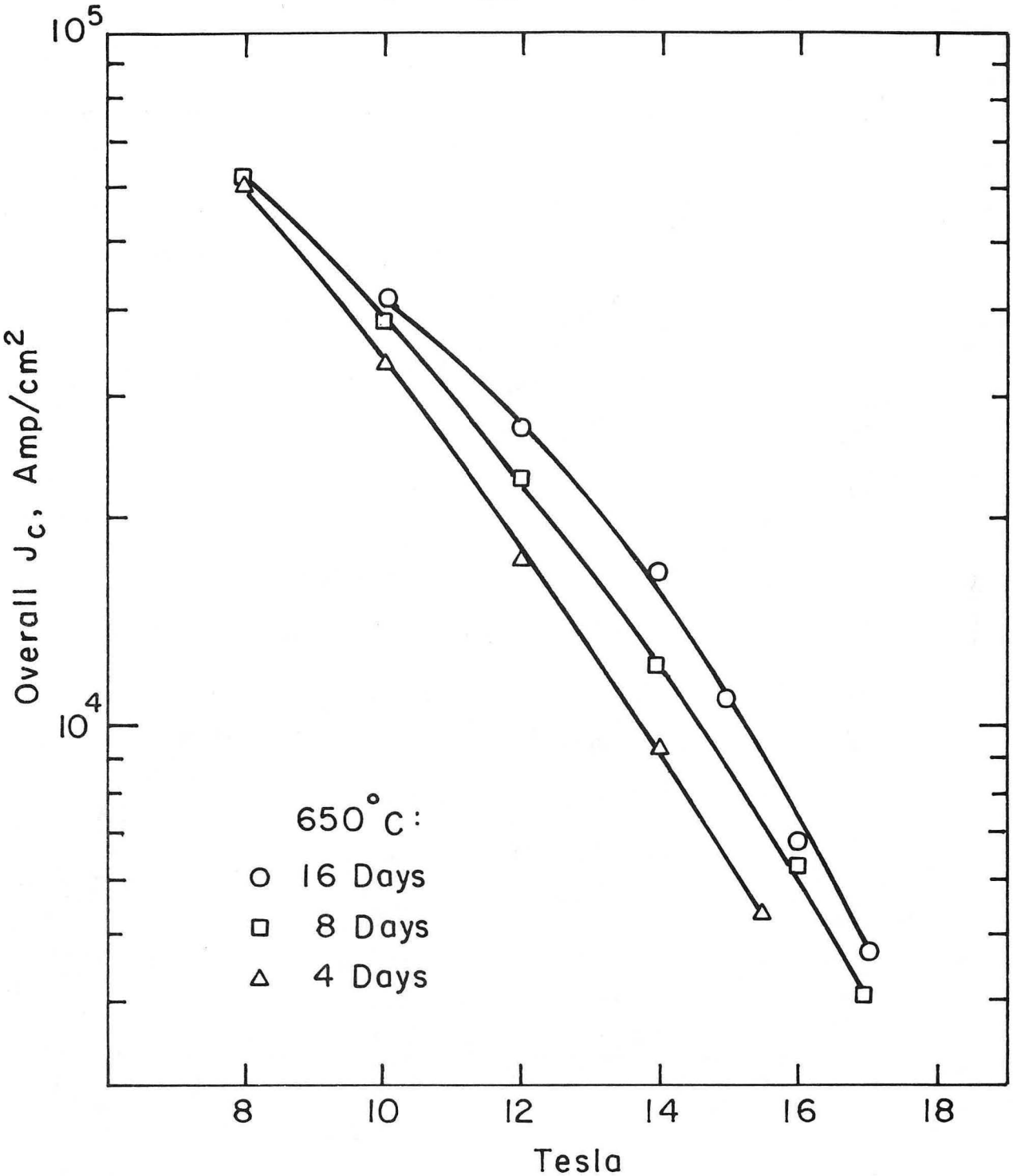

XBL 822-5156

Fig. VII-3. The critical current characteristics, $J_c(H)$, for samples reacted at 650°C for 4, 8, and 16 days.

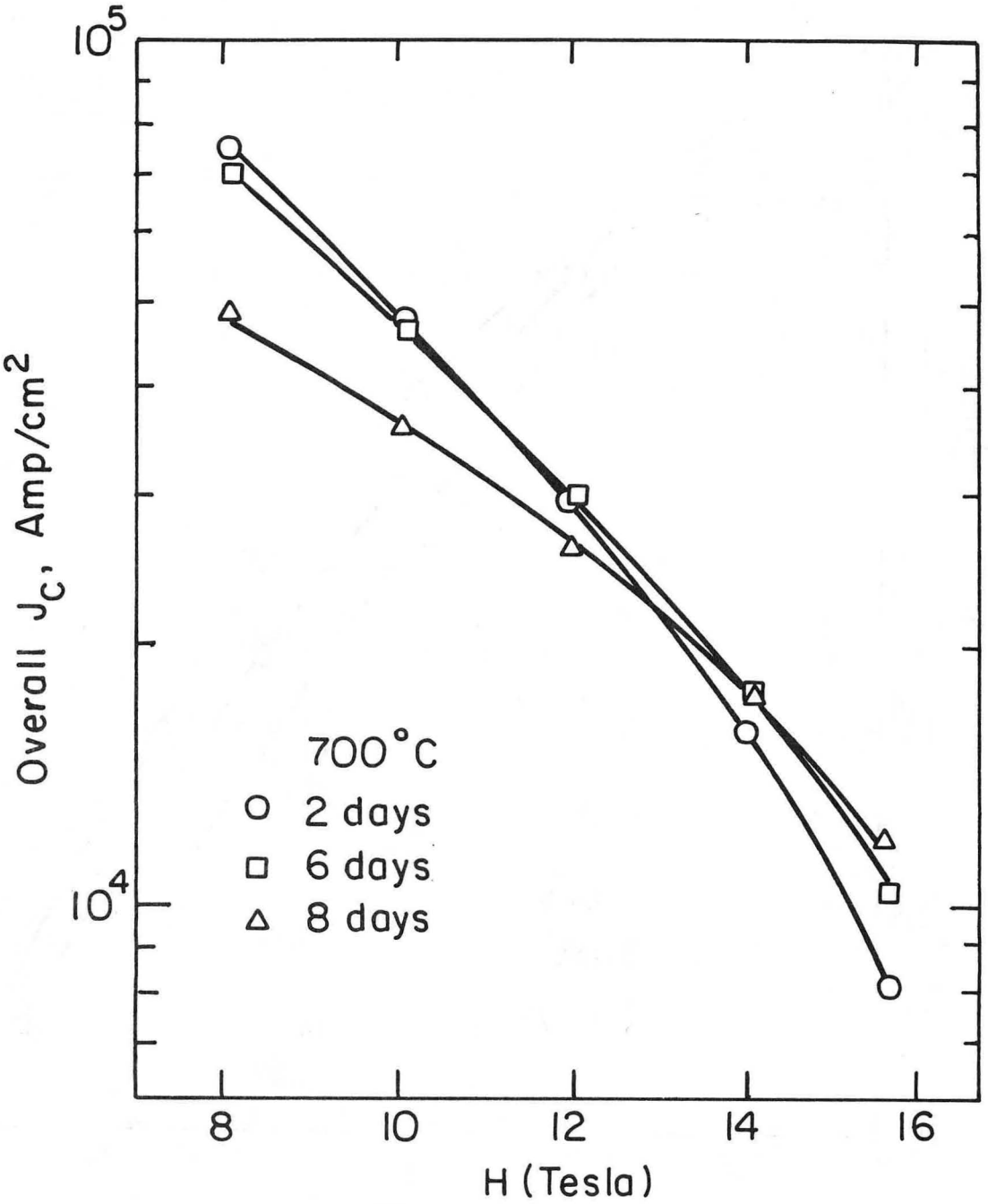

XBL 831-5058

Fig. VII-4. The critical current characteristic, $J_c(H)$, for samples reacted at 700°C for 2, 6, and 8 days.

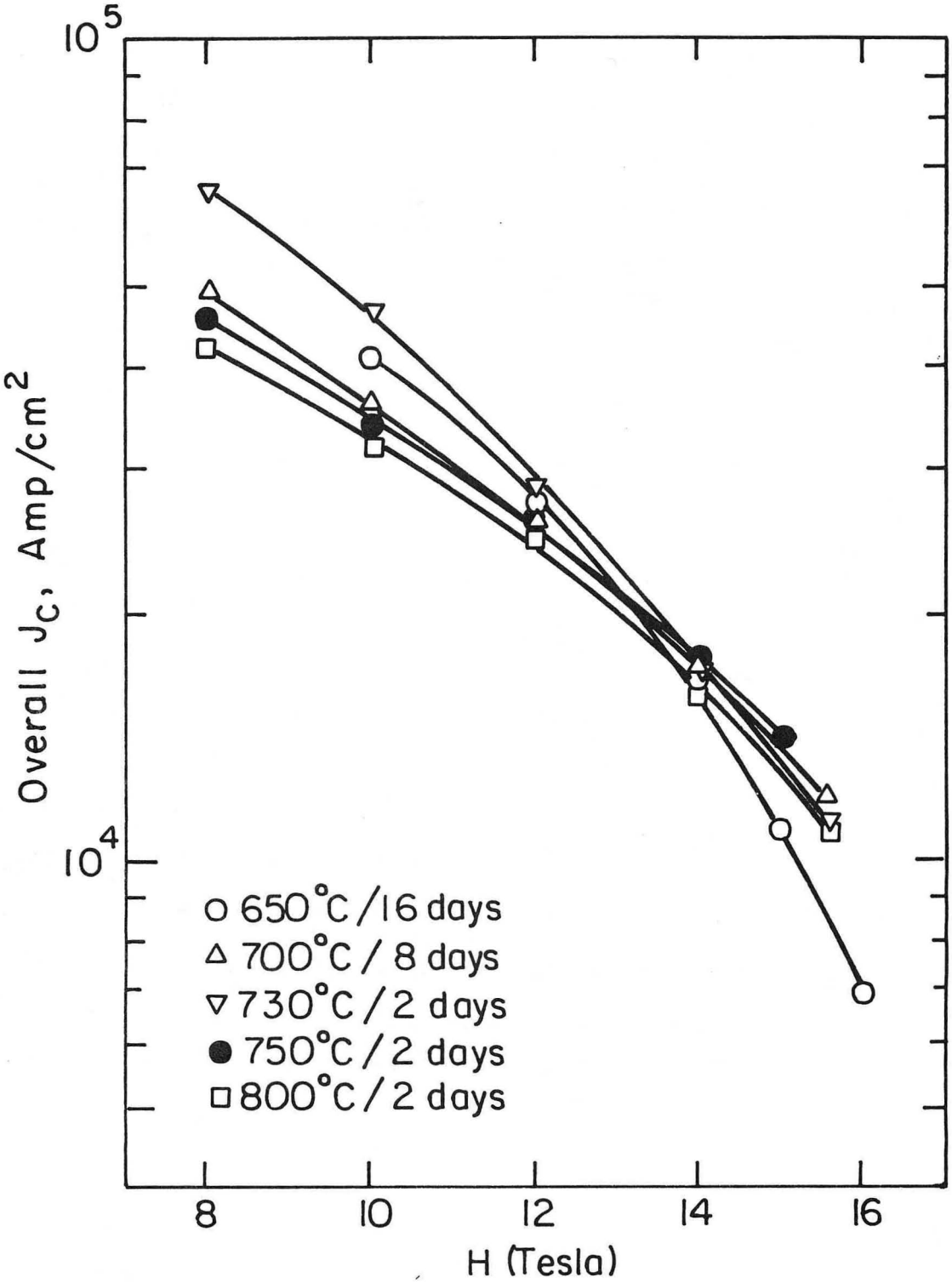

XBL 831-5059

Fig. VII-5. The critical current characteristic, $J_c(H)$, for samples that were isothermally aged to essentially complete reaction at 650, 700, 730 and 800°C.

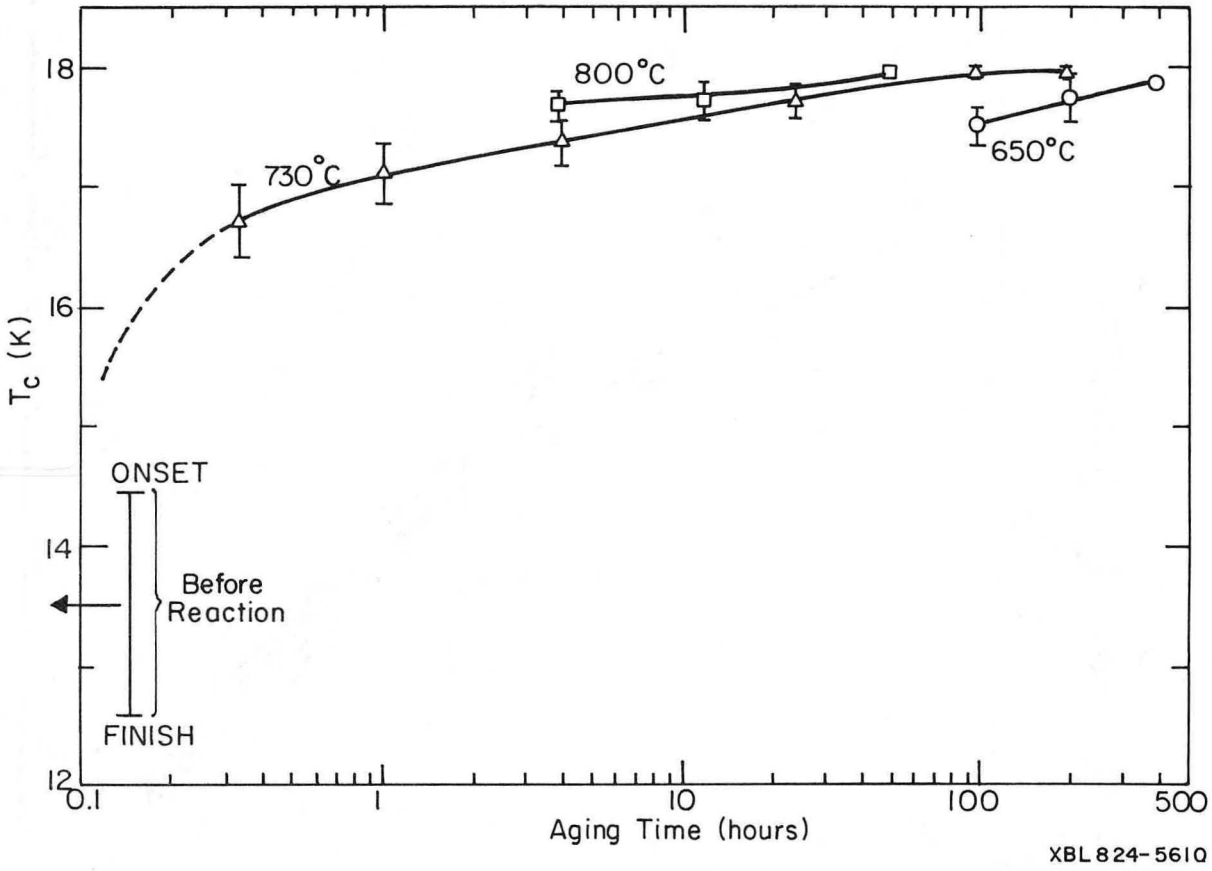

Fig. VII-6. The inductive superconducting transition temperature, T_c, as a function of aging time for samples that were isothermally reacted at 650, 730 and 800°C.

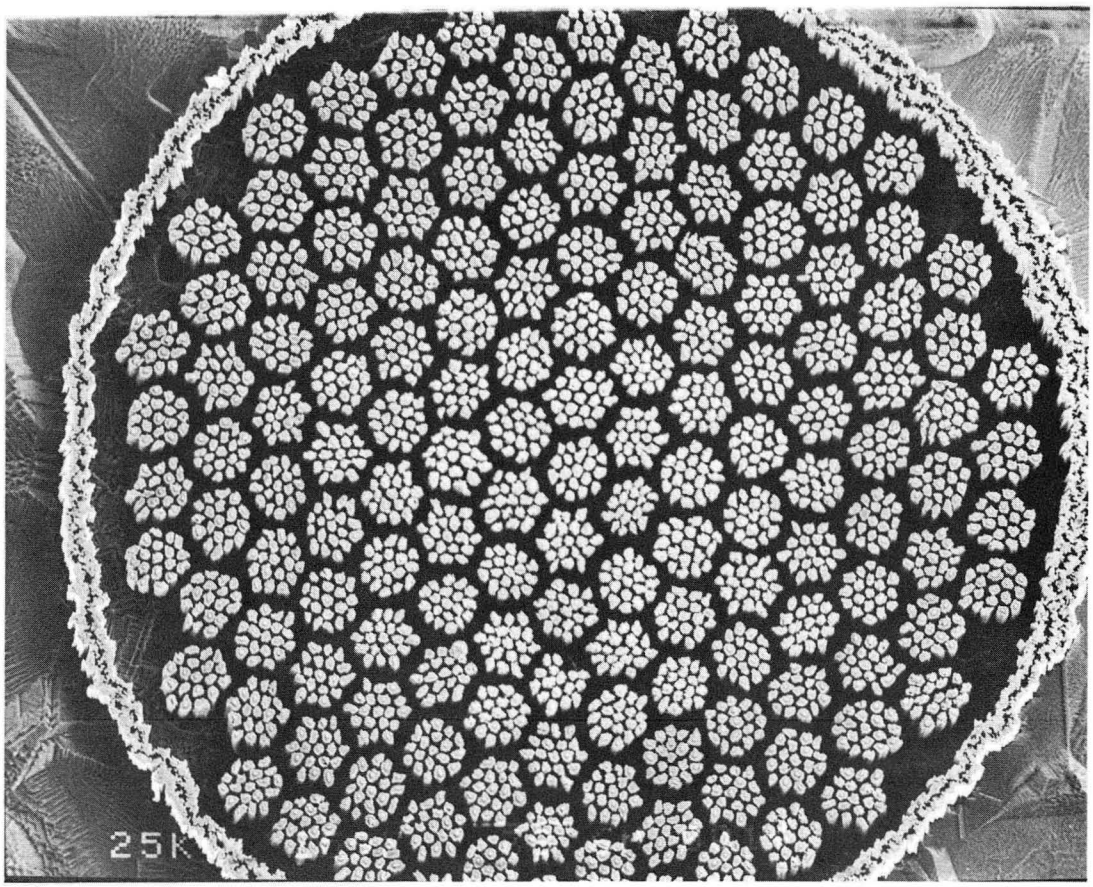

XBB 831-544

Fig. VII-7. A scanning electron micrograph showing the core configuration and Ta diffusion barrier which constrains the expansion of the bronze matrix. The sample was heat treated at 730°C for 2 days.

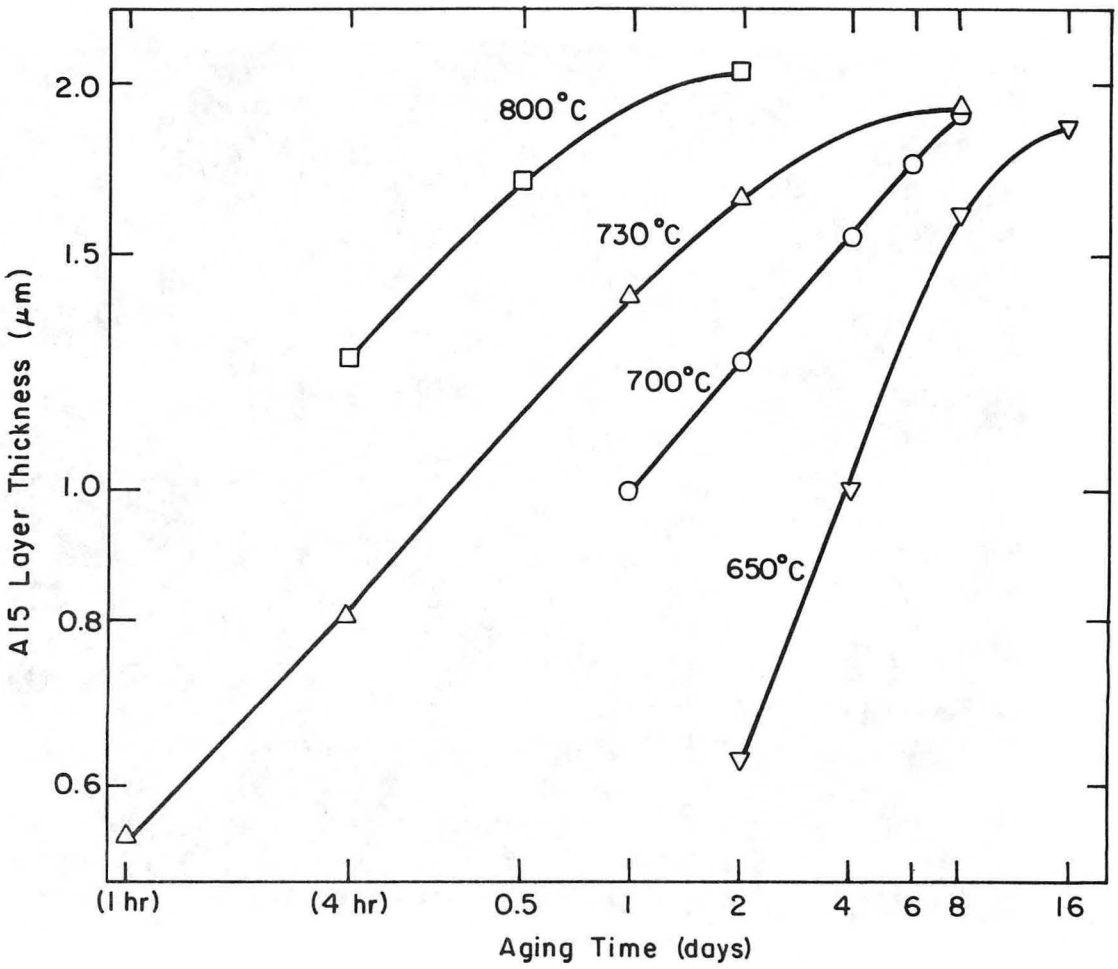

XBL832-5296

Fig. VII-8. The average A15 layer thickness as a function of aging time for samples that were reacted isothermally at 650, 700, 730 and 800°C.

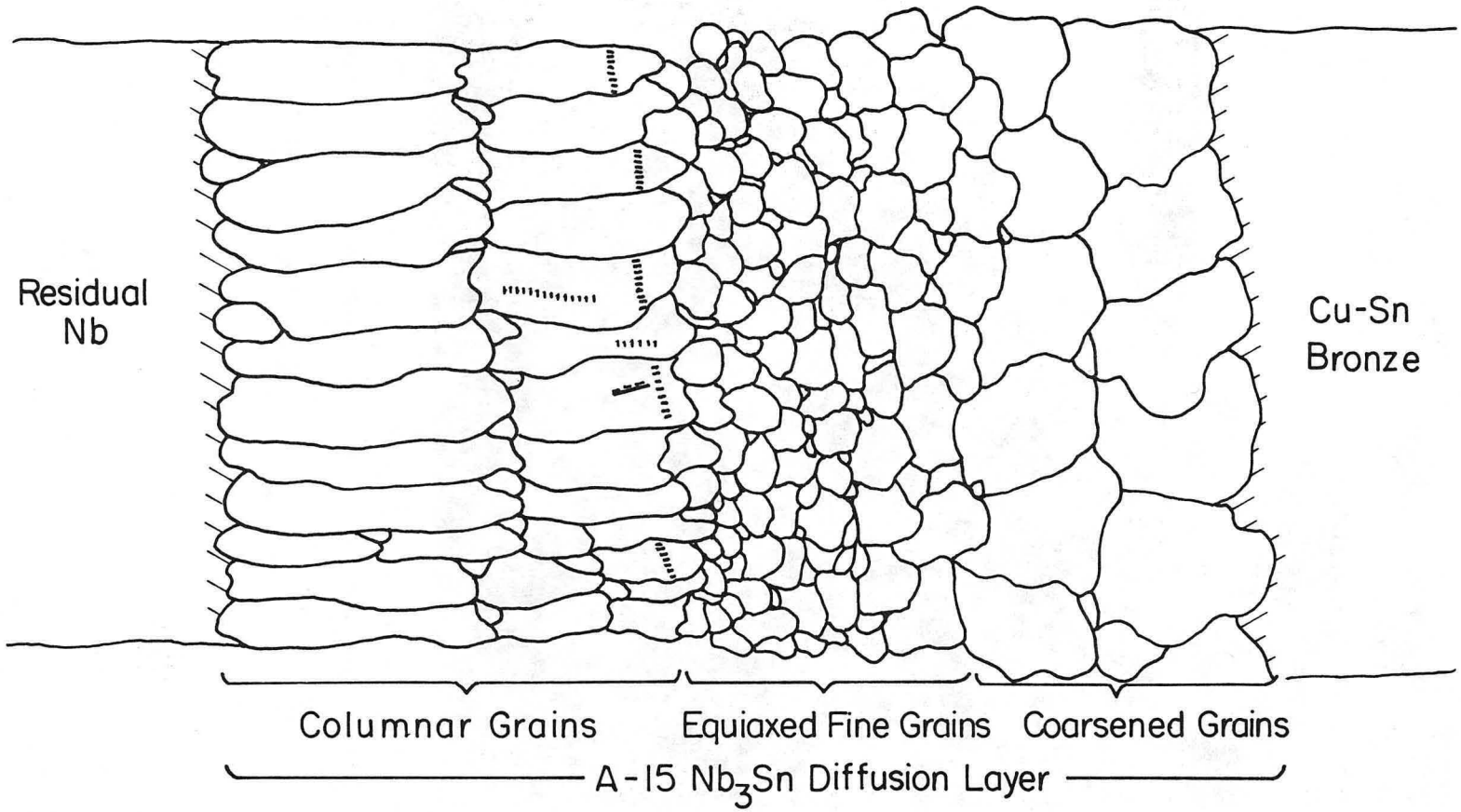

XBL 824-5549

Fig. VII-9. Schematic representation of the overall morphology of a reacted A15 layer (a) with an overlay showing an idealized Sn composition profile through the layer (b).

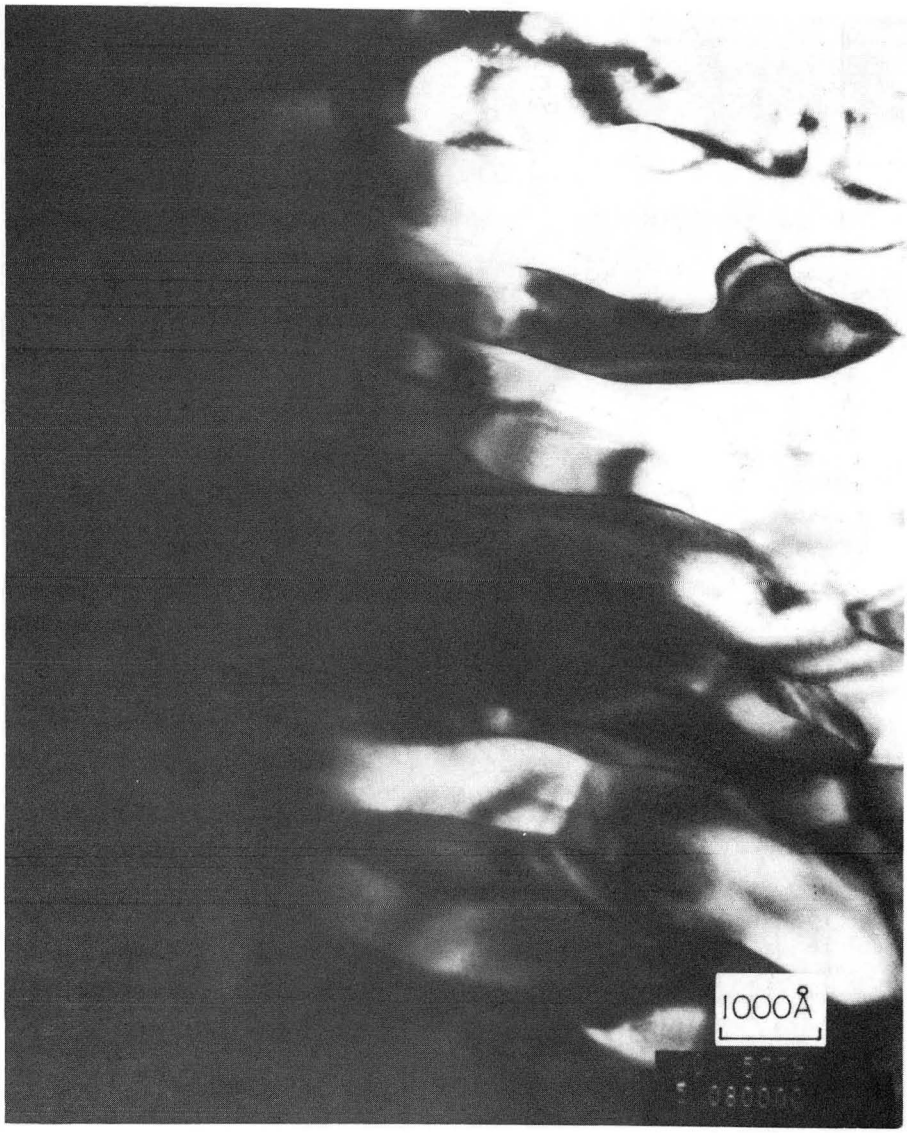

XBB 818-7133

Fig. VII-10. Transmission electron micrograph of the columnar A15 grains near the Nb core of the sample aged at 730°C for 2 days.

Fig. VII-11(a) XBB 822-1159

Fig. VII-11. The selected area diffraction pattern (a) and the corresponding bright field micrograph (b) showing the columnar nature of the A15 grains near the Nb interface. The sample was aged at 750°C for 2 days.

Fig. VII-11(b) XBB 818-7140

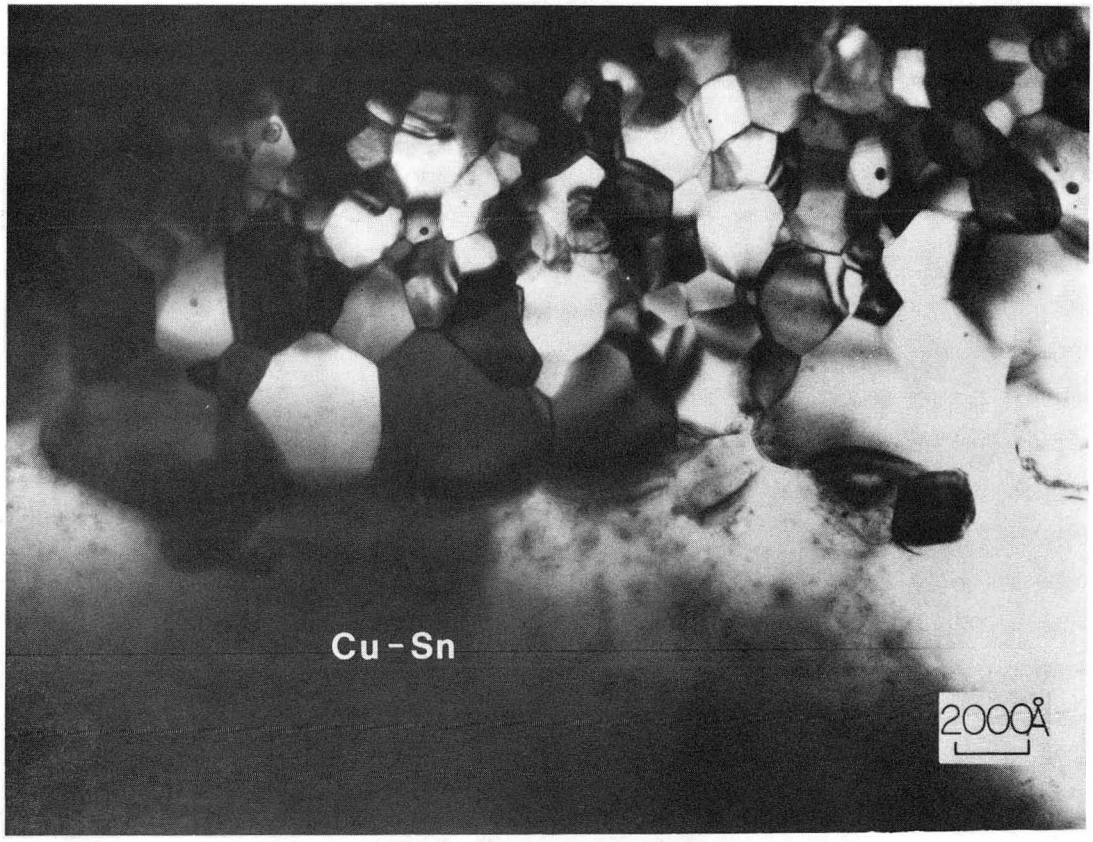

XBB 824-4088

Fig. VII-12. Transmission electron micrograph of the A15 grains within the fine-grained and coarse-grained shells in the reacted layer of the sample aged at 700°C for 8 days.

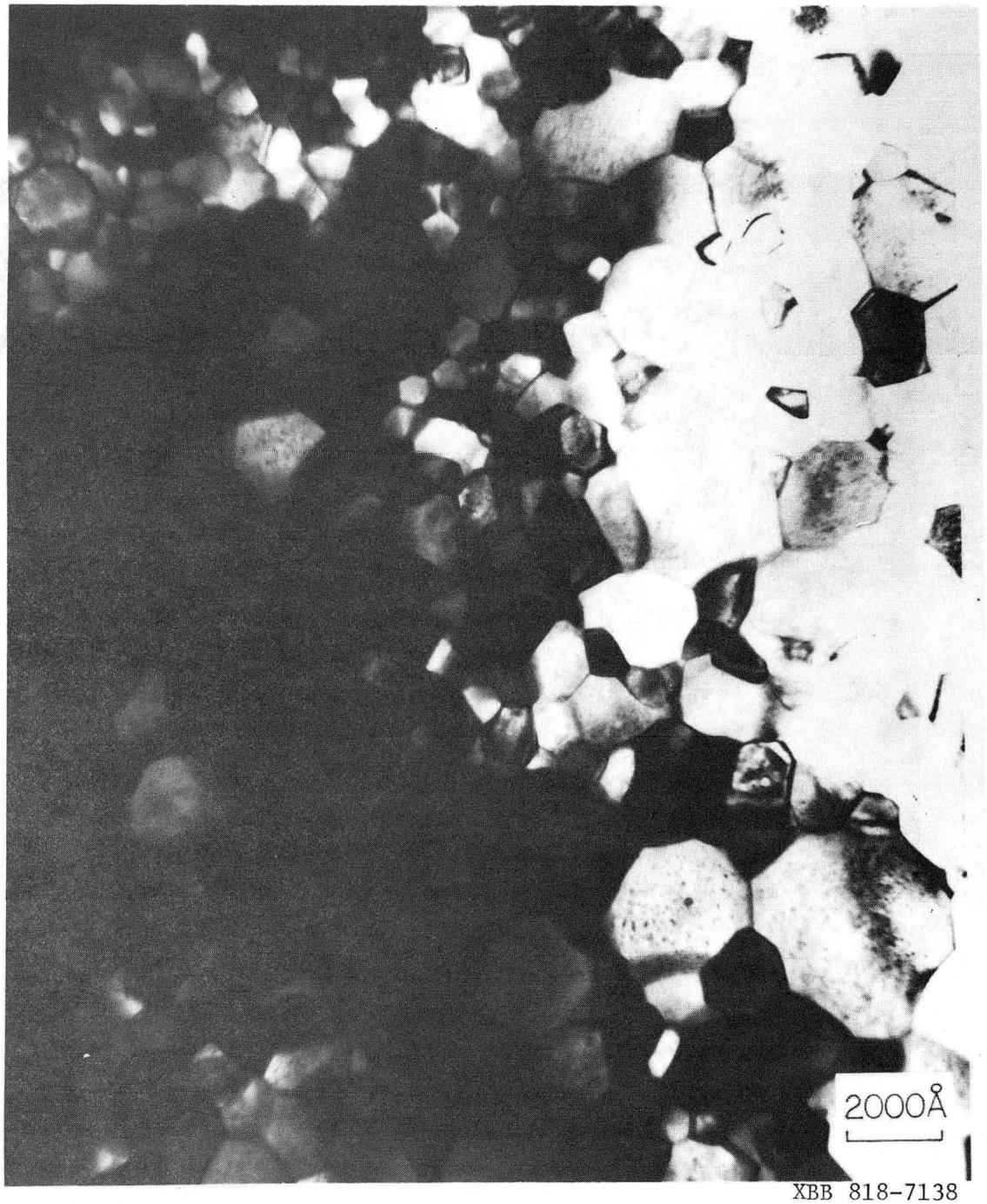

XBB 818-7138

Fig. VII-13. Transmission electron micrograph of the fine-grained region and large-coarsened grains of the reacted layer for the sample aged at 730°C for 2 days.

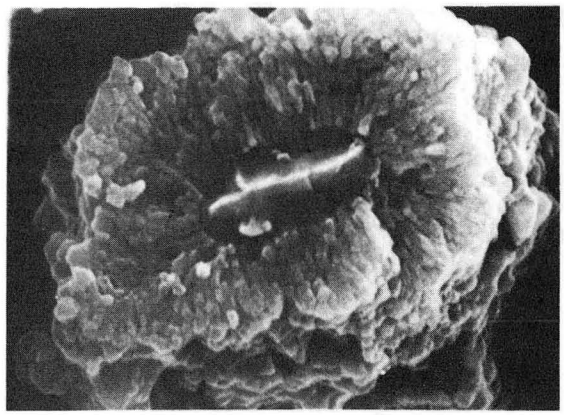

a. 25 KV 18.4 KX 544 nm
650°C / 16 DAYS

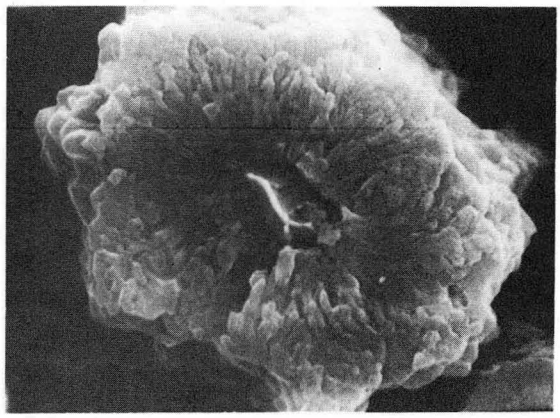

b. 25 KV 18.7 KX 535 nm
700°C / 6 DAYS

XBB 831-226

Fig. VII-14. Scanning electron micrographs showing the fracture surfaces of broken filaments that had been reacted at (a) 650°C for 16 days and (b) 700°C for 6 days. Note that the fine, equiaxed grains in the layer center are not obvious on the fracture surface.

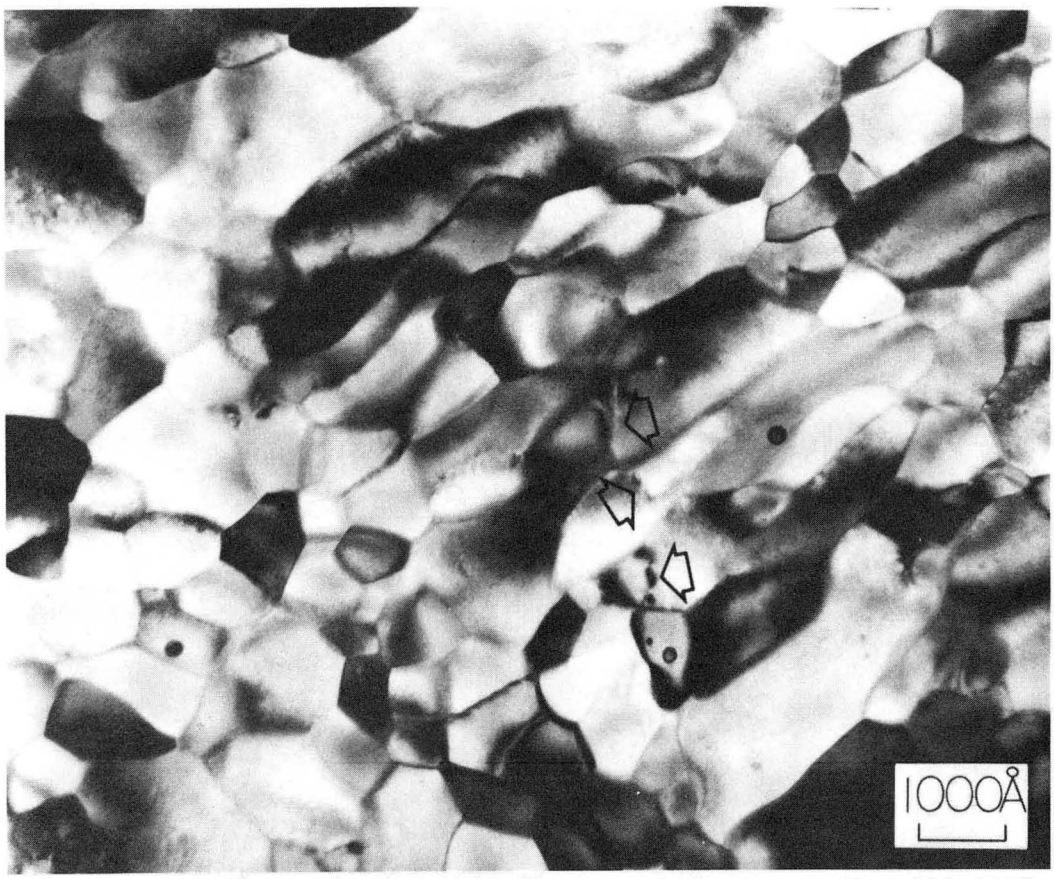

XBB 824-4087

Fig. VII-15. A transmission electron micrograph of a sample aged at 750°C for 2 days, showing the columnar and fine-grained shells. Note that the grain boundaries in the fine-grained shell are primarily low angle boundaries.

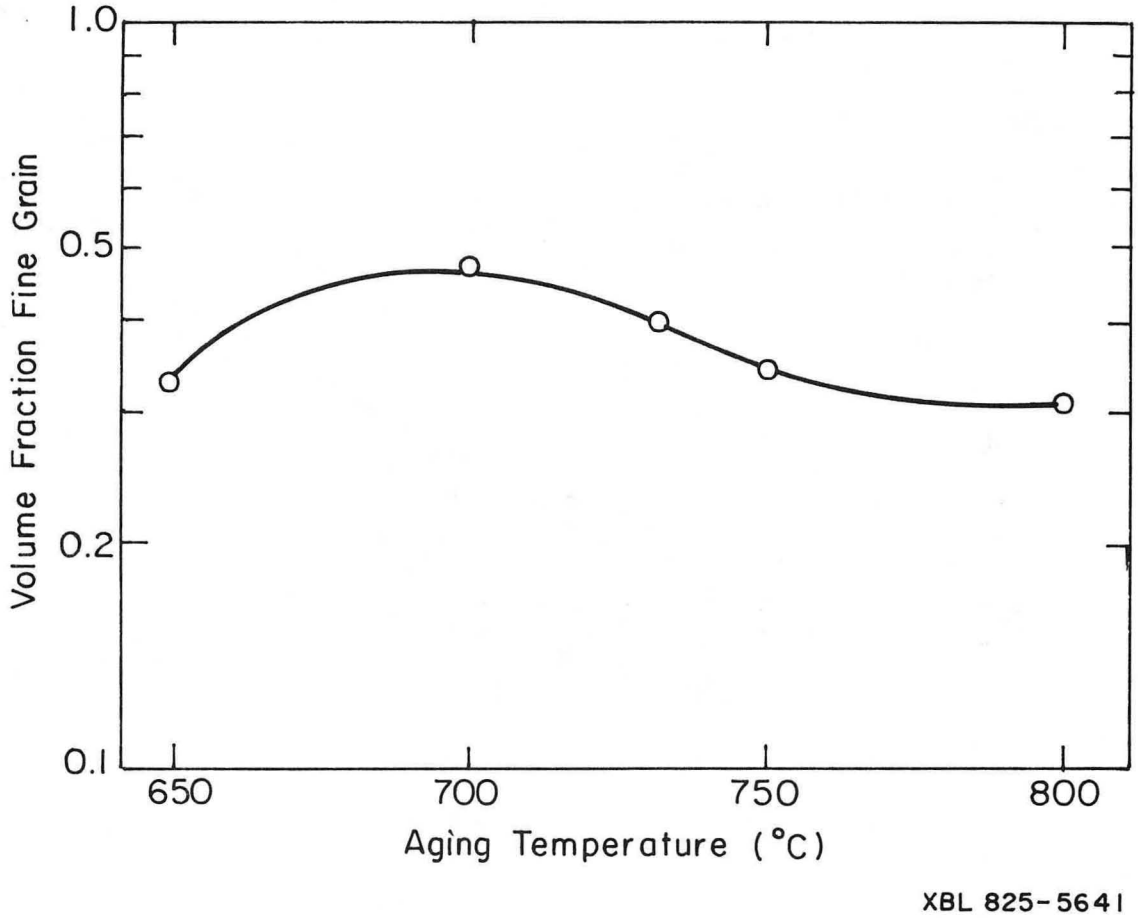

Fig. VII-16. The areal fraction of the fine-grained shell, relative to the original cross section of the Nb filament, as a function of the aging temperature for wires that were aged to essentially complete reaction.

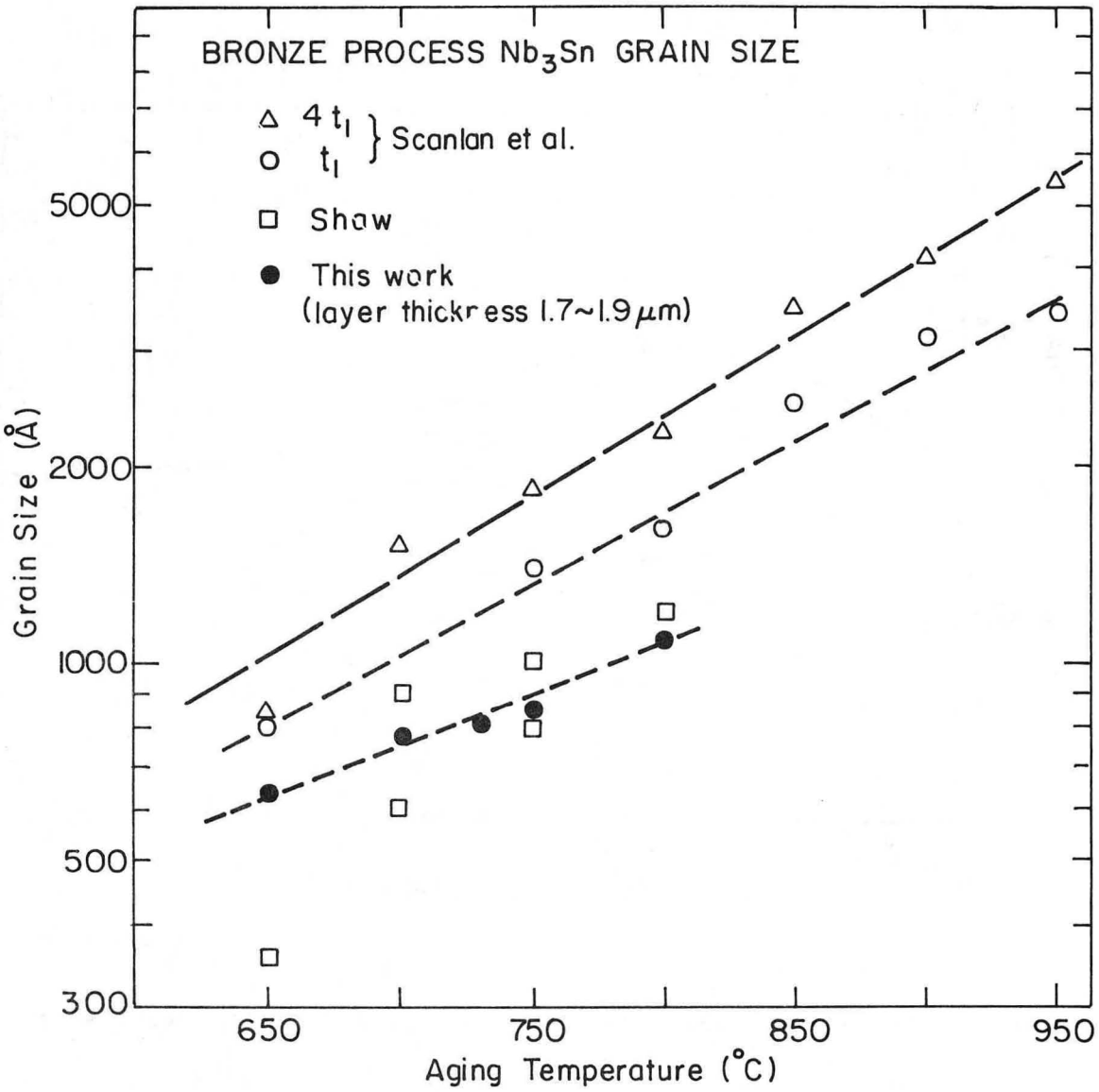

XBL 824-5611

Fig. VII-17. The average grain size within the fine-grained shell as a function of the aging temperature for samples that were isothermally aged to essentially complete reaction. The data of Scanlan et al. [6] and Shaw [7] are included for comparison.

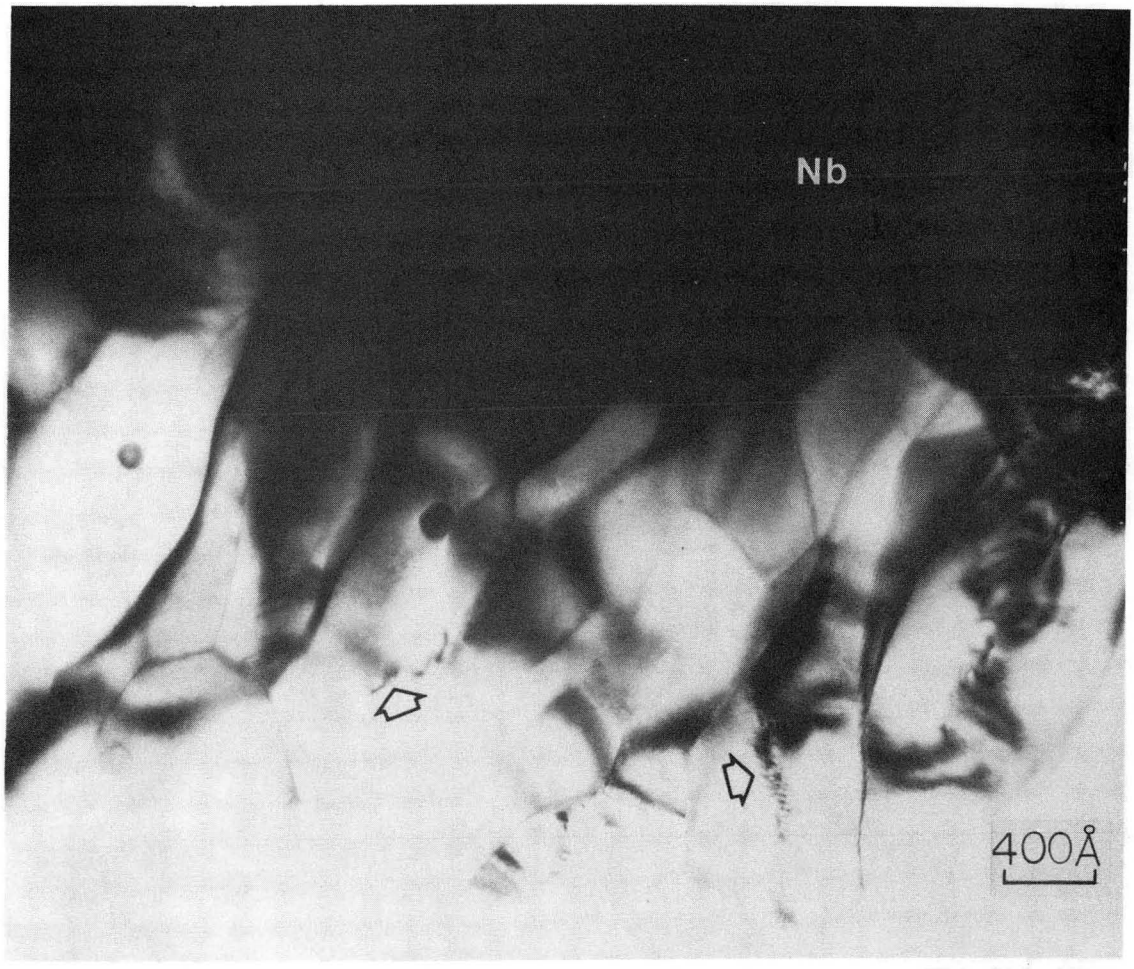

XBB 824-4085

Fig. VII-18. A high resolution transmission electron micrograph of A15 grain morphology near the A15 core. The generation of Frank-Reed type dislocations were evident (arrows). The sample was reacted at 650°C for 16 days.

XBB 824-4086

Fig. VII-19. A transmission electron micrograph under a suitable diffraction condition showing the dislocation pile-ups in the columnar grains for sample reacted at 700°C for 8 days.

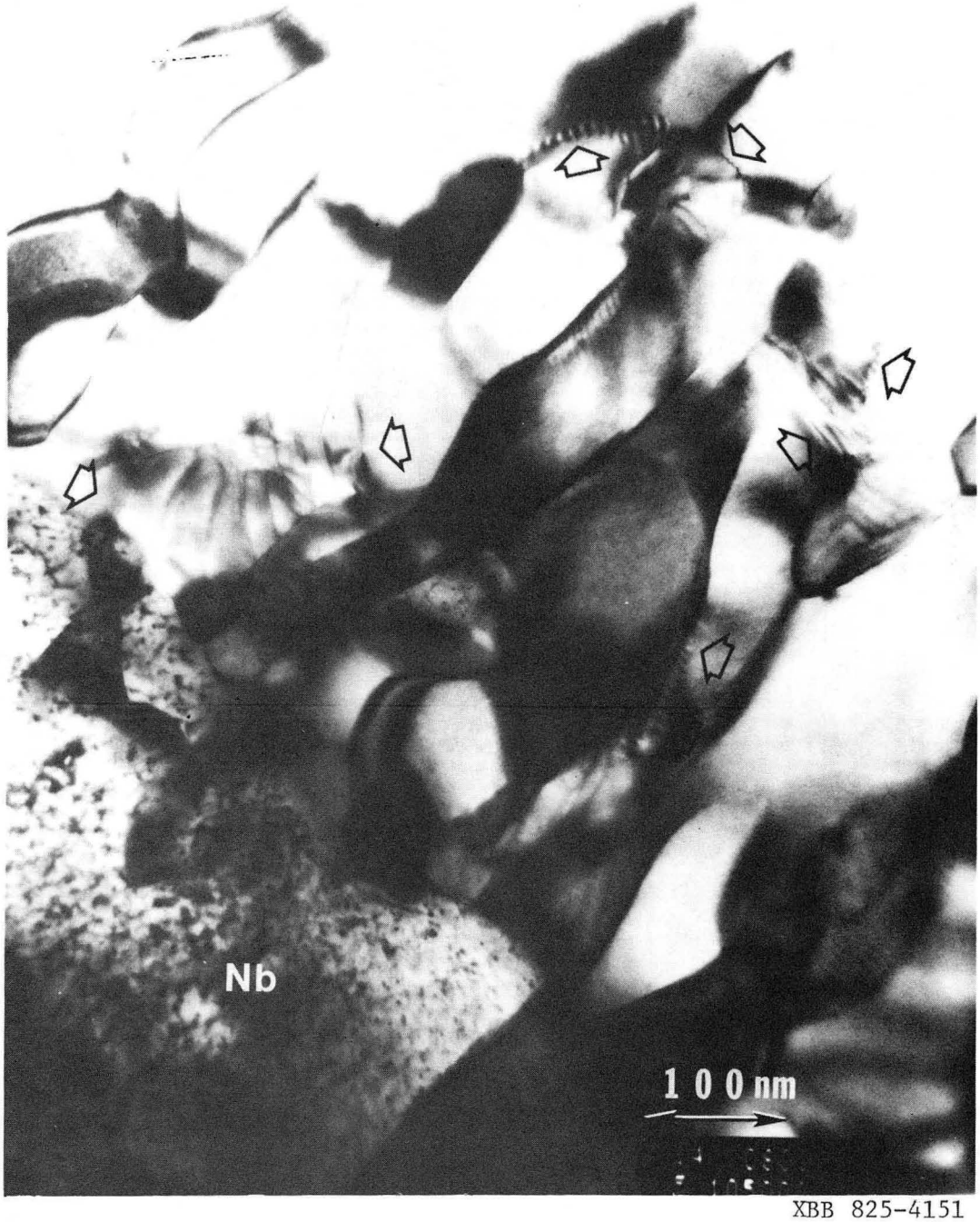

XBB 825-4151

Fig. VII-20. A high resolution transmission electron micrograph showing dislocation pileups in the columnar grains. The sample was isothermally aged at 700°C for 6 days.

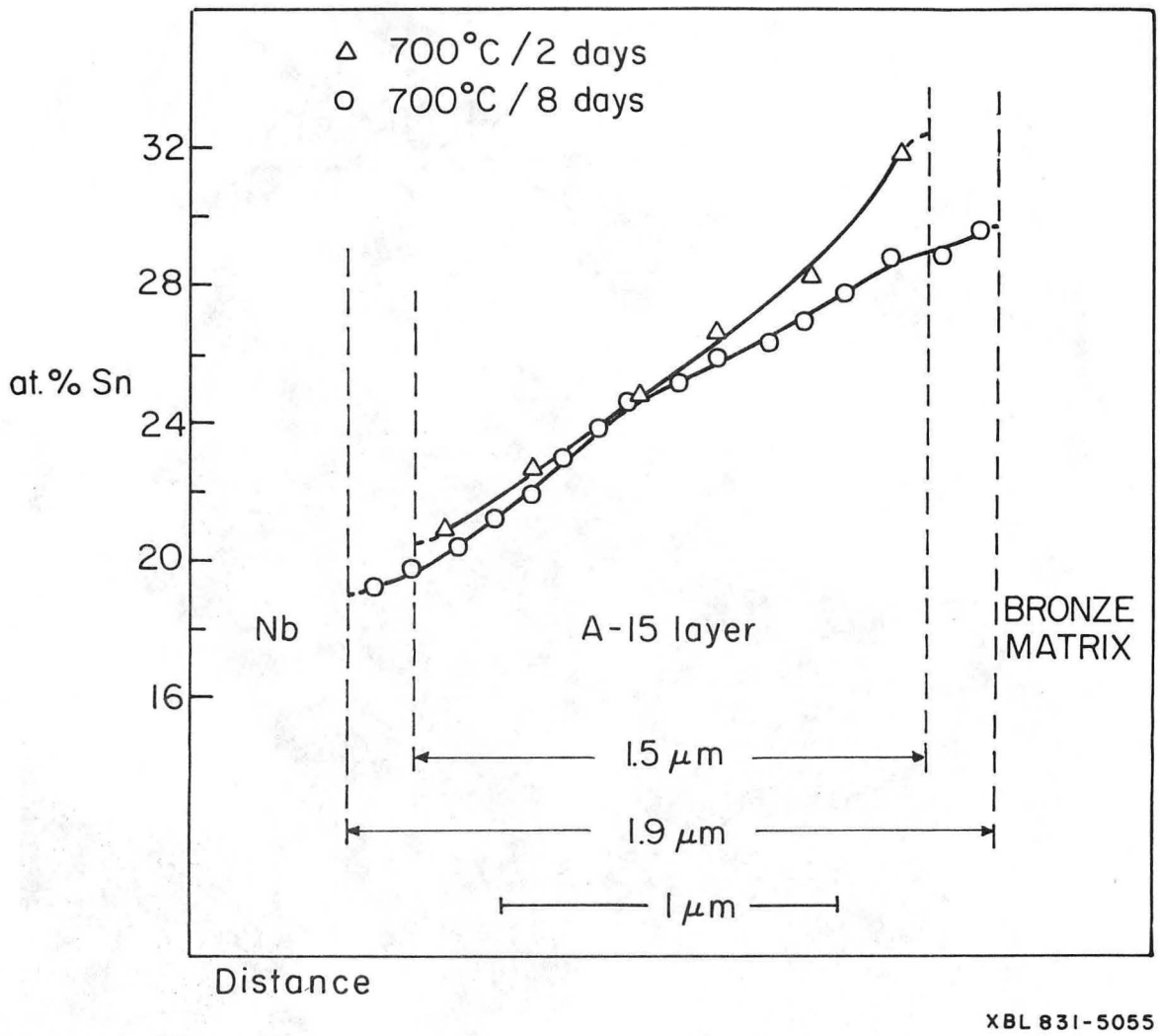

Fig. VII-21. The Sn concentration profile across the reacted layer, as determined by STEM/EDXS analysis for samples aged isothermally at 700°C for 2 and 8 days.

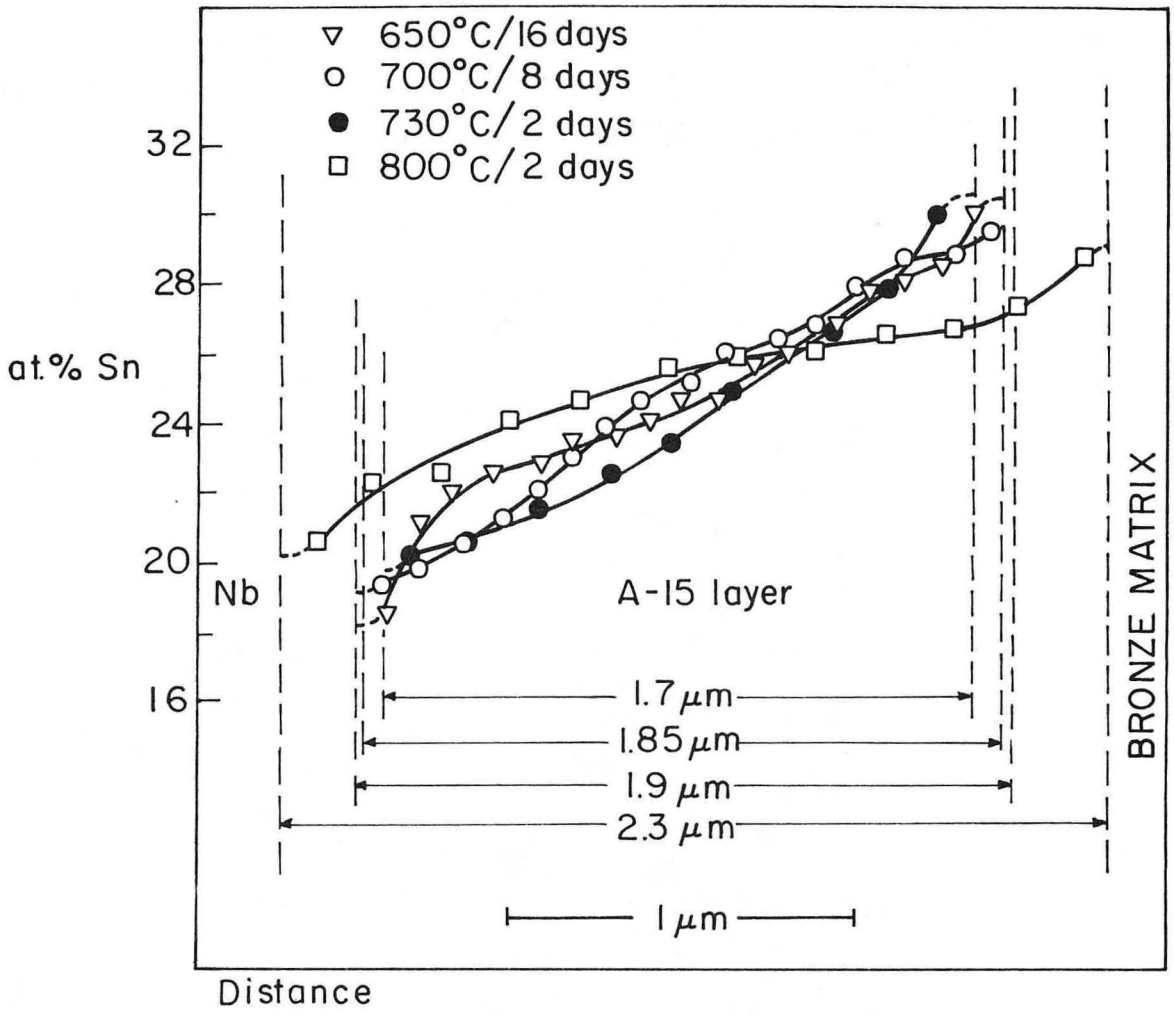

XBL 831-5054

Fig. VII-22. The Sn concentration profile across the reacted layer, as determined by STEM/EDXS analysis for samples reacted isothermally to near completion at temperatures in the range 650 to 800°C.

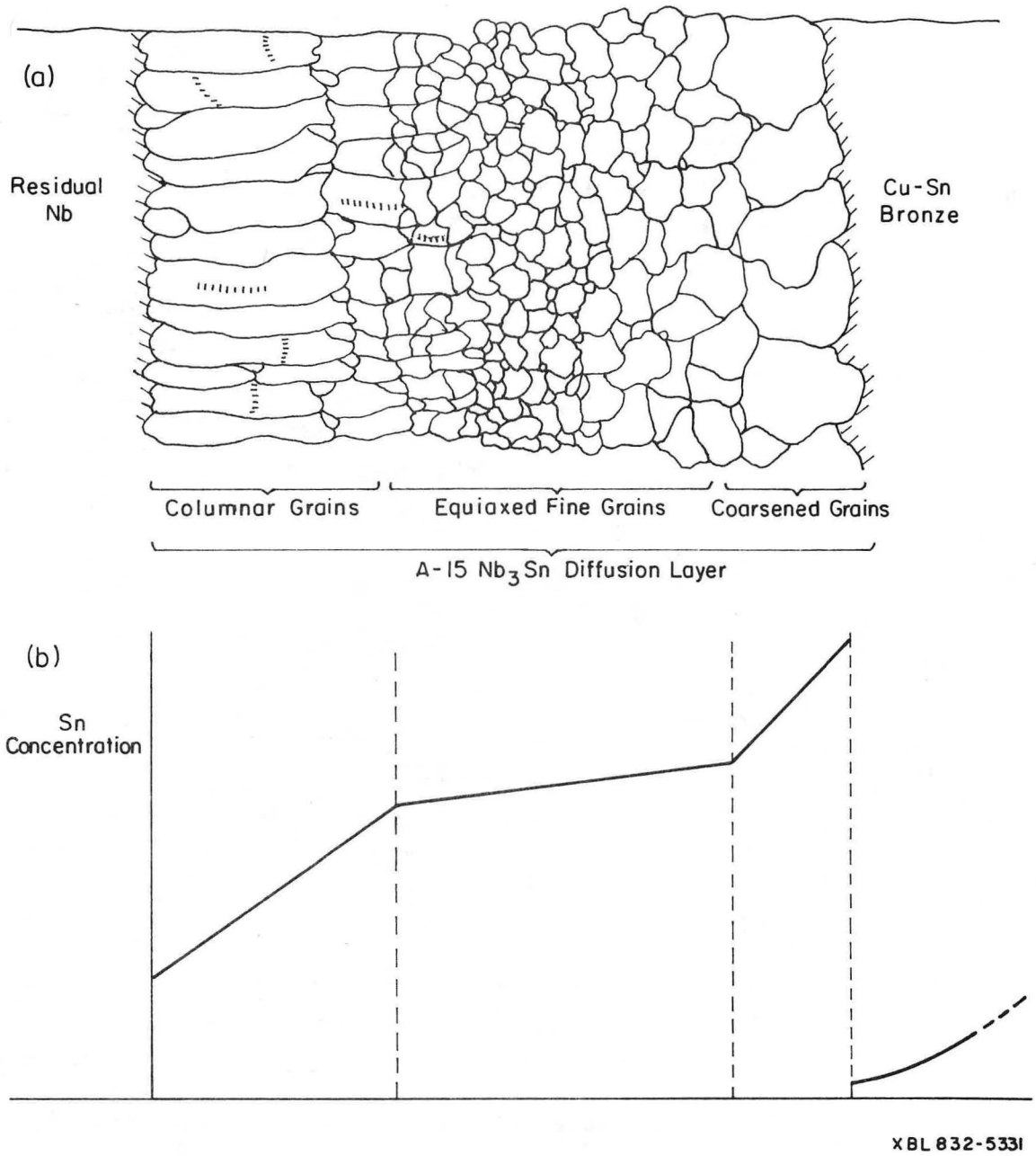

Fig. VII-23. A schematic representation of (a) the grain structure, and (b) the tin concentration profile across the reacted A15 layer.

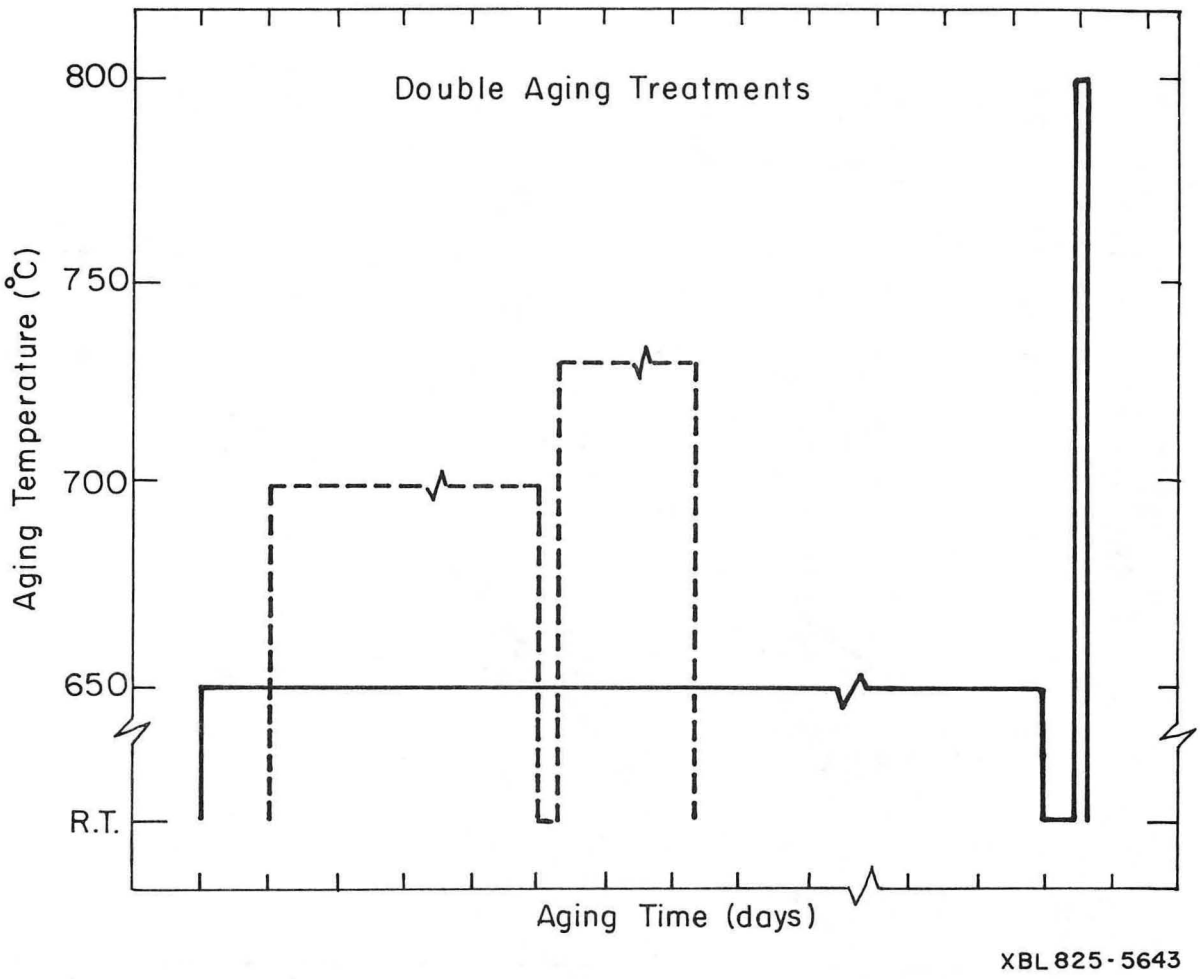

Fig. VII-24. Schematic heat treatment schedules to improve the microstructural state of A15 layers.

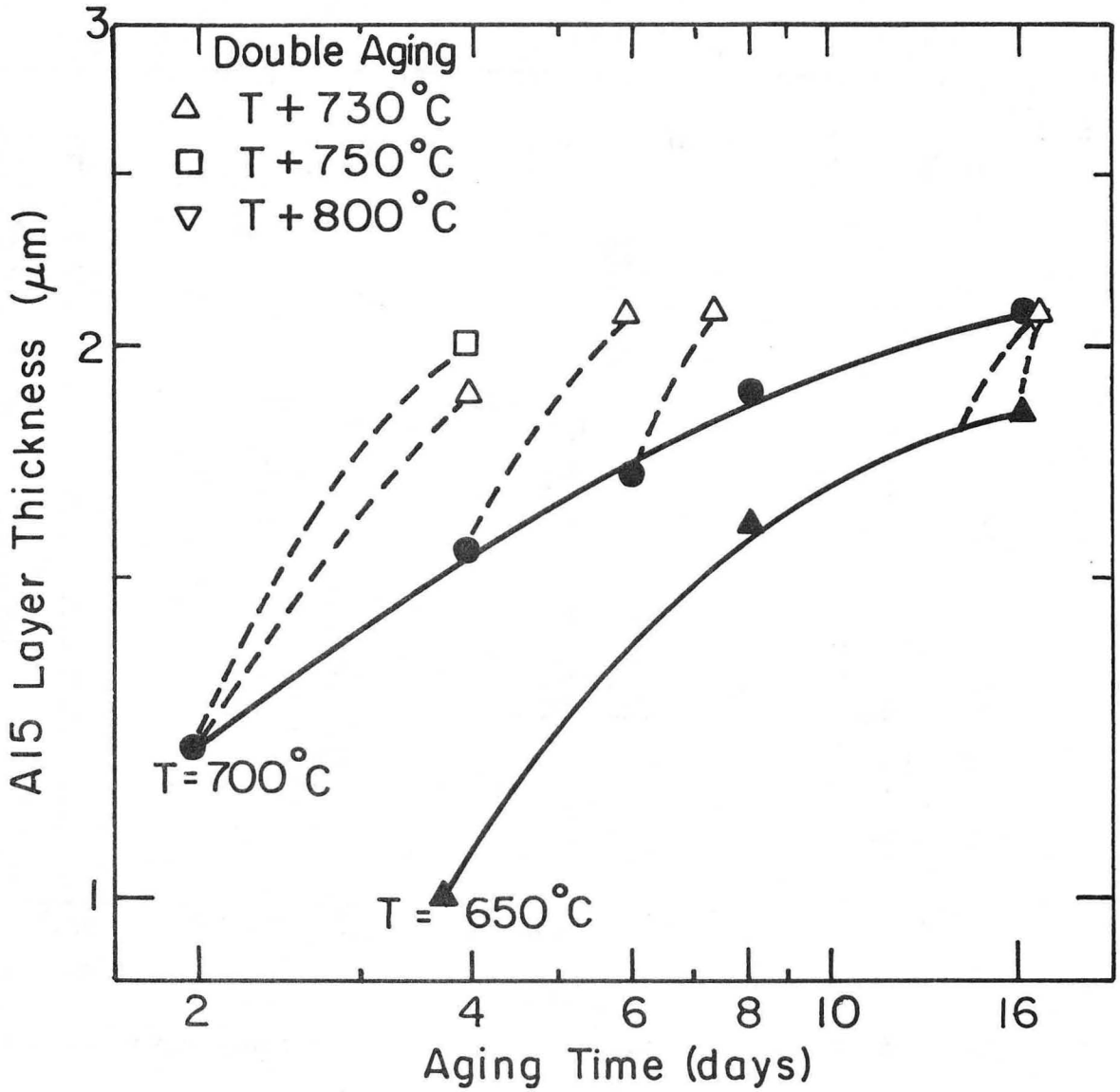

XBL 824-5615

Fig. VII-25. The average thickness of the A15 layer as a function of aging time. The solid lines are for isothermal aging at 650 and 700°C. The dotted lines continue the curves for the temperature and time of double aging.

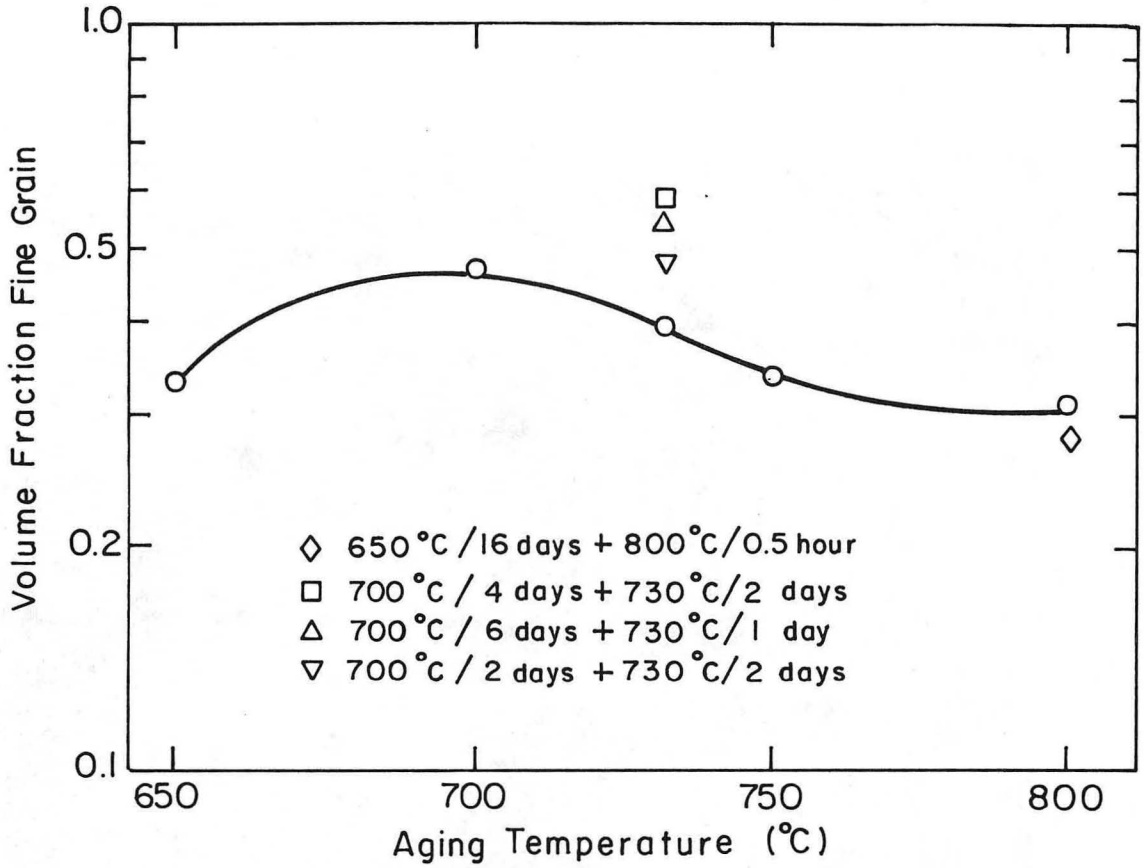

XBL 825-5642

Fig. VII-26. The areal fraction of fine equiaxed grains in the reacted layers of the doubly aged specimens, relative to the original cross section of the Nb filament. The comparable data for singly aged specimens is reproduced from Figure 11.

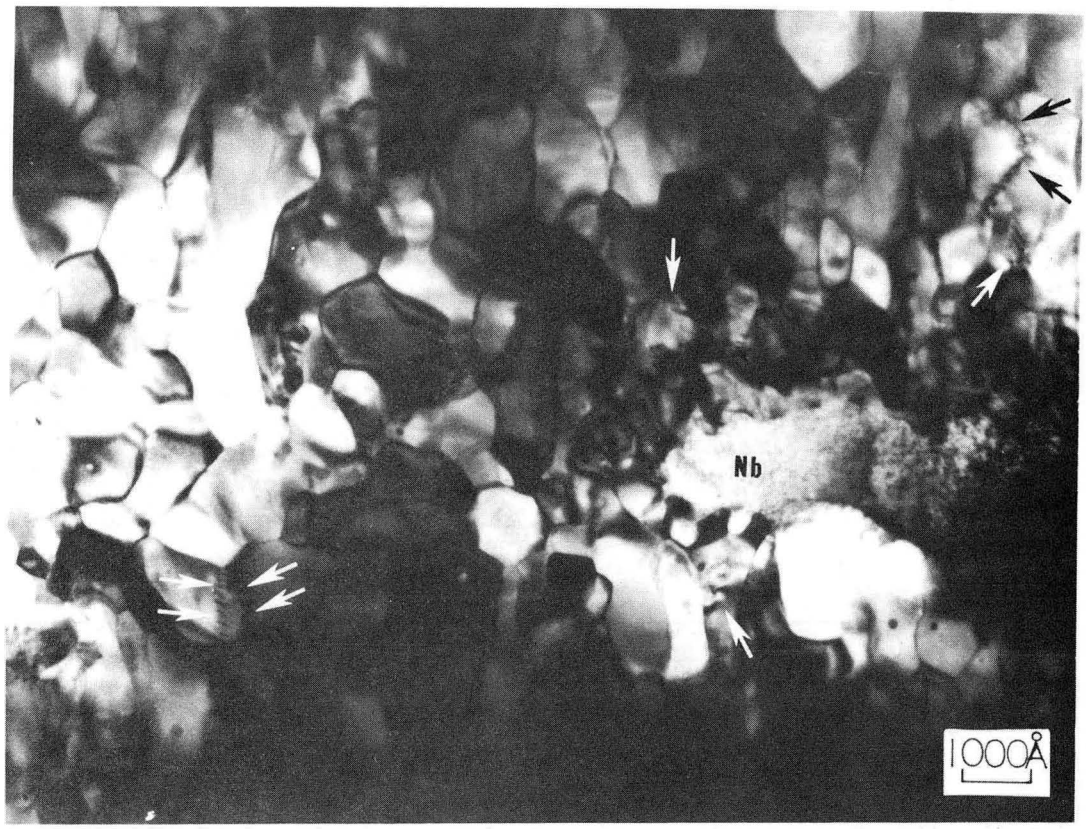

XBB 822-1157

Fig. VII-27. A transmission electron micrograph of the fine-grained shell within a sample that was doubly aged at 700°C for 6 days plus 730°C for 1 day. Examples of dislocation pileups and low angle grain boundaries are indicated by arrows.

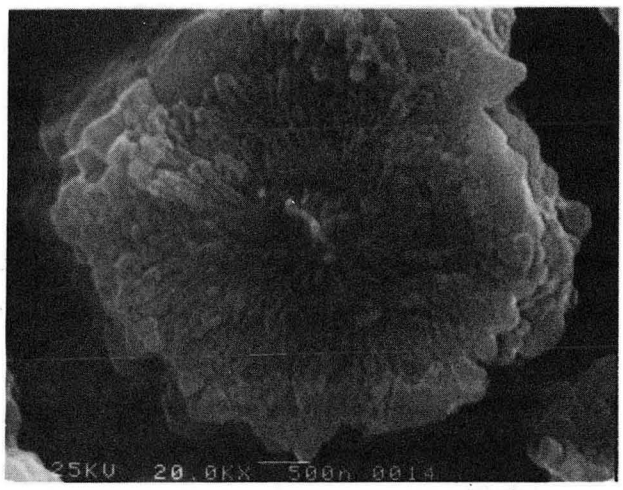

(a) 650°C/14D, 730°C/2D

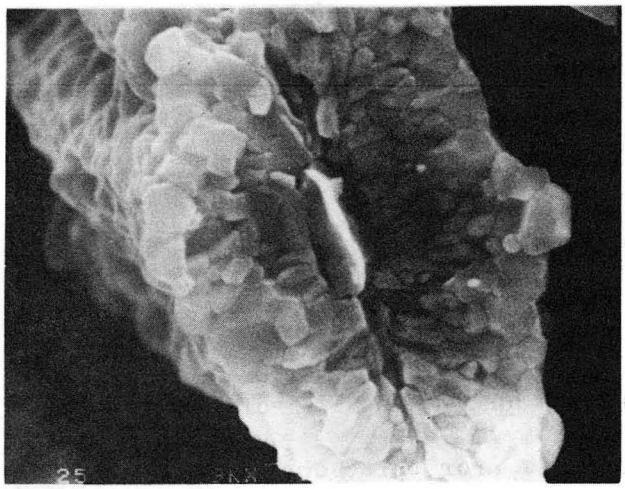

(b) 800°C/2D

XBB 824-4084

Fig. VII-28. The fractographs of the reacted A15 layer for samples heat treated at (a) 650°C, 14 days + 730°C, 2 days, and (b) 800°C for 2 days.

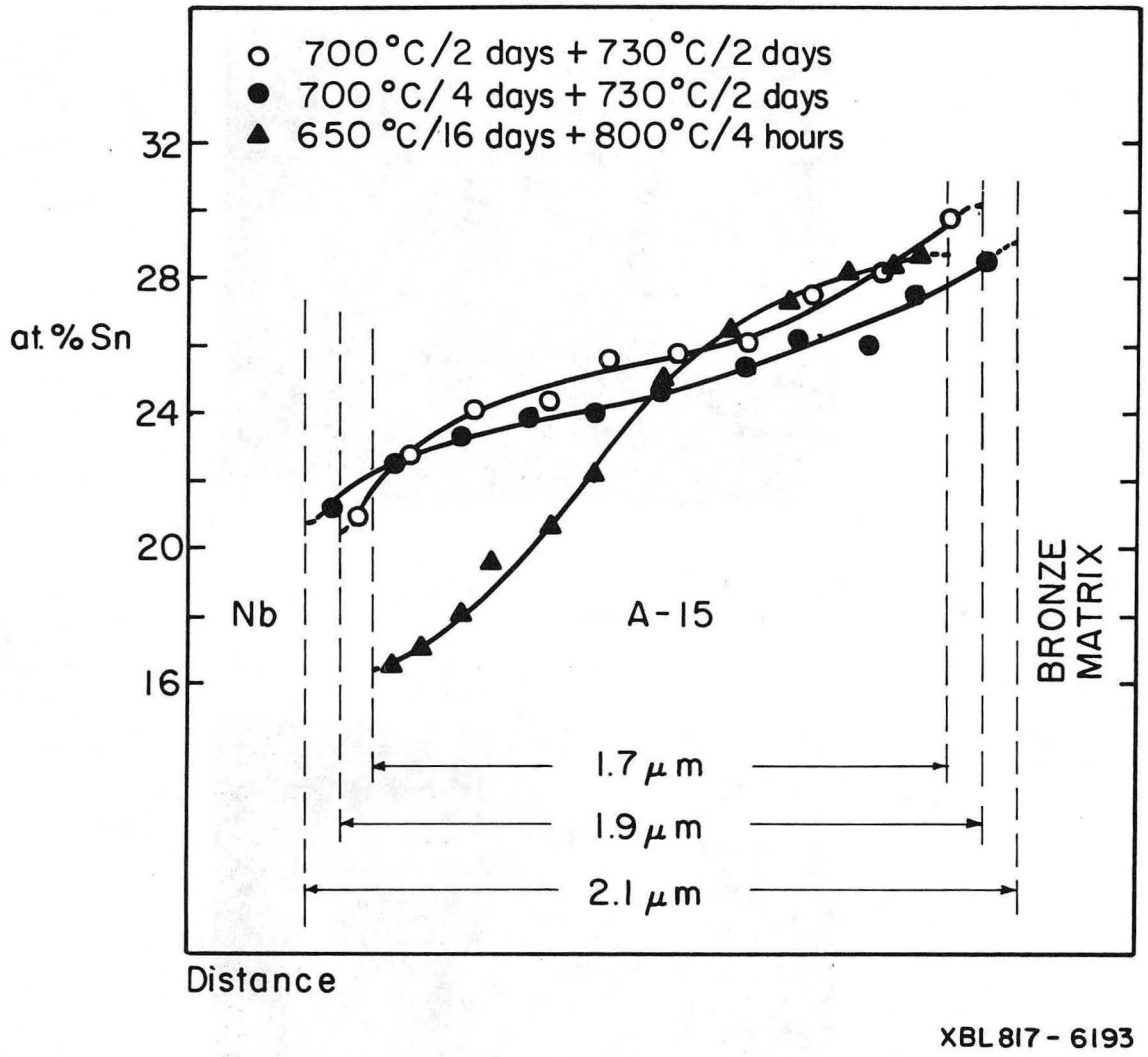

Fig. VII-29. The Sn concentration profiles, as determined by STEM/EDXS analysis, for three doubly aged specimens.

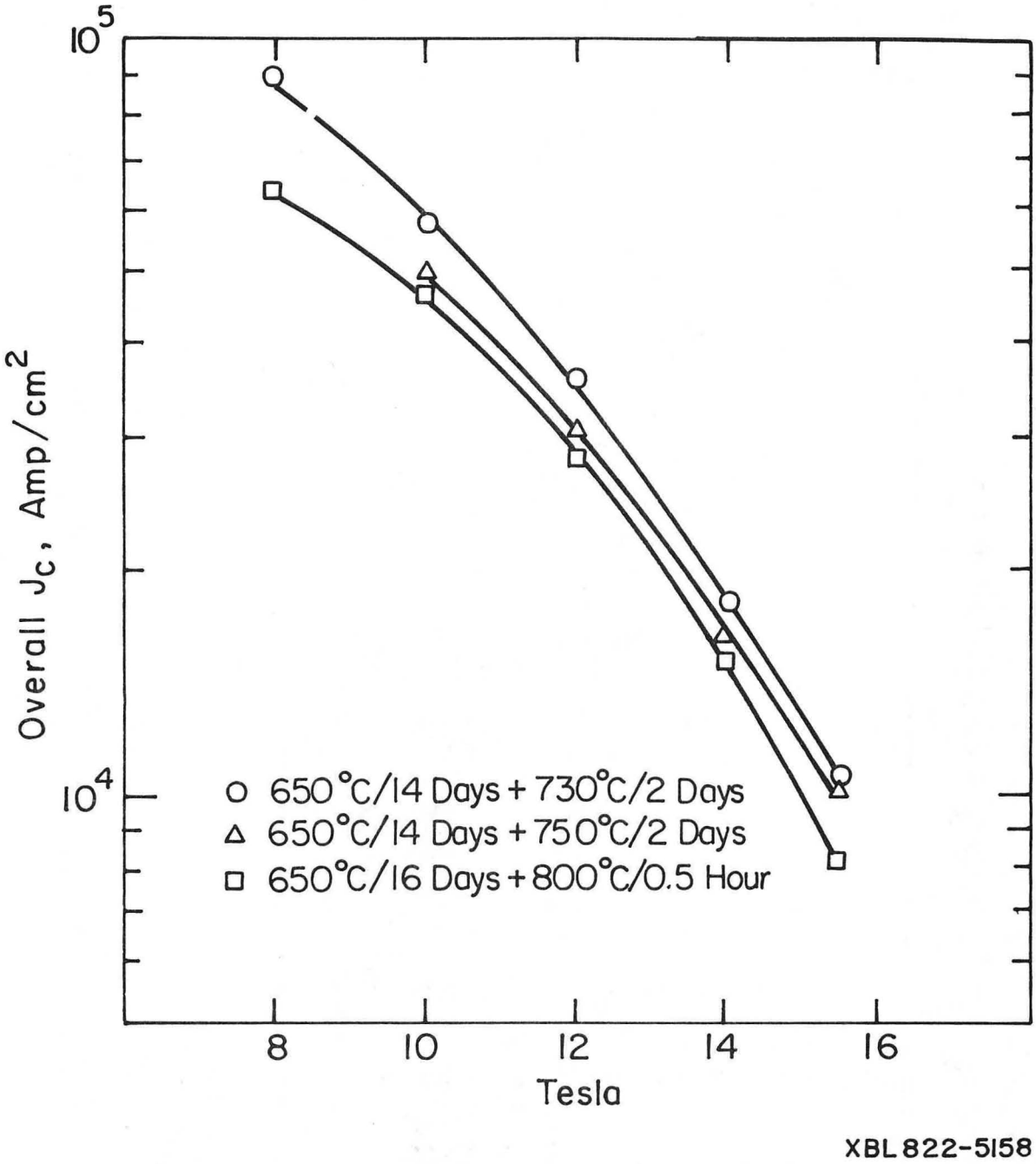

Fig. VII-30. The $J_c(H)$ characteristic of double-aged specimens starting with 650°C and followed by various higher temperature aging.

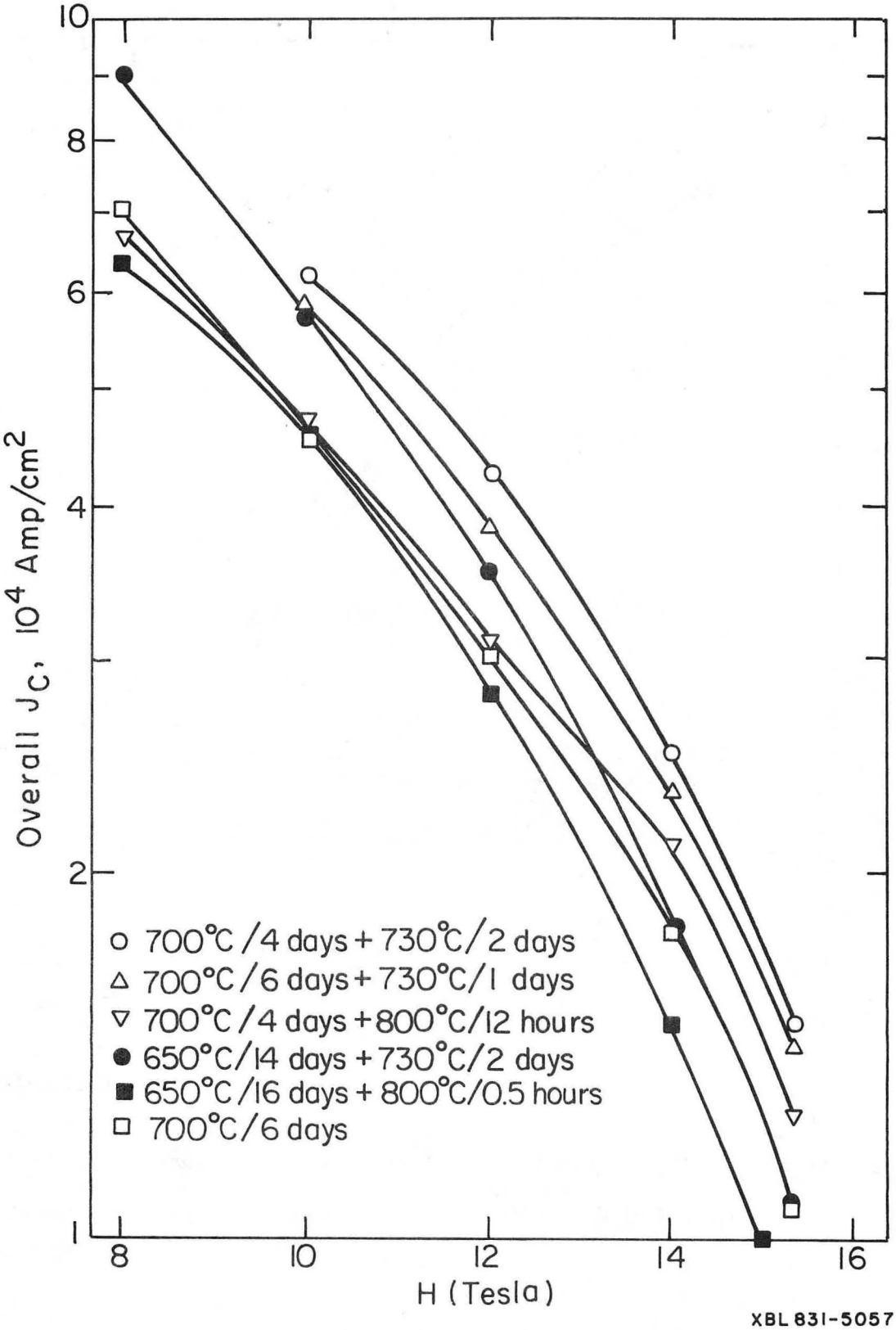

Fig. VII-31. The $J_c(H)$ characteristic of several double-aged specimens with 700°C as the starting heat treatment temperatures. The $J_c(H)$ of the 700°, 6 days sample is also included, representing the best obtained by isothermal aging.

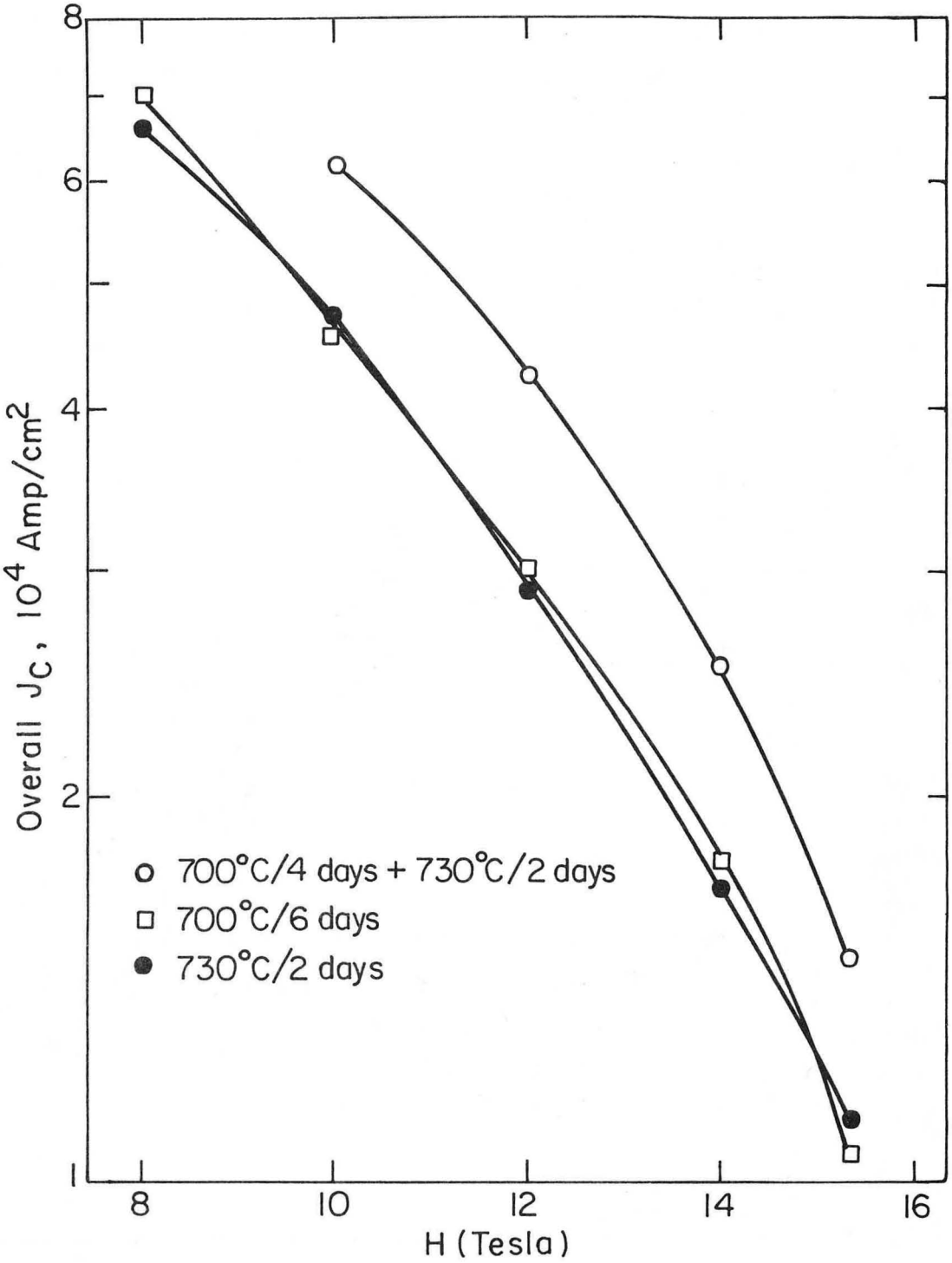

XBL 831-5056

Fig. VII-32. The critical current characteristic, $J_c(H)$, for a sample aged at 700°C/4 days + 730°C/2 days. $J_c(H)$ is compared to those attained by the best isothermal treatments: 700°C/6 days and 730°C/2 days.

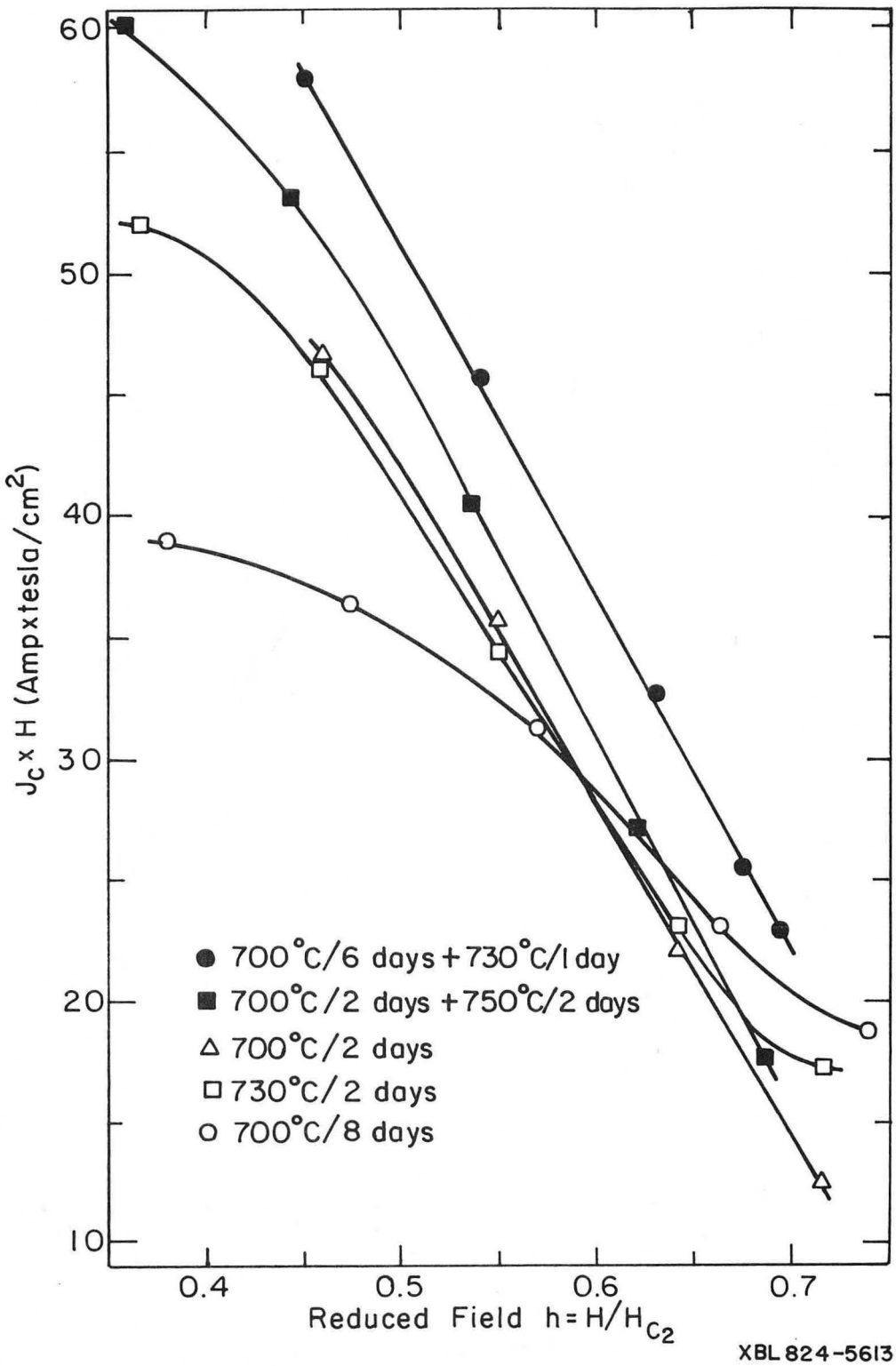

Fig. VII-33. The characteristic of volume pinning force, J_c X H, versus the reduced magnetic field, $h = H/H_{c2}$, for several doubly aged and isothermal treated specimens.

6700 780°C, 4 Days

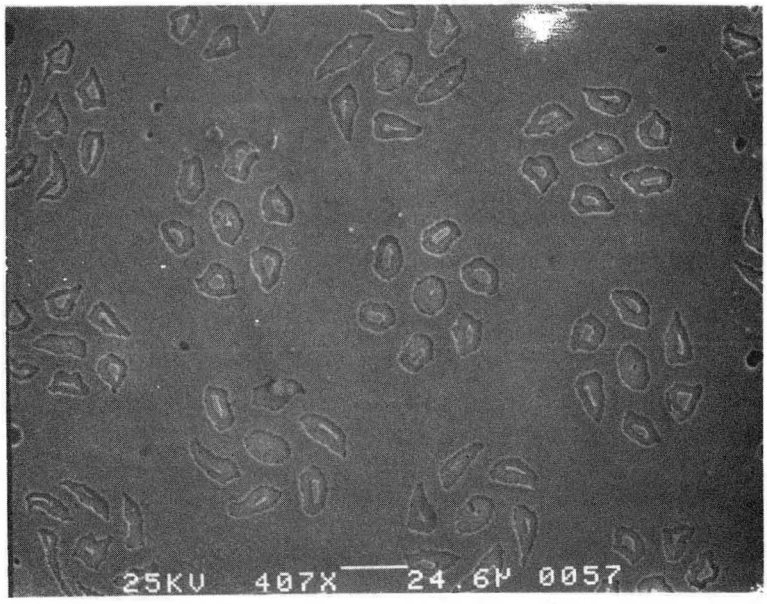

6762 730°C, 9 Days

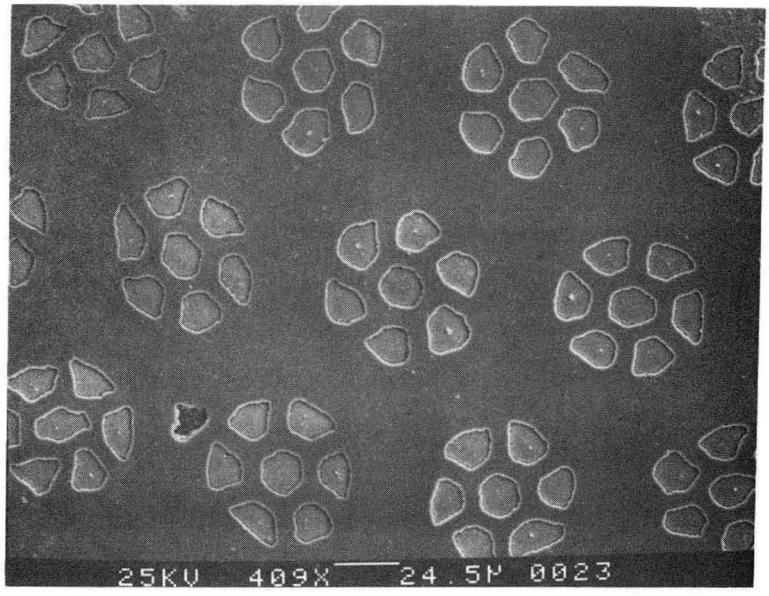

XBB 838-6964

Fig. VIII-1. Sections of two partly-reacted wires.

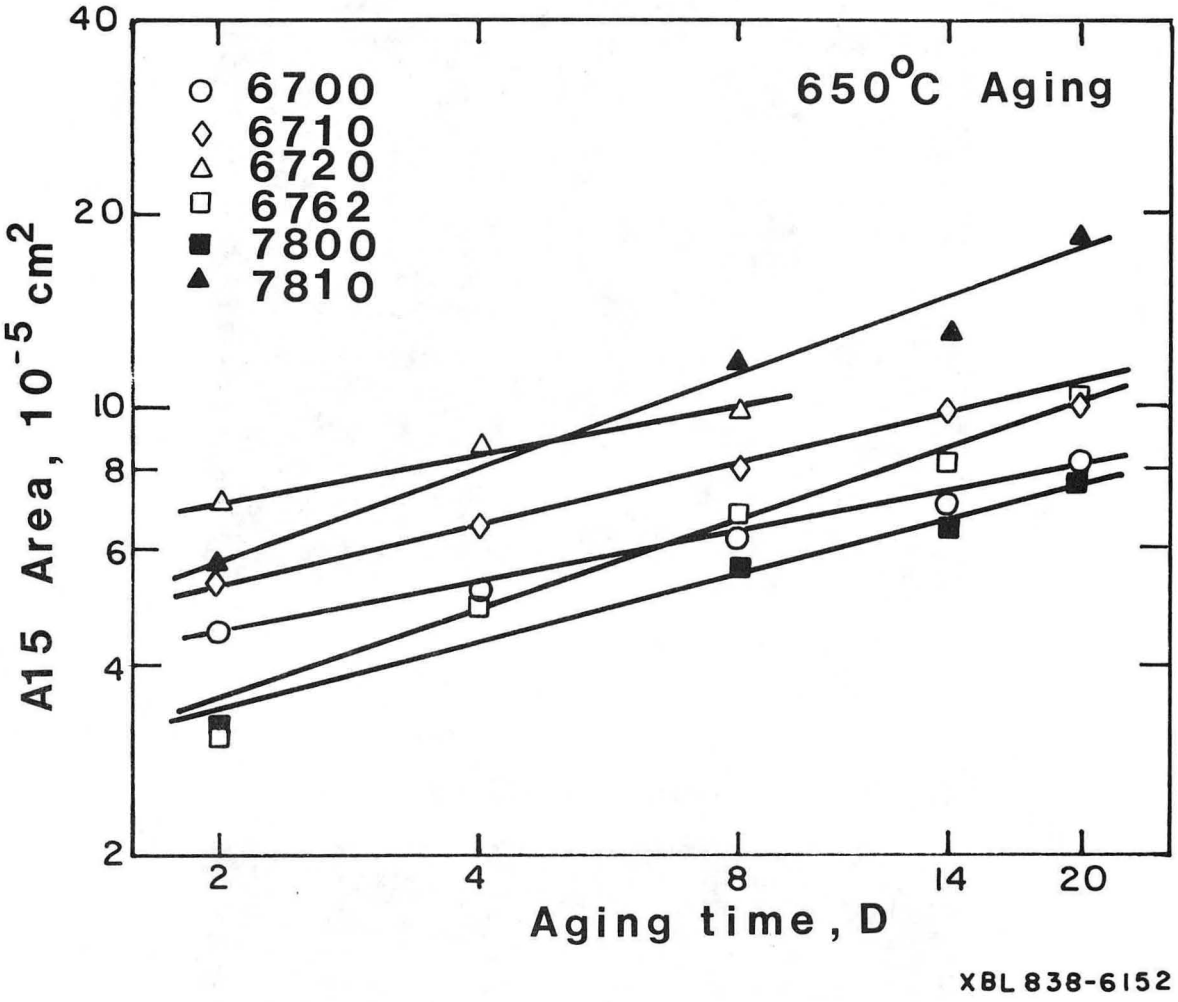

Fig. VIII-2. Cross-sectional area of Nb_3Sn phase versus aging time for samples aged at 650°C.

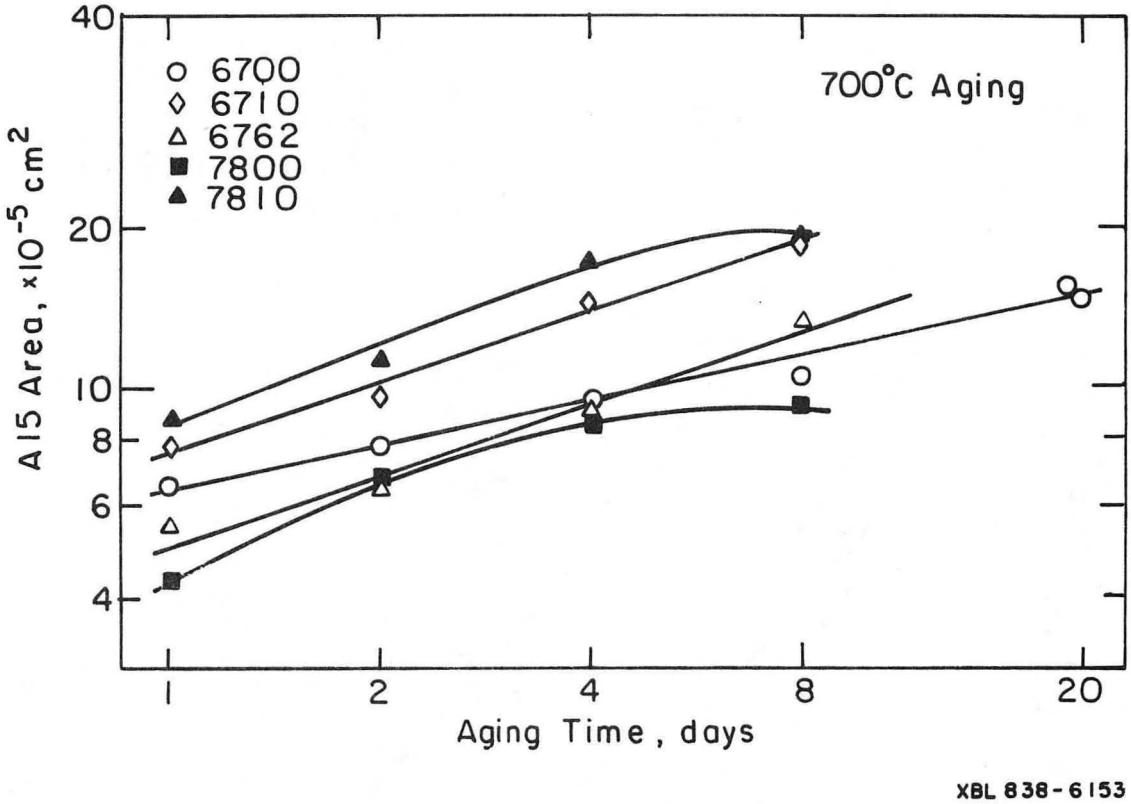

Fig. VIII-3. Cross-sectional area of Nb_3Sn phase versus aging time for samples aged at 700°C.

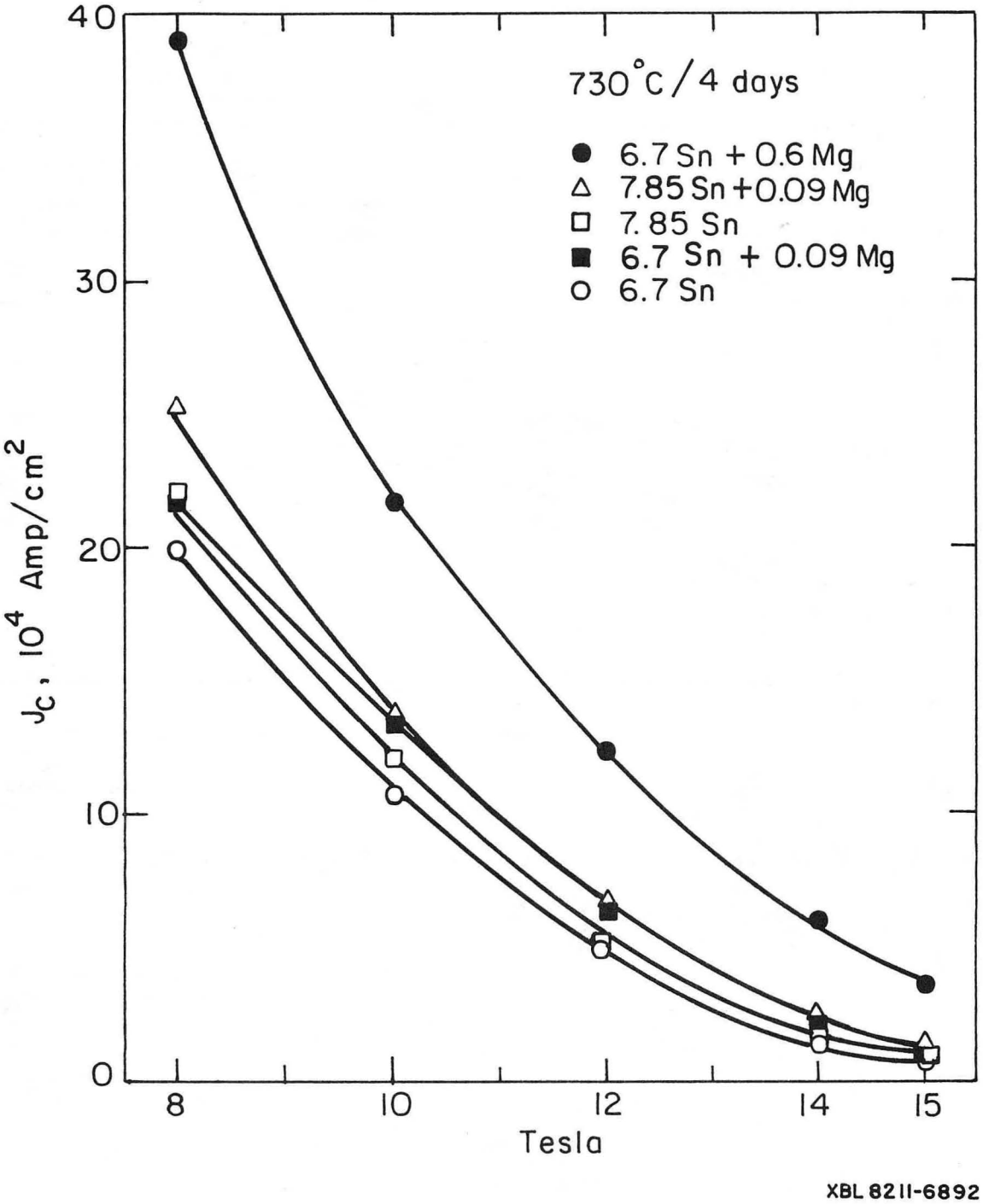

Fig. VIII-4. $J_c(H)$ for wires reacted at 730°C for 4 days.

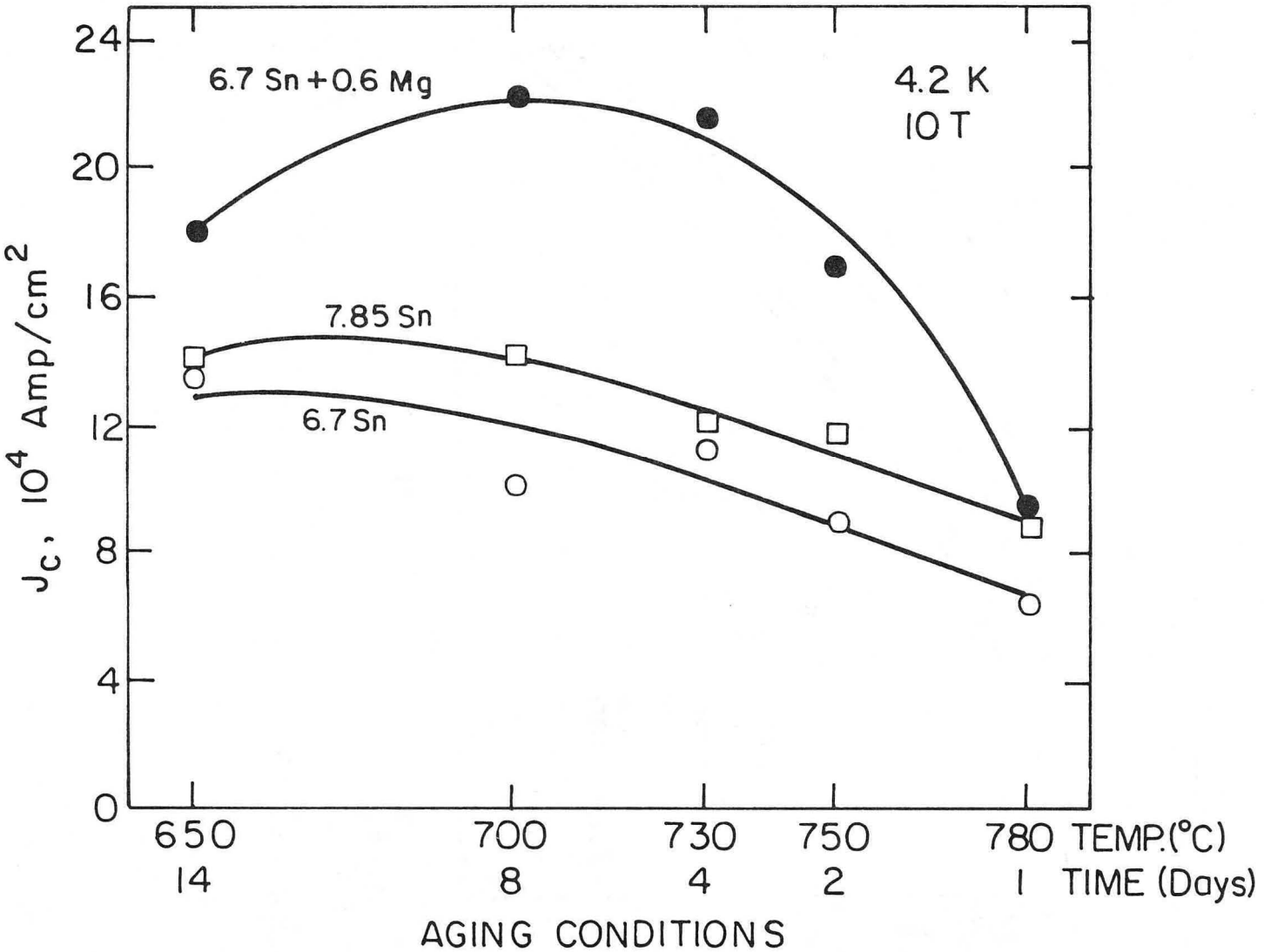

Fig. VIII-5. J_c at 10T versus the bronze-matrix composition and aging temperature. XBL 8211-6901

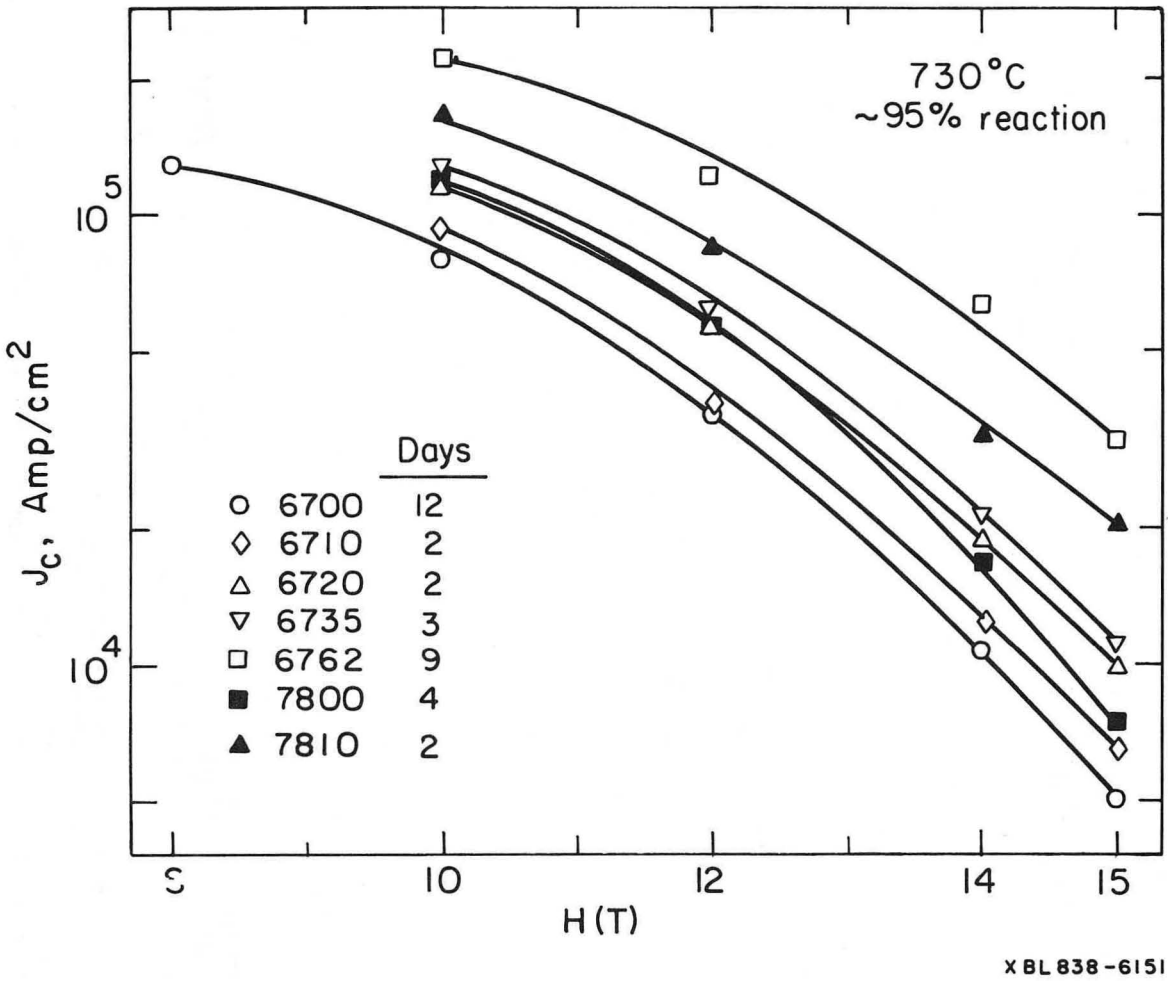

Fig. VIII-6. $J_c(H)$ for wires reacted at 730°C to near fully reaction.

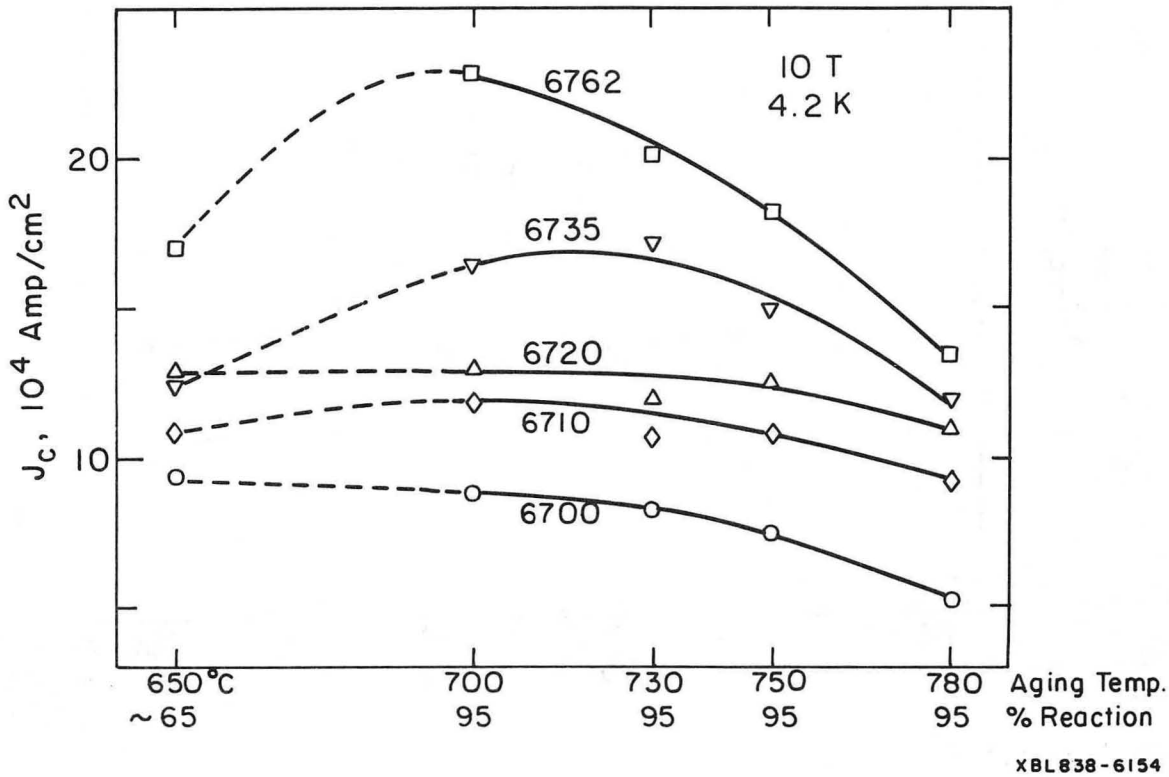

Fig. VIII-7. J_c(10T) versus aging temperature for various Mg concentrationsin 6.7% Sn-bronze at nearly fully reacted state.

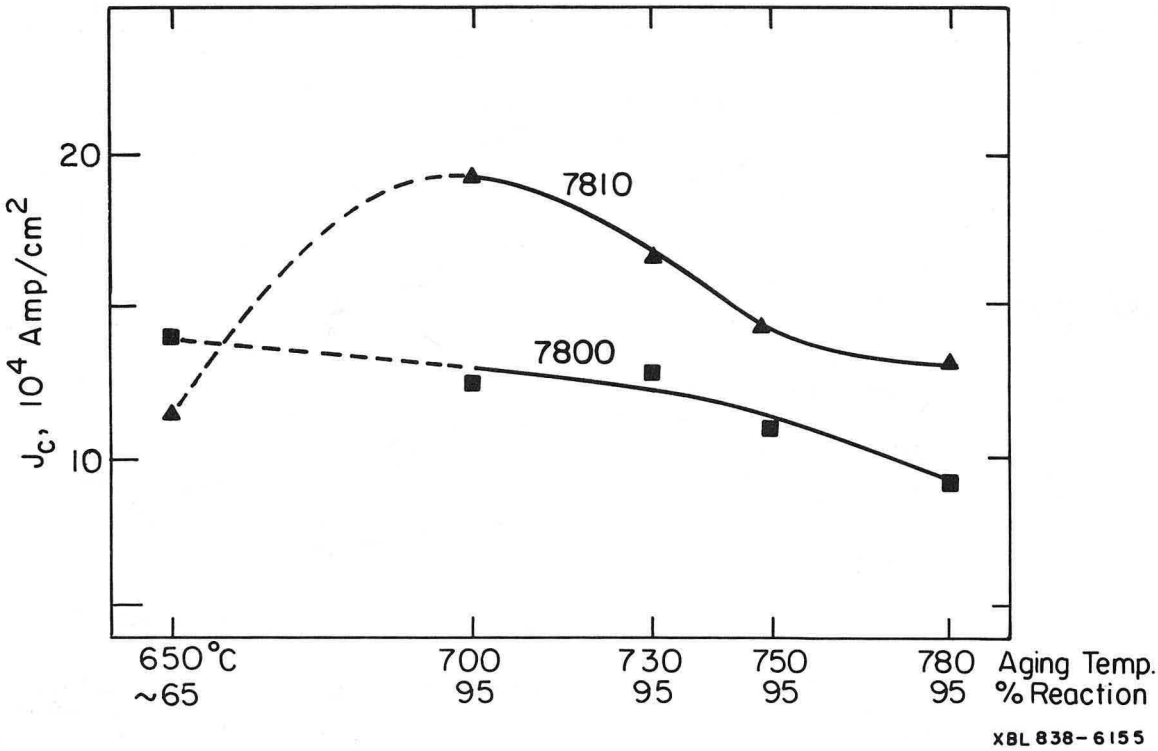

Fig. VIII-8. J_c at 10T versus aging temperature for 0.1% Mg doped and Mg-free wires with 7.8% Sn-bronze matrix.

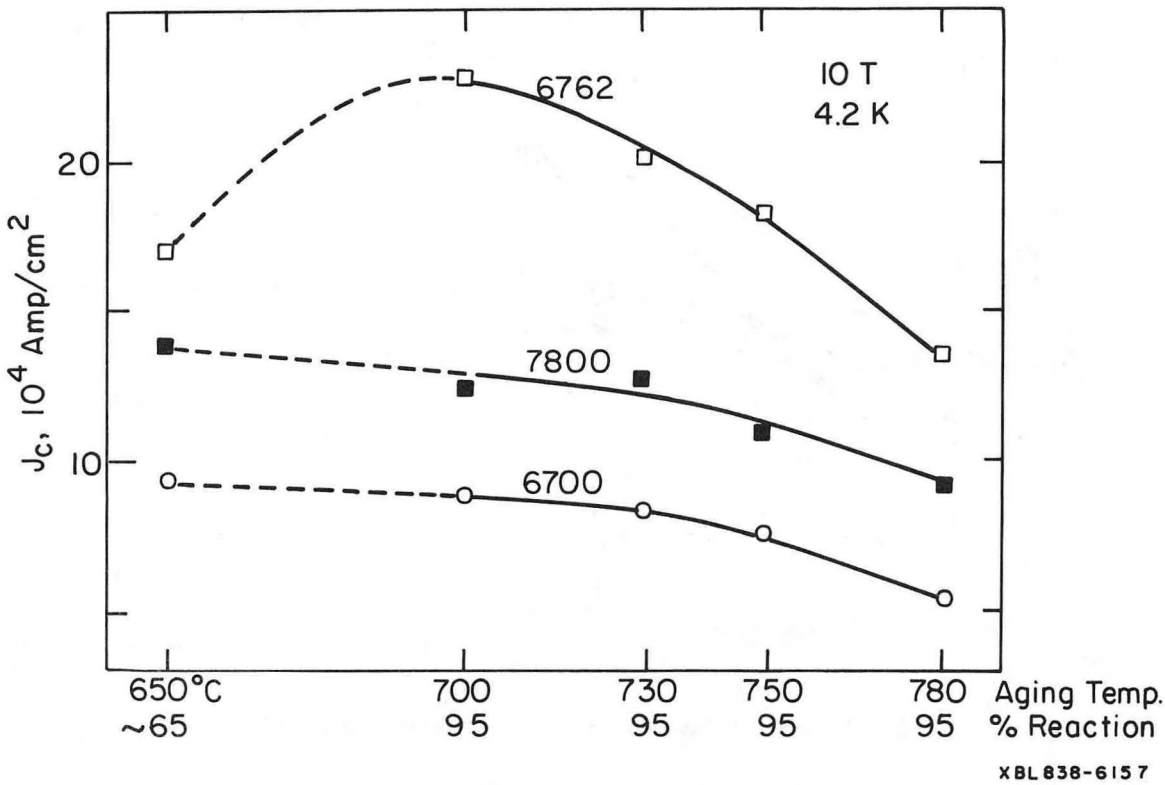

Fig. VIII-9. J_c at 10T versus aging temperature for 6.7 at.% Sn + 0.1% Mg wire comparing to the Mg-free Sn bronze wires.

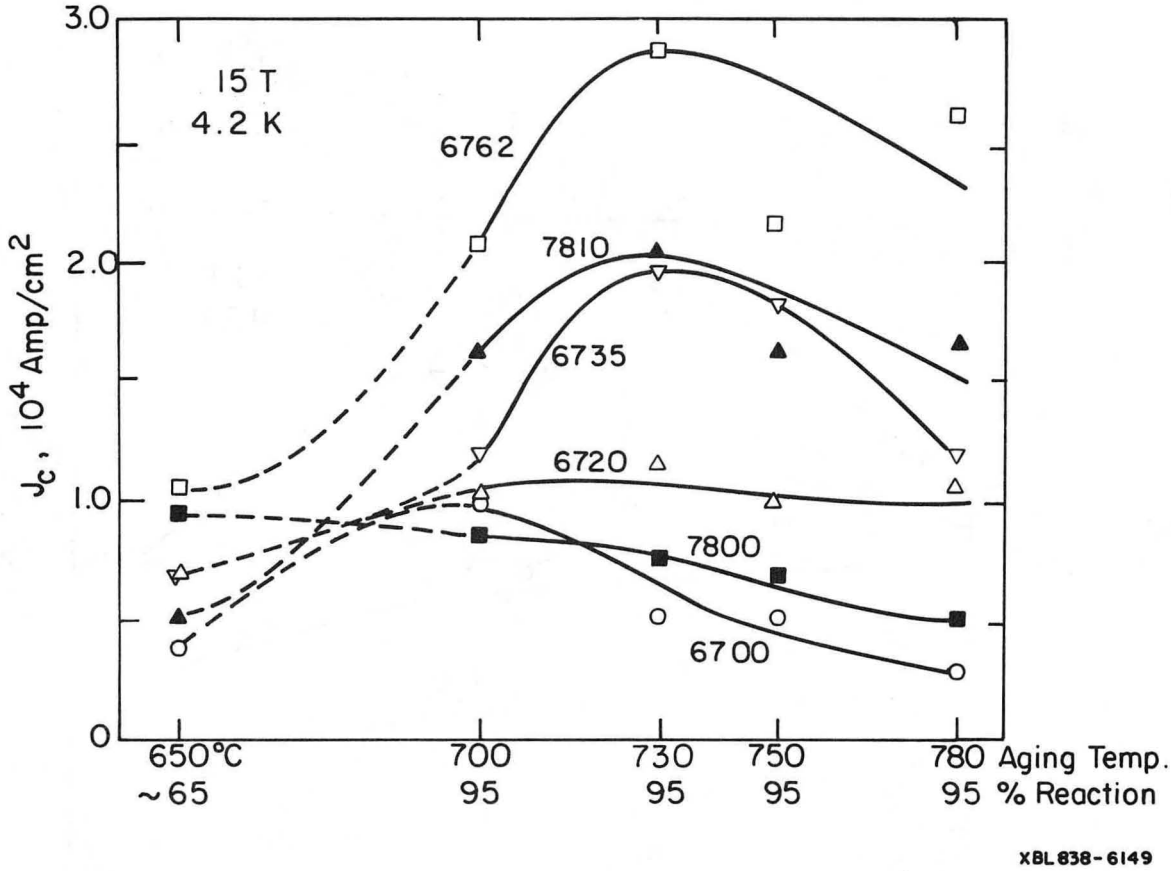

Fig. VIII-10. J_c at 15T versus aging temperature for wires at thrie mostly fully reacted state.

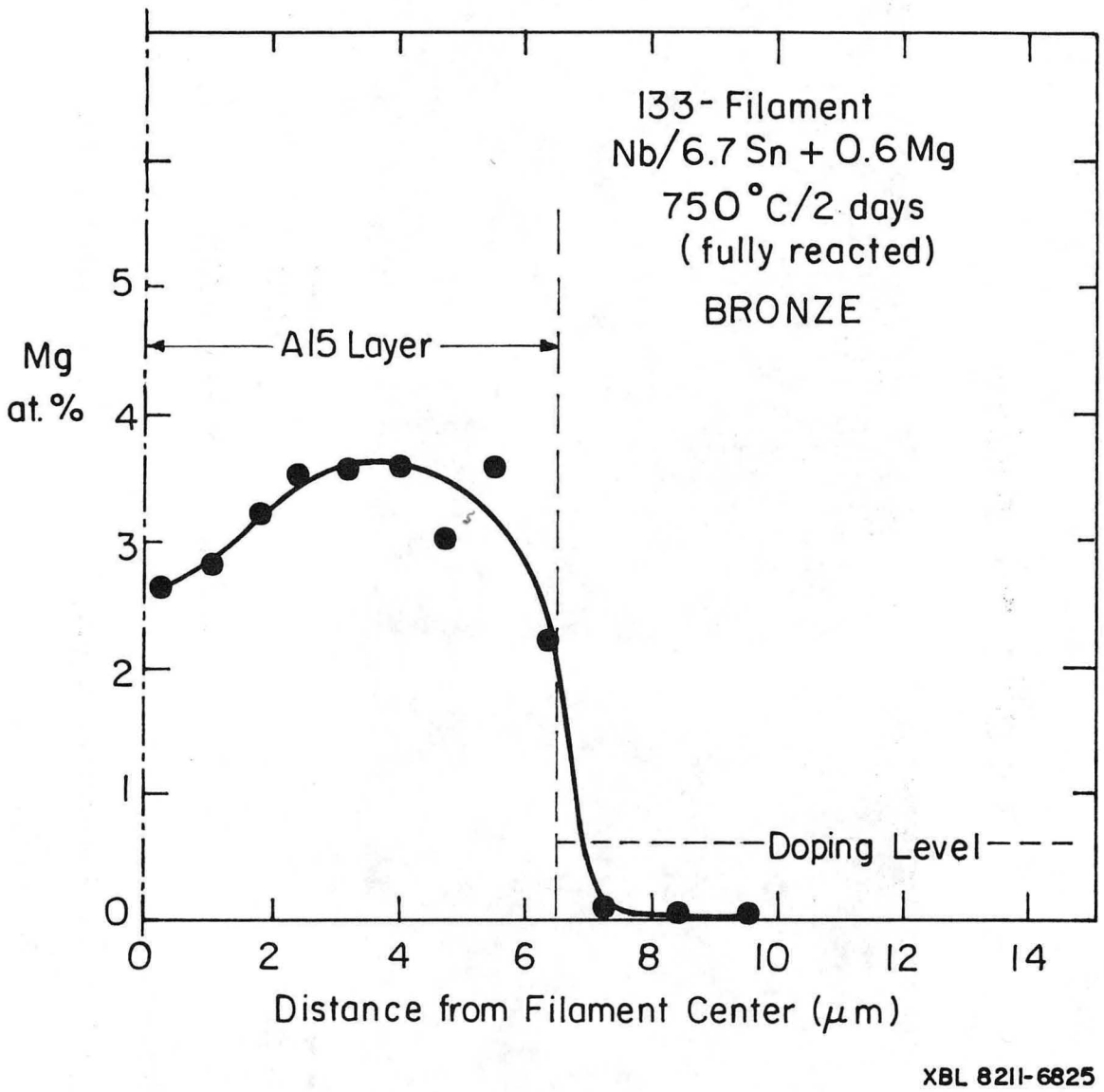

Fig. VIII-11. Electron microprobe composition profile for Mg.

750°C for 2 days

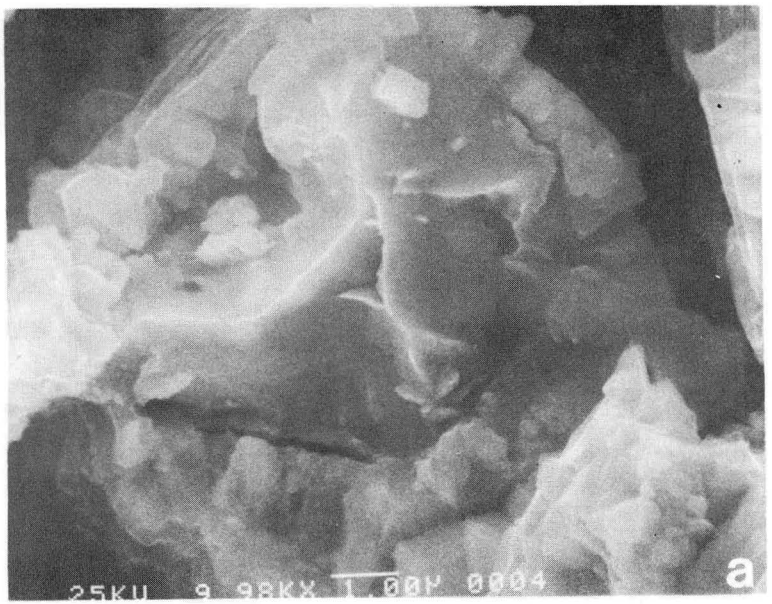

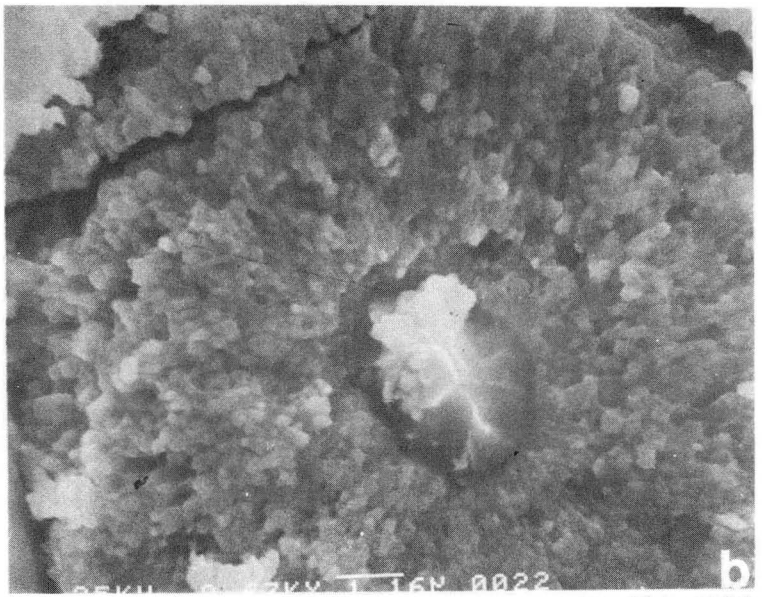

XBB 820-9998

1μm

1μm

6.7% Sn

6.7% Sn + 0.6% Mg

Fig. VIII-12 Scanning electron fractographs showing the Mg effect on the distribution of grain size for wires reacted at 750°C for 2 days.

750°C for 1 day

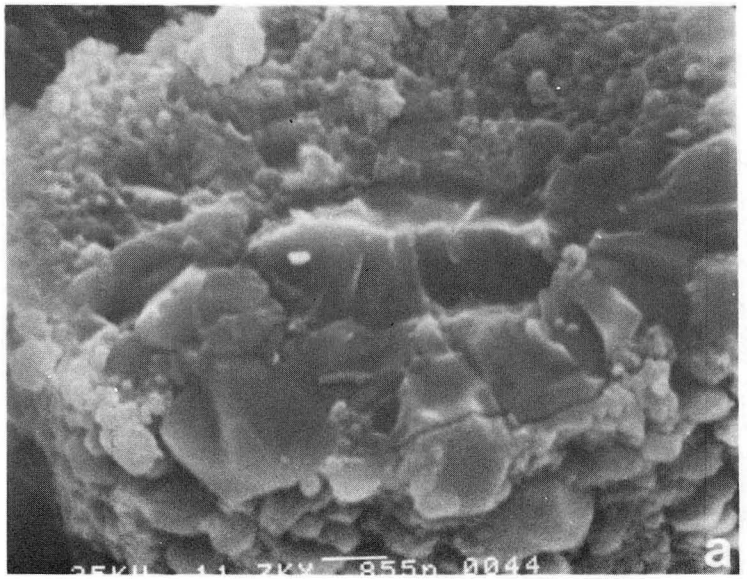

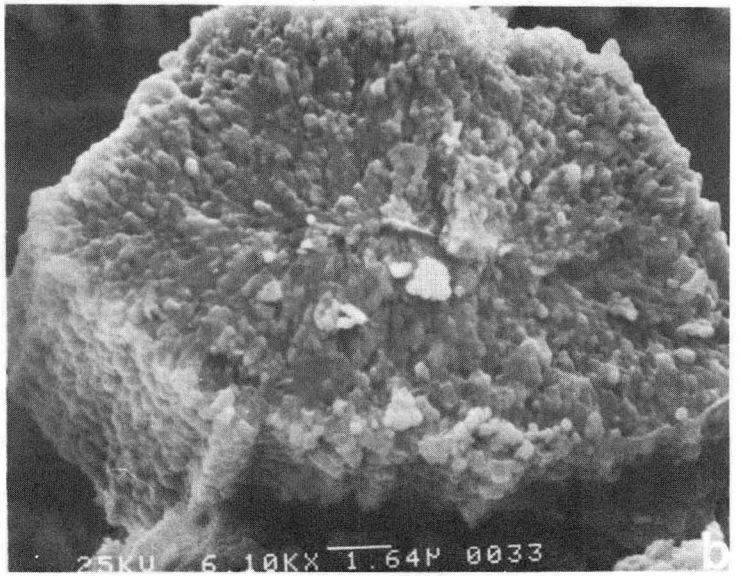

XBB 820-9998A

1 µm

7.85 % Sn

1 µm

7.85 % Sn + 0.085 % Mg

Fig. VIII-13. Scanning electron fractographs showing the grain size variations for wires reacted at 750°C for 1 day.

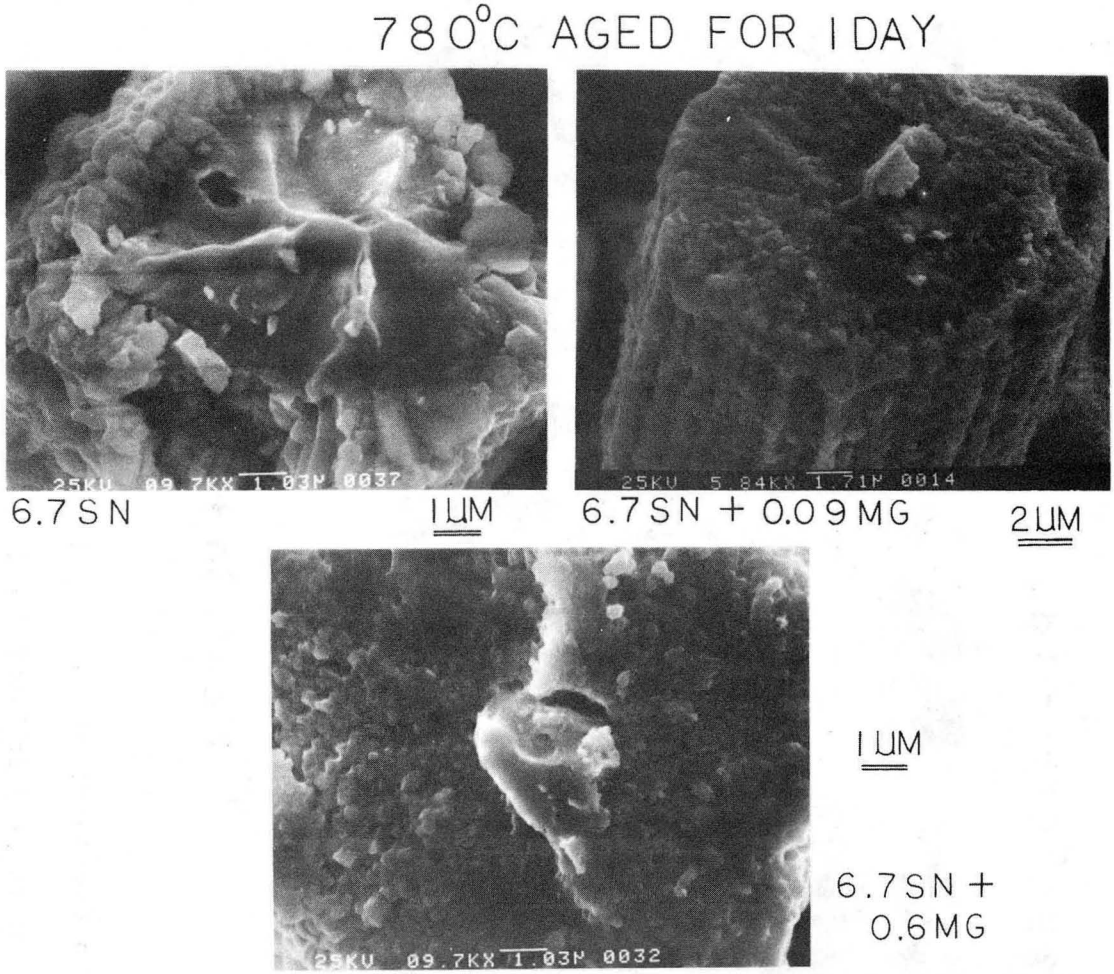

XBB 820-10447

Fig. VIII-14. SEM fractographs showing the grain size variation with Mg addition for wires reacted at 780°C.

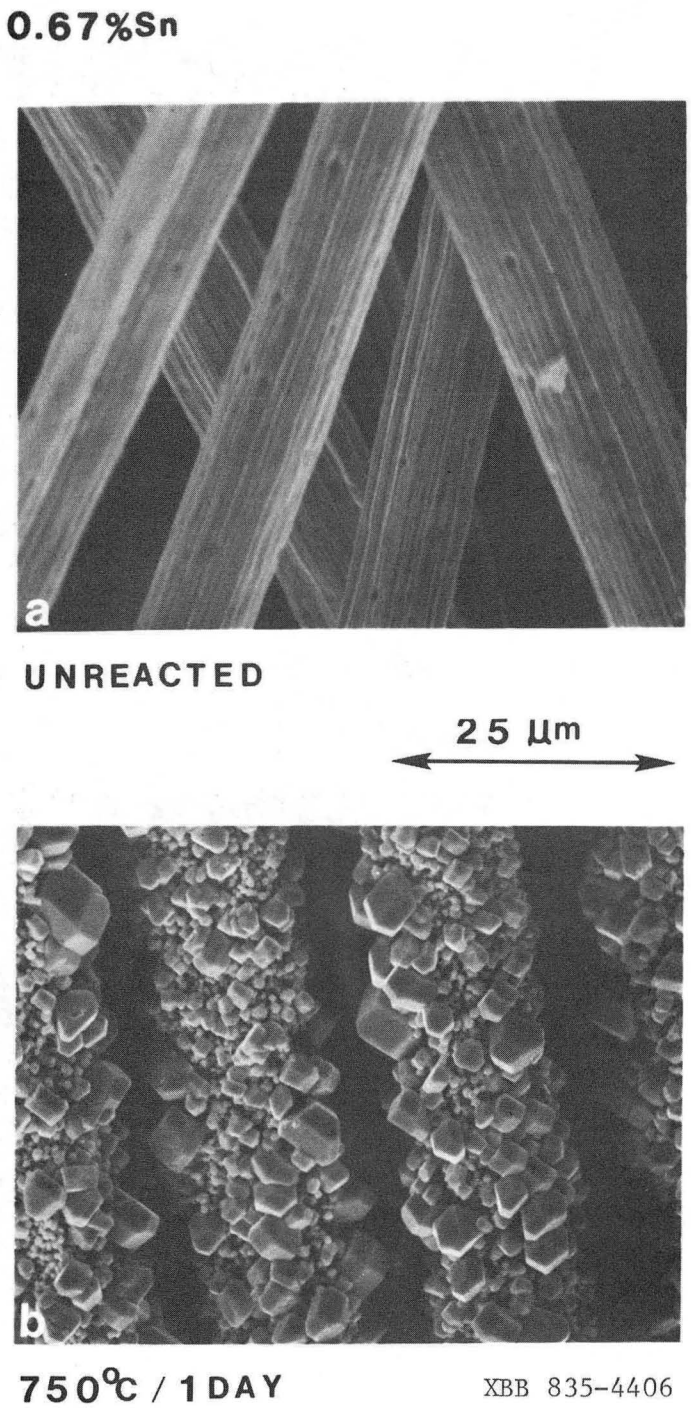

XBB 835-4406

Fig. VIII-15. Deep-etched scanning electron micrographs of filaments' periphery for (a) unreacted and (b) 750°C, 1 day heat treated wires.

6700

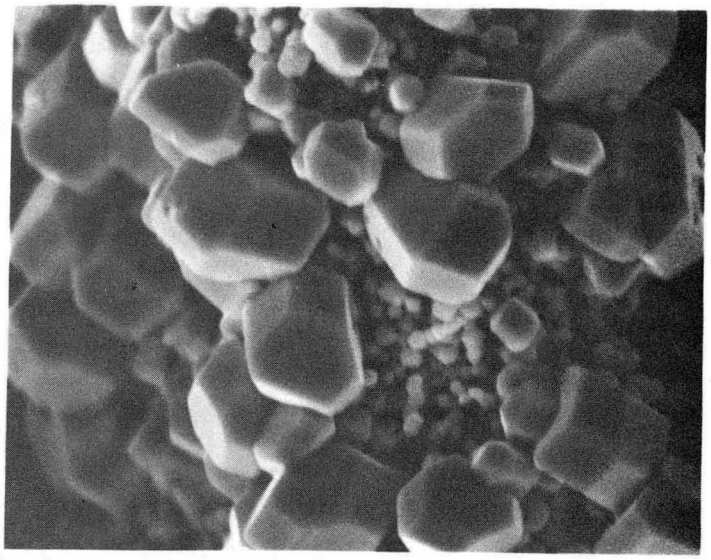

a. 730°C, 12 Days

10 μM

6762

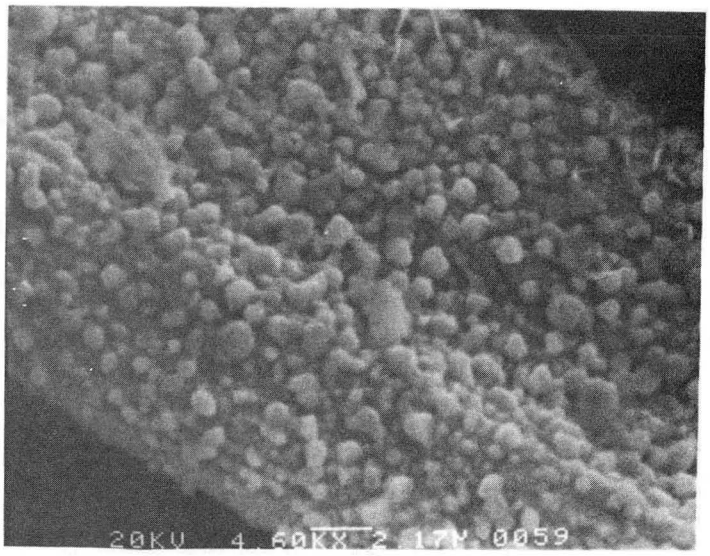

b. 730°C, 9 Days

XBB 838-6886

Fig. VIII-16. Deep-etched scanning electron micrographs of reacted filaments periphery showing the outer layer grains sizes variation.

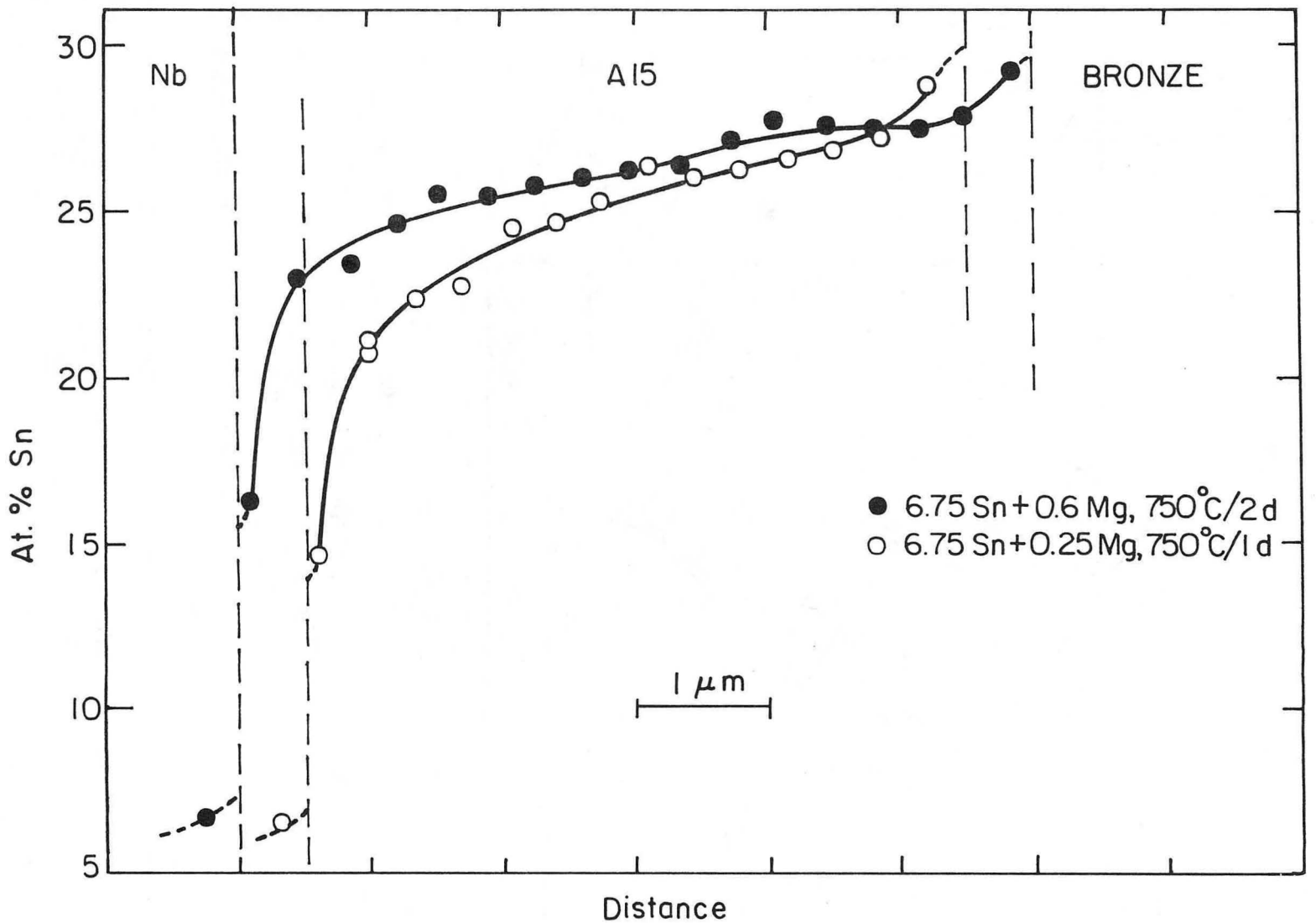

Fig. VIII-17. STEM/EDXS composition profiles for Sn within the reacted layer.

XBL 8211-6895

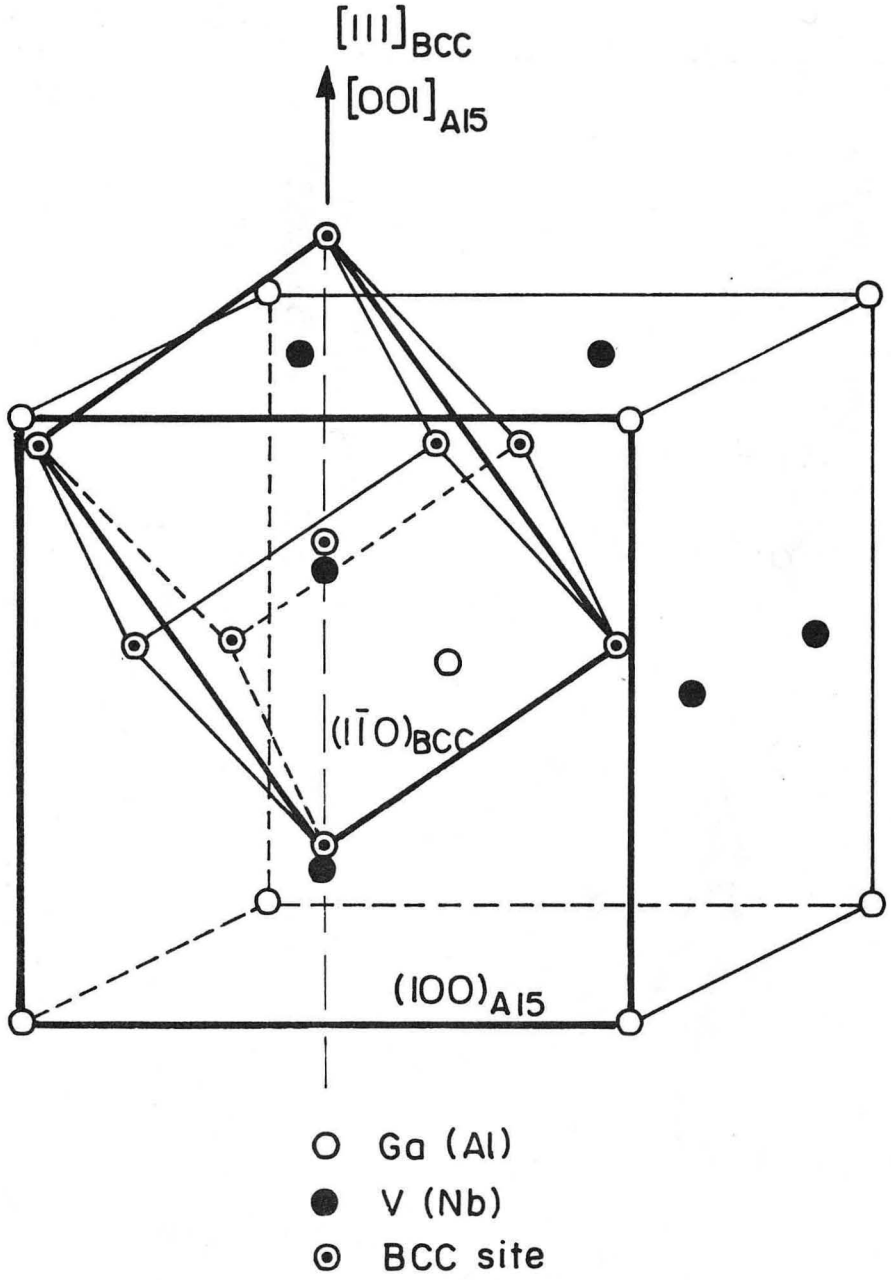

Fig. IX-1. The schematic representation of the orientation relationship between BCC and A15 crystal structure.

XBB 809-11069

Fig. IX-2. A typical TEM micrograph of the Direct-Precipitated V_3Ga.

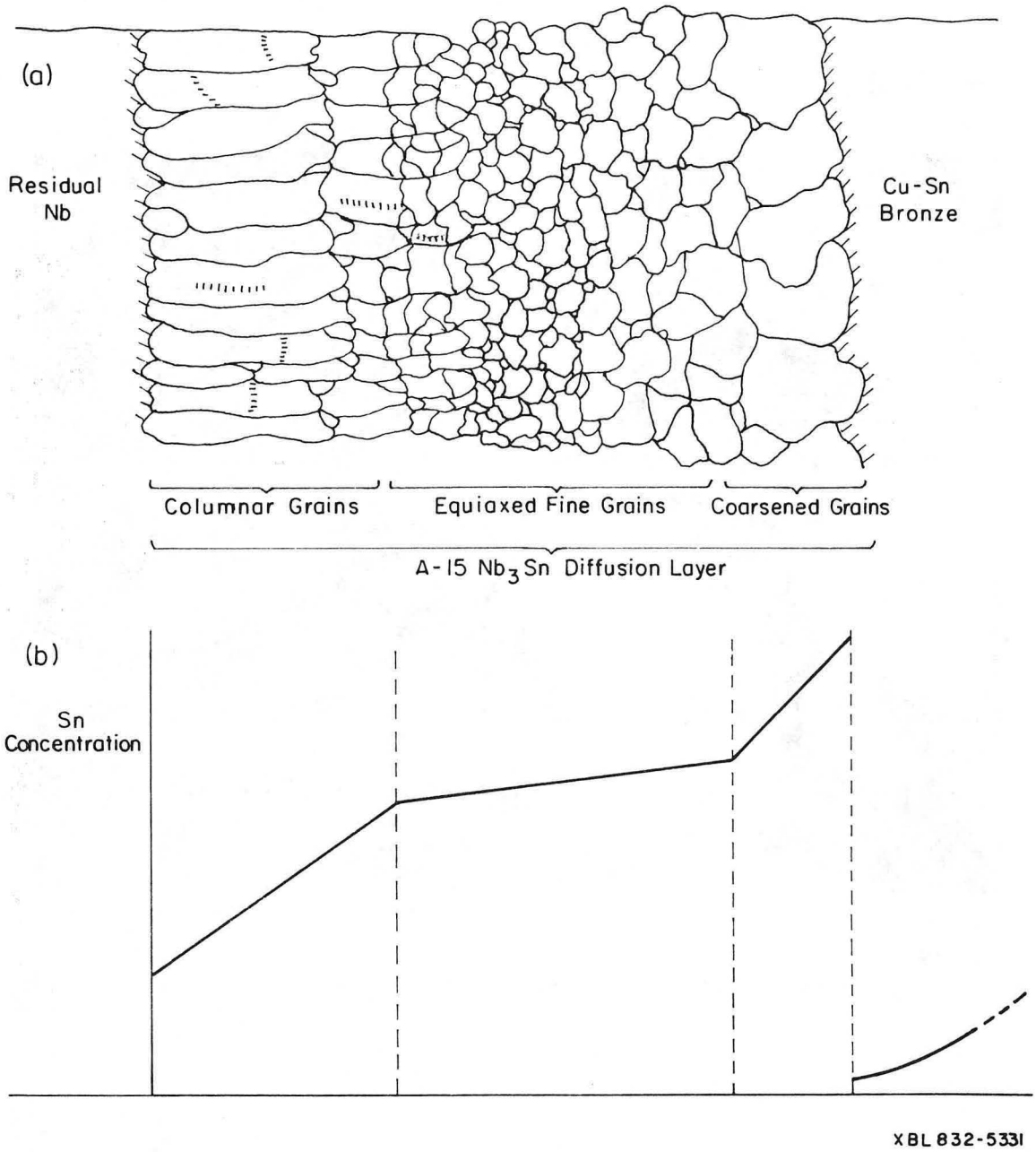

Fig. IX-3. A schematic representation of the three-shell composite structure of the A15 layer formed by the Bronze-process.

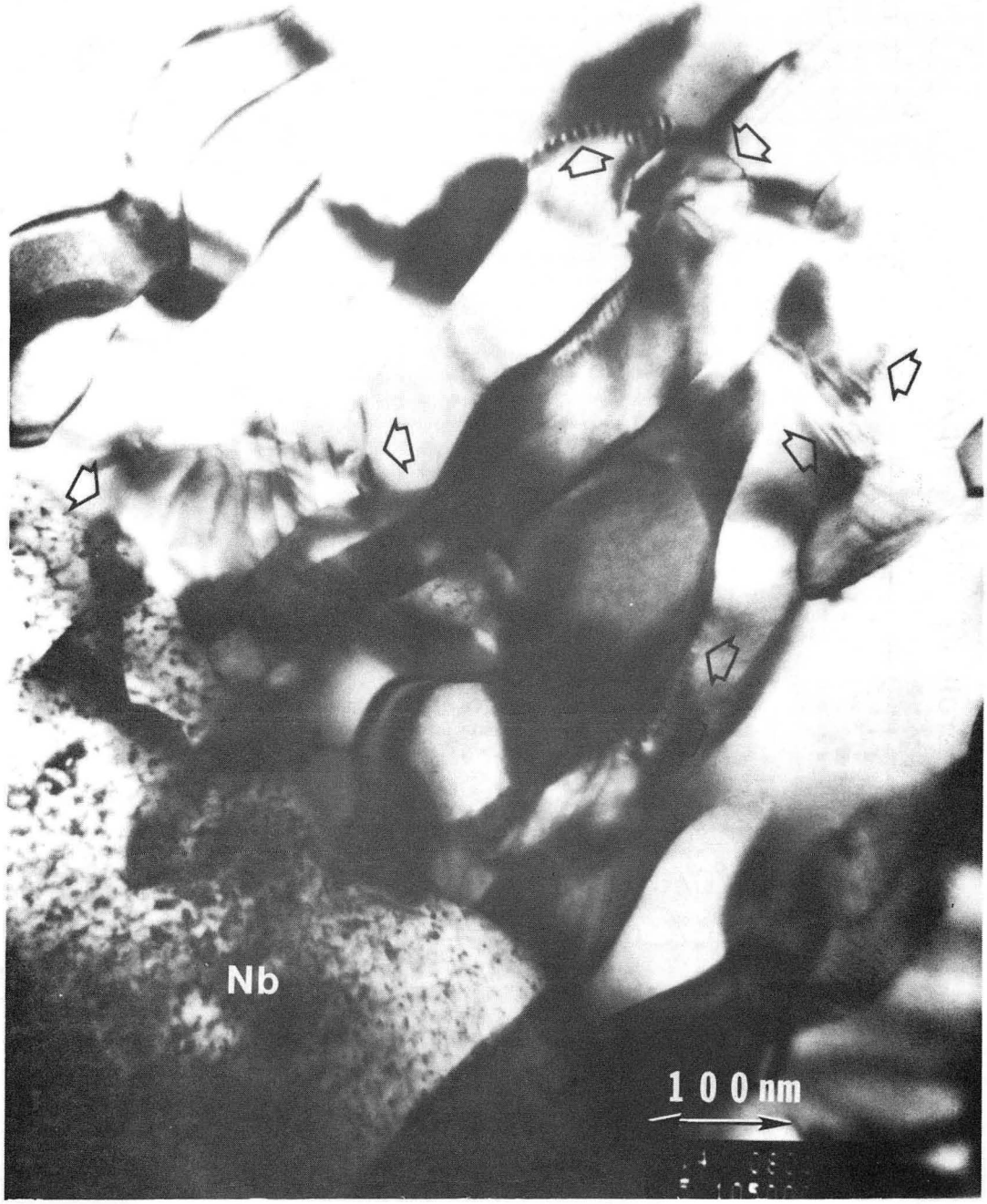

XBB 825-4151

Fig. IX-4. The polygonization of dislocation wall structures in the columnar grains near the residual Nb.

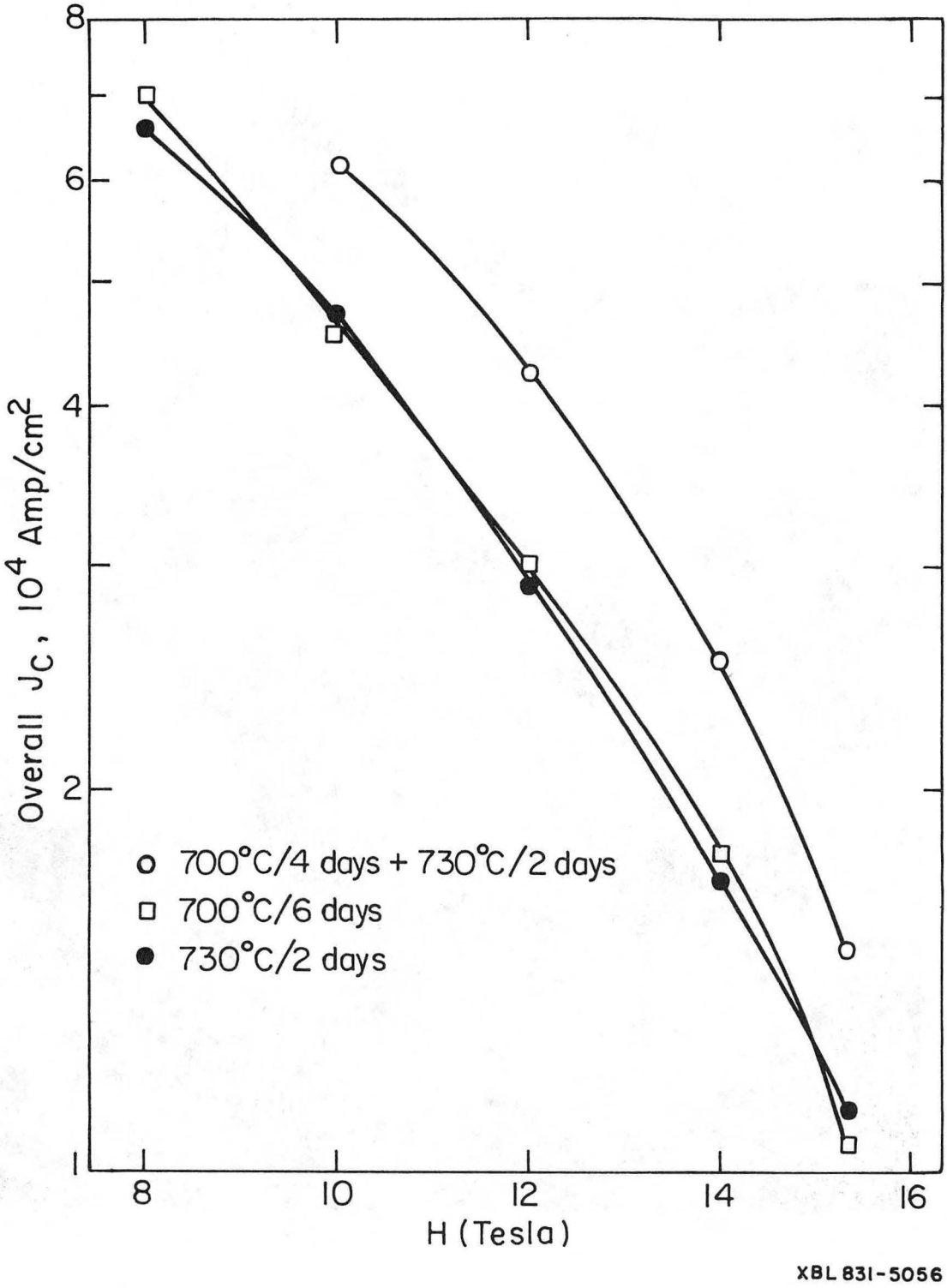

Fig. IX-5. The $J_c(H)$ characteristics of a bronze-processed wire.

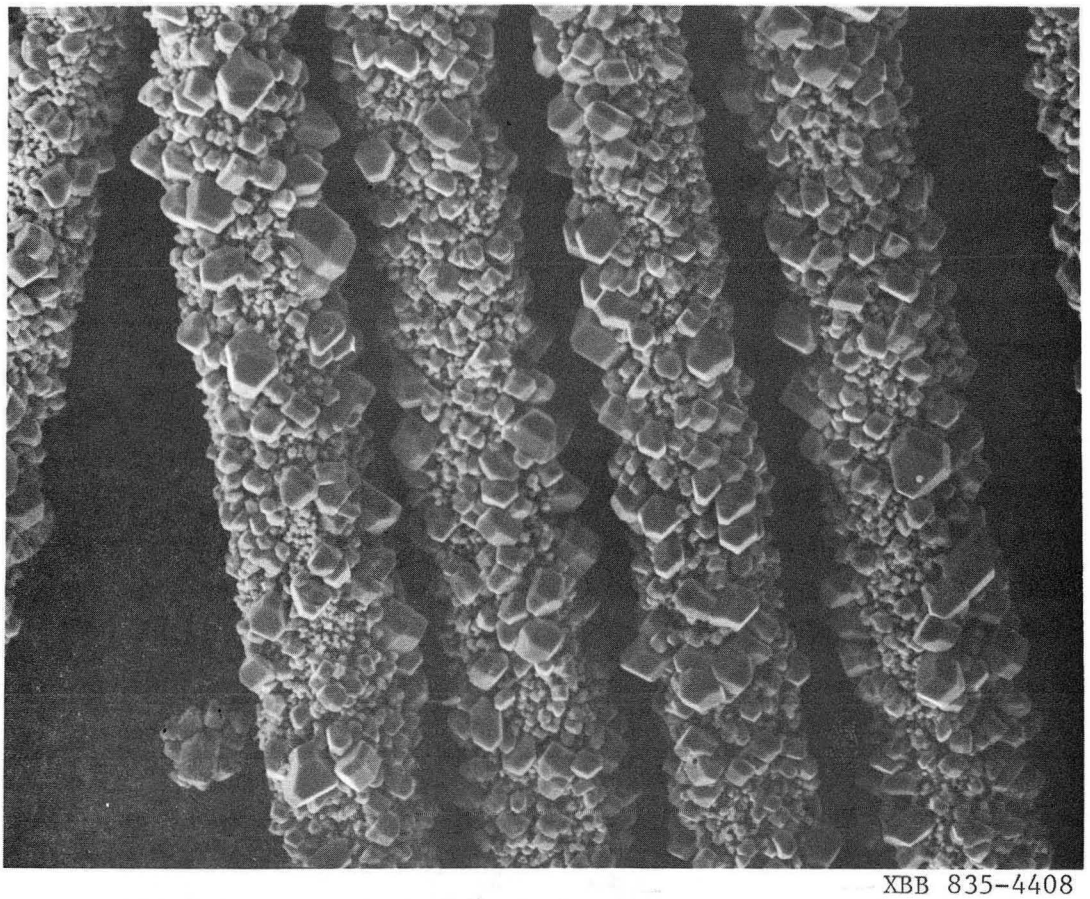

XBB 835-4408

Fig. IX-6. The J_c at 10T of the 6762 wire as compared to the Mg-free wires versus aging temperature.

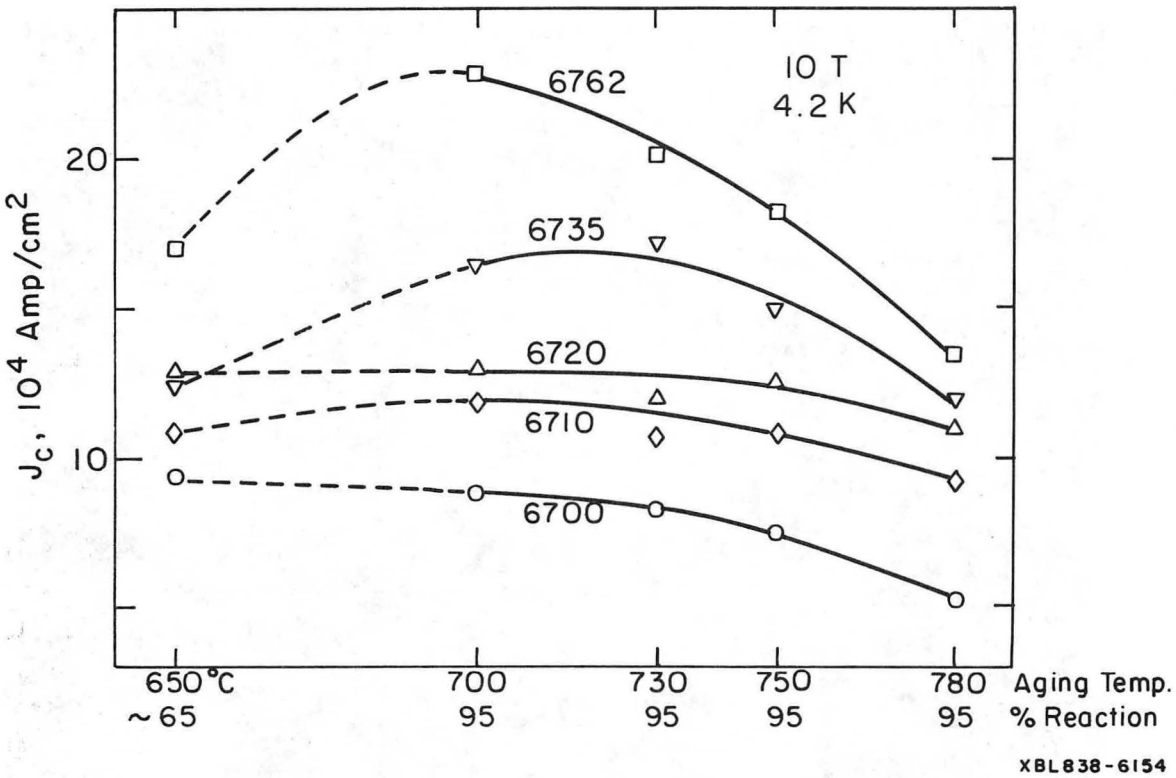

Fig. IX-7 The periperal surface of filaments without Mg addition showing the outer large coarsened grains and the central layer of the fine grains.

This report was done with support from the Department of Energy. Any conclusions or opinions expressed in this report represent solely those of the author(s) and not necessarily those of The Regents of the University of California, the Lawrence Berkeley Laboratory or the Department of Energy.

Reference to a company or product name does not imply approval or recommendation of the product by the University of California or the U.S. Department of Energy to the exclusion of others that may be suitable.

TECHNICAL INFORMATION DEPARTMENT
LAWRENCE BERKELEY LABORATORY
UNIVERSITY OF CALIFORNIA
BERKELEY, CALIFORNIA 94720